

Technische Universität München

Lehrstuhl für Bioverfahrenstechnik

**Modeling of the transient hydrodynamic
behavior of preparative chromatography
columns**

Martin Dorn

Vollständiger Abdruck der von der Fakultät für Maschinenwesen der Technischen Universität
München zur Erlangung des akademischen Grades eines
Doktor-Ingenieurs
genehmigten Dissertation.

Vorsitzende Prof. Dr. rer. nat. Sonja Berensmeier
Prüfer der Dissertation 1. Prof. Dr.-Ing. Dirk Weuster-Botz
2. Prof. Dr.-Ing. Heiko Briesen

Die Dissertation wurde am 27.06.2017 bei der Technischen Universität eingereicht und durch
die Fakultät Maschinenwesen am 27.09.2017 angenommen.

Acknowledgements

The present doctoral thesis was realized at the Institute of Biochemical Engineering at the Technical University of Munich under the supervision of Prof. Dr.-Ing. Dirk Weuster-Botz. During this time, many people contributed to this work and it is a pleasure to thank all of them.

Foremost, I would like to express my sincere gratitude to my advisor Prof. Dr.-Ing. Dirk Weuster-Botz for giving me the opportunity to conduct my doctoral thesis at his Institute and for his excellent guidance and support during the last years. In particular, I would like to thank him for the freedom provided during the development and establishment of the experimental and computational methods. I would also like to thank him for the opportunity to establish cooperations with international institutions and to present my research results at various international conferences as well as for the confidence he has placed in me.

I would like to thank Prof. Dr.-Ing. Heiko Briesen for accepting to be co-examiner and Prof. Dr. rer. nat. Sonja Berensmeier for taking over the position of the chairman of the jury.

I owe a great dept of gratitude to PD Dr.-Ing. Dariusch Hekmat for generously sharing his time and expertise, for his invaluable support and encouragement throughout the research work. I deeply appreciate the insightful discussions and his valuable contributions. I am also thankful to you and Michael Kuhn (Process Systems Engineering, Technical University of Munich) for sharing valuable results from your previous research work regarding the context of this thesis.

I would like to thank DI Dr. Christoph Goniva (DCS Computing GmbH, Linz, Austria) for the fruitful discussions and his excellent support regarding the CFDEM[®] software as well as Dr.-Ing. Carsten Schilde (IPAT, Technical University of Braunschweig, Braunschweig) for performing particle micromanipulation experiments. I am thankful to Prof. Dr.-Ing. Jörg E. Drewes (Urban Water Systems Engineering, Technical University of Munich) and Prof. Dr. Franz Pfeiffer (Biomedical Physics, Technical University of

Munich) for the opportunity to carry out confocal laser scanning microscopy and micro computer tomography analysis in their laboratories as well as Dr. Klaus Achterhold and Jonathan Schock for their excellent support and help. I thank Susanne Schnell-Witteczek (IMETUM, Technical University of Munich) for her help with scanning electron microscopy. I would also thank Achim Sprauer (Tosoh Bioscience, Darmstadt) and Dr. Reinhard Braaz (Roche Diagnostics GmbH, Penzberg) for valuable discussions, sharing their expertise and providing material support.

I am also thankful to Prof. Dr. Andreas Bausch (Biophysics, Technical University of Munich), Prof. Dr. Oliver Lieleg (Biomechanics, Technical University of Munich) and Prof. Dr.-Ing. Michael Manhart (Hydromechanics, Technical University of Munich) for fruitful scientific discussions on granular soft matter and packed bed hydrodynamics.

I would like to thank the German Research Foundation for funding and the TUM Graduate School for additional support of my attendance at the European Symposium on Biochemical Engineering Sciences 2016 in Dublin, Ireland.

I gratefully acknowledge my students for their great assistance, especially Philipp Wurdak, Franziska Eschbach, Florian Weber, Benjamin Münch, Maximilian Daschner, Daniel Helmdach, Michael Geitner, Frederik Luxemburger, Eva Pichlmeier and René Büscher.

My deep gratitude goes to all my colleagues and former colleagues for the practical help in the laboratory and for creating a pleasant working atmosphere at the Institute of Biochemical Engineering. Special thanks to my father Dr. Hans-Peter Dorn, Ann-Kathrin Leidpoldt, Ljubomir Grozdev and Christina Pfaffinger for proofreading of this thesis.

Finally, I owe my deepest gratitude to my family and friends for their wide-ranging support and, of course, to my partner Vivien who has always believed in me.

Table of Contents

1	Introduction	1
2	Motivation and Objectives	3
3	Physical Background	7
3.1	Characteristics of Single Particles	7
3.1.1	Solid Particle Mechanics	8
3.1.2	The Viscoelastic Particle	14
3.1.3	The Particle as a Biphasic Material Compound	19
3.2	Characteristics of Particle Packings	23
3.2.1	Geometric Properties of Particle Packings	23
3.2.2	Packings of Monodisperse and Ideally Rigid Particles	23
3.2.3	Packings of Polydisperse Particles	26
3.3	Fluid Flow in Particle Packings	26
3.3.1	Flow Regimes	27
3.3.2	Correlation of Flow and Packing Pressure Drop	28
3.3.3	Dispersion	30
3.3.4	Force Transmission in Dense Packings	31
3.3.5	Packing Compression	38
4	Computational Background	43
4.1	Computational Fluid Dynamics (CFD)	43
4.1.1	Governing Equations	44
4.2	The Discrete Element Method (DEM)	46
4.2.1	Governing Equations	46
4.2.2	DEM solver	50
4.3	The CFD-DEM Coupling	51

4.3.1	Coupling Algorithm	52
4.3.2	Efficient Parallel Computing by Load-Balancing	54
5	Materials and Methods	55
5.1	Micro-Chromatography Columns and Operating Set-up	55
5.2	Consumables and Further Equipment	57
5.3	Programs and Software	58
5.4	Experimental Methods	58
5.4.1	Characterization of Single Particles	58
5.4.2	Characterization of Bulk Packings	60
5.4.3	Analysis of the Wall Support	65
5.4.4	Analysis of Particle Migration	65
5.4.5	Analysis of Different Column Packing Strategies	68
5.5	Computational Methods	70
5.5.1	Modular Structure of the Simulation Case	70
5.5.2	The Simulation Set-up	72
5.5.3	CFD Solver Adjustment	74
5.5.4	Reduction of Computational Effort by Coarse Graining	75
6	Characterization of Compressible Polymeric Chromatography Particles	77
6.1	Particle Size Distributions	77
6.2	Particle Density	79
6.3	Particle Surface Structure	79
6.4	Compression Load Relaxation Analysis	82
6.5	Quasi-Static Compression Analysis	84
6.6	Viscoelasticity Versus Poroelasticity	87
6.7	Determination of Material Properties	89
6.8	Conclusion	93
7	Characterization of Particle Bulk Packings	95
7.1	Hydrodynamic Load	95
7.1.1	Axial Packing Compression-Relaxation Behavior	97
7.1.2	Particle Deformation and Force Transmission	98
7.2	Mechanical Load	101
7.2.1	Axial Packing Compression-Relaxation Behavior	101

7.2.2	Particle Deformation and Force Transmission	103
7.3	Bulk Packing Porosity	104
7.4	Influence of The Wall Support On The Hydrodynamic Packing Behavior	107
7.4.1	Packing Pressure Drop	108
7.4.2	Packing Compression-Relaxation Behavior	110
7.4.3	Continuum Model of the Wall Support	112
7.5	Conclusion	114
8	Development and Evaluation of the Simulation Model	117
8.1	Selection of a Proper Particle Contact Model	117
8.1.1	Relevant Parameters and Assumptions	118
8.2	Reduction of Computational Effort	120
8.2.1	The Coarse Grain Approach	121
8.2.2	Pseudo Two-Dimensional Simulation Model	124
8.3	Model Evaluation and Accuracy	126
8.3.1	Parameter Studies and Sensitivities	126
8.3.2	Hydrodynamic Packing Compression	129
8.3.3	Mechanical Packing Compression	130
8.4	Conclusion	131
9	Analysis of Particle Migration During Column Operation	135
9.1	Experimental Particle Migration Study	135
9.1.1	Influence of The Column Diameter	135
9.1.2	Influence of The Particle Size	137
9.2	Computational Particle Migration Study	141
9.2.1	Bidisperse Particle Size Distribution	141
9.2.2	Polydisperse Particle Size Distribution	143
9.3	Conclusion	145
10	Analysis of Different Column Packing Strategies	149
10.1	Influence of Friction Forces on the Column Packing Process	149
10.1.1	Comparison of Different Column Packing Methods at Different Hydrodynamic Loads	152
10.1.2	Measured Column Behavior During Long-Term Cyclic Operation	155
10.2	Simulated Column Behavior During Long-Term Cyclic Operation	158

10.2.1	Analysis of Simulated Force Distribution	160
10.2.2	Analysis of Simulated Radial Fluctuations of the Axial Flow Velocity	163
10.2.3	Evaluation of Axial Hydrodynamic Dispersion	165
10.3	Conclusion	166
11	Conclusions	169
12	Outlook	179
13	Glossary	181
13.1	List of Abbreviations	181
13.2	Latin Symbols	182
13.3	Greek Symbols	186
14	List of Figures	189
15	List of Tables	193
16	Bibliography	195
Appendix A	Materials and Equipment	211
Appendix B	Supplementary Information	215
B.1	Laboratory Equipment	215
B.2	CFD-DEM Simulations	216
Appendix C	Supplementary Methods	221
C.1	Fluorescent Labeling of Chromatographic Particles	221
C.1.1	Relevant Particle Properties	221
C.1.2	Contrast Agents for Microscopic Particle Analysis	223
C.2	Derivation of the SLS model	229
C.2.1	Kelvin type of the SLS model	230
C.2.2	Maxwell type of the SLS model	231
C.3	Integration of the SLS model	232

1. Introduction

Chromatography is an essential bioseparation and purification technique in the biotechnological and pharmaceutical industry [Carta and Jungbauer 2010] which was reported for the first time by the Russian scientist M. S. Tswett in his article on chlorophyll substances published in 1903 [Ettre and Sakodynskii 1993; Schmidt-Traub 2005, pp. 1-8]. Since then, chromatographic separation has been evolved as a standard analytical method, or at preparative scale, as a key technology for the purification of a variety of substances in industrial applications. Here, preparative chromatography competes with conventional mechanical and thermal separation techniques such as membrane filtration, extraction or rectification which are primarily designed for high throughput and thus offer competitive operative costs and efficiency. However, the advancement of chromatographic separation during the last century, which is closely linked to the synthesis of novel high value macromolecular products and to the isolation and purification of natural substances, resulted in significant advantages of the chromatographic technology compared to conventional separation techniques. Due to its high compound selectivity, chromatography is able to meet the high demands on product purity of pharmaceuticals, proteins, agrochemicals and food additives [Schmidt-Traub 2005, pp. 1-8].

The performance and efficiency of the chromatographic separation is governed by the properties of the packed bed [Guiochon 2006]. These involve i) the characteristics of the single particles such as particle size distributions, surface modification, porosity, and pore size and ii) the homogeneity of the packed bed. The latter depends on the distribution of interparticle voids and significantly influences dispersion and backmixing. However, the bed characteristics were proven to be highly inhomogeneous in radial as well as in axial column direction [Guiochon 2006]. Especially packings being composed of compressible polymeric resins are known to exhibit a complex transient hydrodynamic and hysteretic behavior when the column being operated at its hydrodynamic design limit [Hekmat et al. 2011]. Particle breakage was observed at flow velocities near the critical flow velocity at which the slope of the pressure-flow profile becomes infinite and

the bed collapses [Stickel and Fotopoulos 2001]. Frequently occurring column integrity breaches, such as medium wall detachment, partial bed subsidence or formation of cracks and flow channels, were also reported [Larson et al. 2003; Hekmat et al. 2011]. This leads to increased dispersion and backmixing as well as to a limitation of the separation efficiency. The origin of this behavior is often ascribed to the interplay of the packing material and the column wall as well as the packing method [Guiochon 2006]. However, detailed experimental investigation of the causes by either optical or acoustic methods (e.g. Photoacoustic Tomography, PAT) is limited due to the opaque and highly porous microscopic particles.

Therefore, intensive research and development is still necessary in order to optimize the design and operating conditions of a chromatography unit for the most economical implementation of a given separation task. Optimizing chromatographic processes in terms of efficiency and throughput means optimizing a nonlinear, multivariate system, a problem which is challenging to analyze experimentally as well as theoretically [Guiochon and Lin 2003; Rathore and Velayudhan 2003; Carta and Jungbauer 2010]. The column and separation performance is affected by adsorption/desorption thermodynamics, mass transfer kinetics, and hydrodynamics [Schmidt et al. 2012], i.e. processes which couple the fluid phase with the solid packed particle phase.

During the last decades, considerable effort has been devoted to i) the improvement of chromatographic performance [Boschetti 1994; Rathore and Velayudhan 2003; Jungbauer 2005], ii) the elucidation of the fundamental thermodynamics of the process [e.g. Knox and Pyper 1986; Snyder et al. 1989], as well as iii) the development of methods in order to maximize the production rate and/or minimize the costs [e.g. Golshan-Shirazi and Guiochon 1989, 1990; Felinger and Guiochon 1993; Larson et al. 2003; Guiochon 2006].

However, due to the limited accessibility and nonconsideration of the parameters influencing the hydrodynamic column behavior, the theoretical understanding is limited and the causes of the previously described effects are still largely unknown. This makes it difficult to develop dedicated guidelines for the optimal design and operation of chromatography columns. Hence, the existing guidelines and design specifications are still based in a large part on empiric approaches.

Detailed mechanistic modeling of the particle phase taking into account interparticle micromechanics and fluid-particle interactions is obviously needed to elucidate the complex hydrodynamic behavior of chromatography columns.

2. Motivation and Objectives

In chromatographic separation science, there has not been done much work on the fundamental analysis and model-based prediction of the behavior of chromatographic packed beds consisting of compressible particles coupled to the fluid flow. In the following, some of this work is summarized. The compression behavior of chromatographic resins was described by Ladisch and Tsao [1978] and Ladisch [2001] for the first time. Jönsson and Jönsson [1992a] reported packing compression–relaxation hysteresis as a consequence of the hydrodynamic compression force. In their work, a steady-state flow column was modeled taking into account elastic packing compressibility and permeability according to the well-known Darcy’s law. Dynamic modeling revealed the time dependency of the packing porosity as a function of packing height and compression force [Jönsson and Jönsson 1992b]. Östergren and Trägårdh [1997, 1998] developed a two-dimensional model of steady flow through a compressible packing. Keener et al. [2002] described the mechanical deformation of purely elastic compressible chromatography beds using a one-dimensional model. Further models deal with the packing and scale-up of chromatography columns and differentiate between mechanical compression and flow compression [Keener et al. 2004a,b; McCue et al. 2007; Tran et al. 2007]. Hekmat et al. [2013] reported a simple modeling approach of transient flow through a chromatography packing considering viscoelasticity of the resins for the first time. In this work, the observed compression–relaxation hysteresis of the packing during flow compression was described by a simple one-dimensional continuum model.

Thus, the mathematical models reported so far are based on continuum models while most of them assume a purely elastic deformation behavior of the chromatographic packing according to Biot’s theory of three-dimensional consolidation [Biot 1941]. These models provide a better understanding of the global packing behavior during hydrodynamic load, but as they approximated the packing as a one or two-dimensional continuum, the models lack in their consideration of local effects leading to packing integrity

breaches, e.g. cracks in the bed, medium-wall detachment or flow channeling which were often observed during column operation [Larson et al. 2003; Hekmat et al. 2011]. Furthermore, these models could not give detailed information about neither local flow fields nor local stress states within the column which might be of considerable interest in terms of packing lifetime and throughput. Therefore, consideration of local column and packing properties is as important as the global column behavior, e.g. the column pressure drop for the description of the hydrodynamic chromatography column behavior. As to the knowledge of the author, there have not been reports of a modeling approach of chromatographic columns that takes into account the individual particle behavior and addresses the local interparticle micromechanics coupled to fluid mechanics.

Here, computer simulations using mechanistic models provide a valuable method to consider the packed bed at the particle scale and to evaluate the impact of those parameters which are not experimentally accessible.

Consequently, the aim of the present thesis was to develop a three-dimensional mechanistic model of a packed-bed chromatography column in order to investigate the hydrodynamic packed bed behavior as a function of the single particle properties and the fluid flow at constant temperature. The focus was set solely on the particle behavior and the physics of particle packed beds regardless of bioseparation related fluid phase properties like protein content, ionic strength, pH-value, or others. Therefore, a three-dimensional model was developed describing the hydrodynamic interaction between chromatographic resin and fluid via a hybrid approach by applying coupled *Computational Fluid Dynamics (CFD)* and *Discrete Element Method (DEM)* models. Such a model has not been developed so far in the field of chromatographic packed bed analysis. In DEM modeling, the packed bed consists of discrete particles of defined sizes and densities and the behavior of each single particle is described by force and momentum equations. Due to the consideration of realistic particle size distributions and the interaction of every single particle of the packing, this modeling approach allows the detailed analysis of local packing properties affecting the column performance. The fluid phase calculations were performed using volume-averaged Navier-Stokes equations.

Using the coupled CFD-DEM modeling approach, answers to the following relevant questions ought to be found:

- Which parameters have a strong influence on the hydrodynamic column behavior?
- How is the packing behavior coupled to the fluid flow?

- How does the packing behavior depend on single particle properties?
- How do particle migration and particle rearrangement affect the packing behavior?
- How does the packing behavior depend on the wall support as well as the column packing method?
- How can packing homogeneity be quantified and improved?

The achieved simulation results were evaluated based on laboratory experiments which required the design, manufacturing, and operation of a novel micro chromatography column. Further issues that were focused on in this thesis are:

- Design and manufacturing of an automated laboratory set-up in order to measure the macroscopic hydrodynamic column behavior.
- Development of optical measurement methods in order to attain information about the outer and inner chromatographic packing structure and particle deformation behavior.
- Development of particle labeling methods and protocols in order to enhance contrast during optical measurements.
- Characterization of the single chromatographic particle compression behavior and determination of relevant mechanical properties.
- Identification of methods for the reduction of computational effort and determination of model parameters which are not experimentally accessible.

3. Physical Background

The dynamic behavior of chromatographic particle packings is closely related to the nature of the interactions between individual particles. The first part of this chapter focuses on these forces at the particle level. Based on the solid contact, which is dominant in the case of dry granular media made of macroscopic particles, the principles of Hertz elastic contact, solid friction and the rules of inelastic collision between solid particles are described. Therein, the mechanical particle properties used in this work such as the Young's modulus and Poisson's ratio are introduced. Based on these definitions and principles, the compression and deformation behavior of the chromatographic particles is described on the background of a biphasic material compound.

The second part of this chapter expands the single particle characteristics and micromechanics to the behavior of particle packed beds as it can be found in chromatographic columns and focuses on packing configuration and homogeneity. The last part gives a brief overview of the hydrodynamic aspects and forces of fluid flow in particle packed beds. The aim in this chapter is to provide some background knowledge in contact physics and hydrodynamics that will be useful for the discussion and interpretation of data provided in this work.

3.1. Characteristics of Single Particles

The materials of chromatographic particles range from very soft and elastic to completely rigid and brittle [Carta and Jungbauer 2010, pp. 108-122]. Hence, some particles are compressible under the applied flow whereas others are not. The mechanical behavior of the particle is therefore governed by the mechanics of the solid porous support material as well as by the interstitial fluid.

3.1.1. Solid Particle Mechanics

The contact force between two particles is usually split into a normal force and a tangential force. The physical origin of these forces at the microscopic level involves many phenomena such as surface roughness, local mechanical properties (elasticity, plasticity, viscoelasticity) and physical and chemical properties (e.g. surface functionalization, charge) [Andreotti et al. 2013, p. 15]. In the following, the focus is set on the macroscopic laws of solid contact regardless of these physical and chemical properties.

Elastic Contact: The Hertz Law

Figure 3.1 shows two spherical particles i and j squeezed together by an external normal force F_n . The normal contact force results from elastic deformation of the bodies in contact which were brought together by a distance of 2δ .

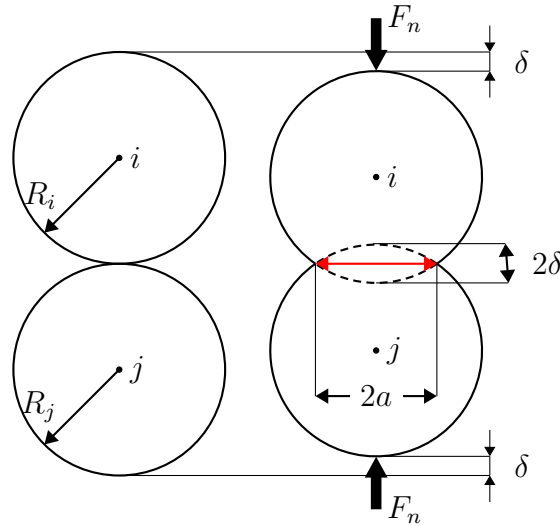


Figure 3.1.: Elastic contact between two spheres. Two particles i and j were brought together by a distance of 2δ by application of a normal force F_n . The radius of the contact area is given by a (modified from Andreotti et al. [2013, p. 16]).

Assuming perfectly elastic and frictionless particles, F_n is given by the Hertz theory of elastic contact [Hertz 1881; Johnson 1985, pp. 84-106]

$$F_n = \frac{4}{3}E^*\sqrt{R^*}\delta^{3/2}, \quad (3.1)$$

where E^* and R^* are the characteristic 'plane-strain' modulus and radius of the relative

curvature of the two particles given by [Johnson 1985, p. 89]

$$\frac{1}{E^*} = \frac{1 - \nu_i^2}{E_i} + \frac{1 - \nu_j^2}{E_j} \quad (3.2)$$

and

$$\frac{1}{R^*} = \frac{1}{R_i} + \frac{1}{R_j}. \quad (3.3)$$

Here, ν_i , ν_j , E_i , E_j and R_i , R_j are the *Poisson's ratio*, *Young's modulus* and *radius* of particle i and j , respectively.

The Poisson's ratio, ν , is a measure of the negative ratio of the transverse to axial strain of a body under application of uniaxial load. For a spherical particle, the Poisson's ratio can be approximately determined by [Heikens et al. 1981]

$$\frac{\Delta V_p}{V_p} = (1 - 2\nu) \frac{\delta}{2R}, \quad (3.4)$$

where $\Delta V_p/V_p$ is the change of material volume and $\delta/2R$ is the uniaxial strain.

During compression of a perfectly elastic particle the deformation extends to regions outside of the contact plane. The *radius of the contact area*, a , as depicted in Figure 3.1, therefore depends on the deformation and the contact pressure distribution within the particle and is given by [Johnson 1985, p. 93]

$$a = \sqrt{\delta R^*}. \quad (3.5)$$

According to Equation (3.1), the contact force does not depend linearly on the indentation depth δ , although the bodies are considered as perfectly elastic. This nonlinearity results from the increase of the contact area with increasing compression, which by then increases the effective stiffness of the particle [Andreotti et al. 2013, p. 17].

Elastic-plastic Contact

The contact of elastic particles discussed in the previous Section (3.1.1) is generally regarded as a reversible process and the resulting forces and deformations are independent of the history of loading [Johnson 1985, p. 179]. Real particles however, are not perfectly elastic, but exhibit some irresistibility during the cycle of loading and unloading. The elastic strain energy of a compressed particle can be calculated from the relationship

between load and compression according to

$$W = \int F d\delta. \quad (3.6)$$

By integral transformation using

$$\delta = \left(\frac{9F^2}{16E^*R^*} \right)^{1/3} \quad (3.7)$$

from Equation (3.1) and

$$\frac{d\delta}{dF} = \frac{2}{3} \left(\frac{9}{16E^*R^*} \right)^{1/3} F^{-1/3} \quad (3.8)$$

the elastic strain energy (Equation (3.6)) gives

$$W = \frac{2}{5} \left(\frac{9F^5}{16E^*R^*} \right)^{1/3}. \quad (3.9)$$

The loss of energy during elastic-plastic contact leads to a lower repulsive force $F' < F$ during the unloading cycle (in the following indicated by primed quantities). The energy of elastic recovery is then given by

$$W' = \int F' d\delta' \quad (3.10)$$

so that the dissipated energy during loading and unloading is the difference $\Delta W = W - W'$.

Solid Friction

If the friction between the particles is considered, the contact force normally has a tangential component in addition to the normal component. Coulomb's law of friction still remains the subject of active research [Baumberger and Caroli 2005; Andreotti et al. 2013, p. 17-19] and states the following:

- There is a minimum tangential force to make two bodies in contact slide against each other which is called the friction force and is defined by $R_s = \mu_s F_n$. Here, μ_s is the *static friction coefficient* of the two bodies in contact.

- When the bodies are sliding against each other the magnitude of the friction force is $R_d = \mu_d F_n$, where μ_d is the *dynamic friction coefficient*. The friction force is then exerted in direction opposite to the direction of sliding.
- The friction coefficients μ_s and μ_d are constant and depend on the materials and surfaces of the contacting bodies.

The existence of two different friction coefficients can be brought together by the phenomenon of "stick-slip" [Baumberger et al. 1994; Andreotti et al. 2013, pp. 20-22]. Thus, the two bodies initially stick together and the tangential force is below the static friction limit of $R_s = \mu_s F_n$. When the threshold is reached, the bodies slide against each other and the dynamic friction resistance is $R_d = \mu_d F_n$, with $\mu_d < \mu_s$.

Rolling Friction

In addition to sliding friction there is also a resistance to rolling motion, i.e. when a sphere rolls on a solid surface. This resistance is called rolling friction [Coulomb 1785; Johnson 1985; Andreotti et al. 2013].

In analogy to the Coulomb law of friction, the rolling friction of a particle on a rigid surface is defined as

$$M_s^r = \mu_s^r R_n R, \quad (3.11)$$

where M_s^r is the minimal torque needed to put the particle into rolling motion, μ_s^r is the *static rolling friction coefficient*, R_n is the normal reaction force and R the particle radius. Similarly, during rolling motion, the dynamic rolling friction is given by $M_d^r = \mu_d^r R_n R$.

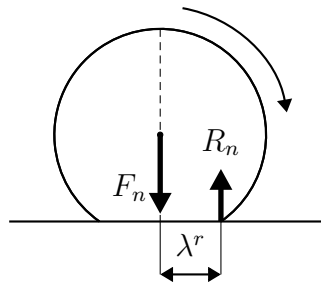


Figure 3.2.: Rolling friction of a sphere at the contact surface. Due to an asymmetry of the contact between the particle and the surface, a normal reaction force R_n in a distance of λ^r can be identified causing a rolling resistance torque $M^r = \lambda^r R_n$ (modified from Andreotti et al. [2013, p. 24]).

Physically speaking, the rolling resistance originates from an asymmetry of the contact between the particle and the surface when a torque is applied to the particle as indicated

in Figure 3.2. Before the rolling motion, the static rolling friction may arise from e.g. adhesive forces between the two contacting surfaces. During rolling motion, the dynamic rolling resistance is caused by viscoelastic or plastic dissipation in the contact zone which creates a hysteretic behavior of compression and repulsion forces [Johnson 1985; Andreotti et al. 2013, pp. 24-26]. In summary, all these mechanisms induce a shift forwards of the normal reaction Force R_n by a distance λ^r causing a rolling resistance torque of $M^r = \lambda^r R_n$. Based on Equation (3.11), the coefficient of rolling friction μ^r can be related to the shift λ^r by $\mu^r = \lambda^r/R$. Compared to the sliding friction, the rolling friction has less impact on the motion of the particle since $\lambda^r \sim a$ (the contact radius) and $a \ll R$ [Andreotti et al. 2013, pp. 24-26].

Collision of Two Particles

So far, the rate of loading on a particle was considered as sufficiently slow for the stresses to be in static equilibrium with the external loads during the time of the contact. During the impact of two particles, which is the case in granular flow, the rate of loading is high and dynamic effects may be important [Johnson 1985, p. 340].

Assume two particles i and j with masses m_i and m_j move toward each other with velocities v_i and v_j , their centers approach each other by a displacement of δ due to elastic deformation during the impact. The relative velocity is then given by $V = v_i - v_j = d\delta/dt$. Applying Newton's second law of motion, gives

$$m^* \frac{d^2\delta}{dt^2} = -\frac{4}{3} \sqrt{R^* E^*} \delta^{3/2} = -K \delta^{3/2}, \quad (3.12)$$

where $1/m^* = 1/m_i + 1/m_j$. Integration with respect to δ leads to

$$\left(\frac{d^2\delta}{dt^2} \right) d\delta = -\frac{K}{m^*} \delta^{3/2} d\delta \quad (3.13)$$

$$dV \frac{d\delta}{dt} = -\frac{K}{m^*} \delta^{3/2} d\delta \quad (3.14)$$

$$\frac{1}{2} \left(V_0^2 - \left(\frac{d\delta}{dt} \right)^2 \right) = \frac{2}{5} \frac{K}{m^*} \delta^{5/2} \quad (3.15)$$

where V_0 is the initial relative velocity of the particles. The maximum compression δ^*

is calculated at $d\delta/dt = 0$ to

$$\delta^* = \left(\frac{15m^*V^2}{16E^*R^{*1/2}} \right)^{2/5}. \quad (3.16)$$

The elastic energy stored in the contact zone is in the order of $W \sim F\delta^*$. The typical collision time is then given by [Andreotti et al. 2013, p. 26-29; Johnson 1985, p. 351-355]

$$t_c \sim \delta^*/V_0 \sim \left(\frac{m^{*2}}{R^*E^{*2}V_0} \right)^{1/5} \sim \frac{R^*}{c} \left(\frac{c}{V_0} \right)^{1/5}, \quad (3.17)$$

where $c \sim \sqrt{E^*/\rho_p}$ is the *characteristic speed of bulk elastic waves* and ρ_p the *density* of the particles [Andreotti et al. 2013, p. 26-29]. Interestingly, the collision time is rather dependent on the material characteristic than on the impact as it only has a weak dependence on the impact velocity V . It is important to note that the above considerations are only valid if the static solution of the equation of elasticity according to Hertz's law remains valid during the impact. This is the case if the region of elastic deformation belongs to the near field of elastic waves radiated from the contact zone [Johnson 1985, p. 351-360; Andreotti et al. 2013, p. 15-17]. This restriction can be formulated as $\lambda \gg a$, where λ is the typical wave length of the radiated waves and a is the radius of the contact zone. Summing up that $\lambda \sim ct_c$ and $a \sim \sqrt{\delta R} \sim \sqrt{vt_c R}$ the condition can be formulated as

$$\frac{a}{\lambda} \sim \left(\frac{v}{c} \right)^{3/5} \ll 1. \quad (3.18)$$

If the two particles collide *inelastically*, the initial kinetic energy of the system is partially converted into elastic energy but also dissipated, e.g. due to plastic deformation of the material. The application of the Hertz quasi-static approach which is based on the restriction that the particle impact velocity is small compared to the elastic wave speed (Equation (3.18)) also holds during inelastic impact. The plastic deformation of the material reduces the intensity of the impact pressure pulse and thereby diminishes the energy converted into elastic waves [Johnson 1985, p. 361].

Up to the instant maximum compression ($\partial\delta/\partial t = 0$) the initial kinetic energy is converted into elastic and plastic local deformation of the particles. Hence, the velocity of the particle after the rebound v' is always smaller than the initial velocity v according

to

$$v' = -ev, \quad (3.19)$$

where $0 \leq e \leq 1$ is the *coefficient of restitution*. The causes of energy dissipation in this case can be manifold, e.g. plastic deformation, viscoelasticity loss, local heating or cracking of the material. The coefficient of restitution, as a measure of energy loss during collision, depends on the size of the particles as well as on the impact velocity, but in many applications e can be considered as constant [Andreotti et al. 2013, p. 26-29].

Again, based on the initial kinetic energy of the system, e can be calculated by a simple energy balance. Hence, the transformation of the kinetic energy of the system into local particle deformation is given by Equation (3.9) to

$$\frac{1}{2}m^*V^2 = W = \int_0^{\delta^*} F d\delta, \quad (3.20)$$

where $1/m^* = 1/m_i + 1/m_j$ and V is the relative velocity of the impact. During the elastic repulsion, the calculation is similar, but the repulsive force F' at the onset of rebound is unknown due to energy dissipation, so that

$$\frac{1}{2}m^*V'^2 = W' = \int_0^{\delta'^*} F' d\delta'. \quad (3.21)$$

The coefficient of restitution then is the square root of the ratio of the repulsive and initial energy of the particles

$$e = \sqrt{\frac{W'}{W}}. \quad (3.22)$$

During almost elastic and viscoelastic contact, where the difference between compression and repulsion is small, the Hertzian compliance relation $F(\delta)$ (Equation (3.1)) holds and e can be calculated using the equations above. For large plastic deformations however this relation is no longer valid. Relations of $F(\delta)$ covering those deformation regimes are available in literature [Johnson 1985, p. 361-369].

3.1.2. The Viscoelastic Particle

Many resins used in chromatographic separation at preparative scale are of polymeric nature and known to exhibit a time-dependent behavior in their relation of stress and strain. Figure 3.3 shows this relation of the strain $\varepsilon(t)$ of a material under the application

of a stress $\sigma(t)$ during a time period $t_1 - t_0$. The strain typically shows an initial elastic response (OA) to the applied stress followed by delayed elastic strain (AC). In the case of creep, the material additionally will acquire a steadily increasing creep strain (BC). By removing the stress, there is an immediate elastic response (CD) followed by a delayed elastic response (DE) [Johnson 1985, p. 184-185].

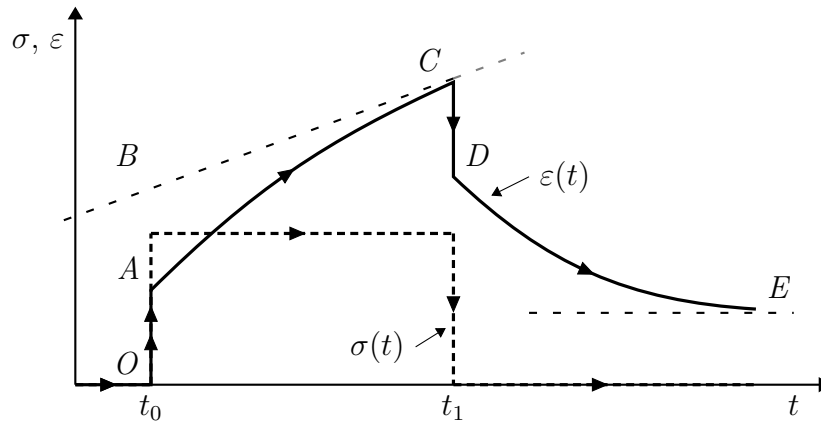


Figure 3.3.: Viscoelastic material behavior in the relationship of stress and strain. The material exhibits a time delayed response $\varepsilon(t)$ on a stress function $\sigma(t)$. The strain shows an initial elastic response (OA) to the stress followed by delayed elastic strain (AC). In the case of a creeping material, a steadily increasing creep strain (BC) can be observed. Removing the stress, an immediate elastic response (CD) followed by a delayed elastic response (DE) is exhibited (modified from Johnson [1985]).

As a result of the action of creep, a permanent strain is left after total relaxation of the material (E). The viscoelastic behavior, having elastic and viscous components, can be treated as a linear stress-strain relationship. This requires that the strains are sufficiently small (as in the Hertz theory of elasticity) and Boltzmann's superposition principle is valid [Johnson 1985, p. 184-185]. Thus, for linearity, an increase in stress by a constant factor causes an increase in strain by the same factor. According to the superposition principle, the strain response to different stress histories acting simultaneously must be identical to the sum of strain responses to the stress histories acting separately [Johnson 1985, p. 184-185]. Consequently, the viscoelastic material behavior is often expressed as linear combinations of springs and dashpots. Different models exist covering various combinations and arrangements of these elements such as the well-known *Maxwell* or *Kelvin-Voigt* model. Therefore, in the former model, spring and dashpot are in series and in the latter in parallel. Nevertheless, these simple models are often proved insufficient as the Maxwell model does not account for creep or recovery and the Kelvin-Voigt model

does not describe stress-relaxation. The *standard linear solid* model (also known as the *Zener* model [Zener 1948]) or the *Prony series model* consider both phenomena. Both models are described in detail in the following sections.

The Standard Linear Solid (SLS) Model

Two types of the Standard Linear Solid (SLS) model are frequently used: The Kelvin type [e.g. Cheng et al. 2005; Toohey et al. 2016] and the Maxwell type [e.g. Nguyen et al. 2009; Tirella et al. 2014; Mattei et al. 2015]. The former is composed of a Voigt element in series with a free spring (Figure 3.4 A) and the latter model consists of a Maxwell element in parallel with an equilibrium spring (Figure 3.4 B). Both types accurately describe the time-dependent behavior in the relation of stress and strain of a viscoelastic material.

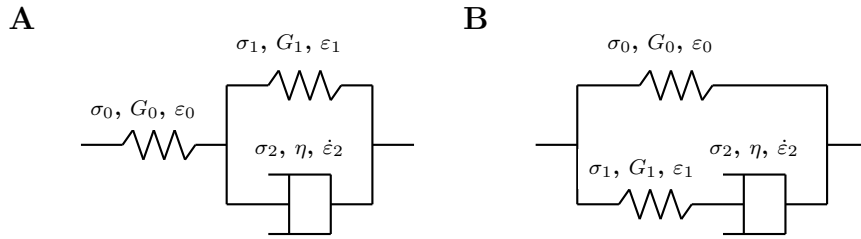


Figure 3.4.: Schematic representation of the SLS model types. (A) shows the Kelvin type of the SLS model as a Voigt-element (spring and dashpot in parallel) in series with a free spring and (B) shows the Maxwell type of the SLS model as a Maxwell-element (spring and dashpot in series) in parallel with an equilibrium spring. G_0 is the shear modulus of the free spring and G_1 and η are the shear modulus and shear viscosity of the spring and dashpot of the Voigt or Maxwell element, respectively. ϵ and $\dot{\epsilon}$ are the strain and strain rates of the springs and dashpots.

The force-displacement relation $F(\delta)$ during the compression of a viscoelastic sphere (radius R_1) by an ideally rigid incompressible flat plate (radius $R_2 \rightarrow \infty$) can be described in analogy to the Hertz elastic theory [Johnson 1985, p. 184-195; Yan et al. 2009]. Assuming a time-independent Poisson's ratio, the time-dependent load based on a rate-controlled displacement, $\delta(t)$, is given in analogy to Equation (3.1) as [Lee and Radok 1960; Johnson 1985, p. 184-195; Mattice et al. 2006; Yan et al. 2009; Mattei et al. 2015; Toohey et al. 2016]

$$F(t) = \frac{4}{3}\sqrt{R}\frac{E(t)}{(1-\nu^2)}\delta^{3/2}(t) = \frac{8}{3}\frac{\sqrt{R}}{(1-\nu)}\int_0^t G(t-t^*)\frac{\partial}{\partial t^*}(\delta^{3/2}(t^*))dt^* \quad (3.23)$$

where the equivalent radius in this case is given by $1/R^* = 1/R_1 + 1/\infty \approx 1/R_1 = 1/R$. $G(t)$ is the time-dependent *shear modulus* of the particle which is correlated to the Young's modulus $E(t)$ by

$$E(t) = 2G(t)(1 + \nu). \quad (3.24)$$

Equation (3.23) exactly describes the Boltzmann postulation that a force increment dF through time t depends on an event happened in the past, which is the increment of strain $d(\delta^{3/2}(t^*))$ at the time t^* , as well as on the stress-relaxation over the time span $(t - t^*)$. The overall shear modulus of the three parameter SLS model can be derived, e.g for the Maxwell type, as (see Appendix C.2 for details)

$$G_{SLS}(t) = G_0 + G_1 e^{-t/\tau}. \quad (3.25)$$

where G_0 and G_1 are the shear moduli of the spring and dashpot, respectively, and $\tau = \eta/G_1$ is the *characteristic relaxation time* of the viscoelastic material. The integral in Equation (3.23) is evaluated using Laplacian transformation (analog to Lee and Radok [1960] and Toohy et al. [2016]; see Appendix C.3 for details) and leads to

$$F(t) = \frac{\sqrt{2Rv^3}}{(1 - \nu)} \left[\frac{2}{3}G_0 t^{3/2} + G_1 \tau t^{1/2} - G_1 \tau^{3/2} \frac{\sqrt{\pi}}{2} e^{-t/\tau} \operatorname{erfi} \left(\sqrt{\frac{t}{\tau}} \right) \right] \quad (3.26)$$

where $v = \Delta(t)/t$ is the displacement velocity of the indenter and erfi is the imaginary error function.

The Force-Relaxation Model

The compression load relaxation answer of a viscoelastic material can be described by a force-relaxation model expressed as Prony series. The modelling framework was presented by Mattice et al. [2006] considering indentation by a spherical probe. This approach was adapted successfully later by Yan et al. [2009] for the compression of spherical agarose micro-particles. Thus the constant $2G(t)$, in Equation (3.24) can be replaced by the following relaxation function $G(t)$ represented by Prony series [Mattice et al. 2006]

$$G(t) = C_0 + \sum_{i=1}^N C_i e^{-t/\tau_i}. \quad (3.27)$$

Then, the load relaxation solution has the form

$$F(t) = B_0 + \sum_{i=1}^N B_i e^{-t/\tau_i}. \quad (3.28)$$

Here, N is the number of force relaxation functions contributing to the overall time-dependent force response. The relaxation time τ_i characterizes the mean time span in which a quantity exponentially decayed to $1/e = 0.368$. The fit coefficients B_0 and B_i are related to the relaxation coefficients C_0 and C_i by

$$C_0 = \frac{B_0}{\frac{\sqrt{2R}}{3(1-\nu)} \Delta_{max}^{3/2}} \quad (3.29)$$

and

$$C_i = \frac{B_i}{\text{RCF}_i \frac{\sqrt{2R}}{3(1-\nu)} \Delta_{max}^{3/2}}. \quad (3.30)$$

where RCF is the ramp correction factor considering the creep that occurs during the ramp loading period of τ_R [Mattice et al. 2006; Oyen 2014; Toohey et al. 2016]

$$\text{RCF}_i = \frac{\tau_i}{\tau_R} \left[\exp\left(\frac{\tau_R}{\tau_i}\right) - 1 \right]. \quad (3.31)$$

From the obtained relaxation coefficients, the *instantaneous shear modulus* $G(t = 0)$ and the *relaxed modulus* $G(t \rightarrow \infty)$ can be calculated by

$$G(t = 0) = \frac{\sum_{i=0}^N C_i}{2} \quad (3.32)$$

and

$$G(t \rightarrow \infty) = \frac{C_0}{2}. \quad (3.33)$$

Instantaneous and relaxed Young's modulus $E(t = 0)$ and $E(t \rightarrow \infty)$ are then given by Equation (3.24) indicating the apparent stiffness of the particle at the onset of compression and at completely relaxed state, respectively.

3.1.3. The Particle as a Biphasic Material Compound

Adsorbent materials used in chromatographic process applications are usually porous and able to swell in a fluid environment. Across the particles used in chromatographic separation, the *intraparticle porosities* ϵ_i vary from nearly zero for pellicular stationary phases to 0.9 for low-density gels such as agarose [Carta and Jungbauer 2010, p. 70]. When the particle absorbs a small amount of solvent molecules, i.e. the liquid phase absorbed by the porous resins in liquid chromatography, the aggregate can be described as a biphasic material compound. The time-dependency of a viscoelastic polymeric particle in its relation of stress and strain was already described in the previous Section 3.1.2. The time-dependency of the deformation of this aggregate results from two concurrent molecular processes: the conformational change of the polymer network, which results in viscoelasticity, and the migration of the absorbed solvent, which results in poroelasticity [Hu and Suo 2012; Wang et al. 2014].

The theory of linear poroviscoelasticity was developed by Biot [Biot 1956, 1962, 1963] and has since been used to study poroelastic phenomena [Nguyen et al. 2009; Hu and Suo 2012; Oyen 2014; Wang et al. 2014]. Therein, the migration of a solvent into a porous compressible material is described by the diffusion equation

$$\frac{\partial C}{\partial t} = D\nabla^2 C, \quad (3.34)$$

where C is the concentration field of the solvent, $\nabla^2 = (\frac{\partial^2}{\partial x^2} + \frac{\partial^2}{\partial y^2} + \frac{\partial^2}{\partial z^2})$ is the laplacian operator, and D is the diffusion coefficient given by [Hu et al. 2011; Wang et al. 2014]

$$D = \frac{2(1 - \nu)Gk}{(1 - 2\nu)\eta}. \quad (3.35)$$

ν and G are the Poisson's ratio and the shear modulus of the particle and k the intrinsic permeability of the particle. k can approximately be calculated by Darcy's law using

$$k = \frac{\epsilon_i r_h^2}{K^*}, \quad (3.36)$$

where ϵ_i is the intraparticle porosity, r_h is the mean hydraulic pore radius of the particle and K^* is the Kozeny constant, which equals 5 for $\epsilon_i \geq 0.66$ [Kapur et al. 1996; Lin et al. 2007].

Equation (3.34) indicates that over a time t a disturbance diffuses over a length \sqrt{Dt} . Assuming that the polymer chains of the material are incompressible and that volume change of the particle is equal to the volume of the absorbed or desorbed solvent the poroelasticity of the particle is characterized by the three parameters G , ν and D .

Hence, the viscoelastic characteristic time and the poroelastic diffusivity of the aggregate define an intrinsic material length scale of the aggregate [Wang et al. 2014]. As viscoelasticity results from molecular processes such as sliding between the polymer chains, the time of viscoelastic relaxation τ (Equation (3.25)) is independent of the length characteristic of any macroscopic observation. In contrast, poroelasticity results from the migration of an absorbed solvent, so that the time of poroelastic relaxation, as shown above, depends on the length of macroscopic observation [Hu and Suo 2012]. In compression testing, the characteristic length is often the sample diameter or during indentation the radius of the contact area a , as indicated in Figure 3.5 [Hu et al. 2011; Hu and Suo 2012; Hu et al. 2012; Kalcioglu et al. 2012; Wang et al. 2014].

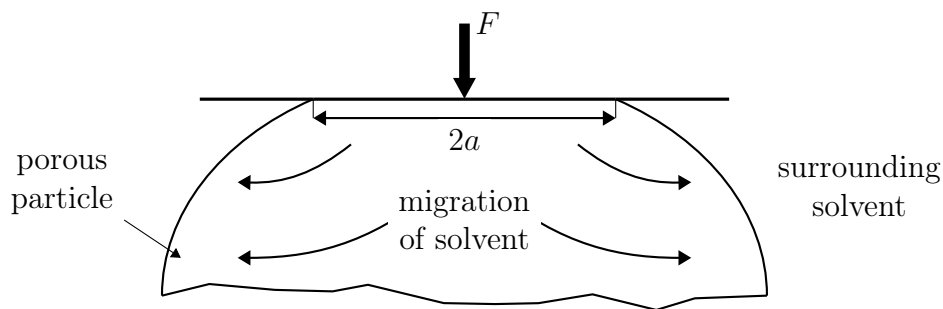


Figure 3.5.: Effect of poroelasticity. A porous particle is submerged and in thermodynamic equilibrium with a surrounding solvent. By application of an external load F by an ideally rigid inelastic compression plate the particle is pressurized locally. This causes the absorbed solvent to migrate exhibiting a poroelastic behavior. a is the contact radius of the particle at the compression plate.

Taking the two material specific parameters τ and D , a length $\sqrt{D\tau}$ can be calculated that represents the distance of the migration of the solvent within a time comparable to the time of viscoelastic relaxation. This length is material-specific and therefore independent of the length scale and time of any macroscopic observation [Hu and Suo 2012]. Hence, the compression behavior of a biphasic material compound can be characterized by two conditions in time. The condition $t \sim \tau$ represents the time of viscoelastic relaxation and the condition $t \sim L^2/D$ represents the time and length (L) of poroelastic relaxation. As an example, when $t \ll \tau$ and $t \ll L^2/D$, both processes have started and the aggregate behaves like an elastic solid with an instantaneous modulus (see e.g.

Equation (3.25) for $t \ll \tau$) and negligible migration of the solvent. When $t \ll \tau$ and $t \gg L^2/D$ viscoelastic relaxation has started, but poroelastic relaxation has already been completed. For $t \gg \tau$ and $t \ll L^2/D$ viscoelastic relaxation has completed, but poroelastic relaxation has already started. Finally, when $t \gg \tau$ and $t \gg L^2/D$ both processes are relaxed [Hu and Suo 2012]. A graphic illustration of various limiting conditions is given in Figure 3.6.

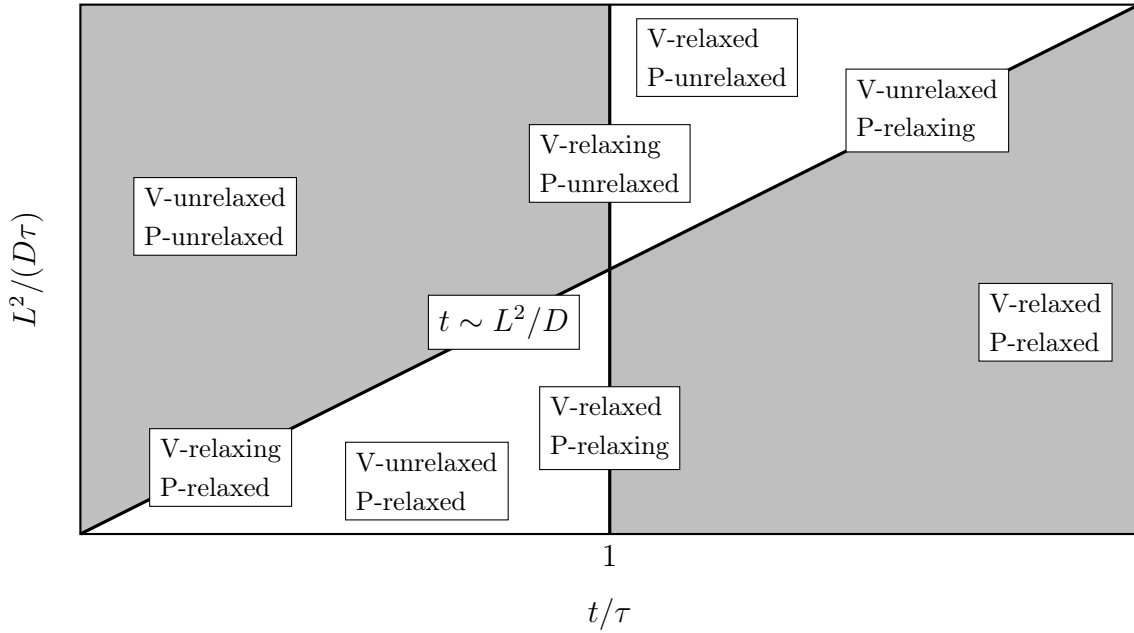


Figure 3.6.: Graphic representation of the limiting conditions of viscoelastic (V) and poroelastic (P) relaxation. Each point in the plane corresponds to a time t and a length L (normed to the material characteristic time τ and $\sqrt{D\tau}$, respectively) of a macroscopic observation. The vertical line at $t \sim \tau$ represents the time of viscoelastic relaxation and the inclined line $t \sim L^2/D$ the time and length of poroelastic relaxation. For example, the point 'V-relaxing, P-relaxed' corresponds to a condition in which the migration of the solvent has already ceased, but the size of the aggregate is so small that the rate of change is limited by viscoelasticity (modified from Hu and Suo [2012]).

Based on the theory of poroelasticity, the time-dependent force-relaxation curve can be derived for a simple indentation of a poroelastic flat disk by a spherical indenter, or equivalently, for a compression of a poroelastic sphere by a flat compression plate (Figure 3.5). For a constant indentation depth or compression, the radius of the contact area, a , remains constant and the compression force decays with time. Hence, as already given above for a short-time limit, the poroelastic material behaves like an incompressible elastic material. Consequently, the force in the short-time limit is F_0 . In the long-time limit, when poroelastic relaxation has completed, a force F_∞ can be measured. Both

forces are correlated by

$$\frac{F_0}{F_\infty} = 2(1 - \nu), \quad (3.37)$$

where ν is the Poisson's ratio of the material [Biot 1941; Hu and Suo 2012; Hu et al. 2012]. The time-dependent decay of the compression force $F(t)$ takes the form

$$\frac{F(t) - F_\infty}{F_0 - F_\infty} = g(\tau_p), \quad (3.38)$$

where g is a function dependent on the type of the experiment and $\tau_p = Dt/a^2$ is the normalized poroelastic time. For a spherical indenter of radius R pressed into a poroelastic material F_0 is given by the Hertz theory of elastic contact (Equation (3.1)) to

$$F_0 = \frac{16}{3}Ga\delta, \quad (3.39)$$

where the Poisson's ratio in the short-time limit is given by $\nu = 0.5$ for an incompressible elastic material and a is given by Equation (3.5). Hu et al. [2010] found out using the finite element method that $g(\tau_p)$ takes the form

$$g(\tau_p) = 0.491e^{-0.908\sqrt{\tau_p}} + 0.509e^{-1.679\tau_p}. \quad (3.40)$$

3.2. Characteristics of Particle Packings

In chromatographic application, the particles are poured into a cylindrical column in which they form a matrix like packing structure containing voids and pores. It is well known that the properties of the particle packed bed significantly influence the performance and quality of the chromatographic separation. Hence, analysis of the column packed bed behavior as a result of the single particle behavior is necessary for the understanding of the hydrodynamic behavior of chromatography columns. This section gives an overview of the parameters and properties characterizing particle packed beds being composed of compressible particles.

3.2.1. Geometric Properties of Particle Packings

A packing of particles is primarily characterized by the *solid volume fraction* or *packing density* ϕ ($0 \leq \phi \leq 1$) or by the *porosity* ϵ ($0 \leq \epsilon \leq 1$) which is defined as the ratio of the solid particle volume V_s or the void volume V_v to the total bulk packing volume V

$$\phi = \frac{V_s}{V} = \frac{V_s}{V_s + V_v}, \quad (3.41)$$

$$\epsilon = \frac{V_v}{V} = 1 - \phi. \quad (3.42)$$

Therein, the total bulk volume is the sum of the volume occupied by the solid particles V_s and the void volume V_v [Bear 1988, p. 43; Andreotti et al. 2013, p. 60].

3.2.2. Packings of Monodisperse and Ideally Rigid Particles

Ordered Packings

Ordered packings of equal spheres are the simplest packing configurations that can be encountered in nature, i.e. in crystallography. These structures are obtained by superposition of layers of particles resulting in either square or triangular contact. Table 3.1 gives the characteristics of these ordered packing configurations.

As can be seen, the packing porosity varies between 0.476 for a cubic packing and 0.260 for a rhombohedral packing configuration which represents the densest packing configuration. The *coordination number* z gives the number of nearest neighboring

Table 3.1.: Characteristics of ordered packings of equal rigid spheres [Yang 2003, p. 41].

Packing type	Porosity	Coordination No.
Simple cubic	0.476	6
Orthorhombic	0.395	8
Tetragonal spheroidal	0.302	10
Rhombohedral	0.260	12

particles and is in this case equal to the number of contacting particles as all spheres do actually touch.

Disordered Packings

Although the ordered crystalline packings correspond to the global minimum of potential energy they are difficult to achieve in practice, i.e. with frictional particles [van Hecke 2010; Mukhopadhyay and Peixinho 2011; Andreotti et al. 2013, p. 62]. The particles arrange in a so called *random close packing* (RCP) [Scott 1960; Scott and Kilgour 1969] with a packing density of order $\phi \simeq 0.64$ [van Hecke 2010; Mukhopadhyay and Peixinho 2011]. The loosest packing able to sustain stresses is the *random loose packing* (RLP) which corresponds to a packing density of $\phi \simeq 0.55$ [Andreotti et al. 2013, p. 62-63].

Geometrical Wall Effect

If the particle packing is formed in a column with impenetrable walls, the particles are unable to form a close packing configuration against the column wall and pack in a rather random disordered fashion. As a result, there is an increased porosity in vicinity of the wall in comparison to the core region of the packing. The effect of the confining walls on the average porosity of the packing depends on the *aspect ratio*

$$A_{ratio} = \frac{D}{d_p} \quad (3.43)$$

of the column diameter D to particle diameter as well as on the aspect ratio of the packing height H to particle diameter

$$H_{ratio} = \frac{H}{d_p} \quad (3.44)$$

For sufficiently high aspect ratios $D/d_p > 20$, the geometrical wall effect can be neglected in a distance from $\sim 5d_p$ to $10d_p$ [Bruns et al. 2012b]. Figure 3.7 shows the porosity profile of packing with aspect ratio $D/d_p = 16$. As can be seen, the porosity

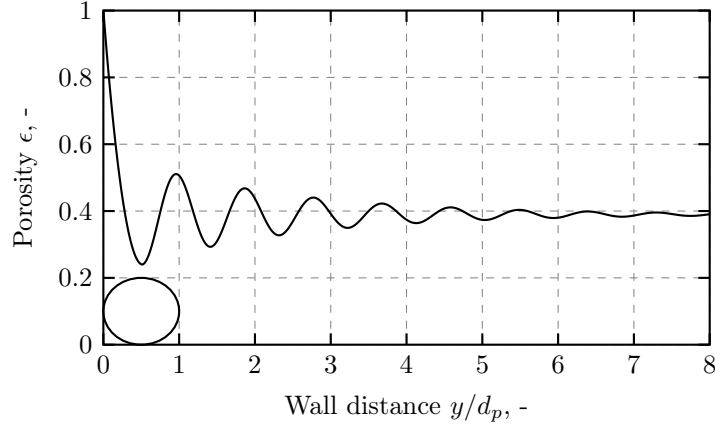


Figure 3.7.: Geometrical wall effect on local packing porosity. Local porosity profile near solid walls in a packing of equal spheres according to Bey and Eigenberger [1997]. The wall distance y is normed to the particle diameter d_p . The porosity profile can be described by a damped oscillating function (Equations (3.45) - (3.48), with $\epsilon_{min} = 0.24$, $\epsilon_{\infty} = \epsilon_{bulk} = 0.39$, $a = 4$ and $b = 0.876$ [Bey and Eigenberger 1997]).

has an maximum of $\epsilon \approx 1$ in direct vicinity of the column wall and decreases with an oscillating manner with increasing distance y from the wall. As a consequence, the local porosity profile can be expressed as a damped oscillation by [Bey and Eigenberger 1997]

$$\text{for } r^* < 0 : \epsilon(r) = \epsilon_{min} + (1 - \epsilon_{min})r^{*2}, \quad (3.45)$$

$$\text{for } r^* \geq 0 : \epsilon(r) = \epsilon_{\infty} + (\epsilon_{min} - \epsilon_{\infty})e^{-r^*/a} \cos(\pi r^*/b), \quad (3.46)$$

where r^* is given by

$$r^* = \left(\frac{R - r}{y_{min}} \right) - 1, \quad (3.47)$$

$$y_{min} = 0.5d_p \left(\frac{D}{d_p} - \sqrt{\left(\frac{D}{d_p} - 1 \right)^2 - 1} \right), \quad (3.48)$$

where R is the column radius and r the the radial coordinate. These wall effects influence the local porosity distribution in packed columns near all solid walls, i.e. the cylindrical shell, the column bottom as well as the adjustable packing compression device, known as the column plunger, in the column top region.

3.2.3. Packings of Polydisperse Particles

Chromatographic media as well as other granular systems involve mixtures of particles of different sizes. These polydisperse particle systems are characterized by the *particle size distribution* (PSD). The whole spectrum of particle sizes is divided into $(n - 1)$ equidistant intervals of width Δd_p . The size of the smallest particle $d_{p,min}$ then corresponds to $d_{p,1}$ and the size of the largest particle $d_{p,max}$ to $d_{p,n}$ [Stieß 2009, pp. 25-29]. The *particle size distribution density* $q(d_p)$ gives the fraction of particles in a defined size range and is determined by [Holdich 2002, pp. 5-18]

$$q(d_p) = \frac{\text{Number of particles in interval } [d_{p,i-1}, d_{p,i}]}{\text{Total number of particles} \cdot \Delta d_p}. \quad (3.49)$$

The *cumulative particle size distribution* $Q(d_p)$ is given by

$$Q(d_p) = \int_{d_{p,min}}^{d_{p,i}} q(d_p) d(d_p^*) = \frac{\text{Number of particles in interval } [d_{p,min}, d_{p,i}]}{\text{Total number of particles}}. \quad (3.50)$$

Furthermore, the *mean* (or *average*) particle size is sum of all particle sizes in the spectrum divided by the number of particles, the *median* particle size is the middle value of the spectrum when all particles are arranged in order of magnitude [Bulmer 1979, pp. 45-54].

3.3. Fluid Flow in Particle Packings

The dynamics of fluid flow in porous media or particle packed beds is complex and notoriously difficult to study due to its opacity and disorder. In high aspect ratio packings the flow is disordered but statistically can be considered homogeneous due to the relative uniform size of the pores and voids. In low aspect ratio packings however, the structure of the packing is considerably more disordered so that interconnecting large voids increase flow channeling and inhomogeneity [Baker 2011, p. 18].

The carriage of flow through a packed bed is described by the same relationships as for basic fluid mechanics. The *superficial fluid velocity*, u_0 , is given as the quotient of the *volumetric flow rate*, Q , and the cross-sectional area of the packing, A ,

$$u_0 = \frac{Q}{A} \quad (3.51)$$

and describes the average fluid velocity that would be present in absence of the packed bed. Within the pores, the average fluid velocity is given by the *interstitial fluid velocity*, u_i , which is correlated to the average porosity of the packed bed, ϵ , by

$$u_i = \frac{u_0}{\epsilon}. \quad (3.52)$$

3.3.1. Flow Regimes

Fluid flow in chromatographic application is generally slow and laminar [Östergren and Trägårdh 1999]. The definition of flow regimes is based by the dimensionless *Reynolds number*, Re , which is defined by the ratio of the inertial to viscous forces of the fluid according to

$$Re = \frac{\rho_f u l}{\eta_f}, \quad (3.53)$$

where ρ_f and η_f are the density and dynamic viscosity of the fluid and l is some length dimension of the porous matrix. In some cases, the kinematic viscosity of the fluid is used which is defined as $\nu_f = \eta_f / \rho_f$ [Bear 1988, pp. 125-128]. As with pipe flow, where usually the pipe diameter, is the characteristic length scale, the flow through packed beds also can loosely be described by the Reynolds number. 'Loosely' in this case means that for a porous medium several forms of the Reynolds number can exist based on different length scales defined in the porous medium [Bear 1988, pp. 125-188]. In particle packings, the average particle diameter, d_p , is often taken as the characteristic length dimension in Equation (3.53) resulting in the particle Reynolds number Re_p . Thus, for real porous media systems, the flow regime is characterized as *laminar* ($Re_p < 10$), *transitional* ($10 < Re_p < 300$) and *turbulent* ($Re_p > 300$) [Ziólkowski 1988; Bear 1988, pp. 125-128].

It can be seen that Equation (3.53) is solely dependent on the properties of the fluid and the particle diameter, but does not take into account the properties of the packed bed, such as the packing porosity ϵ . The heterogeneous nature of a random particle packing causes large fluctuations of the local porosity profiles so that there is a high possibility that all three flow regimes will exist within the porous structure [Ziólkowski 1988]. Hence, bulk porous media Reynolds numbers are defined as

$$Re_B = \frac{\rho_f u_0 d_p}{\eta_f (1 - \epsilon)}, \quad (3.54)$$

and

$$Re_{B'} = \frac{\rho_f u_0 d_p}{\eta_f \epsilon}, \quad (3.55)$$

which are the particle Reynolds numbers divided by the packing density or the packing porosity, respectively. The former Equation (3.54) was found to be useful in describing fluidized bed data and the latter Equation (3.55) in describing packed bed data [Dwivedi and Upadhyay 1977].

3.3.2. Correlation of Flow and Packing Pressure Drop

The earliest theoretical description of flow through a porous medium (including packed beds) was developed experimentally by Darcy in 1856 and has since been derived by the Navier-Stokes equations via homogenization [Bear 1988, pp. 119-176; Whitaker 1986]. Neglecting the contribution of gravitational forces, Darcy's law takes its simplest form and states that the flow u through a porous medium is proportional to a given pressure gradient according to

$$u = -\frac{\kappa}{\eta_f} \nabla p, \quad (3.56)$$

where κ is the intrinsic *permeability* of the porous medium, and ∇p the pressure gradient. Analogous to Ohm's law of resistance, Fourier's law of heat conduction or Fick's law of diffusion which are globally known as linear transport equations, Darcy's law is also a linear law [Dullen 1992]. It requires the flow to be a Hagen-Poiseuille flow, which describes viscous and laminar flow of an incompressible fluid through a cylindrical pipe [Bear 1988, pp. 161-164]. Hence, it is only applicable to low Reynolds number conditions ($Re_p < 10$).

The permeability, κ , is a property of the porous medium and defines the ease of a fluid to percolate through it. It can be regarded as a measure of the hydraulic conductivity of the porous structure. The packing permeability is related to the packing porosity by the Kozeny-Carman equation [Bear 1988, pp. 161-166]

$$\kappa = \frac{d_{32}^2}{180} \frac{\epsilon^3}{(1 - \epsilon)^2}, \quad (3.57)$$

where d_{32} corresponds to the *Sauter mean diameter*, as characteristic particle size, as it defines the diameter of a sphere that has the same volume to surface ratio as a particle of random shape. Consequently using the Sauter mean diameter, a packing with a particle

size distribution can be approximated by a monosized packing of particles with diameter d_{32} which has the same volume to surface ratio. Thus, d_{32} is defined as [Bear 1988, pp. 50-51]

$$d_{32} = 6 \frac{\sum_{i=1}^N V_{p,i}}{\sum_{i=1}^N A_{p,i}}, \quad (3.58)$$

where V_p and A_p are the volume and surface area of the particle and N is the total number of particles considered.

The factor $1/180$ in Equation (3.57) results from the derivation of the equation by Carman. The complicated case of fluid flowing through a random porous structure was approximated geometrically by a simpler case of pipe flow. According to the Hagen-Poiseuille's equation for flow in a pipe, the pressure drop over a distance ds is given by [Bear 1988, pp. 165-167]

$$\frac{dp}{ds} = -\frac{\eta_f u_i}{\frac{1}{2} R_h^2} \quad (3.59)$$

Therein, the void volume was considered as a bundle of parallel capillary tubes of same length and radius. The hydraulic radius, which for a pipe is defined by the cross-sectional area over the wetted perimeter, is calculated from packed bed properties as $R_h = \epsilon V/A_p$ and V being the volume of the packing. As the volume of particles is $V_s = V(1 - \epsilon)$ the hydraulic radius can be calculated by the Sauter diameter as $R_h = d_{32}\epsilon/(6(1 - \epsilon))$. The pressure drop according to Hagen-Poiseuille is then given by

$$\Delta P = \frac{\Delta p}{H} = 72c \frac{\eta_f (1 - \epsilon)^2 u_0}{d_{32}^2 \epsilon^3}, \quad (3.60)$$

where c is a scaling factor considering the tortuosity of the packed bed, H is the packing height, and $u_i = u_0/\epsilon$. It is important to note, that the scaling factor is not a constant, but depends on the packed bed tortuosity. Carman determined a factor of $c = 2.5$ for best agreement with experimental data [Bear 1988, pp.165-167] The combination of the Kozeny-Carman equation (Equation (3.57)) and Darcy's law (Equation (3.56)) is often known as the Blake-Kozeny equation, where c was replaced by $(25/12)$

$$\Delta P = \frac{150\eta_f (1 - \epsilon)^2 u_0}{d_{32}^2 \epsilon^3} \quad (3.61)$$

Due to the linearity $dp/ds \sim u_0$ of Darcy's and Kozeny-Carman's theory the above

equations (Equation (3.56)-(3.61)) are limited to the laminar flow through porous media at low Reynolds numbers ($Re_B < 10$). At large Reynolds numbers the pressure gradient shows a non-linear relationship to the flow velocity which is of the form

$$\frac{dp}{ds} = \alpha u + \beta u^2, \quad (3.62)$$

where α and β are empirical coefficients depending on the fluid and packed bed properties [Bear 1988, pp. 176-183]. Here, the terms αu and βu^2 correspond to the laminar (linear) and turbulent (non-linear) flow contribution to the pressure gradient. Based on the above relationship, Ergun [1952] extended the Kozeny-Carman approach to large Reynolds numbers and turbulent flow

$$\Delta P = 150 \frac{\eta_f (1 - \epsilon)^2}{d_{32}^2 \epsilon^3} u_0 + 1.75 \frac{(1 - \epsilon) \rho_f}{d_{32} \epsilon^3} u_0^2. \quad (3.63)$$

3.3.3. Dispersion

Integral Porosity Deviation

The integral porosity deviation (IPD) [Bruns et al. 2012a] is a measure for the trans-column contribution to eddy dispersion that may result from radial local porosity distributions. The IPD calculates the integral local porosity deviations from the packing bulk porosity ϵ_{bulk} under consideration of all porosity inequalities that a tracer would experience when diffusing from the column wall towards the packing center as [Bruns et al. 2012a]

$$IPD = \int_0^R (\epsilon(r) - \epsilon_{bulk}) dr. \quad (3.64)$$

This parameter can be used as a measure of the heterogeneity of the porosity distribution and packed bed quality.

Flow Induced Hydrodynamic Dispersion

The heterogeneity of the fluid flow field in a packed bed consisting of frictional particles is quantified by the transient hydrodynamic dispersion of the fluid phase flowing through the packed bed. The axial hydrodynamic dispersion (neglecting any diffusion effects) σ_z^2

is determined according to

$$\sigma_z^2(t) = \frac{1}{N} \sum_{i=1}^N [u_{z,i}(t) - \langle u_z(t) \rangle]^2, \quad (3.65)$$

as the second central statistical moment [Sabine and Plumpton 1985] of the local fluid velocity calculated in each incremental volume of the packing. N is the number of volumes, $u_{z,i}(t)$ is the fluid flow velocity in axial direction calculated in the i th volume at time t , and $\langle u_z(t) \rangle$ is the fluid flow velocity in axial direction at time t averaged over all volumes. Neglecting any diffusion effects, this parameter focuses solely on the contribution of the flow velocity differences to hydrodynamic dispersion and, hence, gives a reasonable measure of the packing heterogeneity. A similar approach was made by Tallarek and co-workers [Khirevich et al. 2010; Daneyko et al. 2012].

3.3.4. Force Transmission in Dense Packings

In dense particle packings, such as a pile of grains, all particles are in a complex mechanical equilibrium in which the distribution of forces is highly non-trivial [Andreotti et al. 2013, pp. 70-71]. The behavior of the granular system with respect to external compression or shear forces strictly depends on the distance to the *jamming point* [van Hecke 2010]. The following section is devoted to the organization of a dense particle packing and the problem of force indeterminacy and force distribution.

Isostaticity and the Jamming Point

Granular media can *jam* into a rigid and disordered state where they can withstand finite shear forces before yielding. The transition of freely flowing particle suspensions to the jammed state is called the *jamming transition*, which in general can be induced by various thermodynamic variables such as temperature or density, but also by mechanical variables like applied stress [van Hecke 2010].

The contact number or *coordination number*, z , which is defined as the average number of contacts per particle,

$$z = \frac{2N_c}{N}, \quad (3.66)$$

plays a crucial role in the stability of those systems. Here, N_c is the number of contacts and N the number of particles in the system. The factor 2 results from the fact that a

contact belongs to two particles. Hence, there is a minimum value of z below which the system loses its rigidity and stability which leads to a more fluid like behavior. This threshold value of z is called the *isostatic contact number* z_{iso} .

Frictionless particle systems exhibit a sharp jamming transition whereas frictional particle systems do not [van Hecke 2010]. At the *jamming point*, J , the packing consists of perfectly spherical, i.e. undeformed, particles which just touch. The packing density, ϕ , thereby reaches a critical value, ϕ_{crit} , which is associated with the random loose packing configuration, being ~ 0.84 in two dimensions and ~ 0.64 in three dimensions [O'Hern et al. 2003; van Hecke 2010]. It was found out further, that the packing properties, i.e. the mechanical stiffness or resistance to shear, are controlled by the distance to the point J , $\Delta\phi := \phi - \phi_{crit}$.

Isostaticity. The jamming point J is sharply defined in isostatic systems of frictionless and monodisperse spheres [Alexander 1998]. This means that the contact number at this point attains a sharply defined value which results from the degrees of freedom and constraints of the particle packing. In a d -dimensional packing of N identical soft and frictionless spheres, the interparticle forces are perpendicular to the contact plane of the particles. The number of unknowns, which is the magnitude of contact forces, is equal to the number of contacts $zN/2$, since each contact is shared by two particles. The requirement that the contact forces between all particles are balanced, leads to Nd force balance equations. If the packing is at equilibrium, at least one solution exists for the force distribution [Andreotti et al. 2013, pp. 71-73]. This implies that there must be fewer equations than unknowns which gives $z \geq 2d$.

Besides the equilibrium condition, the particles just touch at point J , so that a non-penetrability condition must be satisfied, which is $\|\vec{r}_i - \vec{r}_j\| = d_p$ and \vec{r}_i and \vec{r}_j are the positions of particle i and j . This condition adds another $zN/2$ equations to the system of Nd degrees of freedom (in position). Consequently, a solution for the force distribution in the packing only exists if the number of contacts is less than the number of degrees of freedom, i.e. $z \leq 2d$.

Combining these two inequalities then yields that the critical contact number, z_{crit} , in a frictionless particle system will attain the isostatic value $z_{crit} = z_{iso} = 2d$ [Tkachenko and Witten 1999; O'Hern et al. 2003]. In this case, the number of unknowns, i.e. the contact forces, is equal to the number of equations so that by knowing the positions of the particles, the contact forces can be calculated [Andreotti et al. 2013, pp. 71-73]. It

is also interesting to note that the contact number increases with the square root of the excess packing density $\phi - \phi_{crit}$ (Figure 3.8 A) independent of the dimension, interaction potential (Hookean, or Hertzian) and polydispersity [O'Hern et al. 2003].

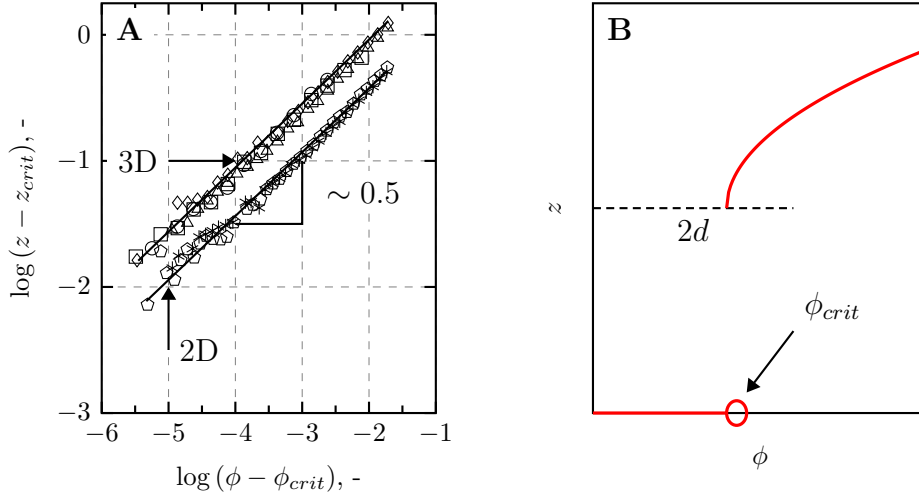


Figure 3.8.: Correlation of the contact number and the packing density. (A) Excess contact number $z - z_{crit}$ as a function of the excess packing density $\phi - \phi_{crit}$ for various monodisperse and bidisperse packings with Hookean and Hertzian contact potential (reproduced from O'Hern et al. [2003]). (B) Schematic drawing of the contact number z as a function of the packing density ϕ showing the jamming transition of frictionless particles (reproduced from van Hecke [2010]).

Hence, the correlation of the contact number and the packing density can be formulated as

$$\Delta z = z_0 \sqrt{\Delta \phi}, \quad (3.67)$$

where $\Delta z = z - z_{crit}$ is the excess contact number and z_0 depends on the dimension and weakly on the polydispersity taking values of 3.5 ± 0.3 in 2D and 7.9 ± 0.5 in 3D [O'Hern et al. 2003]. Figure 3.8 B shows the jamming transition of frictionless particle packings in which below ϕ_{crit} the average contact number is zero and jumps discontinuously to $z = 2d$ for jammed systems. With increasing ϕ , the contact number then scales with a power law.

Since an increase in the average contact number in a system of soft frictionless spheres is related to the deformation of the particles, one might also assume some kind of power law scaling of the packing compression pressure with the excess packing density. O'Hern et al. [2003] found that the compression pressure is $p \sim (\Delta \phi)^1$ for Hookean particle contact and $p \sim (\Delta \phi)^{3/2}$ for Hertzian particle contact, which is similar to the scaling of the

contact pressure with overlap δ during single particle compression. As the *compression bulk modulus* B and the *bulk shear modulus* G are the derivatives of the compression pressure with respect to the deformation strain, one would expect an appropriate scaling of these values from the excess packing density.

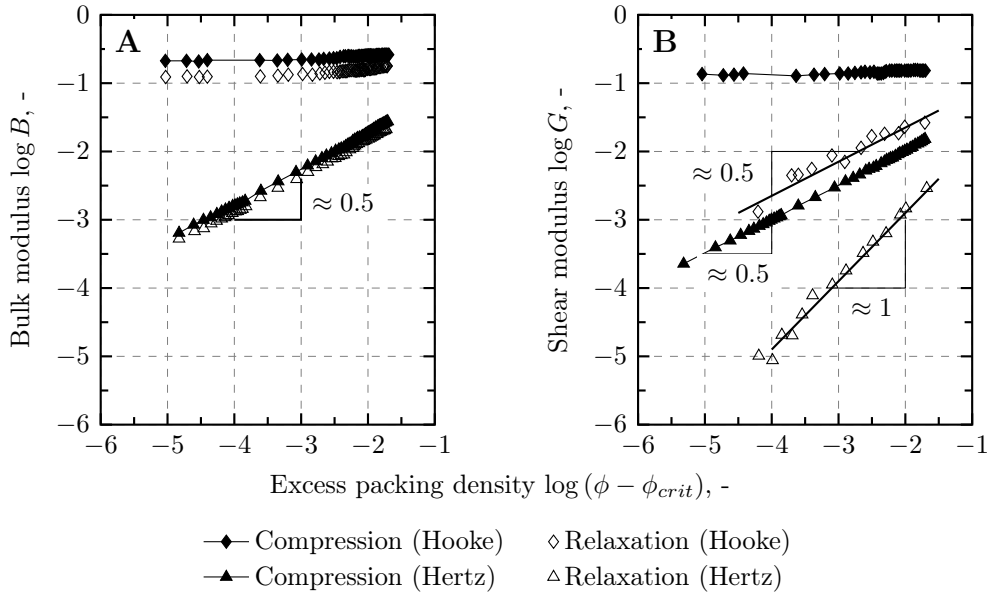


Figure 3.9.: Bulk and shear modulus as a function of the excess packing density. The data represent the scaling of the different moduli for Hookean as well as for Hertzian particle interaction for a bidisperse particle packing (reproduced from O’Hern et al. [2003]). **(A)** Packing bulk modulus B during affine compression and during relaxation. **(B)** Packing shear modulus G during affine compression and during relaxation.

Figure 3.9 shows the scaling of the packing bulk and shear modulus B and G with distance to jamming point J . The data correspond to an affine deformation and subsequent relaxation of a bidisperse particle packing [O’Hern et al. 2003]. ‘Affine’ in this context means that the change in excess packing density $\Delta\phi$ is proportional to the particle overlap δ (no particle rearrangement) and that all bonds contribute similarly to the increase in elastic energy [van Hecke 2010]. Based on these experiments it was found, that during the relaxation of the deformed packing, the particles rearranged non-affine leading to lower values of the bulk and shear modulus. However, the difference between the compression and the relaxation bulk modulus is small, so that it can be concluded that the affine assumption gives the correct prediction for the scaling of the bulk modulus (Figure 3.9 A). Thus, the scaling relation of the bulk modulus can be described

similar to $d_\delta F \sim \delta^{1/2}$ as

$$\text{Hooke: } B \sim \Delta\phi^0, \quad (3.68)$$

$$\text{Hertz: } B \sim \Delta\phi^{1/2}. \quad (3.69)$$

Nevertheless, the non-affine particle rearrangement during the relaxation of the deformed system has a significant influence on the shear modulus of the packing (Figure 3.9 B). Thus, the scaling relation of the shear modulus is [O’Hern et al. 2003; Makse et al. 1999; Ellenbroek et al. 2006, 2009].

$$\text{Hooke: } G \sim \Delta\phi^{1/2}, \quad (3.70)$$

$$\text{Hertz: } G \sim \Delta\phi^1. \quad (3.71)$$

Friction. Taking into account interparticle friction, the forces are no longer perpendicular to the contact plane, which increases the number of force balance equations by $d(d-1)N/2$ torque balance equations for each particle. Hence, there are $zNd/2$ unknowns in the particle system. The non-penetrability condition is the same as in the frictionless case, giving $zN/2$ constraints on the Nd particle positions. This again leads to $z \leq 2d$. In frictional packings however, the $zNd/2$ unknown force components being constrained by Nd force and $d(d-1)N/2$ torque balance equations leads to $z \geq d+1$. Combining these two bounds, frictional particle packings can attain a range of contact numbers $d+1 \leq z_c \leq 2d$.

$d+1 = z_{iso}^\mu$ is then the isostatic value for frictional spheres and it appears that z_c approaches z_{iso}^μ only in the limit of $\mu \rightarrow \infty$. In all other cases it appears to be that the number of contacts at jamming is larger than the minimum number needed for force balance and rigidity. Thus, frictional packings of soft spheres are *hyperstatic* ($z_c \geq z_{iso}^\mu$) and the force network is undetermined. This means that the contact forces are not uniquely determined by the packing geometry but also depend on the history of packing preparation [van Hecke 2010]. Hence, bulk quantities such as the compression or shear modulus do not exhibit scaling with distance to the jamming point, as frictionless particle systems do ($z_c = z_{iso}^\mu$). However, it was found by numerical simulations that the mechanical properties exhibit a non-trivial scaling with the distance to the isostatic limit $z - z_{iso}^\mu$ [Somfai et al. 2007; Magnanimo et al. 2008], whereas the ratio G/B is proportional to $z - z_{iso}^\mu$ [Somfai et al. 2007]. As a conclusion, jamming of frictional particles can be

understood as a two-step process, in which the contact number z is determined by the friction coefficient, pressure and packing procedure and the mechanical properties then scale with $z - z_{iso}^{\mu}$, the distance to isostaticity.

Contact Force Distribution and Force Chains

It has been found by experiments [Drescher and de Josselin de Jong 1972; Geng et al. 2003; Howell et al. 1999] and simulations [Cundall and Strack 1979; Radjai et al. 1999] that granular packings show inhomogeneous networks of 'larger-than-average' contact forces, which are referred to as *force chains*. In homogeneous systems, force chains are usually defined as pertaining to forces that are above a certain cutoff, i.e. the average interparticle force $F > \langle F \rangle$, and whose straight segments are of the order of a few particle diameters in length [Hinrichsen and Wolf 2004, pp. 11-19]. Various methods exist to study the distribution of contact forces in granular systems. For the analysis of 2D systems the method of photo-elasticity (materials like Plexiglass become birefringent when stressed) was proven successful (Figure 3.10 A). 3D systems are currently investigated by theoretical discrete element simulations (Figure 3.10 C) [Andreotti et al. 2013, pp. 73-82]. Figure 3.10 A shows a 2D packing of photo-elastic discs in an isotropically compressed state. The force-chain network is heterogeneous, with some discs being very bright and therefore highly constrained, while others do not show any photo-elastic effect, which means that they are nearly free of stress.

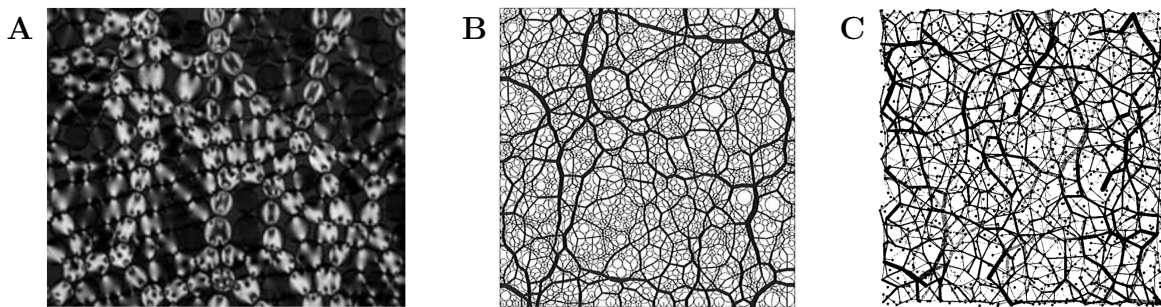


Figure 3.10.: Visualization of force chains. (A) Packing of photo-elastic discs at isotropically compressed state [Majmudar and Behringer 2005]. (B) 2D contact-dynamics simulation of discs of different diameter at isotropic compression [Radjai et al. 1999]. (C) 3D discrete element simulation of particles in a cylindrical container during uniaxial compression [Radjai et al. 1999]. In (B) and (C) the line width scales with the magnitude of the forces.

The observed force chains are an indicator for the anisotropy of a granular packing so that it can be stated that anisotropy is inherent in any discrete particle system, i.e.

in the neighborhood of the point of force application. Further, it has been found that in similar systems of polydisperse frictional particles (Figure 3.10 C) about 70% of the applied forces is carried in force chains and that the range of force magnitude is wide [Hinrichsen and Wolf 2004, pp. 11-19; Andreotti et al. 2013, pp. 73-75]. Figure 3.11 shows the distribution of normal contact forces between the particles, i.e. the probability $P(F)$ that the force is between F and $F + dF$. Here, the force is normalized by the average contact force $\langle F \rangle$. Figure 3.11 A gives the probability distribution of contact forces for the simulated uniaxial compression of a polydisperse particle packing shown in Figure 3.10 C.

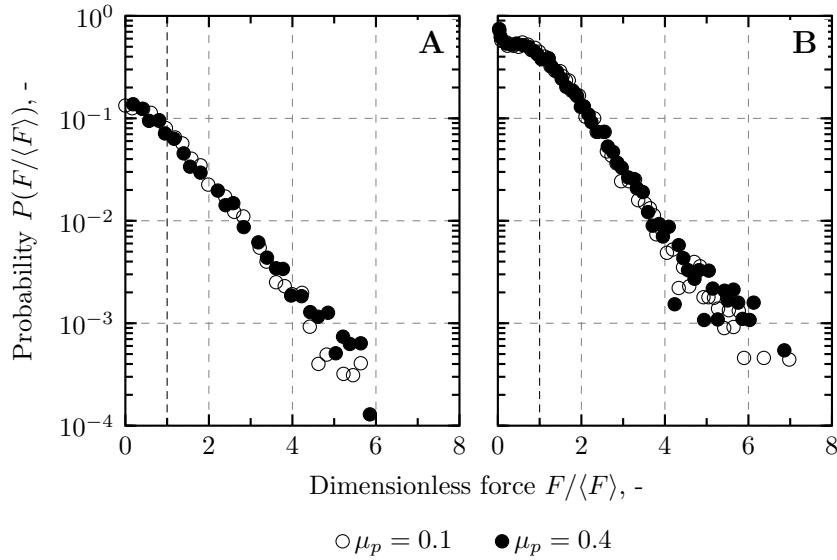


Figure 3.11.: Probability distribution of contact forces in a jammed packing. (A) 3D discrete element simulations of uniaxial packing compression [Radjai et al. 1999] and (B) measured data by Lovoll et al. [1999]. μ_p corresponds to the particle friction.

It can be seen that very large forces, up to six times the average force, and very low forces coexist. The second finding is that the distribution at higher forces $F > \langle F \rangle$ is found to be exponential, whereas at lower forces it is rather flat. The appearance of strong and weak-force networks as well as the existence of an exponential tail are very robust features of a frictional particle packing. Thus, independent of the particle friction and irrespective of whether the packing is regular or random, the force distribution has more or less the same shape [Andreotti et al. 2013, pp. 73-75].

The coexistence of the strong- and weak-force networks and its effect on packing anisotropy can be visualized by the angular distribution of contacts and contact forces.

An exemplary polar diagram for a 2D packing under vertical load is given in Figure 3.12. A slight anisotropy in the direction of the stress' principle axis can be seen by the orientation of the strong and weak-force network.

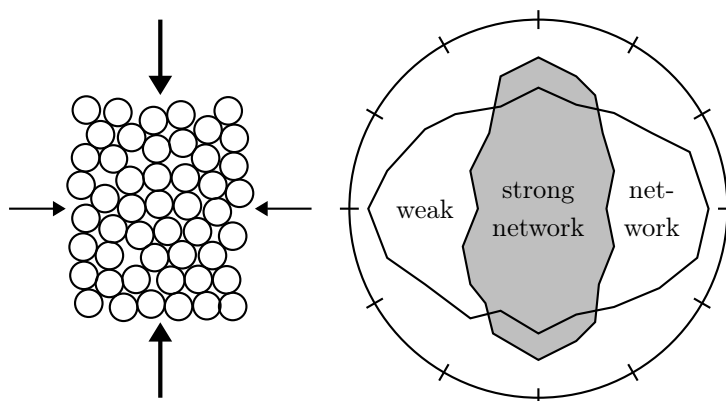


Figure 3.12.: Angular distribution of contacts in a force chain network for vertical loading. The orientation of the weak and strong force network indicates the anisotropy of the granular system (reproduced from [Andreotti et al. 2013, p. 78]).

In this case of nearly uniaxial compression, the strong and weak-force networks are oriented in orthogonal direction. The contacts seemed to be formed preferentially in the direction of higher load. The weak forces and corresponding contacts are distributed more or less isotropically. According to Andreotti et al. [2013, p. 79] a granular medium can be described as *'a solid skeleton, which gives its strength to the structure, immersed in an isotropic phase, ensuring the stability of the skeleton'*. This means that a packing under uniaxial load would not be stable without the presence of small lateral forces required to prevent the buckling of alignments.

3.3.5. Packing Compression

Depending on the method of packing preparation, the particles arrange in a random loose packing configuration. However, in many practical situations it is necessary to increase the density of the packed bed, i.e. in chromatographic applications to maintain the column packing performance. The most common modes of packing consolidation and compaction are shaking or tapping of the column (Figure 3.13 A), compression by high flow velocities (Figure 3.13 B) or uniaxial mechanical compression by lowering a plunger (Figure 3.13 C).

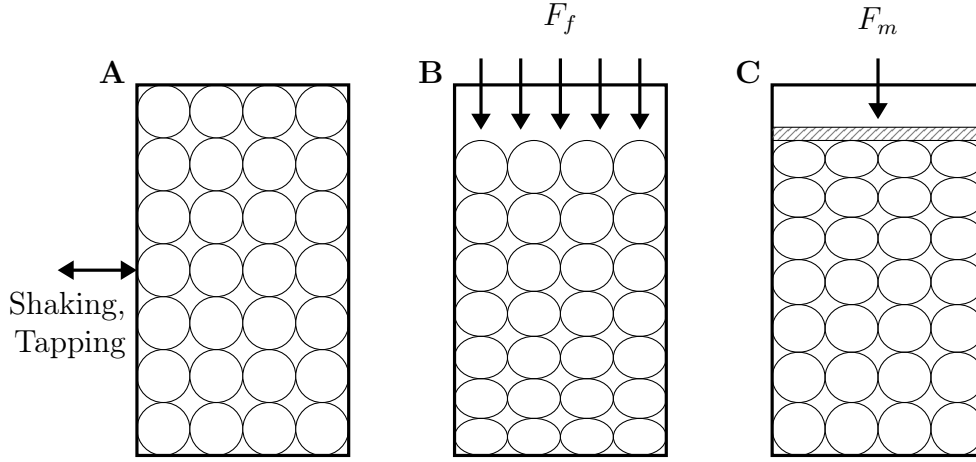


Figure 3.13.: Modes of packing compaction. (A) Shaking or tapping of the column, (B) compression by high flow velocities and drag forces F_f and (C) uniaxial compression by a plunger with F_m .

During compression, the initial volume of the packing V_0 is reduced by a portion $V_0 - V$ so that a compression factor can be defined [Stickel and Fotopoulos 2001]

$$\lambda = \frac{V_0 - V}{V_0}. \quad (3.72)$$

In the case of uniaxial compression or flow compression, which is the usually applied in chromatographic packing preparation, the cross-sectional area of the packed bed remains constant so that $\lambda = (H_0 - H)/H_0$ with H being the height of the packing.

Assuming that the compression of the packing is mainly caused by a reduction of the external porosity ϵ and that the compression of the individual particle is negligible, the packing density ϕ and the compression factor λ are correlated by

$$\phi = \frac{1 - \epsilon_0}{1 - \lambda}, \quad (3.73)$$

where ϵ_0 is the average initial external porosity of the packing in the uncompressed state. By definition, the average packing porosity in the compressed state is given by $\epsilon = (\epsilon_0 - \lambda)/(1 - \lambda)$.

For large packing compressions, i.e. during column packing, Keener et al. [2004a] defined the packing compression as $\lambda^* = (H_0 - H)/H$ referencing to the compressed state. This leads to

$$\phi = (1 - \epsilon_0)(1 + \lambda). \quad (3.74)$$

The compression of the packed bed in liquid chromatography due to hydrodynamic load is a general problem for chromatographers [Verhoff and Furjanic Jr. 1983]. The reduction of the interstitial void fraction due to packed bed compression, causes a non-linear increase in flow rate with pressure drop (see e.g. Equation (3.63)). Hence, the net force acting on any point of the packed bed is the sum of forces originating from the flow, the mechanical compression force caused by the end pieces of the column, the friction between the packing material and the column wall as well as the gravitational force due to density differences of the packing material and the liquid (Figure 3.14).

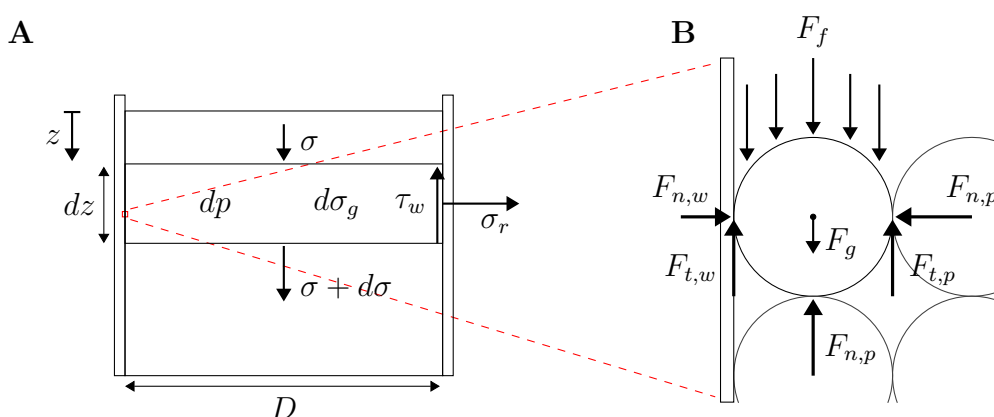


Figure 3.14.: Forces acting on a compressible packed bed. (A) Force balance of an axial segment of thickness dz of the compressible packed bed of diameter D . (B) Forces acting on single particles of the packed bed. F_f denotes the drag force of the fluid, F_g is due to the weight of the particle, $F_{n,w}$ and $F_{t,w}$ are the normal and friction force of the wall, $F_{n,p}$ and $F_{t,p}$ are the normal and friction force of neighboring particles.

A one-dimensional stress balance across a column segment results in

$$\frac{\partial \sigma}{\partial z} = -\frac{\partial p}{\partial z} - \frac{4}{D} \mu_w \frac{\nu}{1-\nu} \sigma + \Delta \rho (1-\epsilon) g, \quad (3.75)$$

where σ is the axial solid stress, $\partial p / \partial z$ is the pressure gradient given by the Kozeny-Carman equation (Equation (3.57)), D is the column diameter, μ_w is the wall friction coefficient, ν the packing Poisson's ratio, $\Delta \rho$ is the density difference between the packing material and the fluid, ϵ is the packed bed porosity and g the gravitational constant. Generally, the stress transmitted from the fluid flow is assumed to be equal to the hydrodynamic pressure drop [Östergren and Trägårdh 1999]. As is can be seen in Equation (3.75), the solid stress σ , due to the wall friction, is less than expected from the pressure drop and the gravitational force. The wall friction force always opposes the motion

of the packing during compression and relaxation, which is known as the *wall support*. The influence of the wall friction on the motion of the packing decreases with increasing column diameter. Thus, the shear stress originating from the wall friction is highest at the column wall and decreases towards the column axis, causing variations in the solid stress σ also in radial direction [Tiller and Lu 1972; Östergren and Trägårdh 1999]. In chromatographic applications, the stress originating from the gravitational force $d\sigma_g$ is usually small compared to the other stress contributions and can thus be neglected [Östergren and Trägårdh 1999].

4. Computational Background

The three-dimensional mechanistic modeling of the hydrodynamic behavior of chromatographic packed beds, being resolved in time and space, requires the explicit consideration of solid particulate phase whose behavior is governed by the interparticle micromechanics coupled to fluid mechanics. Therefore, a hybrid modeling approach was applied coupling Computational Fluid Dynamics (CFD) and the Discrete Element Method (DEM). In DEM, the packing is modeled by discrete particles of defined sizes and densities and the behavior of the particles is described by force and momentum equations. Coupled with CFD, the complex interaction between the packed bed and the percolating fluid can be modeled. The following chapter provides the basic principles of this coupled simulation approach.

4.1. Computational Fluid Dynamics (CFD)

The principles of computational fluid dynamics (CFD) are based on the conservation laws of mass, momentum, and energy, which are known as the *Navier-Stokes equations* [Versteeg and Malalasekera 2007]. Therein, the state variables of the fluid are calculated for a fluid element or a control volume in a fixed coordinate system (Eulerian method of approach). State variables can be the velocity, density, temperature of the fluid and concentrations of chemical species. The Navier Stokes equations form a coupled system of non-linear partial differential equations, which cannot be solved analytically. Numerical solutions require a discretization of the governing equations in space and time which transform the coupled system of differential equations in a system of linear equations. Thus, every equation represents a balance of the state variables of the fluid at a specific point of the computational lattice that only depends on the state variables of the fluid of neighboring lattice points. The most common method of discretization used in computational fluid dynamics calculations is the *Finite Volume Method*, in which the simulation domain and geometry is divided into non-overlapping finite control volumes. Here, the

system of equations is solved on each point on a lattice, which represents the center of the control volume. In the following, a rough overview of the governing equations concerning the CFD part of the CFD-DEM coupling is given. Detailed information of numerical flow simulation and discretization schemes is given in literature [e.g. Patankar and Spalding 1980; Versteeg and Malalasekera 2007; Lecheler 2009; Schwarze 2013].

4.1.1. Governing Equations

Volume Averaged Navier-Stokes Equations

The motion of an incompressible fluid phase ($\rho_f = \text{const.}$) as part of a two-phase solid-fluid mixture is governed by the volume averaged Navier-Stokes (VANS) equations, that can be written as

$$\frac{\partial \alpha_f}{\partial t} + \nabla \cdot (\alpha_f \mathbf{u}_f) = 0, \quad (4.1)$$

$$\frac{\partial (\alpha_f \mathbf{u}_f)}{\partial t} + \nabla \cdot (\alpha_f \mathbf{u}_f \mathbf{u}_f) = -\frac{\alpha_f}{\rho_f} \nabla p + \nabla \cdot (\alpha_f \boldsymbol{\tau}) - \mathbf{R}_{pf}. \quad (4.2)$$

Here, the Nabla operator is defined as $\nabla = \left(\frac{\partial}{\partial x_1}, \frac{\partial}{\partial x_2}, \frac{\partial}{\partial x_3} \right)$. α_f is the volume fraction occupied by the fluid, ρ_f is its density, \mathbf{u}_f its velocity. The term $\frac{\alpha_f}{\rho_f} \nabla p$ represents the pressure forces acting on a fluid volume, and $\boldsymbol{\tau} = \nu_f \nabla \mathbf{u}_f$ is the stress tensor for the fluid phase which takes into account frictional forces. \mathbf{R}_{pf} accounts for momentum exchange with the particulate phase which is calculated for each cell where it is assembled from the particle-based drag forces. Bold symbols represent vector and tensor quantities [Kloss et al. 2012].

Momentum Exchange Between the Fluid Phase and the Particle Phase

For numerical reasons the momentum exchange term is split up into an implicit and an explicit term using the cell-based ensemble averaged particle velocity $\langle \mathbf{u}_p \rangle$ [Goniva et al. 2012; Kloss et al. 2012].

$$\mathbf{R}_{pf} = \mathbf{K}_{pf} (\mathbf{u}_f - \langle \mathbf{u}_p \rangle), \quad (4.3)$$

where

$$\mathbf{K}_{pf} = \frac{\sum_i \mathbf{F}_d}{V_{cell} \cdot |\mathbf{u}_f - \langle \mathbf{u}_p \rangle|}. \quad (4.4)$$

For the calculation of the drag or momentum exchange coefficient \mathbf{K}_{pf} many correlations can be found in literature [Kafui et al. 2002; Tsuji et al. 2008; Zhu et al. 2008]. The model used in this work was published by Koch and Hill [2001].

Therein, the fluid drag force exerted on a particle i is given by [van Buijtenen et al. 2011]

$$\mathbf{F}_{d,i} = \frac{V_i \beta}{\alpha_p} (\mathbf{u}_f - \mathbf{u}_i) \quad (4.5)$$

with

$$\beta = \frac{18\eta_f \alpha_f^2 \alpha_p}{d_p^2} \left(F_0(\alpha_p) + \frac{1}{2} F_3(\alpha_p) Re_p \right) \quad (4.6)$$

$$Re_p = \frac{\alpha_f |\mathbf{u}_f - \mathbf{u}_p| d_p}{\nu_f} \quad (4.7)$$

$$F_0(\alpha_p) = \begin{cases} \frac{1+3\sqrt{\frac{\alpha_p}{2}} + \frac{135}{64}\alpha_p \ln(\alpha_p) + 16.14\alpha_p}{1+0.681\alpha_p - 8.48\alpha_p^2 + 8.16\alpha_p^3} & \text{for } \alpha_p < 0.4 \\ \frac{10\alpha_p}{\alpha_f^3} & \text{for } \alpha_p \geq 0.4 \end{cases} \quad (4.8)$$

$$F_3(\alpha_p) = 0.0673 + 0.212\alpha_p + \frac{0.0232}{\alpha_f^5}. \quad (4.9)$$

Here, α_p is the particle fraction in a CFD cell ($\alpha_f + \alpha_p = 1$). It needs to be pointed out that the definition of the Reynolds number within the Koch-Hill-model is related to the superficial fluid flow velocity.

Given this, the momentum exchange parameter \mathbf{R}_{pf} can be calculated from β according to [van Buijtenen et al. 2011]

$$\mathbf{R}_{pf} = \frac{1}{V_{cell}} \sum_{\forall i \in cell} \frac{V_i \beta}{\alpha_p} (\mathbf{u}_f - \mathbf{u}_i) \quad (4.10)$$

Besides the fluid drag force resulting from a relative velocity between the particle and the fluid other forces such as Magnus force (lift force of a backspinning particle in a fluid stream), virtual mass forces (resulting from particle acceleration) or Saffman force (lift force a fast passing fluid exerts on surface, e.g. an aircraft wing) are neglected so far. In the case of relevance additional force relationships can be added easily.

4.2. The Discrete Element Method (DEM)

The DEM was introduced by Cundall and Strack [1979]. A brief overview of this method will be given in this section. Further details on the contact physics and implementation issues are available in literature [e.g. Di Renzo and Di Maio 2004; Pöschel and Schwager 2005; Zhu et al. 2007, 2008; Norouzi et al. 2016]. The strength of this method lies in its ability to resolve the granular medium at the particle scale, thus allowing realistic contact force calculations and giving rise to phenomena induced by particle geometry combined with relative particle motion. Thereby, it is able to capture many phenomena, describe dense and dilute particulate regimes, rapid and slow flow and equilibrium states or wave propagation within the granular material [Kloss et al. 2012].

4.2.1. Governing Equations

The DEM is a *Lagrangian method*, meaning that all particles in the computational domain are tracked by explicitly solving their trajectories. The force balance and the momentum balance for the i th particle is [Goniva et al. 2012]

$$m_i \ddot{\mathbf{x}}_i = \mathbf{F}_{i,n} + \mathbf{F}_{i,t} + \mathbf{F}_{i,f} + \mathbf{F}_{i,p} + \mathbf{F}_{i,\nu} + \mathbf{F}_{i,b}, \quad (4.11)$$

$$\mathbf{I}_i \frac{d\boldsymbol{\omega}_i}{dt} = \mathbf{r}_{i,c} \times \mathbf{F}_{i,t} + \mathbf{T}_{i,r}, \quad (4.12)$$

where $\mathbf{F}_{i,n}$ is the normal particle-particle contact force and $\mathbf{F}_{i,t}$ is the tangential particle-particle contact force. $\mathbf{F}_{i,f}$ is the fluid drag force, respectively the force that the surrounding fluid phase may exert on the particles. These force contributions are described more in detail in the following sections. $\mathbf{F}_{i,p} = (1/2\rho_f \nabla \mathbf{u}_f^2) V_p + \rho_f g V_p$ and $\mathbf{F}_{i,\nu} = -\nabla \cdot (\boldsymbol{\tau}_f) V_p$ denote the pressure and viscous forces acting on the particle. Body forces like gravity, electrostatic or magnetic forces are summarized to $\mathbf{F}_{i,b}$. $\mathbf{T}_{i,r}$ is an additional torque on the particle that can be used to model non-sphericity by means of a “rolling friction” model. Detailed description of the individual force contributions is given in Zhou et al. [2010] and Goniva et al. [2012]. In the DEM, each particle is mathematically represented as a sphere, another geometrically well defined volume or a combination of them. With the momentum balance the translational and angular accelerations of a sphere are calculated. In the soft particle DEM, the particles are allowed to overlap slightly so that the normal force acting on a particle can then be deduced from this spartial overlap δ

and the normal relative velocity at the contact point, $\Delta \mathbf{u}_n$.

Particle Contact Laws

The mechanical properties of the singular particle are represented by a simple linear spring-dashpot model as shown in Figure 4.1. Based on this model, the following formula

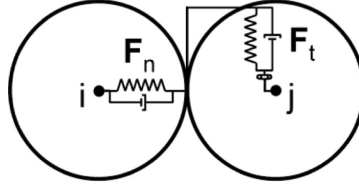


Figure 4.1.: Simple linear spring-dashpot model. During particle impact, the normal and tangential forces, F_n and F_t , are modeled by a system of springs and dashpots [Kloss et al. 2012].

is used for the calculation of the frictional force between two granular particles i and j , when the distance r between those particles is less than their contact distance $d = R_i + R_j$ (i.e. $r = R_i + R_j - \delta$). Here, R_i and R_j are the radii of particle i and j , respectively.

$$\mathbf{F} = \underbrace{\left(\underbrace{k_n \delta_n \mathbf{n}_{ij}}_{\text{Normal overlap}} - \underbrace{\gamma_n \mathbf{v} \mathbf{n}_{ij}}_{\text{Normal rel. vel.}} \right)}_{\text{Normal force } \mathbf{F}_n} + \underbrace{\left(\underbrace{k_t \delta_t \mathbf{t}_{ij}}_{\text{Tangential overlap}} - \underbrace{\gamma_t \mathbf{v} \mathbf{t}_{ij}}_{\text{Tangential rel. vel.}} \right)}_{\text{Tangential force } \mathbf{F}_t}. \quad (4.13)$$

When $r > d$, there is no contact force between both particles [Kloss et al. 2012].

The elastic constants k_n , k_t and the damping constants γ_n , γ_t depend on the contact law, which can be chosen between the nonlinear Hertz contact and the linear Hooke contact. Both are described in detail in the following sections. Equation (4.13) is also used to quantify particle-wall interaction. The tangential Force \mathbf{F}_t is truncated to fulfill the Coulomb friction criterion with μ being the friction coefficient. If the tangential force exceeds the Coulomb friction limit the particles slide over each other with a tangential force proportional to the normal contact force according to $\mathbf{F}_t \leq \mu \mathbf{F}_n$.

By varying k_n , γ_n , k_t and γ_t as a function of the overlap different kinds of contact models and contact laws (linear and non-linear) can be implemented. To account for specific viscoelastic deformation the contact model Equation (4.13) can be modified or replaced by appropriate equations.

Nonlinear Hertz Contact. The nonlinear Hertz contact model is based on the Hertz theory of elastic contact [Hertz 1881; Johnson 1985, p. 84-106]. The normal force between two contacting particles is then given by Equation (3.1), which in terms of Equation (4.13) gives the parameter k_n as

$$k_n = \frac{4}{3}Y^* \sqrt{R^* \delta_n}, \quad (4.14)$$

and k_t as

$$k_t = 8G^* \sqrt{R^* \delta_n} \quad (4.15)$$

Here, Y^* , R^* , G^* are the equivalent Young's modulus, radius, and shear modulus of the two particles in contact and are calculated as the reciprocal sum of the individual Young's moduli, radii, and shear moduli according to Equations (3.2) (with $Y^* = E^*$), (3.3) and

$$\frac{1}{G^*} = \frac{2(2 - \nu_1)(1 + \nu_1)}{Y_1} + \frac{2(2 - \nu_2)(1 + \nu_2)}{Y_2} \quad (4.16)$$

The damping constants γ_n and γ_t , which are coupled to the impact velocity of the contacting particles are expressed as

$$\gamma_n = -2\sqrt{\frac{5}{6}}\beta \sqrt{S_n m^*} \geq 0, \quad (4.17)$$

and

$$\gamma_t = -2\sqrt{\frac{5}{6}}\beta \sqrt{S_t m^*} \geq 0, \quad (4.18)$$

where

$$S_n = 2Y^* \sqrt{R^* \delta_n}, \quad S_t = 8G^* \sqrt{R^* \delta_n}, \quad (4.19)$$

and

$$\beta = \frac{\ln(e)}{\sqrt{\ln^2(e) + \pi^2}}. \quad (4.20)$$

Here, m^* is the equivalent mass of the two particles as described earlier. Detailed information concerning the derivation of these parameters is given in literature [e.g. Pöschel and Schwager 2005; Schwager and Pöschel 2007; Kloss et al. 2012; Norouzi et al. 2016, pp. 17-67].

Linear Hooke Contact. The linear Hooke contact describes a linear dependence of the particle compression force on the particle overlap according to a simple Hookean spring. Therein the elastic constants k_n , k_t and damping constants γ_n and γ_t are defined as

$$k_n = k_t = \frac{16}{15} \sqrt{R^* Y^*} \left(\frac{15 m^* V^2}{16 \sqrt{R^* Y^*}} \right)^{\frac{1}{5}} \quad (4.21)$$

and

$$\gamma_n = \gamma_t = \sqrt{\frac{4 m^* k_n}{1 + \left(\frac{\pi}{\ln(e)} \right)^2}} \geq 0. \quad (4.22)$$

Here V is the *characteristic impact velocity* of two particles in contact, e is the coefficient of restitution and ν the Poisson ratio. The characteristic impact velocity is a parameter that does not have a real physical meaning and appears mostly in mathematical particle models [Pöschel and Schwager 2005]. The different compression force behavior of the Hertz and Hooke contact models as well as the influence of the characteristic impact velocity is illustrated in Figure 4.2. As can be seen, the characteristic impact veloc-

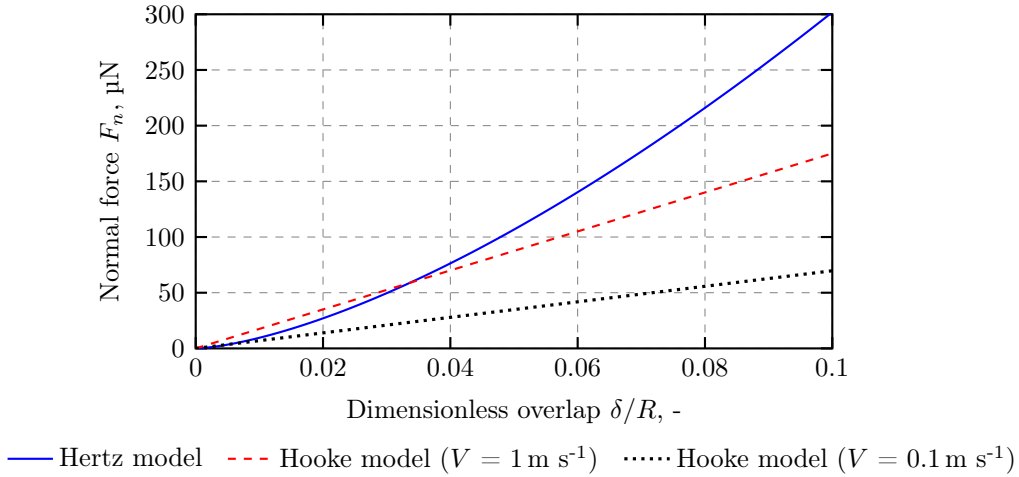


Figure 4.2.: Normal force calculated by the Hertz and Hooke contact model. With increasing overlap, the normal force increases proportionally to $\delta^{3/2}$ using the Hertz contact model, whereas using the Hooke contact model, the normal force is proportional to δ . Simulation parameters were: $R = 45 \mu\text{m}$, $E = 10 \text{ MPa}$ and $\rho_p = 1140 \text{ kg m}^{-3}$.

ity significantly influences the normal force F_n calculated by the linear Hooke model. With increasing V , the particles appear stiffer as the elastic constant k_n scales with V according to $k_n \sim Y^{4/5} V^{2/5}$.

4.2.2. DEM solver

The Discrete Element Method is implemented in the open source software package LIGGGHTS [LIGGGHTS 2016], which stands for 'LAMMPS Improved for General Granular and General Heat Transfer Simulations'. LIGGGHTS is based on the open source Molecular Dynamics code LAMMPS ('Large Atomic and Molecular Massively Parallel Simulator') which was designed by Sandia National Laboratories for massively parallel computing on distributed memory machines [Plimpton 1995]. It uses message-passing techniques (MPI) and spatial-decomposition of the simulation domain.

Particle Contact Detection Algorithm

A particle being situated in a packing of multiple particles cannot be in contact with all the other particles in the system at the same time, but only with its neighboring particles. Thus only the interaction between this small portion of particles needs to be calculated. The determination of particles which are in contact with a specific particle is managed by 'neighbor lists'.

The concept of using neighbor lists has been introduced by Verlet [1967]. Thus, a list is written periodically, meaning that every time step the list is checked and evaluations, based on the actual contacts, are determined. The advantage of such lists is that pairs of particles being too far away from a specific particle are a priori excluded from calculations of interaction forces. A pair of particles i, j is included in a neighbor list when the following criterion is satisfied:

$$\|x_i - x_j\| < R_i + R_j + s, \quad (4.23)$$

being R_i, R_j the radius of the spherical particle i and j and s the so called *Verlet* or *skin* parameter that can be freely chosen. The *Verlet* parameter determines how long the lists stay valid. Assuming a constant time step Δt and a maximum particle velocity v_{max} , the list is valid for

$$N_{Verlet} = \frac{s}{2v_{max}\Delta t} \quad (4.24)$$

time-steps. So, the collision detection is based on this list for the next N_{Verlet} time-steps before a new list is build. The *Verlet* parameter s can therefore be used to enhance the efficiency and performance of the DEM algorithm. Obviously, for $s = 0$ and $s \rightarrow \infty$ the concept of neighbor lists will be useless, as in the former case, no particle pair will be

included in the list and in the latter case all particles contained in the system will be included in the list [Kloss et al. 2012].

DEM Parallel Computing

The parallelization is realized via a MPI (Message Passing Interface) parallelism such that the simulation domain is basically decomposed into several MPI processes using an orthogonal processor grid. Each of the sub-domains contains an owned region, as well as a so called 'ghost' region. The particles residing in the owned domain are therefore called 'owned particles'. Each sub-domain or region is responsible for calculating the trajectories of his owned particles. 'Ghost particles' are particles owned by neighboring processes, which are more likely to interact with particles owned by neighboring sub-domains.

On the basis of particle radii and certain *Verlet* parameters it can be identified which particles of each process have to be copied as ghost particles to the respective neighboring processes. The multiple instances of a particle that can exist at each time-step, make clear, which processor owns a particle, i.e. which processor is responsible for trajectory calculation.

During the simulation, the positions, velocities and other properties of the owned particles are communicated to their ghost counterpart(s) at each time-step before the actual force calculation is executed. The forces that a ghost particle experiences by owned particles is then communicated back, so that the processor that owns the particle can compute the correct trajectory, including all forces properly. Particles can migrate to other processors in the course of a simulation run so both the group of owned particles as well as the group of ghost particles for a process are not a static assignment, but will in general vary over time. [Kloss et al. 2012]

4.3. The CFD-DEM Coupling

The coupling between the DEM and CFD algorithms needs some special attention. Keeping in mind that CFD calculations are based on a computational mesh it has to be distinguished whether the size of the particles is bigger or smaller than the computational grid size.

In the case of bigger particles, multiple cells are assumed to be covered by one particle

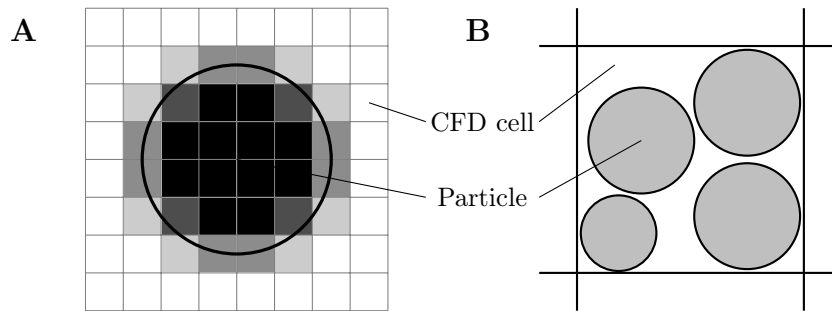


Figure 4.3.: Particle within the computational domain. (A) 'Resolved' particle-fluid interaction: A big particle covers several CFD cells (reproduced from [Hager et al. 2012]). (B) 'Non-resolved' particle-fluid interaction: Several small particles are contained in a CFD cell.

(at least ten cells [Kloss et al. 2012]) so a fictitious domain method [Patankar et al. 2000] is used to represent the particle phase (see Figure 4.3 A). In this 'resolved' method only one velocity and pressure field exists for both phases, thus the regions covered by a particle have the same velocity as the particle itself. This approach might be useful for the simulation of a particle-fluid system (containing a small number of particles) in which the flow around the particles is of primary interest.

However, for the study of hydrodynamics in chromatographic beds consisting of large quantities of small spherical beads, the flow around individual particles is of minor interest. In this case the 'non-resolved approach' is applied, in which the particle sizes are smaller than the CFD-computational grid size (see Figure 4.3 B) [Goniva et al. 2012]. Therefore, the particles are assumed to not completely fill a CFD cell and consequently are not resolved by the CFD simulation. Within the interaction of the particle and the fluid phase, only momentum and mass is considered.

To increase numerical stabilization *smoothing models* can be used, that dampen local fluctuations of the fluid fraction α_f calculated in neighboring CFD cells.

4.3.1. Coupling Algorithm

For solving the above-mentioned equations, a pressure-based solver using the PISO pressure velocity coupling [Issa 1986] is used. The coupling routine can be described as follows [Kloss et al. 2012]:

1. The particle positions and velocities are calculated by the DEM solver (Equation (4.11)).

2. The particle positions and velocities are passed to the CFD solver.
3. For each particle position the corresponding cell is determined in the CFD mesh.
4. For each cell the number of particles and the resulting particle volume fraction is determined, besides, the mean particle velocity is calculated.
5. On the basis of the particle volume fraction the fluid drag forces acting on each particle are calculated.
6. Particle-fluid momentum exchange terms are assembled from particle based forces by ensemble averaging over all particles in a CFD cell.
7. The calculated fluid drag forces are passed to the DEM solver and used within the next time step.
8. The CFD solver calculates the fluid velocity taking into account the local volume fraction and momentum exchange.
9. Additional equations such as species concentrations can optionally be evaluated.
10. The routine is repeated from step 1.

To avoid numerical inaccuracies Kloss et al. [2012] recommend to set the DEM time steps at least one order of magnitude smaller than CFD time step owing to high particle collision dynamics and requirements on maximum particle overlap for particle collision modeling. In special cases such as adsorption kinetic studies within the hydrodynamic modeling it might be desirable to use CFD time steps smaller than the coupling time steps. CFD and DEM timesteps can be set independently of each other and a coupling interval can be chosen by the user to regulate the amount of physical coupling between the particle and the fluid phase.

In step 4 it is necessary to interpolate the particle volumes (a Lagrangian property) from the DEM site to the volume fraction field being defined as a fixed Eulerian grid of the CFD site. Within the 'centered' volume fraction calculation, the volumes of those particles are summed up, whose centers are located in a CFD cell.

A more resolved method is the 'divided' volume fraction calculation, in which a particle is artificially divided into equal portions by a set of distributed marker points. Hence, if a particle extends into two or more CFD cells, the particle volume is evenly apportioned to the cells being partly covered by the particle [Kloss et al. 2012].

4.3.2. Efficient Parallel Computing by Load-Balancing

Load-balancing is a technique to distribute workload evenly across two or more computers, CPUs or other resources to get optimal resource utilization combined with maximized throughput, which is a topic widely interesting to computational mechanics [Hendrickson and Devine 2000].

In the case of DEM simulations, the workload of each processor is proportional to the number of owned particles. The standard approach used by LAMMPS is to decompose the simulation space once at the start of the simulation into equally large parts based on a 3D grid of processors, which will in general lead to an unequal number of particles in each processor's sub-domain. Also, a static one-time domain decomposition that is initially well-balanced can lead to load imbalance for many granular flow situations during the simulation run. In LIGGGHTS the load balance is performed in a way that the domain is decomposed with orthogonal cuts in x-, y- and z-direction so that these cuts divide the particle entity equally.

The DEM and CFD methods treat the fluid and particle calculations in two strictly separated codes, so that individual code development can be allowed on either side. The interaction between the two methods is realized by exchange fields being evaluated in a predefined time interval, where the codes work in a sequential manner. The data exchange between the codes is also done by MPI functionality.

5. Materials and Methods

5.1. Micro-Chromatography Columns and Operating Set-up

To perform the laboratory experiments, novel pressure-resistant micro- chromatography columns of different dimensions were designed. The column corpus was made of B Braun Omnifix[®] Solo polypropylene syringe (Carl Roth GmbH, Karlsruhe, Germany). In total, four columns of 3 mL, 5 mL, 10 mL, and 20 mL, with inner diameters of 9.6 mm, 13 mm, 16.25 mm, and 20 mm, respectively were constructed. The columns were equipped with 3 mm thick porous polypropylene frits with pore sizes of <20 μm (BEKOLut GmbH & Co. KG) at the column inlet and outlet to fix the packing in place. The pressure drop of the frits at a maximum volume flow rate of 2 L h^{-1} was <10 mbar and therefore negligible.

The columns were operated in a fully automated computer-controlled set-up (Figure 5.1 A).

An essentially pulse-free gear pump type Tuthill DGS-19PPPT2NNBG45 was used as feed pump providing a maximum flow rate of 2 L h^{-1} and a maximum pressure of 10 bar (Wagner Mess- und Regeltechnik GmbH, Offenbach, Germany). The flow was measured and controlled by a mass-flow controller type Bronkhorst High-Tech Mini Cori-Flow M13-RAD-22-K-S and the column pressure drop by a digital pressure controller type Bronkhorst High- Tech P-502C-21KR-RAD-33-V (Wagner Mess- und Regeltechnik GmbH, Offenbach, Germany). Fluid temperature and density were also measured by the mass-flow controller and controlled by a water bath (Thermo Haake, Karlsruhe, Germany). All relevant data was logged by the Bronkhorst High-Tech support software FlowDDE, FlowView, and FlowPlot and evaluated with MATLAB release 2014b (The MathWorks, Natick, Massachusetts, USA). The compression–relaxation behavior of the chromatographic packed bed was tracked by photographs taken with a Canon EOS 70D equipped with a Canon EF 100/2.8 L IS Macro USM objective (see Figure 5.2).

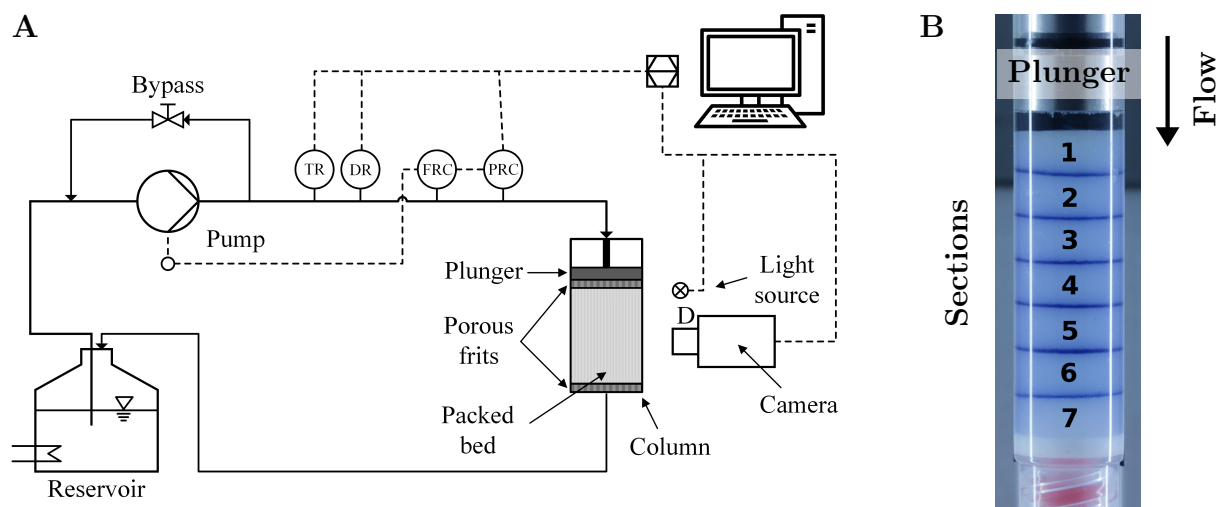


Figure 5.1.: Process flow chart and micro chromatography column [Dorn and Hekmat 2016]. (A) Schematic drawing of the fully automated operating set-up with the micro-chromatography column. The packed bed height was continuously tracked by a camera. The column was operated by controlling the flow rate. Fluid pressure (PRC), temperature (TR), and density (DR) were measured. (B) Photograph of the micro-chromatography column packed with CM Sepharose 6 FF[®] being divided into seven nearly equally sized sections by insertion of thin layers of Blue Sepharose 6 FF[®]. The arrow indicates the direction of flow. The inner column diameter was 9.6 mm.

The fluid was deionized water with 10 mM NaOH added to prevent contamination of the mobile phase and the resins by microorganisms. All experiments were performed at a controlled constant temperature of 20 °C.

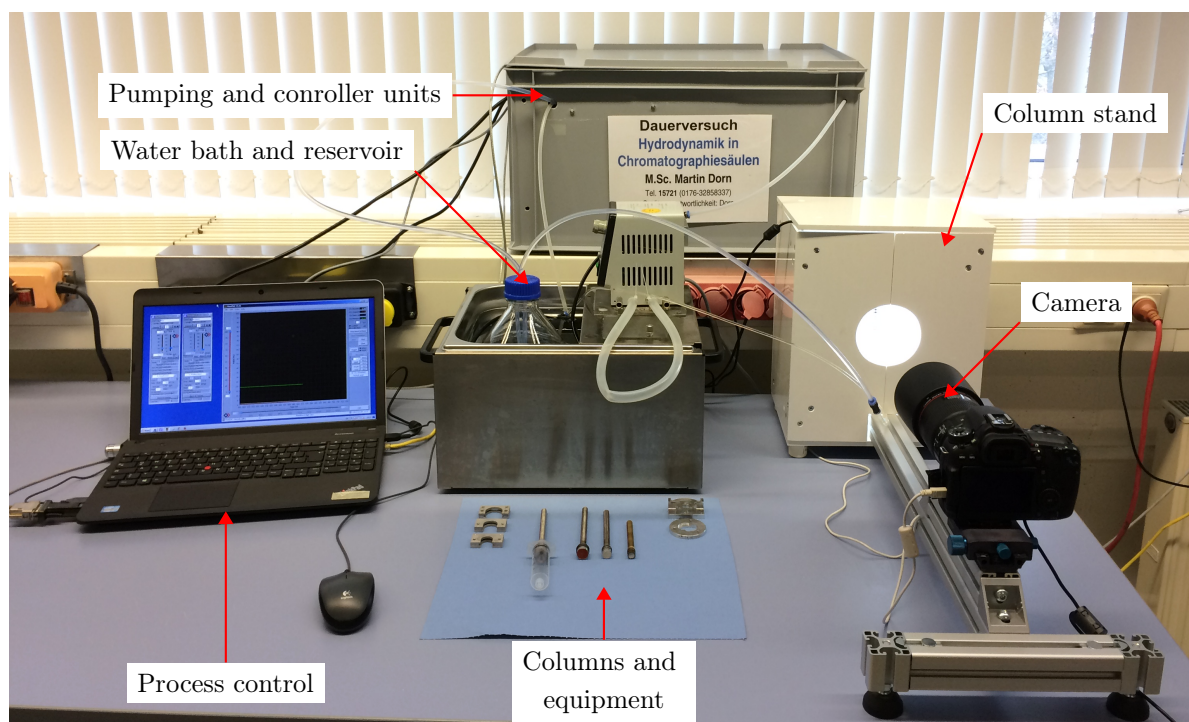


Figure 5.2.: Column operating set-up. The column was located and illuminated in a proper column stand, so that macroscopic changes of the column packing during operation could be recorded by the camera. The pumping and controller units for flow, temperature and pressure drop were located in a portable transport box (see Appendix Figure B.1 for details) and controlled by a computer equipped with the proper process software. The fluid temperature was controlled externally by the water bath.

5.2. Consumables and Further Equipment

The chromatography media used and characterized in this thesis is listed in Appendix Table A.1. Most of the experiments were carried out using the agarose based resin CM Sepharose 6FF[®] and the methacrylic resins Toyopearl[®] AF-Amino-650M and SP-650C (kindly provided by GE Healthcare Europe, Munich, Germany and Tosoh Bioscience, Stuttgart, Germany, respectively). CM Sepharose 6FF[®] (resin SEP) is a weak cation exchange resin made of spherical 6% cross-linked agarose. According to the manufacturer, the sizes of the particles in wet state are within the range of 45–165 μm with a mean diameter of 90 μm . Toyopearl AF-Amino-650 M and SP-650C (resin TOY) are affinity chromatography and cation exchange resins made of spherical methacrylic polymer. According to the vendor, over 80% of the wet particles are within a range of 40–90 μm with a mean diameter of 65 μm .

Chemicals, contrast agents and dyes used for media preparation and particle imaging were purchased from different commercial suppliers and are also given in the Appendix Tables A.2 and A.3.

Optical measurement equipment used for particle imaging and analysis is listed in Appendix Table A.4. Further equipment used for media preparation and processing is listed in Appendix Table A.5.

5.3. Programs and Software

The computer programs and software used for evaluation and post-processing of measurement data is listed in Appendix Table A.6.

5.4. Experimental Methods

5.4.1. Characterization of Single Particles

Particle Size Distribution

The particle size distribution of the chromatographic media in wet state was measured using an optical microscope type Axioplan and particle sizes were calculated by ImageJ version 1.49s (<http://imagej.nih.gov/ij>). The width of the particle size intervals for the determination of the particle size distribution density and cumulative size distribution according to Equations (3.49) and (3.50) was defined as $\Delta d = 5 \mu\text{m}$.

Particle Density

The density of the wet chromatographic particles SEP and TOY was determined by measuring weight and volume. The weight of 30 samples containing 1.5 mL chromatographic slurry (particles submerged in a 20 w% ethanol solution) was measured. Prior to this, the slurry was stirred to assure a nearly equal solid to fluid fraction of the samples. After weighting, the samples were dried carefully at 60 °C for seven days using a drying oven (E28, Bindner, Tuttlingen, Germany) assuring that the total fluid content was evaporated. By weighting the mass $m_{p,dry}$ of the dried particles, the volume of the evaporated fluid V_f having a density of 0.97 g ml⁻¹ (20 w% ethanol solution at 20 °C [Kraul & Wilkening u. Stelling GmbH 2017]) was determined. The volume of the dry polymer

particles was then given by $V_{p,dry} = 1.5 \text{ mL} - V_f$ and the density of the dry polymer by $\rho_{p,dry} = m_{p,dry}/V_{p,dry}$. Given the intraparticle porosity ϵ_i from literature [DePhillips and Lenhoff 2000; Yao and Lenhoff 2006], the density of the particle in wet state was determined by

$$\rho_p = \epsilon_i \rho_f + (1 - \epsilon_i) \rho_{p,dry}, \quad (5.1)$$

where ρ_f is the density of the fluid phase and $\rho_{p,dry}$ is the density of the dried solid particle.

Particle Surface Structure

The surface structure of the Particles SEP and TOY was analyzed by Scanning Electron Microscopy (SEM) (JSM 5900 LV, JEOL, Tokyo, Japan) at 5-10 kV. Measurements were carried out at the TUM Institute of Medical Engineering (IMETUM). Prior to this, single particles were dried carefully at environmental temperature and sputtered with gold afterwards.

Particle Compression-Relaxation Behavior

The mechanical compression properties of single SEP and TOY particles in wet state were measured via nanoindentation (TriboIndenter[®] TI 900, Hysitron, Inc., Minneapolis, USA) at room temperature. Experiments were carried out at the *Institute of Particle Technology (IPAT)* at the Technical University of Braunschweig (Prof. Dr.-Ing. A. Kwade). The particles were manipulated using a diamond “flat punch” indenter tip with a diameter of 100 μm . Each particle was compressed in a fluid environment consisting of deionized water. The aggregates were separated on glass slides before compression using a dispersing device (Rhodos, Sympatec, Clausthal-Zellerfeld, Germany). Figure 5.3 shows the scheme of the micromanipulation technique of a single particle via flat punch indentation.

Because of the large particle size and the much harder glass plate, deformation of the glass plate on the micromechanical measurement could be neglected. Deformation of the particles was examined by standard light microscopy as well as micro computer tomography (XradiaXCT-400, Zeiss, Oberkochen, Germany). Detailed information on the measurement methods is described in literature [Schilde et al. 2014]. In total, 30-50 particles were analyzed in order to obtain statistically meaningful data.

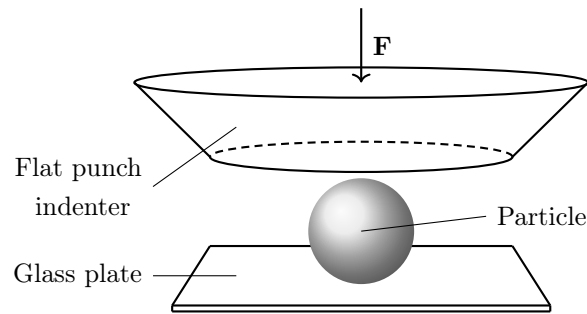


Figure 5.3.: Schematic representation of the micromanipulation method using a flat punch indenter tip. A single particle is compressed between two flat surfaces and the resulting force is measured.

Compression Load Relaxation. During compression load relaxation analysis, the particles were compressed by $1\ \mu\text{m}$, $2\ \mu\text{m}$, and $4\ \mu\text{m}$ using a compression velocity of $1\ \mu\text{m s}^{-1}$. Force relaxation at constant compression was measured over a time span of 10 s. The particles were relaxed afterwards at the same rates of initial compression. Hence, the compression load relaxation experiments lasted 12-18 s. Indentation velocities were kept constant during the loading and unloading sequences.

Quasistatic Compression. Quasistatic compression was carried out using two different maximum compression levels at two different compression velocities. The low-load compression was controlled by a maximum displacement of $4.5\ \mu\text{m}$ at a constant indentation velocity of $0.9\ \mu\text{m s}^{-1}$. The high-load compression was controlled by a maximum displacement of $12.5\text{-}25\ \mu\text{m}$ at a constant indentation velocity of $5\ \mu\text{m s}^{-1}$. The particles were relaxed at the same velocity after reaching the maximum compression level. Hence, the quasistatic compression-relaxation experiments lasted 5-10 s. A displacement controlled load function was applied during the quasistatic compression measurements. Indentation velocities were kept constant during the loading and unloading sequences.

5.4.2. Characterization of Bulk Packings

Macroscopic Compression-Relaxation Experiments

The analysis of the macroscopic packing behavior was carried out using SEP particles. The agarose-based media was chosen because it is a little softer than the methacrylic media and, hence, assured a well detectable amount of compression of the packing at that scale. Moreover, the packed bed was divided into seven equally sized sections by

inserting small layers of Blue Sepharose 6 FF[®] which basically is the SEP resin dyed with Cibacron Blue. The resulting section thickness and the blue layer thickness were about 4 and 0.5 mm, respectively. The total packed bed height was 31 mm. A photograph of the column containing the different layers is shown in Figure 5.1 B.

The changes in bed height and height of each section due to either hydrodynamic or mechanical load were recorded by the camera for both experiments (see Figure 5.2). From the resulting photographs, the packed bed compression and relaxation was calculated by automated image analysis using the public domain image analysis software ImageJ and Matlab. Therein, the changes in packing section height were proportional to the changes of the number of pixels representing a packing section. Using the camera macro objective, the resolution of each of the packing sections was high enough (> 200000 pixels) so that even small changes in the section heights were represented by a sufficiently large amount of pixels. The compression is defined as the ratio of change in section height and initial section height according to Equation (3.72). The packing measurements were repeated five times with freshly packed columns.

Flow Compression. During flow compression experiments, the flow rate was increased every 2 min by 0.1 kg h^{-1} up to 2 kg h^{-1} — being equal to a superficial flow velocity of 2763 cm h^{-1} for the 9.6 mm i.d. column — and decreased afterwards by the same rate. The height of the sections was measured at each flow step. This high superficial velocity beyond velocities typically recommended by the manufacturer for large-scale applications was necessary to exert large enough packed bed compression in order to obtain meaningful experimental data.

Mechanical Compression. The analysis of the macroscopic packed bed behavior during uniaxial mechanical compression was carried out by lowering the plunger manually by 20 mm min^{-1} in absence of any external fluid flow application. The height of the sections was measured at every $1/4$ turn of the screw thread by which the plunger was lowered. Columns packed with wet as well as semi-dry particles were investigated. In the former packing process, the particles were first gravity settled from resin slurry and afterwards compressed mechanically by lowering the plunger. The column inlet valve was then closed so that excess fluid left the column through the outlet. The particles of the packing were still surrounded by fluid. In the latter packing process, the inter-particle fluid was drained by gravity first. Then, most of the fluid contained in the

interparticle void space was removed by a nearly stagnant flow of about one column volume of air through the column. This resulted in a semi-dry gravity settled packed bed. However, the residual moisture content of the resin particles was not quantified because this parameter was not experimentally accessible.

Microscopic Particle Measurements

The analysis of the microscopic column packing behavior was carried out using Toyopearl AF-Amino-650M[®] (kindly provided by Tosoh Bioscience, Stuttgart, Germany). Toyopearl AF-Amino 650M[®] is an affinity chromatography resin made of spherical methacrylic polymer. According to the vendor, over 80% of the wet particles are within a range of 40-90 μm with a mean diameter of 65 μm .

Fluorescent Particle Labeling. Toyopearl AF-Amino-650M and Toyopearl SP-650C particles were labeled with fluorescent dyes according to the suppliers labeling protocol [Johnson and Spence 2010] in order to increase contrast and visibility during fluorescence microscopy measurements. As fluorescent dyes O-10465, O-6185, F-2181, and A-30052 (see Appendix Table A.3) were used. Depending on the reactive group of the chromatographic particles and the dye molecules, slightly different labeling protocols were developed. Detailed information about the labeling process is given in Appendix Chapter C.1.

Confocal Laser Scanning Microscopy (CSLM). Confocal laser scanning microscopy (CSLM) (LSM510 META, Carl Zeiss, MicroImaging GmbH, Jena, Germany) was used to analyze the packing structure, i.e. the particle deformation and rearrangement during mechanical and hydrodynamic load at the particle scale. To use the limited space below the microscopic lens, a microfluidic flow cell was designed (see Appendix Figure B.2) and packed with dyed Toyopearl AF-Amino 650M particles. This aminated resin was optically denser than the resin SEP and therefore more suitable for microscopic analysis. The microfluidic device was further equipped with a water pool in which the objective lenses needed to be submerged during measurements to reduce optical refraction of the laser beam. Measurements were carried out using an Argon laser at 488 nm extinction wavelength. The particles were labeled with fluorescent A-30052 and F2182 dyes (see Appendix Table A.3 and Appendix Chapter C.1 for details).

UV-Light Microscopy. Fluorescent particles were mixed with the unlabeled ones at a ratio of 1:5 (v/v) and packed into the column. The column was then positioned horizontally on the stage of an optical microscope type Axioplan equipped with a 20x/0.45 objective (Carl Zeiss, Göttingen, Germany) (see Figure 5.4).

By applying fluorescence microscopy (see Figure 5.4 B), the emitted light of the labeled beads illuminated the packing from inside and made several layers of the packing structure visible. The pressure-dependent packing structure was then photographed and post-processed using the software AxioVision version 4.7.2 (Carl Zeiss, Göttingen, Germany) and ImageJ.

Micro Computer Tomography. Measurements of the inner particle packing structure were carried out using micro computer tomography (Xradia Versa XRM-500, Carl Zeiss, Oberkochen, Germany) at different energy levels (40-60 keV) at the TUM Institute of Medical Engineering (IMETUM). The X-ray attenuation can be calculated according to Lambert Beer's law

$$\frac{I_A}{I_0} = 1 - e^{(-\frac{\mu}{\rho}x)}, \quad (5.2)$$

where I_A and I_0 are the absorbed and incident photon intensities, (μ/ρ) is the mass attenuation coefficient (units $\text{cm}^2 \text{g}^{-1}$) and x is the mass thickness of the probe ($x = \rho D$ in g cm^{-2} and D the diameter of the probe). From Equation (5.2) it gets clear that the fundamental basis of the attenuation is the number of atoms encountered by the X-ray beam. The mass attenuation coefficient (μ/ρ) is a material property and a strong function of the atomic number Z as well as the X-ray wavelength λ (inverse of energy) that can be described by the relationship $\mu/\rho \sim Z^m \lambda^n$ where m equals three or four and n equals (approximately) three [Stock 2009, pp. 9-21].

Chromatographic packings of agrose- and methacrylate-based particles were prepared in small columns made of a 1 ml B Braun Omnifix[®] Solo polypropylene syringe (Carl Roth GmbH, Karlsruhe, Germany) with inner diameter of 4.6 mm. The packing height was adjusted to 5 mm and not compressed prior to measurements. The following samples were analyzed:

- Dry Toyopearl SuperQ-650C particles; preparation: Washing particles in pure water and incubation in 0.1 M calcium chloride solution for 1 h, drying overnight at 60°C in a drying oven (see Appendix Tables A.5 and A.2).
- Wet Sepharose 6FF and Toyopearl SuperQ-650C particles; preparation: Washing

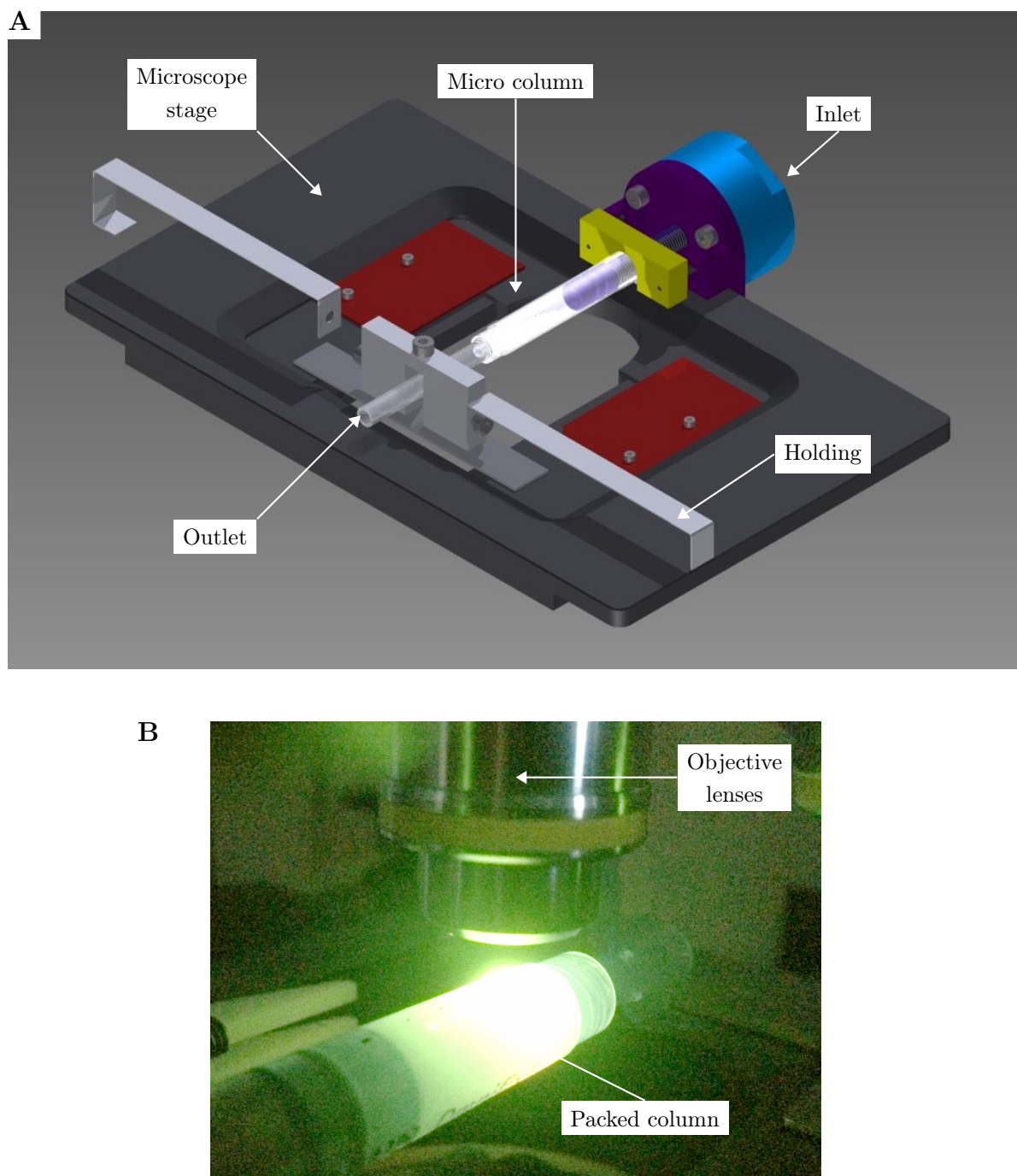


Figure 5.4.: UVM measurements of the packing behavior. (A) CAD drawing of the setup of the micro column fixed on the microscope stage. (B) View of the column during operation and illumination of the packing by UV light.

particles in pure water and incubation in the following contrast agent solutions (see Appendix Table A.2): 0.05 m% iodine in ethanol solution, 1 m% iodine in ethanol solution, 5 m% iodine in ethanol solution, 0.1 m% PTA solution, 10 m% PTA solution, pure Imeron400 solution and 10 m% Imeron400 solution

5.4.3. Analysis of the Wall Support

In order to investigate the effect of column wall support on the packing compression-relaxation behavior and the packing pressure drop, the macroscopic packing compression experiments were repeated in columns of different diameter. Therefore, the columns of 9.6 mm, 12.5 mm, 16.25 mm, and 20 mm in diameter were used and packed with SEP and TOY resins up to a gravity settled packed bed height of 30 mm. Optical sectioning of the packing by insertion of small layers of colored particles was not performed. The maximum fluid flow velocity was calculated to 637 cm h⁻¹ by the maximum pump flow rate of 2 L h⁻¹ in the 20 mm i.d. column. Five hydrodynamic compression-relaxation cycles were applied by stepwise increasing the flow velocity by 63.7 cm h⁻¹ every 2 min up to the maximum flow velocity. The flow velocity profile was kept constant for all columns. The influence of the wall support was evaluated by measuring at every flow step the total packed bed compression λ according to Equation (3.72) as well as the normed packing pressure drop $\Delta P = \Delta p/H$, where H is the packing height at each flow step. Each packing compression-relaxation experiment was repeated five times.

5.4.4. Analysis of Particle Migration

The particle migration experiments were carried out using the methacrylate resins Toyopearl[®] Butyl-650S, Toyopearl[®] Butyl-650C, Toyopearl[®] SP-650M, and Toyopearl[®] SP-650C (see Appendix Table A.1). The former two resins are used for hydrophobic interaction chromatography (HIC). Due to its butyl-ligand these resins have a hydrophobic particle surface. For the study of particle migration, the Toyopearl methacrylate resins have certain advantages over the agarose based resins commercially available. First, Toyopearl resins exhibit a narrow particle size distribution with mean diameters of 35 μm , 65 μm , and 100 μm , so that the effect of particle size on particle migration can be analyzed. Second, labeling and tracking of the Toyopearl particles was much easier compared to the agarose based resins.

Particle migration was evaluated by optical measurements by tracking particles of different color compared to the packed bed. The experimental set-up shown in Figure 5.1 was used. To achieve a sufficient contrast between the packing and the tracer, a small portion of particles were oxidized by the oxidizing agent, potassium permanganate (KMnO_4), which resulted in a black coloring of the particles. Other labeling agents such as bromothymol blue or phenolphthalein were proven to be not suitable as they were washed out very easily during column operation. Migration of particles in the inner packing region was evaluated after column operation by quick-freezing the whole column at -80° for one hour and cutting the packing into half afterwards.

Particle Labeling Method

The labeling of the Toyopearl particles was carried out similar to the method presented by Gilmour [2009] who achieved a successful labeling of Sephadex particles. Therefore, 1 g of the Toyopearl particles were incubated in 5 ml NaCl solution (3 w%) for 6 h. After that, the particles were centrifuged and the supernatant was removed by a pipette. The washed particles were then dispersed in a 100 ml solution containing 5 g KMnO_4 and 3 g NaCl and incubated for at least one hour. Finally, the particles were washed with pure water followed by centrifugation and removing the supernatant. This washing step was repeated multiple times to assure that excess KMnO_4 was removed completely.

Column Packing with Colored Tracer Particles

Columns with diameters of 9.6 mm, 12.5 mm and 16.25 mm, were packed with unlabeled Toyopearl resins as well as with tracer particles in two different ways.

The first packing was built by pouring unlabeled particles in the columns resulting in a sedimented bed height of 18 mm. After that, a small layer of 2 mm of colored tracer particles was given on top of the packing resulting in a final sedimented bed height of 20 mm.

The second packing was built by mixing colored tracer particles and fresh particles in a ratio of 1/3 (v/v). Again, a total sedimented packing height of 20 mm was used. In order to avoid particle size segregation and achieve the best mixing possible, the columns were shaken and rotated while the plunger was lowered slowly until the packing was fixed in place and compressed by 10%.

Table 5.1 gives an overview of the different columns and packings analyzed in this study.

Table 5.1.: Prepared packings and columns to use for the particle migration study.

No.	Column \varnothing , mm	Packing particles (size, μm)	Tracer particles (size, μm)	Tracer distribution
1	9.6	SP-650M (65)	SP-650M (65)	layer on top of the packing
2	12.5	SP-650M (65)	SP-650M (65)	layer on top of the packing
3	16.25	SP-650M (65)	SP-650M (65)	layer on top of the packing
4	12.5	SP-650C (100)	SP-650M (65)	layer on top of the packing
5	12.5	SP-650C (100)	Butyl-650S (35)	layer on top of the packing
6	12.5	Butyl-650C (100)	Butyl-650C (100)	layer on top of the packing
7	9.6	Butyl-650C (100)	Butyl-650S (35)	layer on top of the packing
8	12.5	Butyl-650C (100)	Butyl-650S (35)	layer on top of the packing
9	12.5	Butyl-650C (100)	Butyl-650S (35)	mixed

The first part of the study was dedicated to the effect of the column diameter on the particle migration using Toyopearl SP-650M particles. In the second part of the study, the column diameter was kept fixed and the particle sizes of the packing and tracer particles was varied in order to investigate the influence of the particle size distribution on particle migration. Each experiment was repeated three times.

Column Operation Modes

All packed columns were operated with 450 high-flow/low-flow cycles, each lasting 20 s. Photographs of the packings were taken every 50 cycles. Experiments 1-3 were carried out at a fluid velocity of 964 cm h^{-1} during the high-flow cycle, which is equal to the maximum pump flow rate of 2 L h^{-1} in the 16.25 mm i.d. column. Experiments 1 and 2 as well as 4-9 were further performed at a higher fluid flow velocity of 1630 cm h^{-1} , which is equal to the maximum pump flow rate in the 12.5 mm i.d. column. The low flow cycle was set to 5% of the high flow cycle. Experiment 7 was additionally performed at a the maximum fluid flow velocity of 2763 cm h^{-1} .

5.4.5. Analysis of Different Column Packing Strategies

The experimental analysis of column packing methods was carried out in the 9.6 mm i.d. column using SEP particles as described in Section 5.4.2.

Column Packing Methods and Operation

Columns were prepared by gravity settling of the SEP particles. During this process, thin layers of Blue Sepharose 6 FF[®] were inserted. This resulted in an optical partitioning of the sedimented packed bed into seven equally sized sections. The bed height of the gravity settled packing was adjusted to 30 mm. After gravity settling, the bed was further consolidated and compressed by 20% according to the following five different column packing methods:

1. Dynamic Axial Compression (DAC)
2. Flow packing
3. Flow compression and subsequent DAC
4. DAC and subsequent flow compression
5. Incremental alternating flow compression and DAC

The resulting final bed height was 24 mm in all cases.

The first packing method applied was dynamic axial compression (DAC). Consolidation of the particle packing was achieved mechanically by moving the column plunger downward manually with a rate of 30 mm min⁻¹. The second packing method was flow packing from the top of the column. The typical flow packing method – pumping the resin slurry into the column – was not used in this work as this method would rule out the axial sectioning of the column. However, the effect of particle size classification during gravity settling was largely avoided by stepwise sedimentation of small amounts of chromatographic media. Further consolidation of the packing was then achieved according to the guidelines of the flow packing method described by Bemberis et al. [2003]. The packing fluid flow rate was adjusted to 1.6 L h⁻¹, being equal to a superficial flow velocity of 2210 cm h⁻¹ for the given column geometry. The third packing method was flow packing to reach 10% compression followed by DAC to reach a final compression of 20%. The fourth packing method was DAC compression by 10% followed by flow packing to reach again a final compression of 20%. The fifth packing method was incremental alternating application of flow compression and DAC. Flow packing was applied

first by adjusting the fluid velocity to achieve a 2.5% compression of the packing. The fluid flow was then stopped and further 2.5% compression was achieved by DAC. This was repeated three times resulting in a final bed compression of 20%. As all packing procedures were adjusted to an overall packed bed compression of 20%, the adapter was set to identical heights assuring identical initial conditions for further analysis of hydrodynamic packing stability and homogeneity.

Like in industrial applications, the packed columns were stored overnight after packing allowing the internal packing stress to be equilibrated.

A relative hydrodynamic load of $RHL = 1$ is defined to be equal to the flow rate applied during the flow packing method in order to achieve a 20% packing compression (1.6 L h^{-1}). For flow packed columns using Sepharose resins, it is recommended to not exceed $RHL = 0.75$ during operation [GE Healthcare 2014] and this value is used as a reference load for comparison of the packing methods.

Hydrodynamic stability of the different packings was analyzed by operation at stepwise increase of hydrodynamic load by $RHL = 0.25$ every 20 min up to a maximum of $RHL = 1.25$. Long-term packing behavior was analyzed by repetition of 25 simulated high-flow/low-flow cycles. During each simulated cycle, the fluid velocity was adjusted to $RHL = 0.75$ lasting 10 min and $RHL = 0.05$ lasting 10 min, respectively.

Evaluation Criteria

The variation of packing density profiles of columns, which were packed by different packing procedures, was quantified by common statistical measures [Sabine and Plumptre 1985]. Hence, as an indicator of the inhomogeneity of the axial packing density distribution, the average deviation of the axial packing density from the mean packing density was defined as

$$S_{mean} = \sqrt{\frac{1}{N} \sum_{i=1}^N (\Phi_i - \langle \Phi \rangle)^2}, \quad (5.3)$$

where N is the number of sections in which the packing density was determined, Φ_i is the packing density in section i and $\langle \Phi \rangle$ is the mean packing density of the column. As an example, $S_{mean} = 0$ corresponds to a column with a constant packing density in axial direction. The variation of axial packing density profiles during column operation was described in analogy by the average deviation of the packing density profile during operation from the initial packing density profile right after column packing according

to

$$S_{init} = \sqrt{\frac{1}{N} \sum_{i=1}^N (\Phi_i - \Phi_{i,init})^2}. \quad (5.4)$$

Here, $\Phi_{i,init}$ is the packing density of section i after column packing.

5.5. Computational Methods

The simulations presented in this work were performed on an Intel workstation (XEON E5-2699-v3 processor using 32 cores at 2.3 GHz and 64 GiB RAM). The operating system was Linux Mint 17.3, 64bit.

5.5.1. Modular Structure of the Simulation Case

Numerical simulations were carried out using the open source CFD-DEM framework *CFDEM[®] coupling* [Goniva et al. 2012] which couples the CFD software *OpenFOAM* with the DEM software package *LIGGGTHS[®]*. Graphical evaluation was done using the open source scientific visualization software *ParaView*. Further postprocessing of the simulation data was carried out in the commercial software *Matlab*. All software packages and programmes used in this work are listed in Appendix Table A.6.

In general, a coupled CFD-DEM simulation routine is divided into a *preprocessing*, a *calculation/simulation* and a *postprocessing* step. Appendix Figure B.3 gives an overview of these steps. During the preprocessing step, the fluid and particle properties, boundary and initial conditions are defined as well as the simulation domain and CFD mesh properties. During the calculation step, the simulation is performed and output data is stored at predefined time steps for the postprocessing step. Consequently, during the postprocessing, the simulation output data is visualized and evaluated further using additional software packages and programs, such as ParaView and Matlab.

Due to the separation of the CFD and DEM algorithms a typical CFDEM simulation case is organized in a modular fashion (see Figure 5.5).

All data that needs to be specified during the preprocessing step are located in a specific directory (e.g. **Case 1**). Therein, it is further differentiated between CFD and DEM related data, which consequently are given in separated directories (see Figure 5.5). Within the CFD directory, each property of the fluid phase, such as the density,

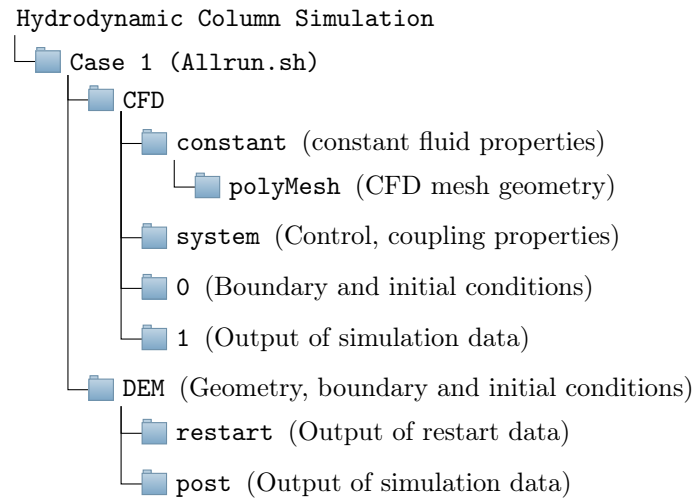


Figure 5.5.: Modular structure of the simulation programs. The simulation 'Case 1' is split up into a *CFD* and a *DEM* part in which the CFD and DEM software routines operate individually based on the simulation properties and conditions defined in the files located in the subdirectories.

viscosity or others, is defined in a specific text-file located in the `constant`-directory. This directory also contains the `polyMesh`-directory in which the simulation domain and the CFD mesh properties are specified. Boundary and initial conditions of the CFD calculation are defined in specific files located in the `0`-directory. The `system`-directory contains files in which the time steps, output writing and simulation control parameters can be set. The simulation output is stored each time step in a directory (e.g. after 1 s in the `1`-directory).

The `DEM`-directory contains all relevant information of the particulate phase, which are also defined in text-files of a specific format. If a simulation needs to be restarted, the directory `restart` contains binary files with all necessary information of the particles (positions, velocities and forces), which are relevant for a restart. Similar to the CFD part, the simulation output is stored at each time step in a text-file located in the `post`-directory, which then can be used for visualization and postprocessing. The routine of preprocessing, calculation and postprocessing is managed and automated by the `Allrun.sh`-file, in which the relevant commands are listed.

In the following, the simulation settings used in this work are illustrated.

5.5.2. The Simulation Set-up

Column Geometry, CFD Mesh, and Domain Decomposition

The chromatography column was approximated geometrically by a vertical cylinder of a diameter of 10 mm. To assure nearly equal cell sizes a special mesh geometry was used as displayed in Figure 5.6.

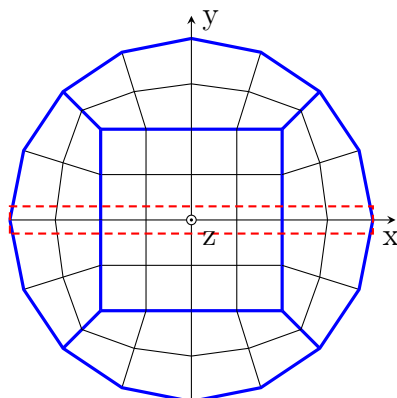


Figure 5.6.: Exemplary CFD mesh geometry for three-dimensional simulation cases. In the xy -direction the mesh is composed of five blocks, resulting in nearly equal cell sizes of the mesh. The coarse mesh shown here is just used for illustration purposes, simulations were carried out using a much finer mesh. The red dashed rectangle illustrates the pseudo two-dimensional simulation domain, representing a slice of the column in the xz -plane, which is of finite thickness in y -direction.

In the xy -plane the mesh is composed of five blocks as surrounded by the blue thick lines, where each of the four side blocks has half the number of cells of the middle block. With nearly equal cell sizes the ratio of particle size to cell size can be considered as nearly constant within the simulation domain, which is required for numerical stability.

Besides the three-dimensional simulations, also pseudo two-dimensional simulations were carried out by simulating a slice of the column in the xz -plane as indicated by the red dashed rectangle in Figure 5.6. By performing pseudo two-dimensional simulations, the computational effort can be reduced significantly. In Table 5.2 further mesh properties are listed.

For parallel computing, the CFD domain is decomposed into smaller subdomains in a three-dimensional orthogonal processor grid. In the `decomposePar`-dictionary (located in `CFD/system/`) the decomposition in x , y , and z -direction is specified. Depending on the domain size and number of cells, 14-32 subdomains were defined.

Table 5.2.: Geometric properties of the CFD mesh.

Dimension	Geometry	Cells in xy-plane	Cells in z-direction	Mesh cells
3D	D, H: 10 mm, 70 mm	588	60	35280
Pseudo 2D	x, y, z: 10 mm, 0.6 mm, 70 mm	30	60	1800

Boundary and Initial Conditions

The simulation of the hydrodynamic packing behavior was carried out in analogy to the laboratory experiments in two separate steps. In the first step the column packing was simulated and in the second step the packed bed behavior during either hydrodynamic or mechanical load.

The column packing process simulation was initiated by sedimentation of randomly distributed particles having the particle size distribution of the SEP particles (see Table 6.1). This was carried out by executing the `in.liggghts_init`-script in which the DEM simulation domain, the particle properties, and boundary conditions are specified (see Appendix Tables B.2 and B.1). The total sedimented packed bed height was 31 mm as in the laboratory experiments being composed of 223379 and 18323 particles in the three-dimensional and pseudo two-dimensional column. Within the CFD simulation, the boundary and initial conditions shown in Appendix Table B.3 were used.

Figure 5.7 shows the location of the boundaries of the computational domain for the three-dimensional simulation case (A) as well as for the pseudo two-dimensional simulation case (B).

As in the laboratory experiments, the flow velocity was controlled at the column *inlet*. A similar flow velocity profile was set, in which the fluid flow velocity was stepwise increased by 5% up to the maximum flow velocity of 2763 cm h^{-1} considering wall friction ($|u|_{wall} = 0$). In contrast to the laboratory experiments the flow velocity was increased every 0.5 s instead of 2 min. Furthermore, a moving mesh was implemented at the column inlet which simulated the column plunger and allowed for mechanical compression of the packed bed.

The column wall was represented as a frictional *wall* boundary. In the case of the pseudo two-dimensional simulation cases, the boundary in y-direction was defined as *empty* for the CFD calculations and *periodic* for the DEM calculations.

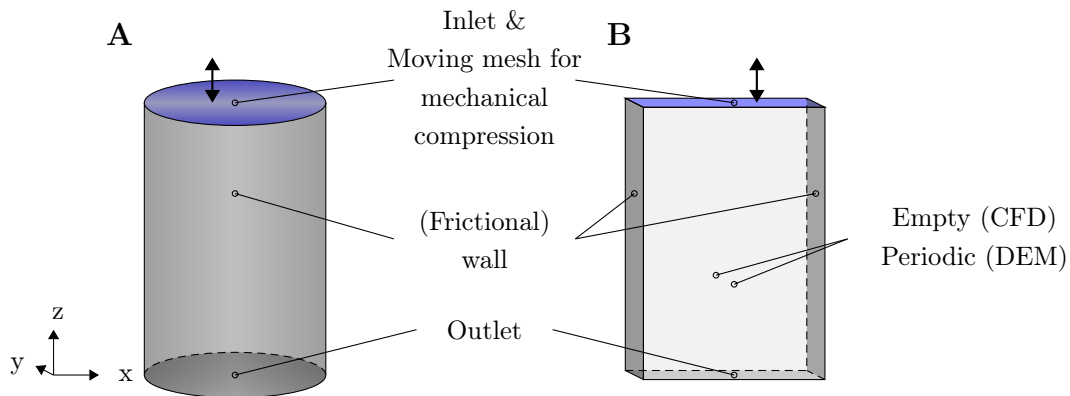


Figure 5.7.: Boundary properties of the simulation cases. (A) 3D and (B) pseudo 2D simulation case. At the column inlet a moving mesh was implemented, so that the packing could be compressed mechanically.

Furthermore, the fluid viscosity η was set to 1 mPas.

CFD-DEM Coupling Settings and Submodels

The settings considering the coupling algorithms and particle-fluid interactions are defined in the `couplingProperties`-dictionary (located in `CFD/constant/`). Appendix Table B.4 lists the settings for the simulations used in this work. The `cfdemSolverPiso`-solver was used and the coupling interval `couplingInterval` was set to 1000 DEM time steps.

5.5.3. CFD Solver Adjustment

The most relevant solver and simulation control parameters are described in the following.

CFD Time Step

The time step in which each CFD calculation is performed as well as the start and end time of the simulation is set in the `controlDict`-dictionary (located in `CFD/system/`). The choice of the right time step has a significant impact on the convergence behavior of the simulation and thus on the physical relevance of the simulation output. As an indicator for the stability of the simulation, the *Courant number* Co is controlled. This dimensionless number indicates the distance (in CFD cells) a fluid element flows within

one CFD time step Δt and is defined as

$$Co = |u| \frac{\Delta t}{\Delta x}, \quad (5.5)$$

where Δx is the CFD cell length. Hence, for a stable simulation $Co < Co_{max} = 1$ is required. This was satisfied by using a time step of 0.001 s.

Numerical Schemes and Particular Solvers

The difference schemes determine the way the governing equations are discretized in time and space. These settings are defined in the `fvSchemes`-dictionary (located in `CFD/system/`). Based on an extensive study of various difference schemes, the choice of the schemes given in Appendix Table B.5 resulted in the best numerical performance.

Detailed information about the different numerical schemes can be found in literature [e.g. OpenFOAM Foundation 2016].

The particular solvers used within the CFD calculation routine and the PISO loop (found in `CFD/system/fvSolution`) were adapted from the *ErgunTestMPI*-tutorial, which is delivered with the CFDEM coupling software package.

5.5.4. Reduction of Computational Effort by Coarse Graining

In a *coarse grain* model, a group of original particles is simulated using a large-sized particle termed a coarse grain particle, where the total energy is modeled and adjusted to agree between the coarse grain and the original particles (see Figure 5.8) [Goniva et al. 2012; Sakai et al. 2014]. Here, a group of 8 particles of diameter d_1 is modeled as one coarse grain particle of diameter $d_2 = CG \cdot d_1$. CG is the coarse graining factor.

The energy exchange between the fluid and the solid particle phase is achieved by the drag force correlation according to Koch and Hill [2001]. Therein the drag force F_f is calculated by

$$F_f = \frac{V_p \beta}{\alpha_p} (u_f - u_p), \quad (5.6)$$

$$\beta = f(\alpha_p, d_p^{-2}, Re_p). \quad (5.7)$$

V_p is the particle volume, $\alpha_p = 1 - \epsilon$ the particle phase ratio, u_f and u_p the fluid and particle velocities. d_p is the particle diameter and Re_p the particle Reynolds number.

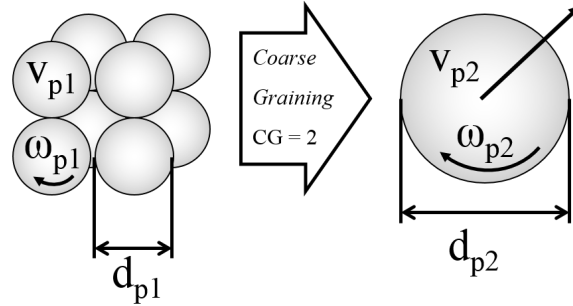


Figure 5.8.: Schematic representation of the *coarse grain* method. Using a coarse graining of $CG = 2$, a group of $2 \times 2 \times 2$ particles of diameter d_1 is represented as one coarse grained particle of diameter d_2 .

Hence, the drag force needs to be scaled by

$$\frac{F_f(d_2)}{F_f(d_1)} = \frac{V_{p,2}\beta_2}{V_{p,1}\beta_1} = \frac{d_2}{d_1} = CG. \quad (5.8)$$

The simulated particle quantity scales with CG^3 . This approach significantly speeds up the simulation time and finally enables the simulation of large scale packed chromatography beds. The disadvantage of this technique in the context of the CFDEM-coupling software is the decreasing resolution of the CFD calculations as the CFD mesh cell size needs to be increased if particle size increases.

In-silico coarse graining studies were carried out using a rectangular box with the dimension of 2 mm, 2 mm, 12.5 mm (x, y, z) and periodic boundaries in x and y direction. Further boundary and initial conditions are given in Appendix Tables B.2, B.1 and B.3. The fluid velocity profile applied at the column inlet was the same as in the laboratory experiments. The coarse graining is realized by increasing the particle size in the `in.liggghts_init`-script prior to particle initialization. The drag force is adjusted by the appropriate *CG*-value in the `couplingProperties`-file (located in `/CFD/constant/`).

6. Characterization of Compressible Polymeric Chromatography Particles ¹

The modeling of chromatographic particle systems using the *Discrete Element Method (DEM)* requires information about the mechanical properties of the particles. Being highly porous, the polymeric particles are biphasic material compounds with a solid polymeric backbone containing interstitial fluid. However, the corresponding material parameters describing the complex mechanical properties of those particles can hardly be found in literature. Therefore, the following chapter is dedicated to the characterization of selected chromatographic particles based on an agarose as well as methacrylic polymer matrix. Besides the particle size distribution, density, and surface structure, detailed information about the complex particle compression-relaxation behavior is given.

6.1. Particle Size Distributions

The particle size distribution of various chromatographic particles on methacrylic and agarose basis was measured. Figure 6.1 shows the dimensionless particle size distribution density $q(d_p)\Delta d_p$ as well as the cumulative size distribution $Q(d_p)$ for *Toyopearl[®] AF-Amino-650M* and *CM Sepharose 6FF[®]* particles in wet state. As can be seen, the particle size distribution of the Toyopearl particle was clearly narrower. The measured particle sizes of a sample of 279 particles ranged from 43.6 - 95.1 μm . The mean particle diameter was determined to 66.4 μm which confirmed the data provided by the vendor (65 μm). The median particle diameter of the sample was 64.6 μm .

¹Selected results presented in this chapter were published in: Dorn M, Schilde C, Burmeister CF, Hekmat D (2017): Mechanical characterization of compressible chromatographic particles. *Powder Technol* **320**: 213-222.

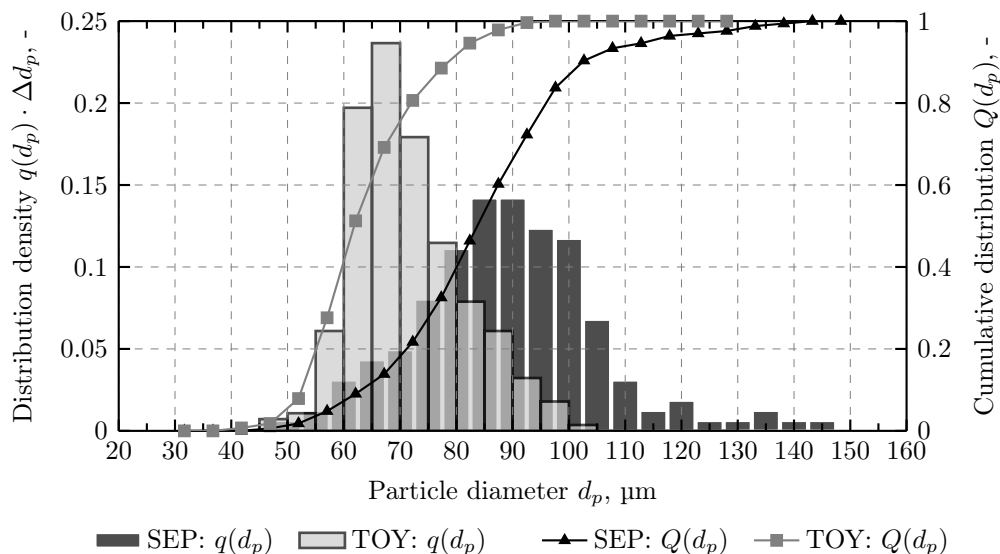


Figure 6.1.: Particle size distribution of used resins. Measured dimensionless particle size distribution density $q(d_p)\Delta d_p$ as well as the cumulative size distribution $Q(d_p)$ for *Toyopearl*[®] *AF-Amino-650M* (light gray bars and line) and for *CM Sepharose 6FF*[®] (dark gray bars and line) in wet state. Each bar represents a particle size interval of 5 μm .

The particle sizes the Sepharose resins (sample of 166 particles) ranged from 49.7 - 142.7 μm with a mean and median particle diameter of 86.9 μm and 86.2 μm , respectively. The mean particle size of this sample was slightly smaller than the value provided by the vendor (90 μm). Table 6.1 gives an overview of different chromatographic resins used in

Table 6.1.: Particle size distribution of various chromatographic resins on methacrylic and agarose basis. The spread give the number of particles analyzed.

Resin	Spread	Size range, μm	Mean size, μm
CM Sepharose 6FF [®]	166	49.7 - 142.7	86.9
Toyopearl [®] AF-Amino-650M	279	43.6 - 95.1	66.4
Toyopearl [®] SuperQ-650M	262	52.0 - 95.0	68.0
Toyopearl [®] SuperQ-650C	242	79.1 - 142.0	103.6
Toyopearl [®] SP-650M	308	42.0 - 105.0	65
Toyopearl [®] SP-650C	228	77.1 - 138.4	101.0
Toyopearl [®] Butyl-650S	291	18.4 - 53.6	30.4
Toyopearl [®] Butyl-650C	400	65.1 - 134.5	98.2

this work. The Toyopearl particles are all based on the same matrix material (HW-65, see Section C.1 for details) and differ in size and surface modification only.

6.2. Particle Density

Values for the average particle density of Sepharose and Toyopearl particles are rarely documented in literature. Nevertheless, this parameter influences the buoyancy or sedimentation velocity of particles in a fluid environment. Therefore, it is one of the crucial simulation model parameters that needed to be determined. The average density of Toyopearl[®] SP-650M and Sepharose 6FF[®] was calculated by the weight and volume of dried particles. The density of dried particles, however, does not characterize their behavior in chromatographic columns as they usually are found in swollen wet state. Hence, the density of the particles in wet state was determined as described in Section 5.4.1. The results are given in Table 6.2 using an intraparticle porosity of 0.84 for the Sepharose and 0.63 for Toyopearl particles which were obtained from literature [DePhillips and Lenhoff 2000; Yao and Lenhoff 2006].

Table 6.2.: Measured particle density of resin SEP and TOY.

Resin	Dry density, g cm ⁻³	Wet density, g cm ⁻³
SEP	1.87 ± 0.98	1.14 ± 0.16
TOY	1.76 ± 0.47	1.34 ± 0.13

The calculated values are in good accordance with literature data of similar resins. Hence, the average particle density of *Q Sepharose 6FF[®]* is given with 1.131 g cm⁻³ [Chang and Chase 1994; Thömmes 1999], 1.11-1.33 g cm⁻³ for *STREAMLINETM DEAE Sepharose* particles [Hassan et al. 2005] and 1.47 g cm⁻³ for *Toyopearl[®] DEAE-650* particles [Soriano et al. 2000].

6.3. Particle Surface Structure

Frictional forces between the particles and between the particles and the column wall are basically governed by the particle surface structure, i.e. the surface roughness. Scanning

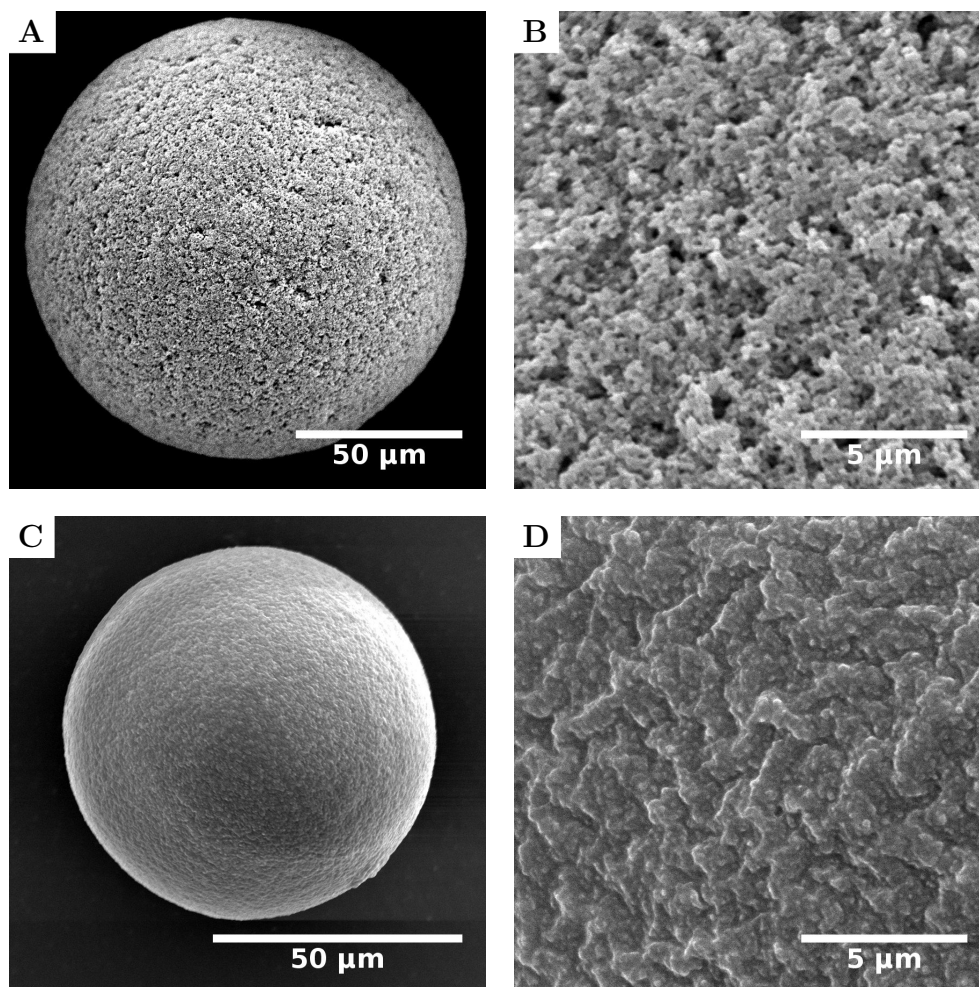


Figure 6.2.: Scanning Electron Microscopy (SEM) images of the surface of selected resins at different magnification levels. (A, B) *Toyopearl*[®] SP-650C and (C, D) *CM Sepharose 6FF*[®] having a mean wet particle diameter of 101 μm and 86.9 μm, respectively.

Electron Microscopy (SEM) was used to obtain a detailed view of the outer surface and pore structure of resins Toyopearl and Sepharose particles (Figure 6.2 A and B).

It needs to be taken into account that prior to the SEM measurements, the particles were dried carefully. Hence, the particle size shown in Figure 6.2 does not correspond to the particles size in swollen wet state, but to the size in dried state. The Toyopearl particle kept its spherical shape after drying and its size was slightly reduced (Figure 6.2 A, B). The surface shows a rather rough and sponge-like structure with open pores of different sizes.

The Sepharose particle (Figure 6.2 C, D) in contrast shrank during the drying process so that its diameter got noticeably smaller than the mean particle size of 86.9 μm given in Table 6.1. However, the particle remained in its spherical shape. As can be seen further, the surface is rather smooth compared to the Toyopearl particle. No distinct pore structure can be identified. It is assumed that the pores were closed as an effect of the drying process.

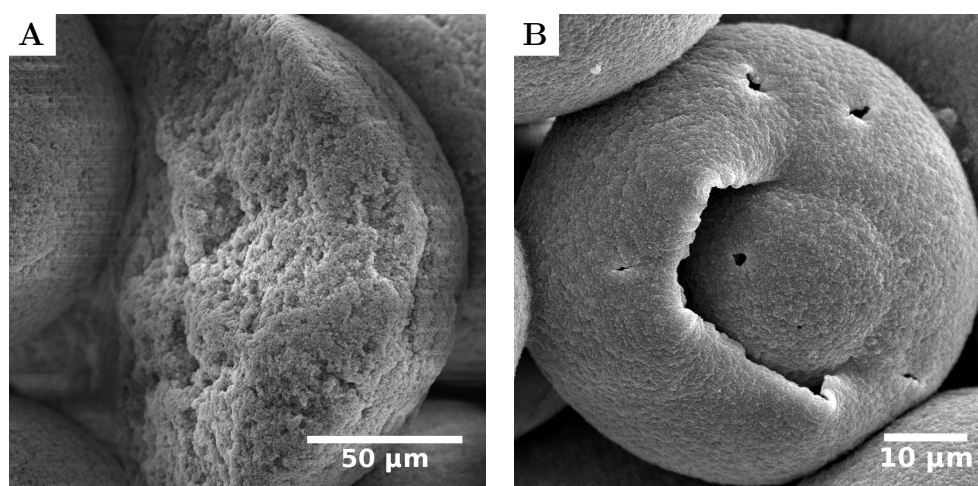


Figure 6.3.: SEM images of a broken Toyopearl and Sepharose particle. (A) *Toyopearl*[®] SP-650C and (B) *CM Sepharose 6FF*[®] .

Figure 6.3 shows a broken Toyopearl (A) and Sepharose particle (B). According to these images, the Toyopearl particle showed a dense inner porous structure that is nearly identical with the sponge-like particle surface. It is assumed that the dense inner pore structure is kept in wet state. The Sepharose particle in contrast seems to be a hollow sphere with a rather solid shell of shrunken polymer matrix.

However, this again might be an effect of drying, as the Sepharose particle is known to have a high inner porosity or water content in swollen state [DePhillips and Lenhoff 2000; Yao and Lenhoff 2006] and the polymer matrix was condensed to the particle shell during drying.

6.4. Compression Load Relaxation Analysis

The compression behavior of wet *CM Sepharose 6FF*[®] (in the following abbreviated as SEP) as well as wet *Toyopearl*[®] *SP-650C* (in the following abbreviated as TOY) particles was investigated using high-resolution nanoindentation measurements at different compression levels. In case of existing adhesive interaction of particle and probe, negative contact forces would have been measured. However, this was not the case in the experiments. Furthermore, it was observed by microscopy that no sticking of the particle to the indenter occurred.

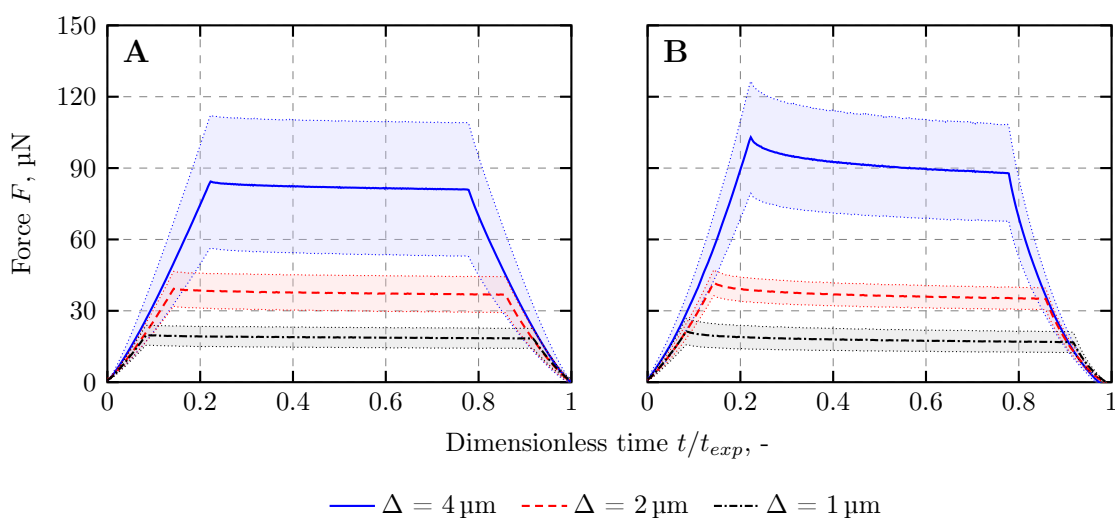


Figure 6.4.: Measured force relaxation of SEP and TOY particles at three compression depths. The particles were compressed by $1 \mu\text{m s}^{-1}$ up to a depth of $1 \mu\text{m}$, $2 \mu\text{m}$ and $4 \mu\text{m}$. Average compression force (thick solid, dashed and dash-dotted lines) and standard deviation (dotted lines) are given. Viscoelastic relaxation took place during a hold time of 10 s. Particles were relaxed at the same rates of initial compression. t_{exp} is the total time of each experiment. (A) particle SEP and (B) particle TOY.

Figure 6.4 shows the results of conducted compression load relaxation experiments as mean compression force (thick solid, dashed and dash-dotted lines) and standard deviation (dotted lines) for both SEP and TOY particles. The particles were compressed individually by $1 \mu\text{m}$, $2 \mu\text{m}$, and $4 \mu\text{m}$ and then kept constant.

As can be seen, the force being imposed on the particles increased with increasing compression. However, force relaxation can be observed for both particle types. TOY particles exhibited a stronger force relaxation than the SEP particles. Moreover, the average compression force is higher for TOY than for SEP.

As both chromatographic particles have a polymeric matrix structure and high intra-particle porosity [DePhillips and Lenhoff 2000; Yao and Lenhoff 2006], the relaxation of the compression force may be due to water flowing out of the inner particle pores and/or the viscoelastic property of the matrix material. The former is due to the fact that at the onset of particle compression, the interstitial fluid is pressurized locally causing the material to appear stiffer. Subsequent fluid redistribution within the particle and fluid exiting the particle results in local stress relaxation. Hence, the measured force not only depends on the matrix material stiffness itself, but also on how quickly the fluid redistributes within the porous particle [Zhao and Zhang 2004].

The force relaxation data of each particle during constant hold was adequately described by Equation (3.28) using $N = 2$ resulting in a model with two relaxation times [Yan et al. 2009]. The compression load relaxation model with $N = 1$ (one relaxation time) was unable to describe the force relaxation at the beginning of the holding time (see Figure 6.5).

The fit coefficients of the compression load relaxation model with $N = 2$ are given in Table 6.3 as average \pm standard deviation. According to the applied compression

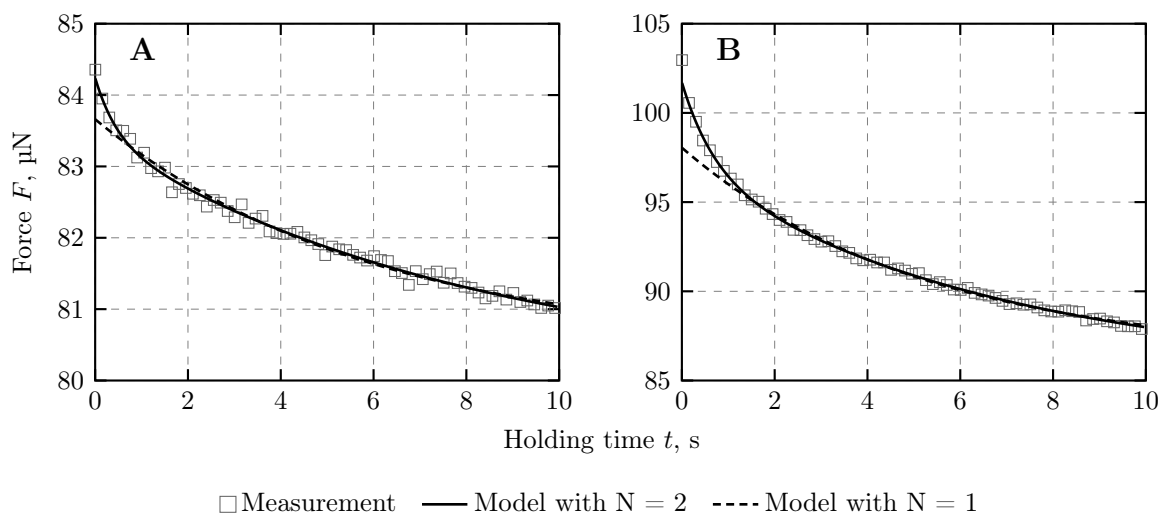


Figure 6.5.: Exemplary compression force relaxation data of SEP and TOY particles. Measurements show every 60th data point. Best fits according to the compression load relaxation model at a compression depth of $4\ \mu\text{m}$. **(A)** Particle SEP, ($N = 2$: $B_0 = 80.0\ \mu\text{N}$, $B_1 = 3.4\ \mu\text{N}$, $\tau_1 = 12.2\ \text{s}$, $B_2 = 0.8\ \mu\text{N}$, $\tau_2 = 0.5\ \text{s}$. $N = 1$: $B_0 = 80.5\ \mu\text{N}$, $B_1 = 3.2\ \mu\text{N}$, $\tau_1 = 5.9\ \text{s}$). **(B)** Particle TOY ($N = 2$: $B_0 = 85.3\ \mu\text{N}$, $B_1 = 11.6\ \mu\text{N}$, $\tau_1 = 6.8\ \text{s}$, $B_2 = 4.8\ \mu\text{N}$, $\tau_2 = 0.5\ \text{s}$. $N = 1$: $B_0 = 86.4\ \mu\text{N}$, $B_1 = 11.7\ \mu\text{N}$, $\tau_1 = 5.2\ \text{s}$).

Table 6.3.: Coefficients of the compression load relaxation model using $N = 2$. Calculated values according to Equation (3.28) (average \pm standard deviation).

Depth, μm	B_0 , μN	B_1 , μN	τ_1 , s	B_2 , μN	τ_2 , s	R^2
SEP						
1	17.07 ± 5.13	2.54 ± 1.72	15.45 ± 4.38	0.49 ± 0.13	0.50 ± 0.26	0.99
2	33.36 ± 10.63	5.53 ± 0.92	15.26 ± 3.57	0.74 ± 0.32	0.51 ± 0.18	0.99
4	82.22 ± 23.97	4.95 ± 0.69	13.79 ± 3.54	0.99 ± 0.25	0.51 ± 0.20	0.99
TOY						
1	15.01 ± 3.44	3.52 ± 0.85	6.41 ± 1.05	1.76 ± 0.54	0.47 ± 0.12	0.99
2	37.26 ± 4.92	5.67 ± 0.91	6.43 ± 0.93	2.55 ± 0.38	0.48 ± 0.13	0.99
4	88.01 ± 13.91	12.99 ± 3.96	6.41 ± 1.55	5.33 ± 1.65	0.47 ± 0.06	0.99

load relaxation material model, the coefficient B_0 corresponds to the long-time limit of the compression force after relaxation, whereas the coefficients B_1 and B_2 correspond to the force contributions of either poroelastic or viscoelastic material behavior within the short-time limit. While the coefficients B_0 are approximately equal for both particle types, large differences can be noticed for the first relaxation time τ_1 , which for SEP is more than twice the value of the TOY particles. In contrast, τ_2 did not show significant differences. Moreover, the relaxation times are largely independent of the applied compression level. Comparing relaxation times and force contributions for both particle types, it appears that the first relaxation (τ_1) is the dominant process during compression load relaxation experiments. Independent evidence cannot be obtained at this point to ascribe either poroelasticity or viscoelasticity to the two relaxation times. However, due the fact that there is a remarkable difference between both relaxation times and force contributions B_1 and B_2 (see Table 6.3), it is reasonable to conclude that two different mechanisms are involved.

6.5. Quasi-Static Compression Analysis

During quasi-static compression, the particles were compressed at two different compression velocities up to two different compression levels. During the high compression velocity, it was observed that the particles showed a strongly non-linear behavior when

being compressed up to 25 μm (see Figure 6.6 C and D), which according to the definition of strain, $\varepsilon = a/R$, is equivalent to a particle strain of nearly 55 and 65 % based on the measured mean particle diameter of 60 and 83 μm of the SEP and TOY particle samples analyzed. While the force exhibited approximately Hertzian dependency on strain ($F \sim \Delta^{3/2}$) during the lower compression rate (Figure 6.6 A, B), a different power law dependency is measured during the higher compression rate (Figure 6.6 C, D). Power-law fitting according to $F \sim \Delta^\alpha$ revealed that the compression up to displacement levels of 25 μm was fitted to the power of $\alpha = 2.4$, which is nearly 1.5-fold the Hertzian power.

Nevertheless, earlier studies of the chromatographic packing behavior of methacrylic particles during high hydrodynamic load revealed that the individual particles nearly retained their spherical shape and that only a slight compression was detected [Dorn and Hekmat 2016].

Therefore, high particle displacement levels of 25 μm can be considered as unlikely during standard operation of chromatographic columns, so that the following analysis of the particle compression behavior for the high compression rate was focused on maximum displacements of 12.5 μm that was equivalent to a compression time of 2.5 s. Figure 6.7 exemplary shows quasi-static compression plots of both chromatographic particles studied using the low compression ($v = 0.9 \mu\text{m s}^{-1}$) and the high compression velocity ($v = 5 \mu\text{m s}^{-1}$). The measured data as well as the best fit corresponding to the Standard Linear Solid (SLS) model are given. The SLS model describes the time-dependent correlation of stress on a given strain rate. All particles showed a similar behavior.

The three element SLS model showed excellent fit to the experimental quasi-static compression data. The three fit coefficients, the shear moduli of the two springs and the viscosity of the damper as well as the calculated characteristic relaxation time are given in Table 6.4. According to the model, G_0 represents the shear modulus of the free spring, G_1 and η the shear modulus and viscosity of the Maxwell element. Comparing the obtained coefficients of the high compression velocity with those of the low compression velocity for both particles, the shear moduli of the free spring G_0 increased only slightly. The shear modulus of the Maxwell element G_1 however, increased significantly as a consequence of the time-dependent material behavior. The viscosity of the damping element was fitted to identical values for each particle. The calculated relaxation time τ at the high compression velocity decreased significantly according to the relation $\tau = \eta/G_1$. The strong dependency of G_1 and τ on the experimental conditions, i.e. the compression

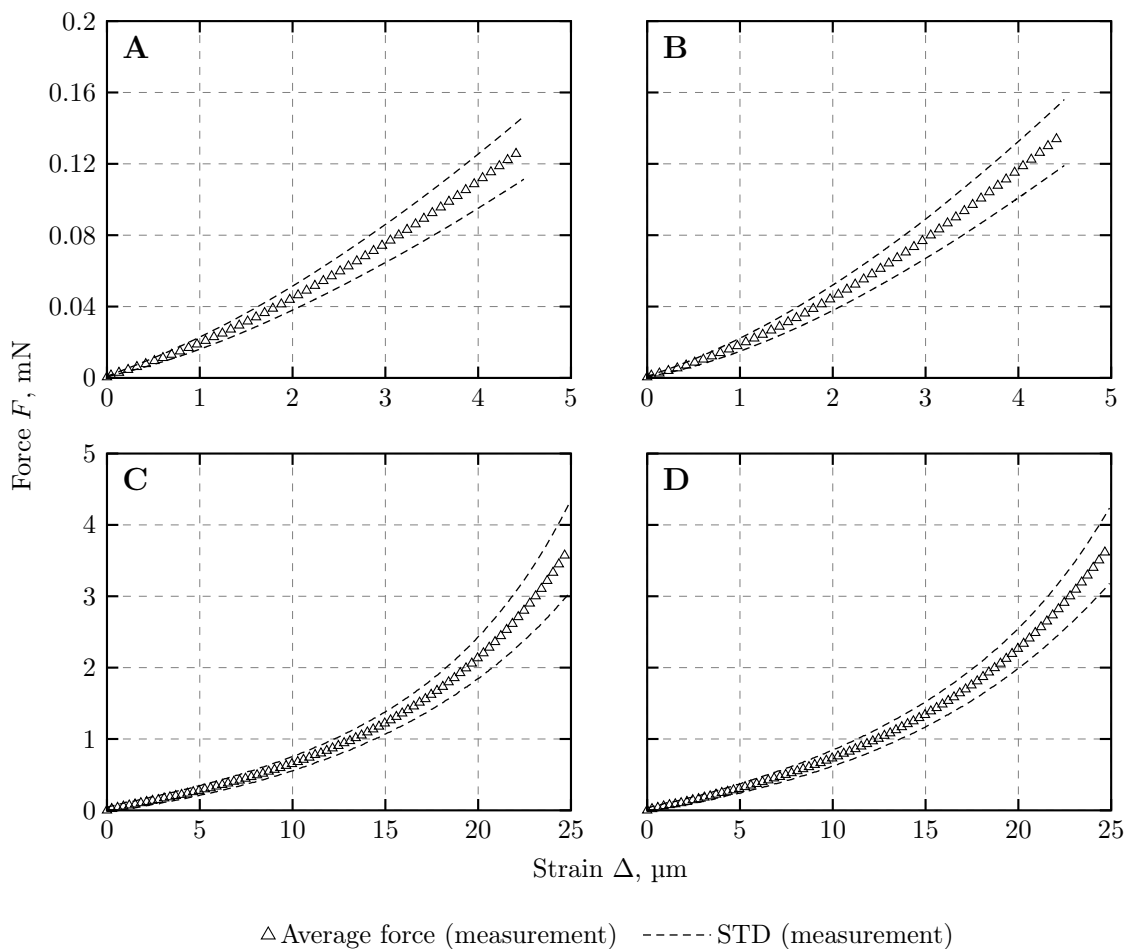


Figure 6.6.: Quasi-static compression of chromatographic particles. Compression of particle SEP (**A**) and particle TOY (**B**) at 900 nm s^{-1} . Compression (average and standard deviation (STD)) of particle SEP (**C**) and particle TOY (**D**) at 5000 nm s^{-1} .

velocity, suggests that the effect of water flowing out of the particle may be the dominant effect during fast quasi-static compression.

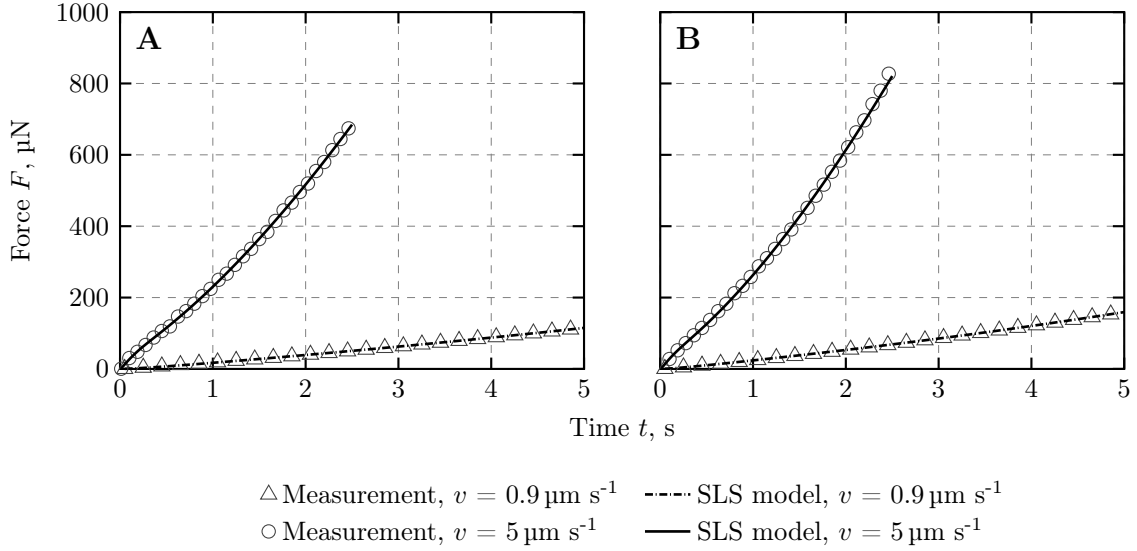


Figure 6.7.: Exemplary quasi-static compression data (every 60th data point is displayed) of both chromatographic particles. (A) particle SEP, (B) particle TOY. Maximum displacement was $4.5 \mu\text{m}$ for the low compression and $12.5 \mu\text{m}$ for the high compression velocity.

Table 6.4.: Fitted and calculated parameters of the SLS model. Calculated values according to Equation (3.26) (average \pm standard deviation).

Particle	$v, \mu\text{m s}^{-1}$	G_0, MPa	G_1, MPa	η, Pas	τ, s	R^2
SEP	0.9	1.62 ± 0.11	3.51 ± 0.90	0.90 ± 0.34	0.27 ± 0.12	1
SEP	5	2.21 ± 0.27	25.60 ± 11.87	0.90 ± 0.41	0.04 ± 0.01	1
TOY	0.9	1.76 ± 0.17	2.56 ± 0.86	0.68 ± 0.22	0.28 ± 0.09	1
TOY	5	2.42 ± 0.18	19.21 ± 6.43	0.68 ± 0.17	0.04 ± 0.02	1

6.6. Viscoelasticity Versus Poroelasticity

One of the important characteristics of porous biphasic, i.e. fluid filled, materials is that the force relaxation can depend on both the time scale and length scale of measurements, whereas the time dependency of a linear viscoelastic material is independent of the length scale. In order to differentiate between the visco- and poroelastic regimes, the method of Hu et al. [2010, 2012] was adapted. The compression force $F(t)$ was normalized according to Equation (3.38) using the values given in Table 6.3, where $F(0) = B_0 + B_1 + B_2$ and $F(\infty) = B_0$. The relevant length scale of this experiment is the contact radius a of the particle at the flat punch indenter. Figure 6.8 illustrates the average normalized force

as a function of time (left) and as a function of scaled time by the relevant length scale a^2 (right).

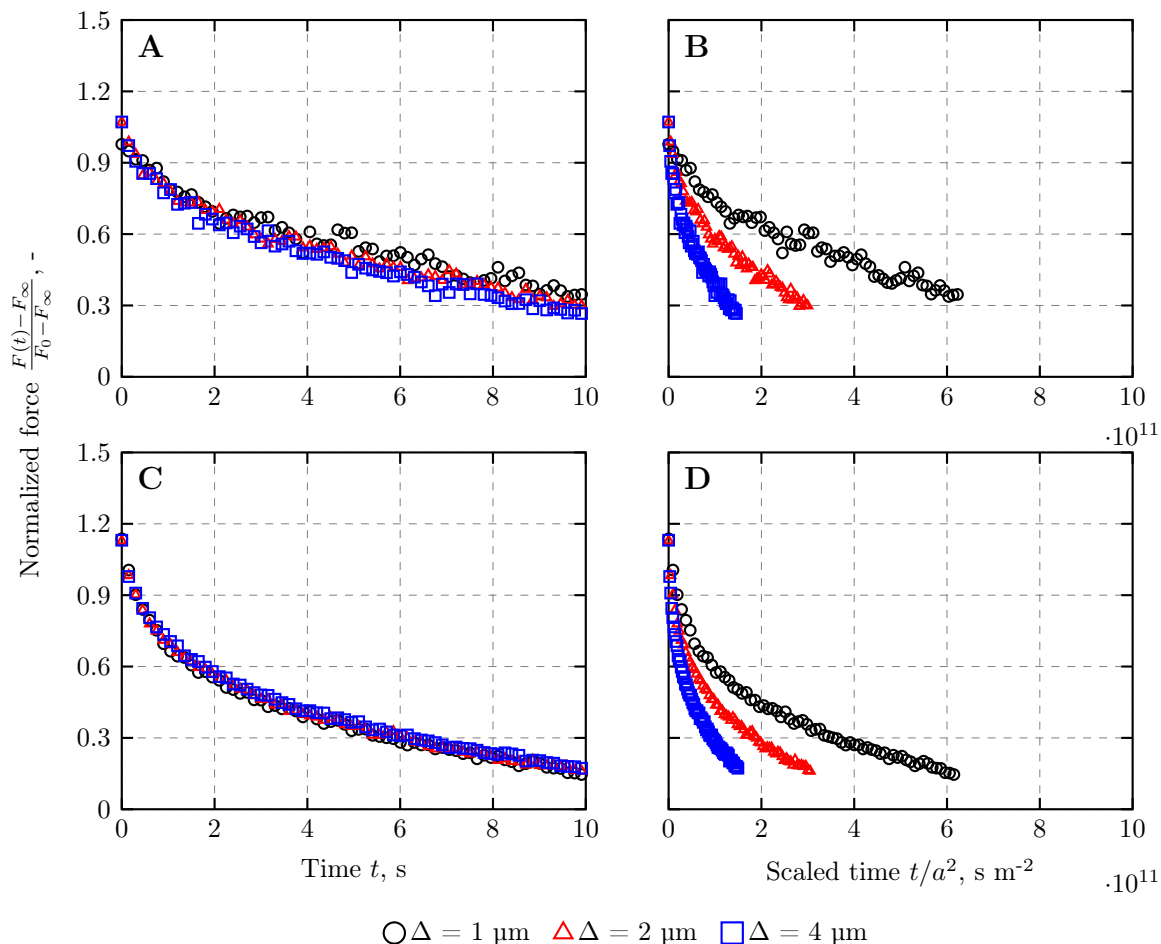


Figure 6.8.: Normalized force relaxation responses for particles SEP and TOY. The response curves of particles SEP (A) and TOY (C) collapse into a single curve when time is not scaled by the relevant length scale a^2 . Scaling in contrast led to a spread of the response curves at different compression levels for SEP (B) and TOY (D).

It can be seen that without scaling time by the relevant length scale a^2 , the force responses for both particles SEP and TOY collapsed into a single curve (Figure (6.8) A, C). Scaling time by a^2 in contrast led to a spread of the force responses at different compression levels (Figure (6.8) B, D). Hence, the force relaxation is independent of the contact radius and therefore of the compression depth. This quantitative assessment of the force relaxation curves may indicate that both particle types exhibit a rather viscoelastic than poroelastic response to an external force during compression force re-

laxation. However, this does not necessarily mean, that the influence of poroelasticity can be excluded completely. As the compression load relaxation model with $N = 2$ fitted to the force relaxation data revealed two relaxation times that differ by a factor of 13-31, it is reasonable to conclude that the longer relaxation time of $\tau_1 = 6.4-15.4$ s (see Table 6.3) corresponds to force relaxation due to inherent viscoelastic characteristics of the polymer matrix. The shorter relaxation time $\tau_2 = 0.47-0.51$ s can be attributed to the poroelastic relaxation during particle compression. Therefore, viscoelasticity and poroelasticity are dominant at different time scales during particle compression. It can be deduced that poroelastic relaxation may have already been completed during the ramp loading sequence of 1-4 s of the compression load relaxation experiments at a compression rate of $1 \mu\text{m s}^{-1}$. Consequently, the loading time during quasi-static compression, which was 2.5-5 s, might be too short for viscoelastic force relaxation to have significant effect on the particle compression behavior. Thus, it can be concluded, that the force relaxation observed during quasi-static compression results from transport of water out of the interior of the particles. This is in agreement with the fact that the relaxation time $\tau = 0.27-0.28$ s (see Table 6.4) obtained for the lower compression rate of $0.9 \mu\text{m s}^{-1}$ during quasi-static compression was in the order of magnitude of the poroelastic relaxation time τ_2 obtained from the compression load relaxation experiments.

6.7. Determination of Material Properties

On the basis of the particle compression behavior, particle parameters such as Young's modulus, Poisson's ratio and coefficient of restitution were determined that can be used for DEM simulations of chromatographic packings. The Poisson's ratio characterizes the ratio of transverse strain to axial strain during uniaxial compression. Based on microscopic images of particles during compression, the Poisson's ratio was calculated according to Equation (3.4) to be 0.2 ± 0.03 for both materials. Therein, the volume of the deformed particle can be approximated by the calculation of the spherical segment of a sphere. Due to volumetric strain, the radius for this calculation is greater than the radius of the uncompressed sphere (see Figure 6.9).

This value was in accordance with the value assumed by Yan et al. [2009] for agarose micro-particles. A similar approach was used by Kaufman et al. [2008].

Table 6.5 and 6.6 show the instantaneous and relaxed shear and Young's moduli

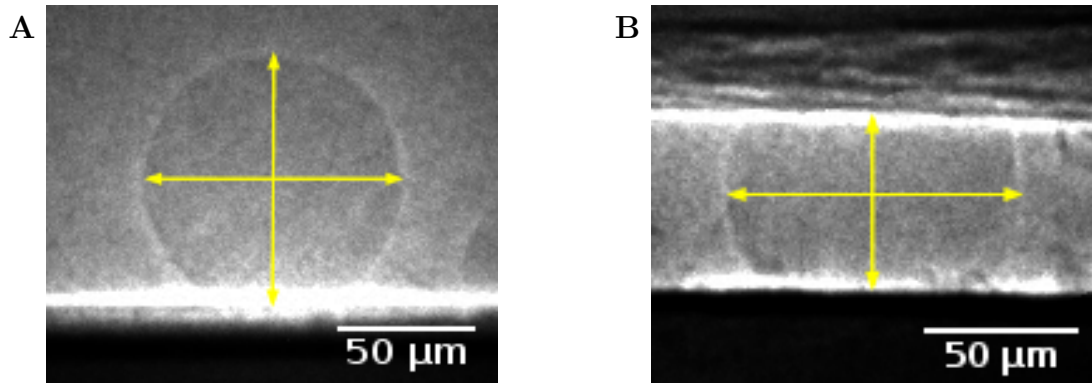


Figure 6.9.: Micro Computer Tomography (Micro CT) images of a SEP particle during micro manipulation. (A) uncompressed state and (B) compressed by 25 μm .

Table 6.5.: Instantaneous and relaxed shear and Young's moduli of SEP and TOY particles obtained by compression load relaxation experiments. (average \pm standard deviation).

Δ , μm	$G(t = 0)$, MPa	$G(t \rightarrow \infty)$, MPa	$E(t = 0)$, MPa	$E(t \rightarrow \infty)$, MPa
SEP				
1	3.00 ± 0.78	2.59 ± 0.78	7.21 ± 1.88	6.22 ± 1.67
2	2.14 ± 0.42	1.85 ± 0.52	5.14 ± 1.01	4.44 ± 1.26
4	1.63 ± 0.46	1.56 ± 0.44	3.92 ± 1.10	3.74 ± 1.33
TOY				
1	2.48 ± 0.67	2.27 ± 0.58	6.82 ± 1.62	5.45 ± 1.39
2	2.20 ± 0.27	1.94 ± 0.24	5.27 ± 0.66	4.72 ± 0.54
4	1.93 ± 0.44	1.75 ± 0.39	4.63 ± 1.05	4.20 ± 0.95

obtained by the compression load relaxation model and by the SLS model, respectively.

The moduli were computed for each compression experiment and average values and standard deviation were determined. The instantaneous shear moduli $G(t = 0)$ at the high compression velocity significantly increased according to the relation $G(t = 0) = G_0 + G_1$ (see Table 6.6). Consequently, the instantaneous Young's moduli $E(t = 0)$ at the high compression velocity increased. Both experiments can be compared to each other on the basis of nearly equal compression velocities ($0.9\text{-}1 \mu\text{m s}^{-1}$) and compression depths ($4\text{-}4.5 \mu\text{m}$). At these conditions it can be noticed that the relaxed Young's moduli

Table 6.6.: Instantaneous and relaxed shear and Young’s moduli of SEP and TOY particles obtained by quasi-static compression experiments. (average \pm standard deviation).

$v, \mu\text{m s}^{-1}$	$G(t = 0), \text{MPa}$	$G(t \rightarrow \infty), \text{MPa}$	$E(t = 0), \text{MPa}$	$E(t \rightarrow \infty), \text{MPa}$
SEP				
0.9	5.13 ± 0.94	1.62 ± 0.11	12.32 ± 2.26	3.89 ± 0.26
5	27.81 ± 11.99	2.21 ± 0.27	66.76 ± 28.78	5.31 ± 0.65
TOY				
0.9	4.32 ± 0.89	1.76 ± 0.17	10.36 ± 2.14	4.22 ± 0.40
5	21.33 ± 6.42	2.42 ± 0.18	51.19 ± 15.41	5.81 ± 0.44

$E(t \rightarrow \infty)$ of the load relaxation and the quasi-static compression experiments give nearly identical values of 3.74-3.89 MPa for SEP and 4.2-4.22 MPa for TOY particles. The relaxed moduli of particle TOY were consistently larger compared to particle SEP. During compression load relaxation (see Table 6.6), the values of the instantaneous and the relaxed particle moduli increased steadily with decreasing compression depth.

In theory, the moduli should be independent of the compression depth. It is likely that the higher values resulted from an uncertainty regarding the experimental evaluation of the contact radius at smaller compression levels as discussed earlier by Toohey et al. [2016]. Concerning the quasi-static compression at the high compression velocity of $5 \mu\text{m s}^{-1}$, it is assumed on the basis of the different time scales of viscoelastic and poroelastic relaxation that poroelastic relaxation dominated. Then, locally pressurized pore fluid leads to an apparently stiffer particle at small time scale leading to the high instantaneous shear and Young’s moduli $G(t = 0)$ and $E(t = 0)$. The large standard deviations of the instantaneous moduli $G(t = 0)$ and $E(t = 0)$ during quasi-static compression at the high compression velocity of $5 \mu\text{m s}^{-1}$ (see Table 6.6) may indicate that structural differences of the particle backbone resulting from the particle manufacturing process led to variations of the poroelastic behavior (the hydraulic permeability) of the intraparticle pores. Hence, fluid is pushed out faster or slower, depending on the matrix structure. The relaxed modulus as a property of the solid particle matrix characterizes the stiffness of the particle backbone depending on the polymer content and the degree of crosslinking of the polymer chains. However, the slightly higher values of $G(t \rightarrow \infty)$ and $E(t \rightarrow \infty)$

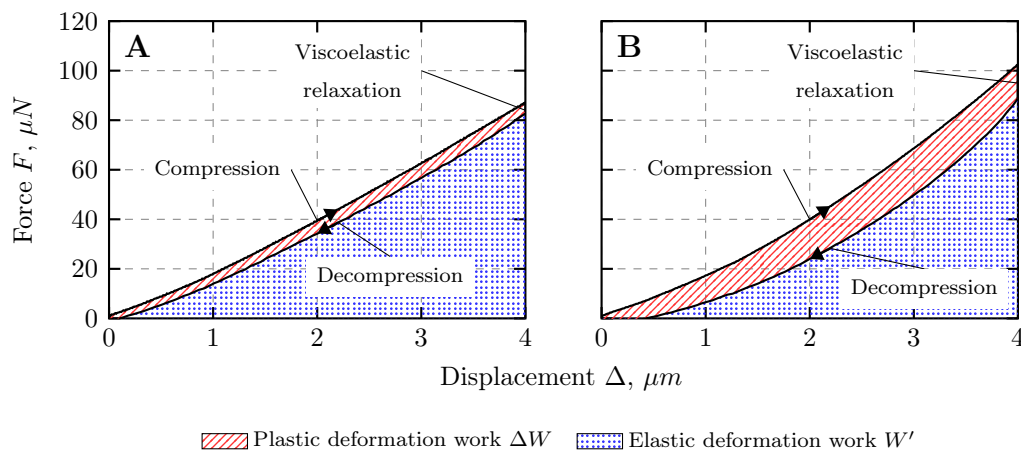


Figure 6.10.: Measured hysteresis of SEP and TOY particles during compression load relaxation experiments. The compression depth was $4\ \mu\text{m}$ and lasted 4 s. Viscoelastic relaxation during hold lasted 10 s, relaxation lasted 4 s. Red stroked and blue dotted areas define the plastic and elastic deformation work of particle SEP (A) and particle TOY (B), respectively.

during the high compression velocity of $5\ \mu\text{m s}^{-1}$ might be attributed to fluid being pressurized locally in pores that have been narrowed during particle compression. Fluid migration out of these narrowed pores would then take considerably longer and as a result, the particles appear to be slightly stiffer.

The determination of the coefficient of restitution was carried out by analyzing the force-displacement data of the compression load relaxation experiments at the maximum compression depth of $4\ \mu\text{m}$. Based on the short poroelastic relaxation time of $\tau_2 \sim 0.5\ \text{s}$ (see Table 6.3), the compression process of 4 s was slow enough to assume that poroelastic relaxation was nearly completed. In this case, the calculation of the coefficient of restitution is based on viscoelastic deformation only and thus characterized the behavior of the particle backbone in the long-time range. Figure 6.10 exemplarily shows the elastic and plastic deformation work of a compressed SEP particle as well as a compressed TOY particle. The compression-relaxation of single chromatographic particles showed hysteretic behavior in both cases.

However, both particles exhibited a different compression-relaxation behavior. As it was already seen in Figure 6.4, the viscoelastic force relaxation of the TOY particles was more pronounced compared to the SEP particles. Only a small fraction of compression work resulted in plastic deformation of the particles, as depicted in Figure 6.10 by the red stroked area. The fraction of plastic deformation of particle TOY was larger compared

to particle SEP. The coefficients of restitution were calculated according to Equation (3.22) and resulted in $e = 0.93 \pm 0.04$ for particle SEP and $e = 0.80 \pm 0.03$ for particle TOY.

These values indicate, that both particle types were not able to completely recover to their initial shape [Govedarica et al. 2012].

6.8. Conclusion

The purpose of the work presented in this chapter was the mechanical characterization of compressible polymeric particles that are commonly used in preparative chromatography as information about the mechanical properties such as the particle Young's modulus, Poisson's ratio or coefficient of restitution of chromatographic particles is extremely limited. Sepharose 6FF[®] (SEP) and different Toyopearl[®] (TOY) particles were chosen as representatives as both differ in backbone material, the former is made of agarose and the latter of methacrylic base.

The particles analyzed exhibited pronounced particle size distributions which were larger for the agarose-based particle compared to the methacrylic particles. The resulting mean particle size of SEP was 86.9 μm and the mean particle diameter of TOY particles was in a range of 30.4 μm , 65 μm , and 103.6 μm for small, medium, and large sized particles. The measured particle sizes were similar to the data provided by the manufacturers.

The densities of SEP and (medium sized) TOY particles in wet state were determined to 1.14 g cm^{-3} and 1.34 g cm^{-3} . However, the density of a wet swollen particle was calculated from the measured particle density in dried state using information about the intraparticle porosity of the swollen particle which was obtained from literature. A similar approach was used by Hassan et al. [2005]. The resulting calculated particle densities were comparable to literature data of similar resins.

The compression behavior of SEP and (large sized) TOY particles was analyzed using a high-resolution micromanipulation method. Two different compression experiments were carried out, compression load relaxation and quasi-static compression. Both experiments were adequately described by two different material models, the former by a load relaxation model expressed as *Prony-series* and the latter by a *Standard Linear Solid* model. SEP and TOY particles showed pronounced time-dependent compression

and relaxation behavior during both experiments. As chromatographic particles can be characterized as biphasic materials consisting of a solid polymeric matrix and interstitial fluid, this time dependency is caused by either the solid material viscoelasticity or by poroelasticity or by a combination of both. Using the load relaxation model with $N = 2$, two characteristic force relaxation times were identified. It was concluded that the longer relaxation time τ_1 , which was ~ 15 s for the SEP particles and ~ 6 s for the TOY particles, characterized the viscoelastic force relaxation. The shorter relaxation time τ_2 , being in the range of 0.5 s, was attributed to poroelastic relaxation.

Based on the different material models, instantaneous and relaxed shear and Young's moduli could be identified, the first characterizing the particle stiffness on the short time range and the second on the long time range. The calculated relaxed Young's moduli obtained by the compression load relaxation experiments (SEP: 3.74 MPa, TOY: 4.20 MPa) were in the same order of magnitude as the values obtained by the quasi-static compression experiments at low compression velocity (SEP: 3.89 MPa, TOY: 4.22 MPa).

Increasing the compression velocity from $0.9 \mu\text{m s}^{-1}$ to $5 \mu\text{m s}^{-1}$, the calculated instantaneous Young's moduli using the SLS model were increased approximately by a factor of 5 (SEP: 12.32-66.67 MPa, TOY: 10.36-51.19 MPa). This increase in instantaneous particle stiffness is assumed to be attributed to the influence of poroelastic water flow out of the particle. In contrast to the instantaneous modulus which exhibited a strong correlation with the compression velocity, the relaxed modulus predominantly depends on the viscoelastic solid matrix behavior and characterizes the particle stiffness after poroelastic effects have decayed.

The Poisson's ratio was determined on the basis of microscopic images and calculated to 0.2 for both particle types. The coefficient of restitution was 0.93 for SEP and 0.8 for TOY particles. These values indicate that the former and the latter showed the ability to recover up to 93% and 80% of their initial form as there was only a relative small fraction of plastic deformation corresponding to the maximum compression depth of $4 \mu\text{m}$. The determined values confirmed that TOY particles exhibit a stronger viscoelastic force relaxation than SEP particles due to the different matrix material.

The presented results give valuable information about the compression-relaxation behavior of individual particles and show the differences between the agarose and methacrylic particles. Based on these findings, the particle contact mechanisms contributing to the overall packed bed behavior can be estimated so that a detailed modeling of the hydrodynamic chromatographic column behavior is possible.

7. Characterization of Particle Bulk Packings ²

Chromatographic packings being composed of compressible polymeric particles are known to exhibit a complex hysteretic compression-relaxation behavior during cyclic column operation which is often ascribed to the viscoelasticity of the particles themselves. The aim of this chapter is to give detailed information about the dynamic packing behavior with focus on the packed bed structure, influence of the column wall support as well as force transmission during hydrodynamic or mechanical load. For this purpose, a novel micro chromatography column was designed that fitted into high resolution optical measurement instruments such as Micro Computer Tomography (Micro CT), Confocal Laser Scanning (CLSM) or UV Microscopy (UVM) and enabled the analysis of the packing behavior at the particle scale.

7.1. Hydrodynamic Load

The analysis of the macroscopic packed bed behavior during hydrodynamic load was carried out in the micro chromatography column with an inner diameter of 9.6 mm. The experimental set-up as well as a photograph of the column are shown in Figure 5.1. The packing was divided optically into seven equally sized sections by the insertion of blue dyed SEP particles. Here, section 1 is the uppermost and section 7 the lowermost region of the packing as indicated in Figure 5.1 B. The softer agarose-based resin SEP was used to assure a well detectable amount of compression of the packing at that small laboratory scale. The packing pressure drop as well as the bed height as a function of the superficial fluid velocity are given in Figure 7.1.

²Selected results presented in this chapter were published in: Dorn, M and Hekmat, D (2016): Simulation of the dynamic packing behavior of preparative chromatography columns via discrete particle modeling. *Biotechnol Prog* **32**: 363–371.

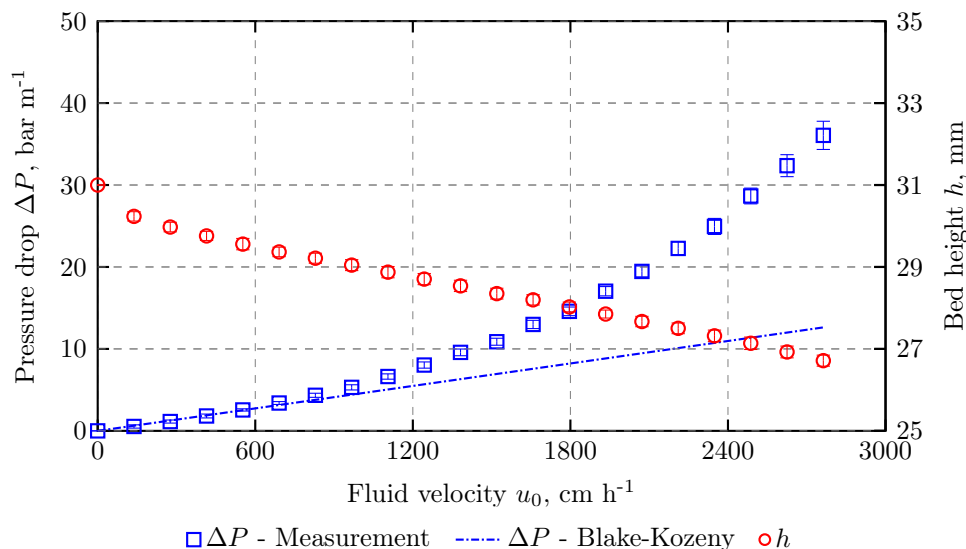


Figure 7.1.: Packing pressure drop and bed height as a function of the fluid velocity. The superficial fluid velocity was controlled and the packing pressure drop measured. The initial packed bed height was 31 mm. Calculated pressure values were obtained by the Blake-Kozeny equation (Equation (3.61)) using a prefactor of 180, $d_{32} = 93 \mu\text{m}$, $\epsilon = 0.36$ and $\eta = 1 \text{ mPas}$.

The packing pressure drop can be approximated to be linearly dependent on the fluid velocity up to about 500 cm h^{-1} . In this range, the pressure drop can be approximated using the Blake-Kozeny equation (Equation (3.61)) and a prefactor of 180, $d_{32} = 93 \mu\text{m}$, $\epsilon = 0.36$ and $\eta = 1 \text{ mPas}$. Here, d_{32} is the Sauter diameter of SEP particles which was obtained from the particle size distribution measurements and Equation (3.58).

With increasing flow velocity the pressure drop showed a pronounced exponential dependence. Furthermore, the packed bed height is constantly decreasing with increasing hydrodynamic load (Figure 7.1) which indicated that the packing is compressed with increasing flow velocity. According to Darcy's law (Equation (3.56)) the pressure drop is linearly depending on the fluid velocity, so that an increase in pressure is equivalent with an decrease in the packed bed permeability. On the background of the Kozeny-Carman theory, the permeability κ only depends on the particle diameter d_{32} and the packed bed porosity ϵ (Equation (3.57)). Hence, a reduced permeability means that either the particle diameter or the interparticle porosity is reduced or both at the same time. Analysis of the packing during hydrodynamic load at the particle scale can answer this question.

The applicability of the Blake-Kozeny equation is restricted to laminar flow regimes

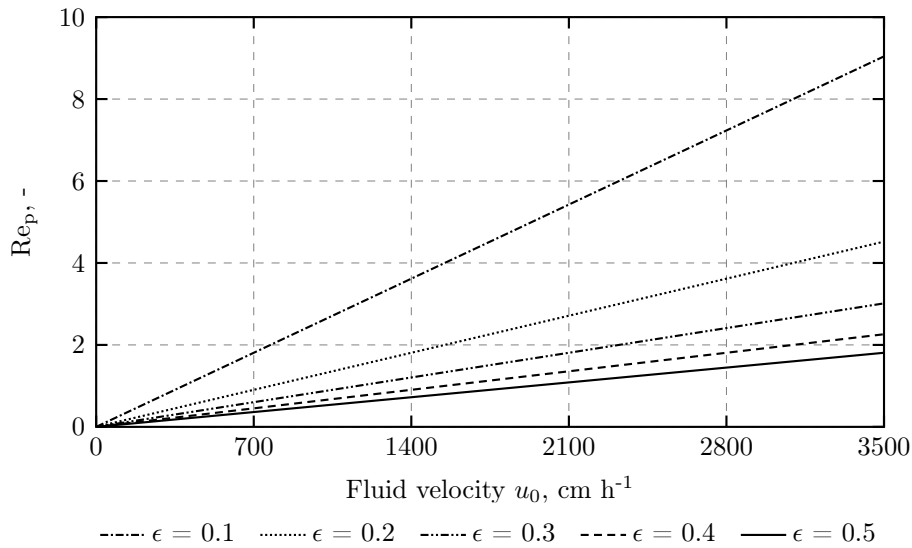


Figure 7.2.: Particle Reynolds number as a function of the fluid velocity. ($Re_p = \rho u_0 d_{32} / (\eta \epsilon)$).

($Re_p < 10$). Figure 7.2 shows the calculated particle Reynolds number as a function of the superficial fluid velocity for packing porosities ranging from 0.1 to 0.5.

As can be seen, Re_p is always below the critical value of $Re_p = 10$. Thus, within the range of applied superficial fluid velocities and assuming packing porosities $\epsilon > 0.1$ the flow can be seen as laminar and the Kozeny-Karman approach is valid.

7.1.1. Axial Packing Compression-Relaxation Behavior

Figure 7.3 A shows the packing compression as a function of the dimensionless packing height and different hydrodynamic loads. As can be noticed, a pronounced axial packing compression gradient is exhibited. The compression nearly linearly increases along the packing height resulting in a most compressed region at the column outlet.

Figure 7.3 B illustrates the dynamic packing compression-relaxation behavior resulting from the applied hydrodynamic load. The compression-relaxation behavior of the different sections varied along the column axis, but all sections exhibited a pronounced hysteretic shape. Interestingly, flow compression led to a more pronounced hysteretic shape for the lower sections. The shape of the hysteresis is an indication for the compression and relaxation time and reflects the dynamic behavior of the packing during load. Hence, a more pronounced hysteretic shape of the lower sections indicates a longer relaxation time compared to the upper packing region. The hysteresis of the total packing

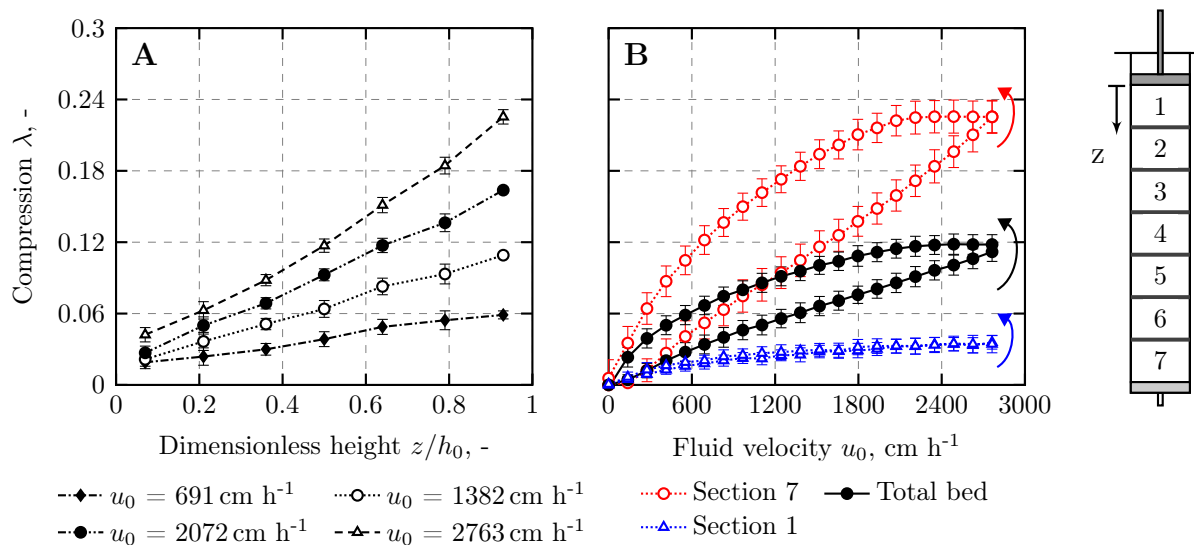


Figure 7.3.: Packing compression-relaxation behavior at different hydrodynamic loads. (A) Axial packing compression gradients. The z -coordinate goes from top to bottom of the packing. (B) Hysteretic packing compression-relaxation behavior exemplary shown for sections 1 and 7 as well as for the total packing. The arrows indicate the direction of the hystereses.

is located between the upper section and the lower section.

As a consequence of the compression–relaxation experiments, the overall packing behavior can be interpreted as the average of the behavior of the single sections. Hence, the observed packed bed hysteresis is not a global packing property but rather the sum of individual interparticle dynamics and particle–wall friction effects at different heights of the packing. For further analysis, the packed bed structure during flow compression was analyzed at the particle scale.

7.1.2. Particle Deformation and Force Transmission

Confocal laser scanning microscopy (CLSM) was used to analyze the packing structure, i.e. the particle deformation and rearrangement during hydrodynamic load. For this purpose, a microfluidic device (see Appendix Figure B.2) was designed that can be used with high resolution CLSM measurements. The device was equipped with a small channel with a cross-sectional area of 2 mm and a porous filter frit to retain the particles. *Toyopearl[®] AF-Amino-650M* particles labeled with a fluorescent dye were used which were optically denser than the resin SEP and therefore more suitable for microscopic analysis.

Figure 7.4 shows the microscopic image of the channel outlet section at the initial flow packed state (packed with 500 cm h^{-1}) (Figure 7.4 A) and during flow velocities of 1000 cm h^{-1} (Figure 7.4 B) and 1500 cm h^{-1} (Figure 7.4 C). Higher hydrodynamic loads were not applied to the microfluidic cell due to reasons of leakage.

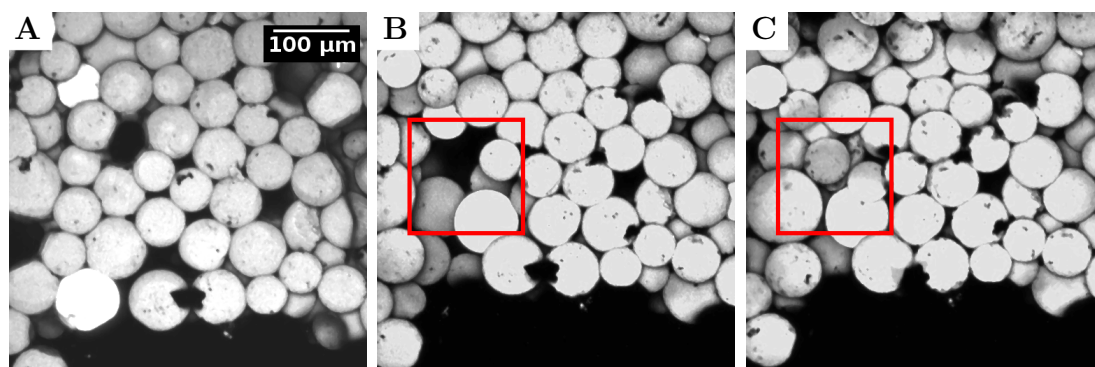


Figure 7.4.: Confocal laser scanning microscopy of an array of methacrylic resins under hydrodynamic load. The images were taken near the porous filter frit in the microfluidic device (see Figure B.2) at 500 cm h^{-1} (A), 1000 cm h^{-1} (B), and 1500 cm h^{-1} (C). The red rectangles indicate a region in which particle migration and rearrangement was detected.

The images show that most of the particles retained their spherical shape and did not show any significant deformation as it was assumed previously for single particles [Müller et al. 2005]. A significant reduction of interparticle porosity was not noticed. This might be due to the small channel cross-sectional area of 2 mm and the high wall roughness due to the manufacturing process. However, remarkable particle rearrangement was observed with increasing flow velocity. As indicated by the red rectangles (Figures 7.4 B and C), void spaces were created during one flow step and subsequently closed by migrating particles during the next flow step.

Comparable results were obtained with the micro chromatography column packed with the same resin by applying UV-microscopy. Figure 7.5 shows the resulting measurement of the lower section 7 at the gravity settled state (Figure 7.5 A) as well as at a highly compressed state during flow compression at a high superficial flow velocity of 2763 cm h^{-1} (Figure 7.5 B). The bright particles shown in the Figure are those labeled with the fluorescent dye.

It can be seen that the fluid drag led to a denser packing, even denser than in the microfluidic flow cell experiment which is a consequence of the larger cross-sectional area of the column ($A = 72.4 \text{ mm}^2$). Void spaces were reduced compared to the gravity settled

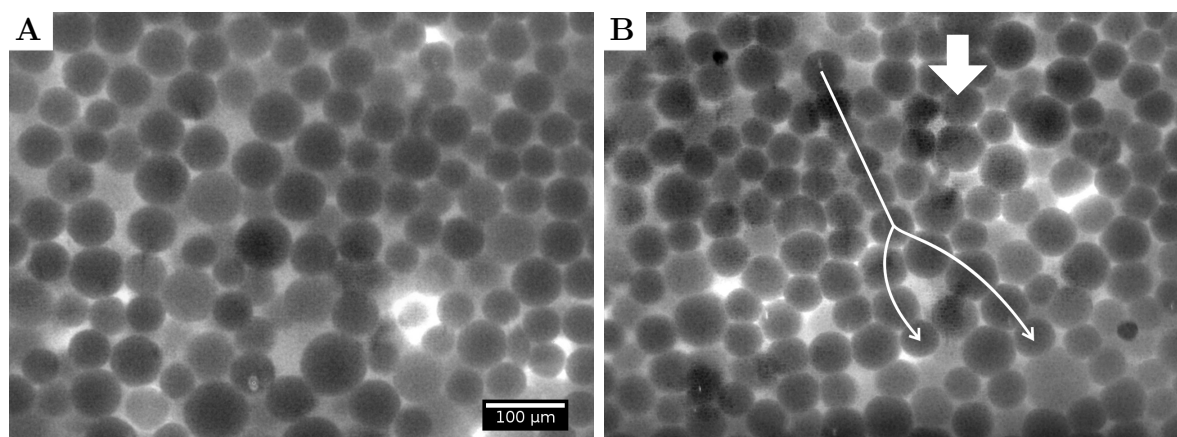


Figure 7.5.: UV-fluorescence microscopy of lowermost section 7 of the packing during hydrodynamic load. (A) Gravity settled packed bed at zero flow. (B) Particle bed during flow compression at a superficial flow velocity of 2763 cm h^{-1} ($\Delta P = 37 \text{ bar m}^{-1}$). The particles appear not to be deformed under high hydrodynamic stress. Several void spaces are visible.

state but still exist. Here again, most of the particles retained their nearly spherical shape. An increased number of smaller particles was visible that could possibly be caused by particle rearrangement, migration of smaller particles, or by shrinking because of reduction of intraparticle porosity.

Furthermore, a branched network of slightly overlapping particles can be identified as indicated by the arrows in Figure 7.5 B. In contrast to this, almost no particle overlapping is visible in Figure 7.5 A. This network represents a network of force-chains which is assumed to carry the major force exerted on the packed bed and may explain the still existing voids. Therefore, the assumption of a highly heterogeneous and anisotropic character of the internal structure of the chromatographic packed bed seems to be comprehensible. The force-chain network was predominately visible in the lower packing regions at high flow rates. As a consequence, the stress on those particles situated in force-chains seems to be higher than on the other particles of the packed bed.

Particle rearrangement and size segregation were already reported by Kong et al. [2010] as the major causes for packing compaction of a liquid-saturated packing of grains during air injection. Therein, the rearrangement of grains was caused by self-induced pressure fluctuations during flow channel migration. The existence of a similar mechanism is assumed during chromatographic packing compression. High particle stresses and the existence of a force chain network can give an explanation of the causes of damaged

particles reported in literature [Hekmat et al. 2011]. As a consequence, it is further assumed that the force on the packed bed is transmitted by those force-chains as it is known for heterogeneous “jammed” packings of rigid and soft monodispersed spheres [e.g. Jaeger et al. 1996; de Gennes 1999; Makse et al. 2000; van Hecke 2010]. In these publications, the compression of hard sphere disordered packings is described in phase transition diagrams of random loose packing to random close packing configurations [Jin and Makse 2010; Song et al. 2010].

7.2. Mechanical Load

The macroscopic packed bed behavior during uniaxial compression was carried out by lowering the plunger in absence of any external fluid flow application. The 9.6 mm i.d. column was packed using wet as well as semi-dry SEP particles and the height of the individual sections was measured analogously to hydrodynamic compression experiment. Details about the measuring method are given in Section 5.4.2.

7.2.1. Axial Packing Compression-Relaxation Behavior

Figure 7.6 shows the dynamic packing compression behavior of the semi-dry packing at different packing compression levels. During all compression levels the packing exhibited a pronounced axial packing compression gradient (Figure 7.6 A). The uppermost packing section 1, which is closest to the plunger, showed the highest, whereas the lowermost packing section 7 showed the lowest packing compression. Moreover, as can be seen in Figure 7.6 B, section 7 exhibited a delayed compression. Up to a packing compression of 2.5%, no compression was observed in this section, which means that the compression force was dissipated in the upper packing region.

During relaxation, the packing followed the up-moving plunger without delay. Hence, no hysteretic behavior of the overall packing was observed. However, the resulting compression-relaxation behavior of the sections differed, i.e. the upper sections were more compacted than the lower sections.

Moreover, it was observed that the direction of the hystereses for axial compression switched from clockwise for the upper sections to counter-clockwise for the lower packing sections (Figure 7.6 B). The same observation was made for higher compression levels up to 50% (data not shown). The change of hysteresis direction means that the upper

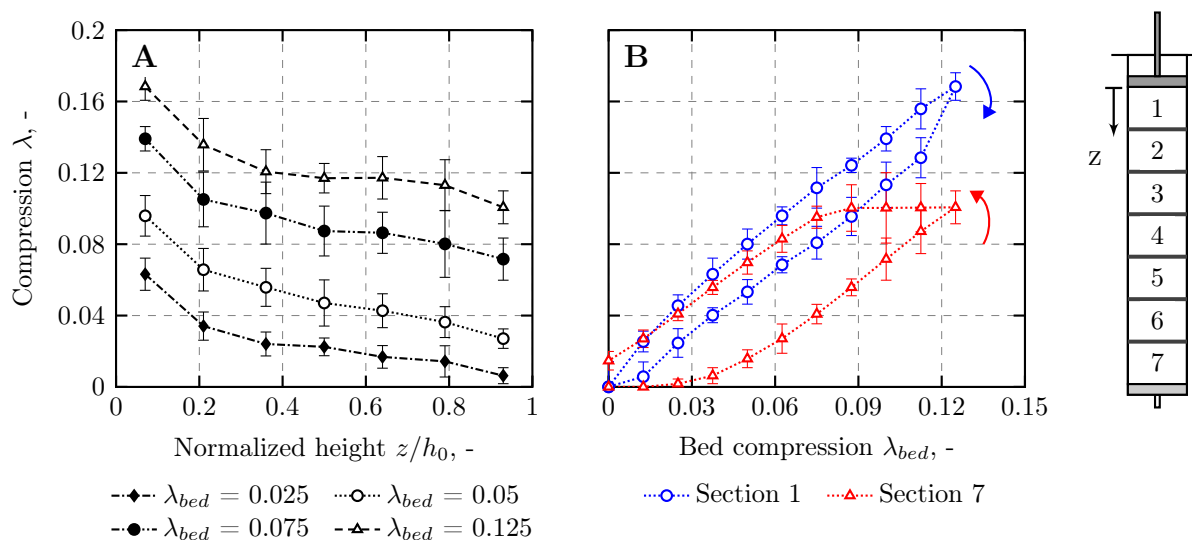


Figure 7.6.: Semi-dry packing compression-relaxation behavior at different mechanical loads. (A) Axial packing compression gradients. The z -coordinate goes from top to bottom of the packing. (B) Hysteretic packing compression-relaxation behavior exemplary shown for sections 1 and 7 as a function of the total packing compression. The arrows indicate the direction of the hystereses.

sections relaxed faster than the lower packing sections. This effect was assumed to arise from increased friction of the chromatographic beads with the column wall during axial compression.

Figure 7.7 shows the dynamic packing compression behavior of the wet packing at the same packing compression levels as in Figure 7.6.

Compressing the wet packing material resulted in a more homogeneous and constant packing compression from $z/h_0 = 0.2$ to $z/h_0 = 0.8$, where z goes from top to bottom of the column (Figure 7.7 A). Here again, the upper packing region, which is closest to the plunger, showed the highest packing compression. However, the lowermost packing section 7 also showed a higher packing compression than the middle sections. As this section is opposite to the plunger and closest to the column outlet, the compression was most likely induced by drag forces of the outflowing fluid. In contrast to Figure 7.6, the lower packing section 7 was compressed without delay, indicating that the compression force was transmitted to the bottom of the packing. Interestingly, switching of the hystereses from the upper packing sections to the lower packing sections as by the compression of the semi-dry packing (Figure 7.6) was not observed. All packing sections showed a delayed relaxation behavior, which is equivalent to hystereses going counter-clockwise. On the background of a wet packing compression, this observation can be

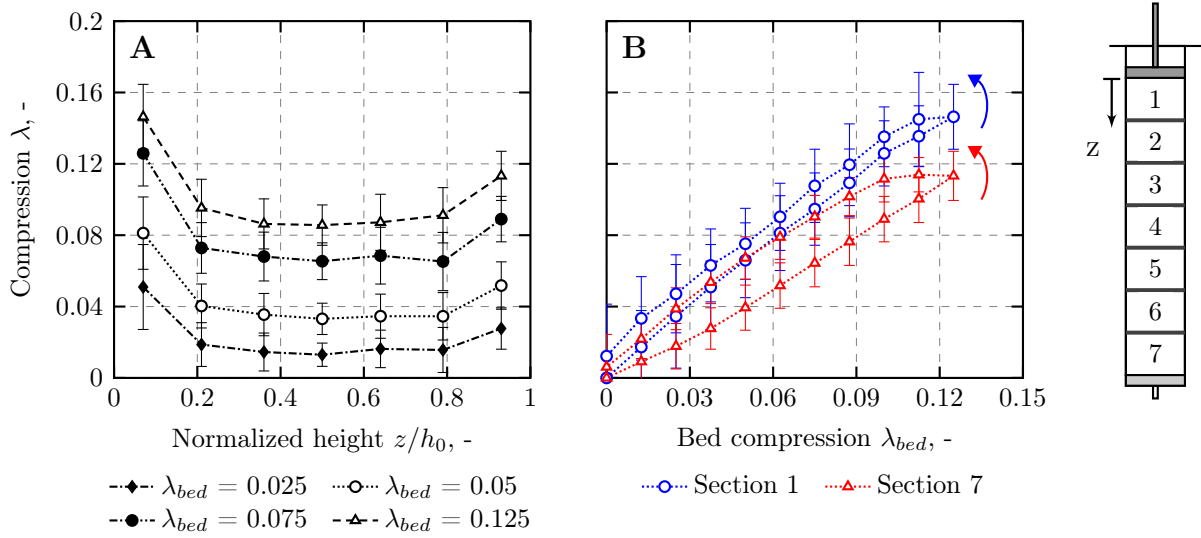


Figure 7.7.: Wet packing compression-relaxation behavior at different mechanical loads. (A) Axial packing compression gradients. The z -coordinate goes from top to bottom of the packing. (B) Hysteretic packing compression-relaxation behavior exemplary shown for sections 1 and 7 as a function of the total packing compression. The arrows indicate the direction of the hystereses.

explained by the fluid flow induced by the movement of the plunger. Thus, during relaxation and the plunger moving upwards, external fluid was sucked in at the bottom of the column inducing an upwards fluid flow. As a consequence, packing expansion and fluid flow act in the same direction causing the packing to relax faster. This can be seen in Figure 7.7 B, showing that the hysteresis of section 7 is less pronounced than in Figure 7.6 B. Hence, the relaxation time of the uppermost packing section 1 is increased by the upmoving lower packing section. This may explain the differences in the compression-relaxation behavior of the semi-dry and wet packings.

7.2.2. Particle Deformation and Force Transmission

The particle deformation and force transmission was analyzed via optical UV-fluorescence microscopy, similar to the hydrodynamic packing compression experiments. Figure 7.8 shows the packing top region right below the movable plunger during gravity settled state (A), during 33% (B) and 50% (C) packing compression.

The degree of packing compression was considerably higher than during flow compression ($\lambda_{bed} \approx 0.12$). Thus, a much denser particle network can be identified in the upper packing region. During packing compression of 33%, only a small amount of void

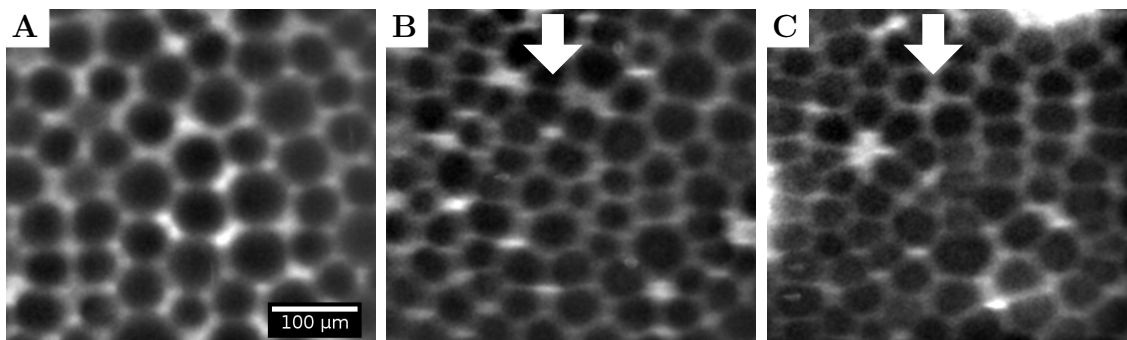


Figure 7.8.: UV-fluorescence microscopy of the uppermost section 1 of the particle bed during mechanical load. (A) Gravity settled packed bed at zero compression. (B) Particle bed being during a mechanical compression of $\lambda_{bed} = 0.33$. (C) Particle bed being during a mechanical compression of $\lambda_{bed} = 0.5$. The arrows indicated the direction of compression.

space is visible between the particles, whereas during 50% almost all voids are closed. The single particles then almost show an oval shape as a result of high compression pressure. Similar to the indicated force-chains in Figure 7.5 (B) force transmission along individual particle chains can be identified in Figures 7.8 (B) and (C).

7.3. Bulk Packing Porosity

The hydrodynamic behavior of chromatographic packings, and particle packings in general, is governed by the packed bed porosity distribution. The analysis of the three-dimensional packing porosity distribution as well as the particle packing configuration was first carried out with dried TOY particles using Micro Computer Tomography (Micro CT). To enhance contrast, the particles were coated with a CaCl_2 layer. Figure 7.9 shows a Micro CT image of the packing. As can be seen, the dry packing porosity slightly fluctuated around a mean value of $\epsilon \approx 0.4$. This value is between the lower and upper limit of random sphere packings $\epsilon_{RCP} \simeq 0.36 \leq \epsilon \leq 0.45 \simeq \epsilon_{RLP}$ and hence in good accordance with theoretical predictions.

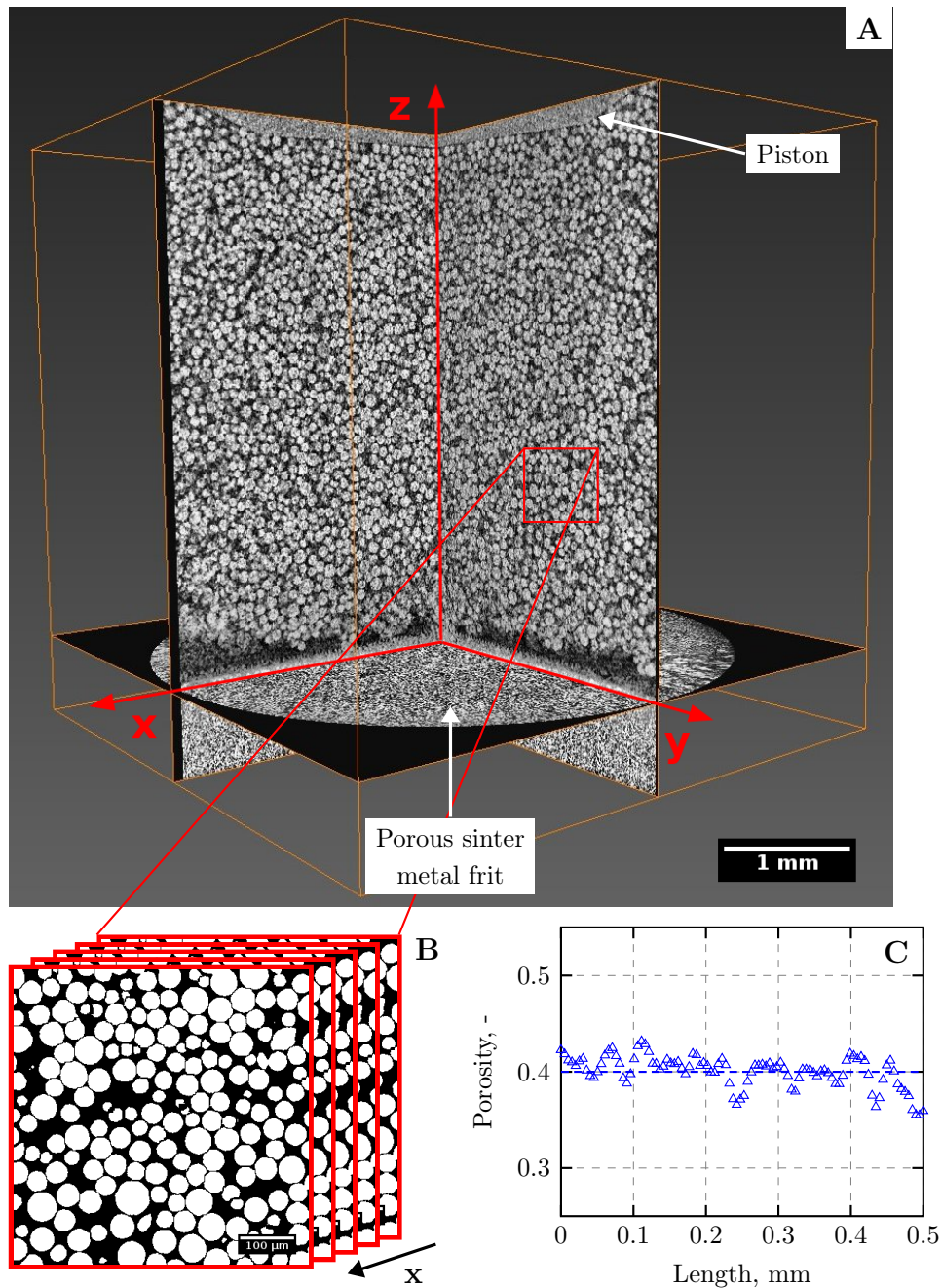


Figure 7.9.: Micro CT image of a packing of CaCl_2 coated TOY particles. (A) View of the total packing of 4.6 mm in diameter. (B) and (C) exemplarily show the procedure of packing porosity determination. The whole 3D packing was divided into incremental 2D slices which were analyzed regarding packing porosity. Each slice then gives a local porosity value along one dimension of the packing. This was plotted against the x-dimension in this case.

However, exact measurements of the bulk packing porosity in a wet packing remains challenging. Figure 7.10 shows calculated X-ray attenuation for different materials as a function of the photon energy. The values were calculated using the exponential attenuation law given by Equation (5.2).

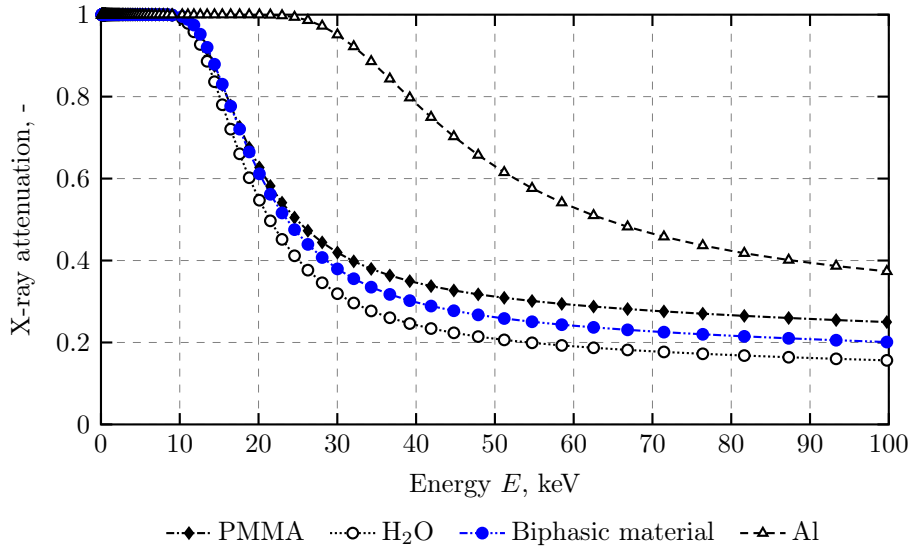


Figure 7.10.: X-ray attenuation of different material packings as a function of the photon energy. PMMA is very similar to the methacrylate matrix of the TOY particles. The attenuation of the TOY particle was approximated by a combination of PMMA and H₂O according to Eq (7.1). Aluminum (Al) is shown for comparison. The thickness of the probe was set to the packing diameter of 9.6 mm.

The mass attenuation coefficients of PMMA, which can be seen as a similar to the particle matrix material, water (H₂O) and aluminum (Al) were taken from Chantler et al. [2005]. The mass attenuation coefficient of the biphasic material was calculated by simple additivity according to

$$\mu/\rho = \sum_{i=1}^2 w_i (\mu/\rho)_i, \quad (7.1)$$

where w_i is the mass ratio of either phases, fluid and polymer, of the particle. w_i is related to intrinsic particle porosity by $w_i = \epsilon \rho_i / \rho_p$ with ρ_p being the density of the material compound (see Table 6.2).

As can be seen in Figure 7.10 the X-ray attenuation of a packing of TOY particles submerged in water is very similar to the attenuation of pure water over a broad range

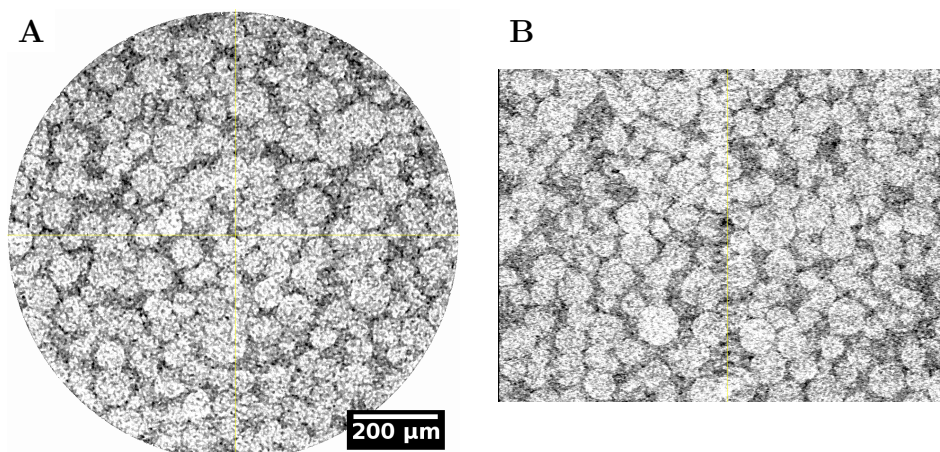


Figure 7.11.: Micro CT image of TOY particles submerged in a contrast enhancing agent solution. (A) Top view and (B) side view of the packing. "Negative" labeling, by labeling the void instead of the particles resulted in the best contrast.

of photon energy. This resulted in a significantly diminished contrast of the Micro CT images so that a clear separation of particle and void space was not possible.

Several measurements using different contrast enhancing agents were carried out. It was found, that labeling the void space by submerging unlabeled particles in contrast enhancing agents gave the best result. Figure 7.11 shows the best result of a TOY packing submerged in a 10 % (w/w) PTA solution. However, the contrast agent significantly diffused into the particles so that it was present in both phases. Methods to achieve selective labeling of either the particles only or the surrounding fluid are not known. Attempts by labeling the particles first led to the removal of the contrast enhancing agent under investigation during the washing step. Hence, it will not be possible to analyze labeled particles in an operated column under hydrodynamic load.

7.4. Influence of The Wall Support On The Hydrodynamic Packing Behavior

Wall support is one of the most important factors influencing the packing pressure drop as well as the dynamic packing compression and relaxation behavior as already discussed in the previous sections. It is known that the influence of the wall friction effects scales anti-proportionally with the column diameter (see Equation (3.75)). In this section, the influence of the column wall support is evaluated with regard to the packing pressure drop

as well as the dynamic packing compression-relaxation behavior in columns of different diameters. For this purpose, larger chromatography columns of diameters 12.5 mm, 16.25 mm, and 20 mm were designed similar to the micro chromatography column used for the previous studies. A scale-up correlation was determined on the basis of a simple continuum model that gives the dependency of the packing compression and pressure drop as a function of the column diameter at constant operating conditions.

7.4.1. Packing Pressure Drop

Packed beds being composed of TOY and SEP particles were analyzed in the four columns which differed in diameter. Due to reasons of availability, the TOY particle used here was the same resin as used in the studies before but with a smaller particle diameter of $65\ \mu\text{m}$ (*Toyopearl*[®] *SP-650M*). The packed bed height was set to 30 mm. Figure 7.12 shows the measured packing pressure drop as a function of the fluid flow velocity and for varying column diameters.

Figure 7.12 A represents a packing composed of TOY particles and Figure 7.12 B a SEP particle packing. Within the range of fluid velocities applied, both packings showed an exponential increase of packing pressure drop. The figure shows clearly that the diameter of the column affects the packing pressure drop, i.e. the larger the column

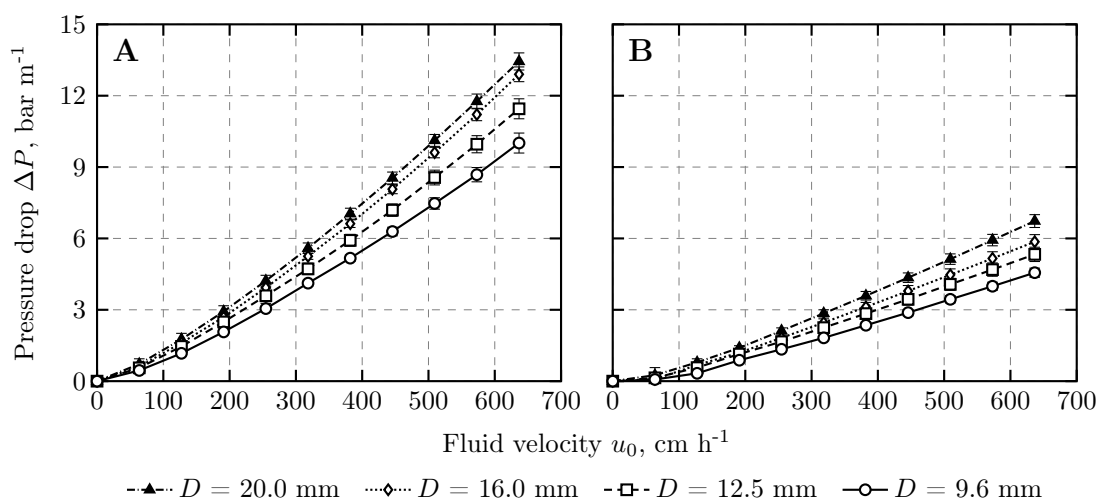


Figure 7.12.: Influence of the column diameter on the packed bed pressure drop. (A) Pressure drop of a packing of TOY particles and (B) pressure drop of a packing of SEP particles as a function of the fluid flow velocity. The gravity settled packed bed height was 30 mm in all columns. D is the column diameter. The experimental error was $< 5\%$ as indicated by the error bars.

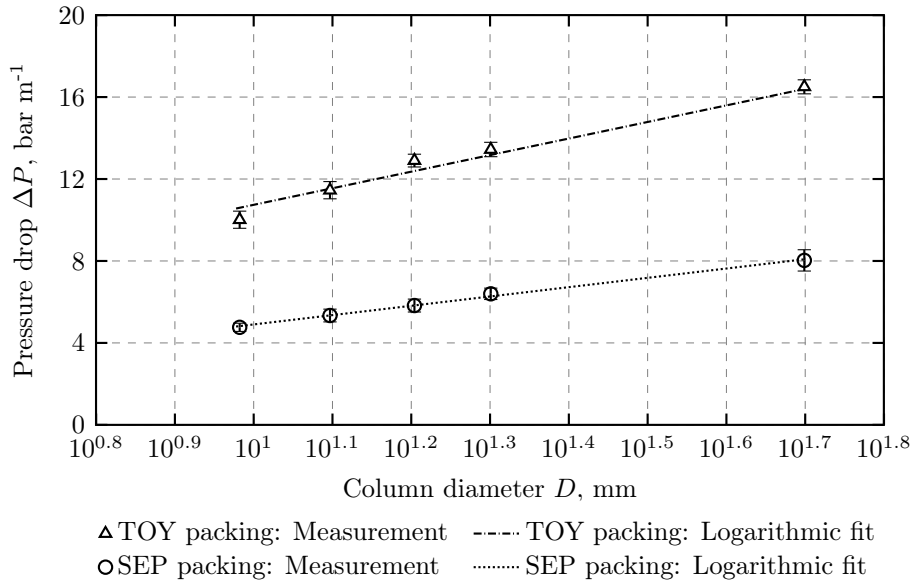


Figure 7.13.: Logarithmic dependency of the packing pressure drop on the column diameter. The packing pressure drop is given at the maximum fluid flow velocity of 637 cm h⁻¹. Logarithmic fits were given by Equations (7.2) and (7.3).

the higher the packing pressure drop. Comparing both packing materials a significant difference in the absolute pressure drop can be noticed. The TOY particle packing exhibited a pressure drop that was nearly the 1.75-fold of the pressure drop of the SEP packing. Although the TOY particles are slightly stiffer than the agarose based SEP particles, this difference may be explained by the smaller particle size of the TOY particles. According to the Kozeny-Carman relation (see Equation (3.57)) the pressure drop is inversely proportional to the square of the particle diameter. Hence, the packing of TOY particles having a mean diameter of 65 μm (see Table 6.1) is expected to exhibit a $\Delta p_{TOY}/\Delta p_{SEP} = (86/65)^2 = 1.75$ fold higher pressure drop than a SEP packing of 86 μm particles.

Figure 7.13 shows the maximum packing pressure drop at a fluid velocity of 637 cm h⁻¹ for both packing materials as a function of the column diameter. The analysis of the column scale up was further extended by measuring the packing pressure drop and compression at the same fluid flow velocity in a 50 mm i.d. column. Data at lower fluid flow velocities were not available. It can be noticed that the packing pressure drop showed a nearly logarithmic dependency on the column diameter which can be described as

$$\Delta P_{TOY} = 3.5121 \ln(D) + 2.6535, \quad R^2 = 0.98 \quad (7.2)$$

$$\Delta P_{SEP} = 1.9751 \ln(D) + 0.3544, \quad R^2 = 0.99 \quad (7.3)$$

for the TOY and SEP particle packings. In Equations (7.2) and (7.3), the column diameter D was used in mm.

7.4.2. Packing Compression-Relaxation Behavior

The dynamic packing compression-relaxation behavior was analyzed by measuring the packed bed height as a function of the fluid flow velocity. Figure 7.14 shows the characteristic packed bed compression-relaxation hystereses of TOY (A) and SEP (B) packings in columns of four different diameters. The arrows indicate the direction of the hystereses.

As expected, the maximum packing compression increased with increasing column diameter. It can be seen further that the wall support not only influenced the maximum packing compression but also the dynamic packing compression-relaxation behavior. So did the 20 mm i.d. column exhibit a rather narrow hysteresis (see the blue curve in Figures 7.14 A and B), whereas the hysteresis of the smaller 9.6 mm i.d. column was

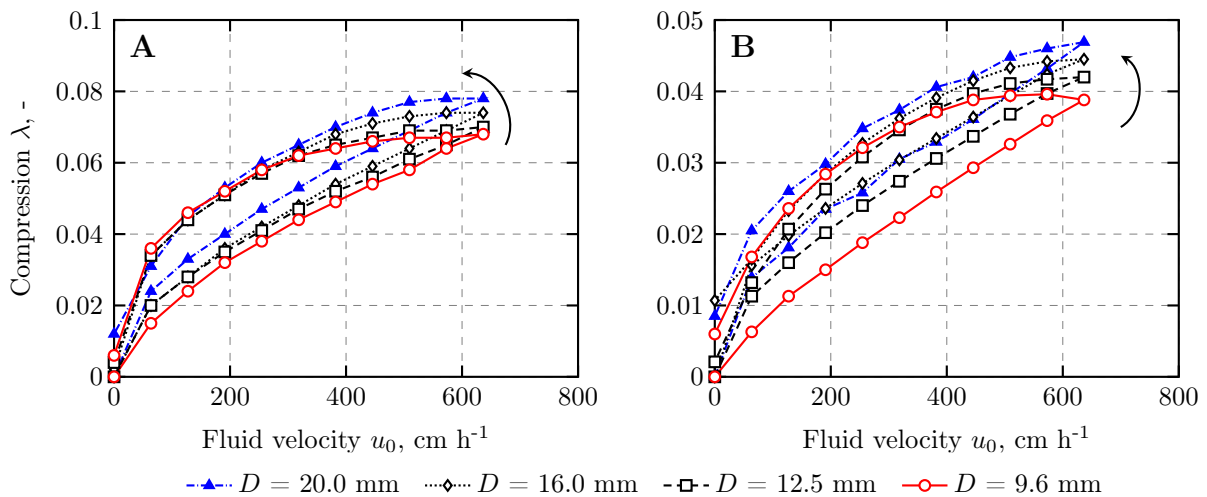


Figure 7.14.: Characteristic packing compression-relaxation hystereses at different column diameters. (A) Compression of a packing of TOY particles and (B) compression of a packing of SEP particles as a function of the fluid flow velocity. The gravity settled packed bed height was 30 mm in all columns. D is the column diameter. The arrows indicate the direction of the compression-relaxation hystereses. The experimental error was $< 15\%$. Error bars were not shown for reasons of clarity.

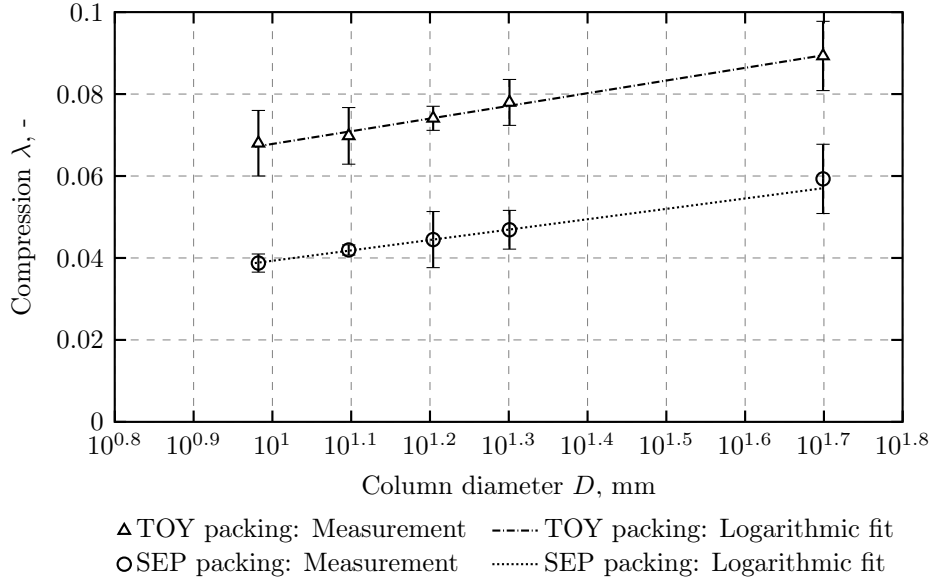


Figure 7.15.: Logarithmic dependency of the packing compression on the column diameter. The packing pressure drop is given at the maximum fluid flow velocity of 637 cm h⁻¹. Logarithmic fits were given by Equations (7.2) and (7.3).

more pronounced (see the red curve in Figures 7.14 A and B). This means that i.e. the time of packing relaxation is larger in the smaller column. As the wall friction acts against the direction of packing movement, it becomes clear that the smaller the column the slower the packing compression and relaxation. Comparing both, TOY and SEP, packings, it attracts attention that the TOY packing exhibited a larger (≈ 1.75 fold) packing compression than the SEP packing, although the TOY particles are a little stiffer than the SEP particles. However, this may be explained by the higher packing pressure drop of the TOY packing as a result of the smaller particle size TOY particles.

Here again, a logarithmic dependency was observed (see Figure 7.15) that can be described by

$$\lambda_{TOY} = 0.01344 \ln(D) + 0.03688, \quad R^2 = 0.98 \quad (7.4)$$

$$\lambda_{SEP} = 0.01100 \ln(D) + 0.01398, \quad R^2 = 0.99 \quad (7.5)$$

7.4.3. Continuum Model of the Wall Support

The approach of Verhoff and Furjanic Jr. [1983] has been used to develop a continuum model of the wall support during packed bed compression in cylindrical columns of different diameter. Here, the net force acting on any point of the packed bed is considered as the sum of forces originating from the flow, the mechanical compression force, the friction between the packing material and the column wall as well as the gravitational force of the packing material (see Figure 3.14). Hence, following this approach, the simple force balance of an axial segment (see Equation (3.75)) considering the previously mentioned force contributions reads

$$\frac{\partial \sigma(z)}{\partial z} = \frac{180(1 - \epsilon(z))^2}{d_{32}^2 \epsilon(z)^3} \eta u_0 - \frac{4}{D} \mu_w \frac{\nu_p}{1 - \nu_p} \sigma(z) + \Delta \rho (1 - \epsilon(z)) g \quad (7.6)$$

and the boundary condition at the packings top (i.e. $z = 0$):

$$\sigma(z = 0) = 0. \quad (7.7)$$

Equation (7.6) cannot be solved analytically due to the fact that the local packing porosity $\epsilon(z)$ is coupled to the local packing stress $\sigma(z)$. A numerical solution of this first order differential equation boundary value problem can be obtained by using simple constitutive models, that relate the packed bed porosity to other packing parameters. In this case, a simple relation of packing stress $\sigma(z)$ to packing compression or packing strain $\lambda(z)$ according to Hooke's law of elastic deformation is used

$$\sigma(z) = B \cdot \lambda(z), \quad (7.8)$$

where B is the packed bed bulk compression modulus. Here, the packed bed modulus is considered as constant during hydrodynamic packing compression. However, assuming a more or less linear Hookean interaction between the single particles due to simultaneous force relaxation, the packing compression modulus was shown to be nearly constant during packing compression of frictionless spheres (see Figure 3.9). The second constitutive equation relates the packed bed porosity to packing compression under the assumption that the single particle is nearly incompressible and the packed bed compression is

achieved by reduction of interparticle void space only. Then,

$$\epsilon(z) = \frac{\epsilon_0 - \lambda(z)}{1 - \lambda(z)}, \quad (7.9)$$

where ϵ_0 is the gravity settled packed bed porosity. Using the equations and boundary condition of (7.6)-(7.9), the boundary value problem was solved numerically using Matlab. From the resulting axial packing stress profile $\partial\sigma/\partial z$ the axial porosity profile $\epsilon(z)$ was calculated using Equations (7.8) and (7.9). Then, the packing pressure drop was given by the Kozeny-Carman relation

$$\Delta p = \int_0^H \frac{180(1 - \epsilon(z))^2}{d_{32}^2 \epsilon(z)^3} \eta u_0 dz \quad (7.10)$$

which was calculated using the trapezium rule in Matlab. The whole boundary value problem was then solved in a *constrained nonlinear optimization* algorithm (using the function *fmincon* in Matlab) in order to fit the calculated pressure drop as a function of the column diameter to the measured values.

Figure 7.16 shows the results of the simple continuum wall support model. As can be seen, the continuum model gives an adequate prediction of the pressure drop depen-

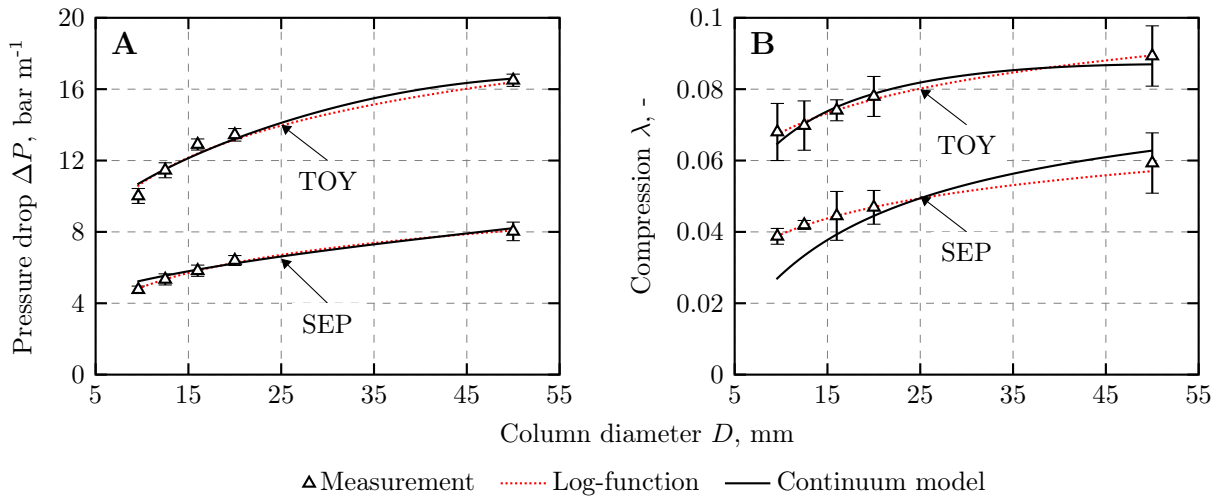


Figure 7.16.: Simulated packing behavior as a function of the column diameter according to the wall support model. (A) Packing pressure drop for the TOY and SEP packing. (B) Packing compression for the TOY and SEP packing. Both plots represent the data at maximum fluid flow velocity of 637 m s^{-1} . The values of the logarithmic model result from Equations (7.2) and (7.2). The continuum model results are based on the fit parameters given in Table 7.1.

dency on the column diameter for both packing materials. With respect to the packing compression, the continuum model only matched the packed bed behavior of the TOY packing with sufficient accuracy. The packing compression behavior of the SEP packing in contrast was over-predicted, i.e. a stronger influence of the wall support was calculated by the model resulting in a steeper packing compression with increasing column diameter. However, laboratory measurements resulted in only a slightly increasing packing compression with increasing column diameter.

The parameters that were fitted within this routine are summarized in Table 7.1. The

Table 7.1.: Fitted parameters according to the TOY and SEP packings used in the continuum wall support model.

Description	Parameter	TOY	SEP
Packing compression modulus, MPa	B	0.164	0.101
Hydrodynamically relevant average particle size, μm	d_p	61.958	78.334
Wall friction coefficient, -	μ_w	0.274	0.189
Packing Poisson's ratio, -	ν_p	0.269	0.499
Relative packing density, kg m^{-1}	$\Delta\rho$	360.844	189.851
Gravity settled packed bed porosity, -	ϵ_0	0.372	0.375

values d_{32} , $\Delta\rho$, and ϵ_0 were close to the values obtained by laboratory measurements (see Tables 6.1 and 6.2) and literature values [e.g. Chang and Chase 1994; DePhillips and Lenhoff 2000; Soriano et al. 2000; Cherrak et al. 2002]. The values obtained for the packing bulk compression modulus B , the wall friction μ_w , and the packing Poisson's ratio ν_p in contrast are difficult to verify, as no literature data is available and experimental determination resulted as challenging.

7.5. Conclusion

The analysis of chromatographic packings during hydrodynamic and mechanical load revealed that the dynamic packing behavior was governed by the mechanical processes at the particle scale. Hence, the total packing compression was the sum of the individual particle compression as well as particle rearrangement which led to a reduction of interparticle void space. As a result, the hydrodynamic permeability decreased leading

to an exponential increase of the packing pressure drop.

Both, hydrodynamic and mechanical load had different effects on the packing compression behavior. The former acted as a surface force on every particle of the packing and increased from the column inlet towards the outlet. As a result, the packing showed a pronounced increase in packing compression from the top to the bottom of the packing.

The latter was exerted on the uppermost layer of particles, which was located adjacent to the compression device. This uniaxial compression force acted as a point force on the particles and was transmitted by particle contacts only. It was shown that uniaxial packing compression led to a decreasing compression profile from the packing top to the bottom section.

Frictional forces determine the way the compression force is transmitted within the packing. The friction itself is influenced by the fluid content of the packing which is important during uniaxial compression by lowering the plunger. It was observed that a semi-dry packing exhibited an exponentially decreasing compression profile in which the section adjacent to the plunger experienced the highest compression and the section opposite to the plunger the lowest. In contrast, in a wet packing, a nearly constant and more homogeneous compression of the middle packing sections was observed. It is assumed that the interstitial fluid acts as a lubricant during packing compression making the particles slide more easily against each other which leads to a more homogeneous distribution of the compression force within the packing.

UV-fluorescence microscopy of the packing during compression revealed an inhomogeneous force transmission at the particle scale. The compression force was transmitted in a force-chain network of highly stressed particles. In this context it was observed that during packing compression the interparticle void space was reduced but still existed even at high packing compression (see Figures 7.5 and 7.8). In the context of packing lifetime, high particles stresses need to be avoided because of the possibility of particle breakage. To preclude particle breakage, the stress exerted on the packing should be distributed evenly among the particles. This means, the higher the number of contacts per particle, the better is the force distributed among the particles. Low friction then may abet particle migration and rearrangement which increases the number particle contacts and the packing turns from a random loose packing to a random close packing configuration. As a consequence, increased particle rearrangement could be the reason why the difference in compression from the first to the second section in Figure 7.7 is higher than in Figure 7.6.

Three dimensional analysis of the packing structure by application of Micro Computer Tomography resulted as challenging. Due to the high intraparticle porosity, the packed bed exhibited a similar X-ray attenuation as the surrounding fluid. This resulted in a significantly diminished contrast and a clear separation of particles from void space was not possible. A screening of several contrast enhancing agents let to a marginally improvement of the measurement quality.

The influence of the column wall support on hydrodynamic packing behavior was analyzed by using columns of different diameter. It was shown that both, the packed bed pressure drop as well as the dynamic packing compression-relaxation behavior increased in a nearly logarithmic fashion with increasing column diameter. However, by taking into account the relevant forces that act on the packing (such as the fluid drag, wall friction, and gravitational forces), an incremental force balance of a cross-sectional segment of the packing revealed that the dependency of the packing pressure drop on the column diameter is much more complex. The local packing porosity, which significantly influences the pressure drop, is inherently coupled to the local packing stress and packing compression. This resulted in a complex boundary value problem with a non-linear differential equation. The pressure drop is then given by the boundary solution of that problem. Furthermore, knowledge of bulk packing parameters such as the bulk packing compression modulus, a column wall friction coefficient as well as a packing Poisson's ratio was required. However, these parameters can be seen as problem specific, as they depend on the column wall material, surface structure of the particles and the interstitial fluid which influences the rearrangement and shear forces between the particles. As no literature data were available for these parameters, the boundary value problem was solved in a constrained nonlinear optimization algorithm from which the parameters were adjusted. The resulting continuum model was then able to describe the measured data adequately.

8. Development and Evaluation of the Simulation Model

This chapter is dedicated to the development and evaluation of the simulation model using the coupled CFD-DEM approach. The experimental findings discussed in the previous chapters form the basis for the definition and determination of parameters, boundary and initial conditions that are required by the CFD and DEM framework. Besides details of the modeling, also model simplifications and assumptions, as well as methods for reducing the computational effort are discussed and evaluated in this chapter. The final model is then compared and evaluated by experimental data.

8.1. Selection of a Proper Particle Contact Model

As the overall dynamic packing behavior is governed by the mechanics and interactions at the small particle scale, a proper particle contact model needs to be defined. Within the DEM package, non-linear Hertzian as well as linear Hookean particle interaction can be defined. Figure 8.1 shows the measured force displacement data resulting from compression of SEP particles at both compression velocities applied and the calculated data using the different particle contact models.

As already pointed out in Chapter 6, the chromatographic resins exhibited a pronounced force relaxation during compression. The relaxing effect was attributed to either poroelasticity due to fluid flow and equilibration of intraparticle pore pressure or viscoelasticity due to conformational changes of the polymer network or a combination of both effects. Based on the assumption, that particle compression is in a realistic range of $\Delta < 10 \mu\text{m}$ (see Figure 7.5) a rather linear than nonlinear force displacement relation is expected. Thus, in good approximation to the measured behavior, the linear Hooke particle contact model was chosen for DEM simulations.

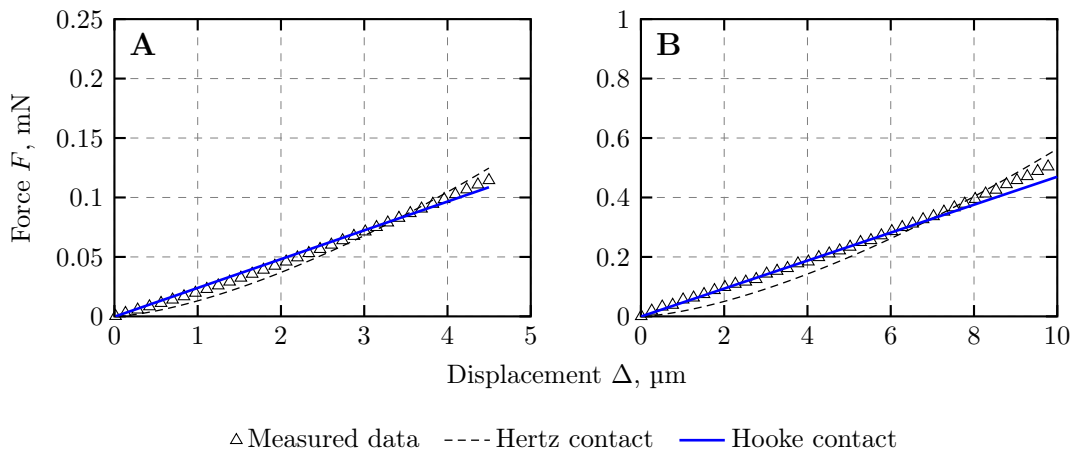


Figure 8.1.: Comparison of nonlinear Hertz and linear Hooke particle contact models. Measured particle force displacement data (SEP resin) is given for a realistic range of particle displacement (data from Figure 6.7) as well as best fits according to the Hertz and Hooke contact laws for normal contact $F_n = k_n \delta_n$ (see Equations (4.14) and (4.21)). Mean particle diameter and density of the SEP particle were taken from Table 6.1 and 6.2. **(A)** Compression velocity of $0.9 \mu\text{m s}^{-1}$: Hooke: $E = 13 \text{ MPa}$, $V = 0.1 \text{ m s}^{-1}$, $R^2 = 0.99$. Hertz: $E = 4.06 \text{ MPa}$, $R^2 = 0.96$. **(B)** Compression velocity of $5 \mu\text{m s}^{-1}$: Hooke: $E = 30 \text{ MPa}$, $V = 0.1 \text{ m s}^{-1}$, $R^2 = 0.99$. Hertz: $E = 5.53 \text{ MPa}$, $R^2 = 0.94$.

8.1.1. Relevant Parameters and Assumptions

Table 8.1 gives an overview of the parameters required by the linear Hooke model. Some parameters were already determined by micro-manipulation experiments and given in Section 6.7.

Using the linear Hooke particle contact model, a few assumptions were necessary in order to build a realistic simulation model. As already discussed in Section 4.2.1, the normal particle contact force calculated by the Hooke model is correlated with the characteristic impact velocity V (see Figure 4.2). This parameter results from the theoretical derivation of the contact model and defines the relative velocity of two approaching particles before collision. However, in dense particle packed beds, where each particle already is in contact with its neighboring particles, a characteristic impact velocity is not clearly defined. Furthermore, particle movement and hence, particle velocity is influenced by the surrounding particle network. As a first approximation, the interstitial fluid velocity u_i (see Equation (3.52)) can be used as a characteristic impact velocity which is assumed to not exceed 0.1 m s^{-1} (based on $u_{0,max} = 2763 \text{ cm h}^{-1}$ and $\epsilon_{min} \geq 0.07$). This would be the maximum velocity a particle would be able to achieve under the assumption of free movement within the packing pore network.

Table 8.1.: DEM model parameters required by the Hooke contact model.

Parameter	Description	Value	Comment
E , MPa	Young's Modulus	E(V)	Can be fitted to experimental data using a specific characteristic impact velocity
ν , -	Poisson's ratio	0.2	Determined by micro-manipulation experiments (see Section 6.7)
μ_p , -	Particle-particle friction coefficient	0..1	Parameter needs to be adjusted by CFD-DEM simulations
μ_w , -	Particle-wall friction coefficient	0..1	Parameter needs to be adjusted by CFD-DEM simulations
μ_R , -	Particle rolling friction coefficient	0..1	Parameter needs to be adjusted by CFD-DEM simulations
e , -	Coefficient of restitution	0.. e_{max}	Value depends on the viscosity of the surrounding fluid as well as on the local Stokes number [Legendre et al. 2005]; calculated by the model
e_{max} , -	Maximum coefficient of restitution	0.9	Determined by micro-manipulation experiments (see Section 6.7)
V , m s ⁻¹	Characteristic impact velocity	0..0.1	Parameter needs to be adjusted by CFD-DEM simulations
η_{DEM} , Pa·s	Characteristic fluid viscosity	0.001	Viscosity of water at 20°C
St_{crit} , -	Critical Stokes number	0..10	Parameter needs to be fitted by CFD-DEM simulations
ρ_p , g cm ⁻³	Particle density	1..3	Particle density is greater than 1 g cm ⁻³ (water) but smaller than 3 g cm ⁻³ (dry polymer, see Table 6.2)

Friction coefficients of particle-particle as well as particle-wall interactions are difficult to determine experimentally for a dense packed bed submerged in a fluid and the development of specific shear cell measurements might be necessary in order to determine these values. Similar measurements are required to measure single particle rolling friction. This parameter influences the particle movement and rearrangement during dynamic packing compression-relaxation. Adequate values for the friction coefficients are therefore determined by stepwise adjustment of these parameters and comparing the simulation results with laboratory measurements.

Within the Hooke interaction law, the influence of the viscous fluid surrounding on particle impact was also considered. Additional energy dissipation that is attributed to

the lubrication of the liquid film between to colliding particles is therefore taken into account. Using this “viscous”-model option the coefficient of restitution is adapted as proposed by Legendre et al. [2005]. Therein the coefficient of restitution depends on the viscosity of the surrounding fluid and the Stokes number (Equation (8.1)). Legendre et al. [2005] stated that a no-rebound situation ($e = 0$) may be observed below a critical Stokes number of $St_{crit} = 10$. The restitution coefficient quickly increases after the transition at St_{crit} and monotonically reaches an asymptotic value close to the value of e obtained in air, where viscous effects are supposed to be negligible during collision. This calculation is restricted by the maximum coefficient of restitution.

However, in low Reynolds number flows ($Re_B < 10$), the Stokes number is inversely proportional to the Reynolds number itself and defined as [Norouzi et al. 2016]

$$St = \frac{t_p}{t_f} = \frac{\rho_p d_{32}^2}{18\eta_f} \left(\frac{d_p}{u_0} \right)^{-1}. \quad (8.1)$$

For SEP particles submerged in water, the Stokes number can be approximated as $St \approx 0.046 \ll 1$, given a Sauter diameter of 93 μm and the particle properties determined so far.

8.2. Reduction of Computational Effort

Although the DEM method is well established, it has the disadvantage that the computational effort scales with the number of particles to be simulated. Hence, when the simulation needs to be finished within practical time, e.g. using a desktop computer, the quantity of calculated particles is limited. However, simulation of industrial applications, i.e. hydrodynamic chromatographic packing behavior, requires the simulation of large scale systems and realistic column dimensions. The laboratory column used in this work, given a packing diameter of 9.6 mm and a gravity settled packing height of 30 mm, used to contain about $3.5 \cdot 10^6$ particles with a diameter of 90 μm and packed to a packing density of 62%. As an example, the calculation of 223000 particles during a simulation of column operation of 30 s lasted about 65.28 h (Intel XEON E5-2699-v3 processor using 32 cores at 2.3 GHz and 64 GiB RAM). Hence, based on the assumption of linear scaling of the computational effort with number of particles, a total calculation time for a $3.5 \cdot 10^6$ particle simulation would last 1024.5 h or 42 d and 16.5 h. A reduc-

tion of the computational effort is therefore strictly needed in order to assure practical simulation times and fast simulation post processing and data evaluation.

Two methods were applied to reduce the number of particles, the reduction of three-dimensional simulation domains to pseudo two-dimensional simulation domains and the coarse grain approach. Both methods will be discussed in the following.

8.2.1. The Coarse Grain Approach

In the coarse grain model, a group of particles is simulated using a large-sized particle termed a *coarse grain particle*, where the total energy is modeled to agree between the coarse grain and the original particles.

Simulations of hydrodynamic as well as mechanical packing compression using a coarse graining of $CG = 1, 2, 3$ were carried out and the results were compared to each other. Here, $CG = 1$ corresponds to the reference simulation without coarse graining. The simulation set-up is given in Section 5.5.4. The particle size distribution of Sepharose particles was still considered, but with coarse grained particles. Table 8.2 gives an overview of the simulation performance and the computational effort of the different simulations.

As can be seen, the number of particles to consider was reduced by a factor of 8 using $CG = 2$ and by a factor of 27 using $CG = 3$. This resulted in a significant reduction in computational time from 33h to 1.87h using $CG = 3$ within the given simulation conditions. The *-indexed time data give information about how the total calculation time is distributed to the corresponding algorithms the DEM code uses. For example, the *pair time* gives the time needed for the calculation of pairwise interaction of the single particles, the *neighbor time* gives the time consumed by the building of neighbor lists and the *communication time* corresponds to the time the CPU cores need to exchange information due to parallel computing, e.g the time for shifting particles to new processors and time for updating new particle positions. The *output time* defines the time needed to write data files to the hard drive and *other time* sums up the time needed by the remaining algorithms involved in the calculation [Reid and Smith 2005]. These time data give valuable information about the efficiency of the simulation in terms of domain composition and parallel computing or the simulation setup, e.g. neighbor list parameters. The Table shows that by increasing the coarse graining led to a reduction of the pair time and neighbor time, as less particle interactions needed to be calculated

Table 8.2.: Computational effort and performance of simulations using different coarse graining values. Simulation set-up: rectangular box with 2 mm, 2 mm and 12.5 mm in x, y and z direction and periodic boundaries in x and y direction. The number of particles as well as different performance parameters are given. Times* give the average time needed by the model to perform the corresponding operation (per 1000 DEM calculations)

Parameter	CG = 1	CG = 2	CG = 3
Particles	120000	15000	4444
Simulated time, s	28	28	28
Calculation time, h	33	4.75	1.87
CPU cores	32	32	32
*Pair time, s (%)	4.16 (52.57)	0.54 (49.58)	0.18 (44.21)
*Neighbor time, s (%)	2.60e-4 (3.14e-3)	3.31e-3 (0.30)	1.11e-6 (2.69e-4)
*Communication time, s (%)	0.35 (4.47)	0.09 (8.49)	0.06 (15.17)
*Output time, s (%)	0.19 (1.09)	0.02 (0.98)	6.57e-3 (0.92)
*Other time, s (%)	3.34 (41.86)	0.45 (40.63)	0.16 (39.69)
*Total time, s (%)	8.04 (100)	1.10 (100)	0.41 (100)

and less neighbor lists needed to be build. However, as keeping the number of cores constant, the communication time consumed by the MPI communication of the CPU cores increased to 15.17%. This might be due to the increased size of the coarse grained particles that required more frequent updates of particle positions and forces between the processors.

Figure 8.2 displays the data of the hydrodynamic packing compression simulations using different coarse graining values in terms of packing pressure drop (A), packed bed subsidence (B), axial packing compression profile (C) as well as average particle overlap (D).

As can be seen, all simulations led to the same hydrodynamic packing behavior. The calculated pressure drop curves are nearly identical, which means that the energy exchange between fluid and particle phase was nearly the same as in the reference simulation with CG = 1. The packed bed subsidence and axial packing compression profiles indicate that also the force transmission within the packing did not change by applying the coarse grain method. Figure 8.2 (D) shows the average particle overlap $\hat{\delta}_p$ as a function of the hydrodynamic load. The fact that the average particle overlap directly scaled

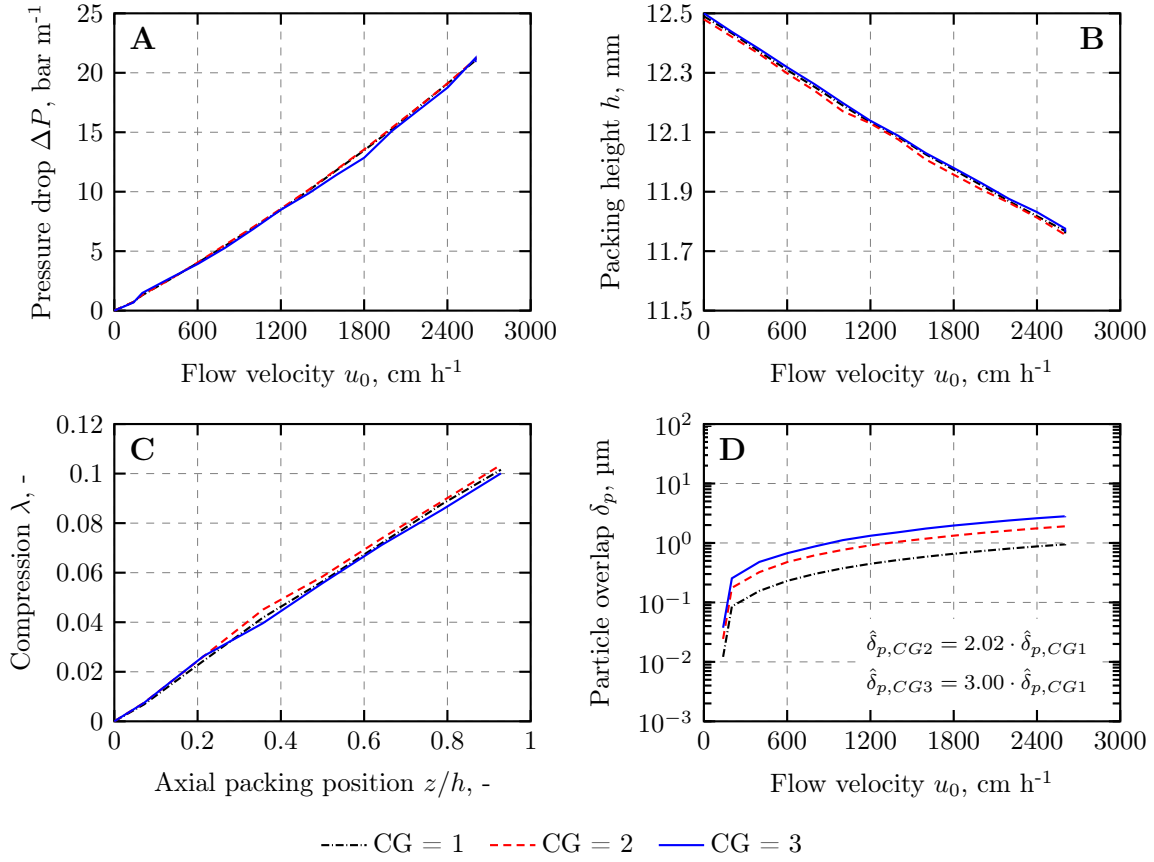


Figure 8.2.: Effect of the amount of coarse graining on hydrodynamic column performance. (A) Packing pressure drop ΔP as a function of the superficial flow velocity u_0 . (B) Packing height h as a function of the superficial flow velocity u_0 . (C) Local packing compression λ as a function of the axial packing position z/h at maximum hydrodynamic load and (D) particle overlap δ_p as a function of the superficial flow velocity u_0 .

with the coarse graining revealed that also the particle micromechanics are similar to the reference simulation. This proportionality further means, that also particle rearrangement and local porosity distribution is similar to the reference simulation. As an example, if particle rearrangement would be decreased by increased coarse graining, the particles would keep in their position and the packing compression would be translated directly to particle deformation, which then would lead to increased particle overlap.

Figure 8.3 presents the data of the coarse grain simulations during mechanical packing compression. The compression force, which was calculated by the compressing device at the top of the packing, also gives the same values irrespective of the coarse graining. This means that the overall packing stiffness is similar to the reference simulation. Here

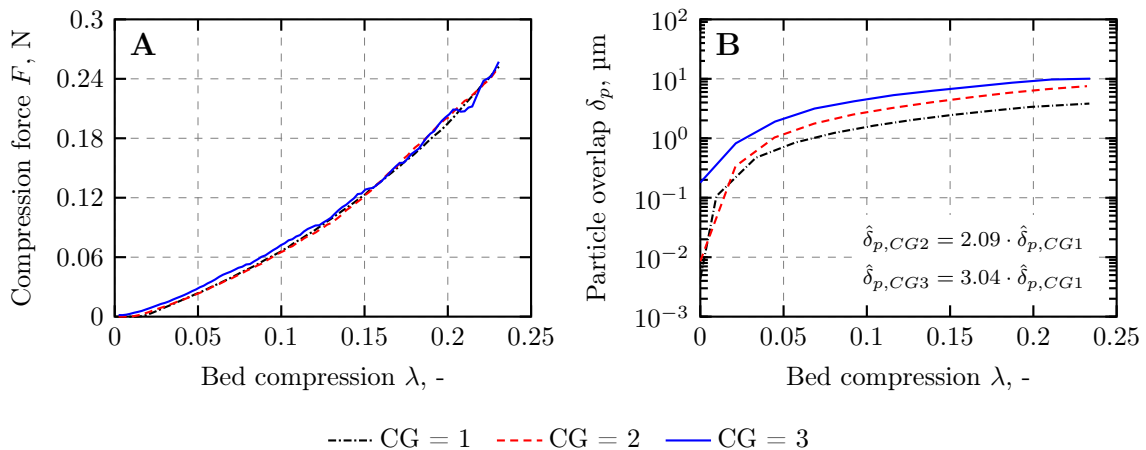


Figure 8.3.: Effect of the amount of coarse graining on mechanical packing compression behavior.. (A) Comparison of the packing bulk compression force F as a function of the compression ratio λ . **(B)** Comparison of the particle overlap δ as a function of the packing compression ratio λ .

again, the average particle overlap scaled directly with the amount of coarse graining.

This confirmed that the coarse grain approach is a successful method to significantly reduce the computational effort and speed up the simulation without the risk of increasing model uncertainty.

The only disadvantage of increased coarse graining is the fact that the CFD cell size also needs to be increased in order to match the requirements of the CFD-DEM coupling algorithm. The *divided voidfraction* model [Goniva et al. 2012; Kloss et al. 2012] used in this work required the CFD cells to be large enough to contain a least 3 particles for realistic cell void fraction calculation and to assure certain numeric stability. Thus, increasing the size of the coarse grained particle leads to minor CFD resolution. Within the simulation domain sizes used in this work, a coarse graining of $CG = 3$ was found to give the best compromise in terms of computational effort and simulation accuracy and resolution.

8.2.2. Pseudo Two-Dimensional Simulation Model

Reducing the simulation domain from a three-dimensional column model to a pseudo two-dimensional column model, representing a slice of the column in axial direction (see Figure 5.7) was found to be an effective method to further reduce the computational effort of the simulation. Details about the domain geometry, boundary and

Table 8.3.: Computational effort and performance of simulations using 3D and pseudo 2D models. 3D simulation setup: Cylindrical column with a diameter of 10 mm and a packing height of 31 mm. Pseudo 2D simulation setup: rectangular box with 10 mm, 0.6 mm, 31 mm in x, y and z direction and periodic boundaries in y direction. The number of particles as well as different performance parameters are given. *Times give the average time needed by the model to perform the corresponding operation (per 1000 DEM calculations).

Parameter	3D	Pseudo 2D
Particles	223379	18323
Simulated time, s	28	28
Calculation time, h	65.28	9.98
Cores	32	14
*Pair time, s (%)	7.74 (49.30)	1.58 (64.33)
*Neighbor time, s (%)	0.05 (0.31)	3.33e-3 (0.12)
*Communication time, s (%)	0.48 (3.08)	0.09 (3.54)
*Output time, s (%)	0.37 (1.08)	0.01 (0.44)
*Other time, s (%)	7.35 (46.23)	0.79 (31.56)
*Total time, s (%)	15.99 (100)	2.49 (100)

initial conditions are given in the Sections 5.5.2 and 5.5.2. The packing height of the three-dimensional and pseudo two-dimensional column was 30 mm.

Table 8.3 gives an overview of the simulation performance and simulation time data. The number of particles required to obtain a packing of equal height was reduced by a factor of 12.2 from 223379 to 18323 particles. This led to a total calculation time of 9.98 h (on 14 CPU cores) which is only 15.3% of the calculation time required by the reference simulation (on 32 CPU cores) (see Table 8.3).

Figure 8.4 compares the pseudo two-dimensional model and the three-dimensional model based on the packing pressure drop ΔP (A), the packing height h (B) as a function of the superficial flow velocity u_0 as well as the axial packing compression profile (C) at maximum hydrodynamic load. Both simulations used the same set of parameters. The 2D model had periodic boundaries in y and frictional solid walls in x and z direction. As can be seen, the pseudo 2D model accurately reproduced the hydrodynamic behavior of the reference 3D simulation. The data are nearly identical in terms of packing pressure drop, bed subsidence and axial packing profile.

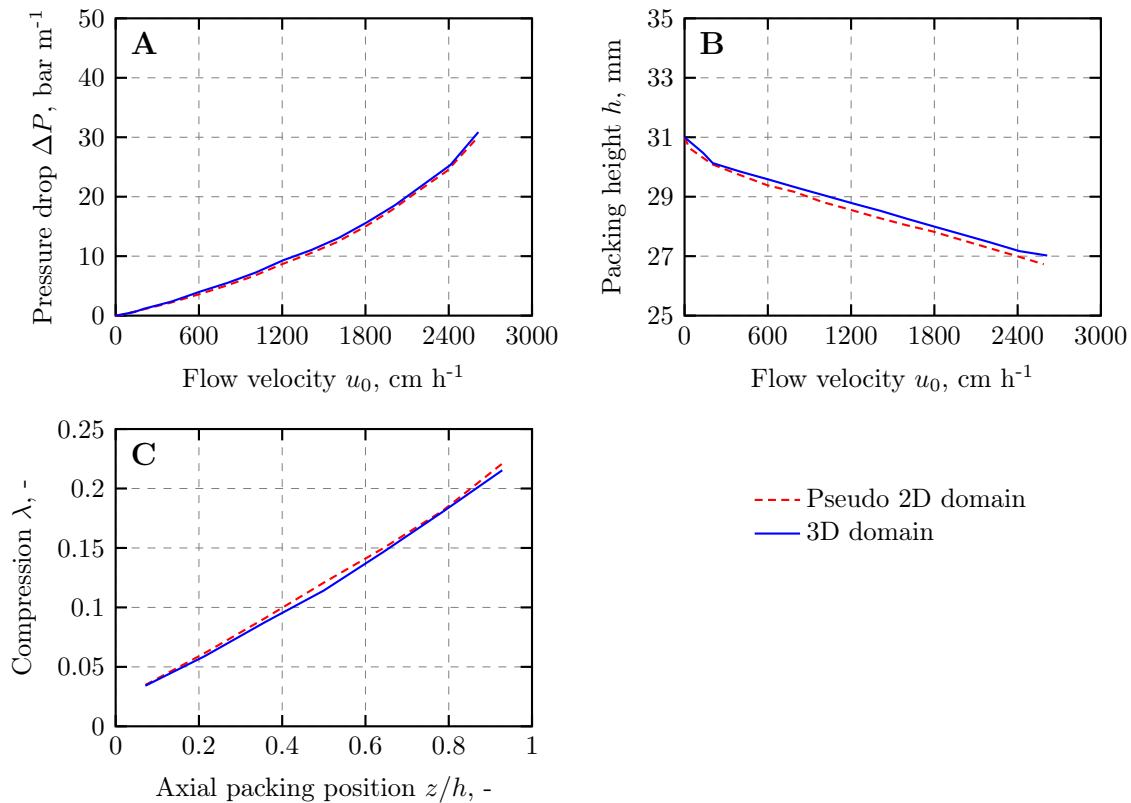


Figure 8.4.: Variation of the particle-particle as well as the rolling friction coefficients. (A) Comparison of the normed packing pressure drop as a function of the fluid flow velocity. (B) Comparison of the bed height as a function of the fluid flow velocity. (C) Comparison of the axial packing compression profile at maximum hydrodynamic load.

This confirmed that the simulation of a rotationally symmetric slice of finite thickness was sufficient to reproduce the realistic three-dimensional hydrodynamic packing behavior. As a consequence, further simulations were carried out using the pseudo 2D model and a coarse graining of $CG = 3$.

8.3. Model Evaluation and Accuracy

8.3.1. Parameter Studies and Sensitivities

As already pointed out in Table 8.1 a few parameters could not be determined experimentally, i.e. the friction coefficients μ_p , μ_w , μ_R , the characteristic impact velocity V and the critical Stokes number St_{crit} . By performing parameter studies, reasonable

Table 8.4.: DEM model parameters required by the Hooke contact model. The sensitivity of the parameters on the simulation results of pressure drop and packing compression was investigated. Pressure fluctuations, as an indicator of numerical stability of the simulation, were also considered. The parameters were varied in at least five steps within the range given in the Table. The arrows indicate an increase (\uparrow) or decrease (\downarrow) of a parameter or effect.

Parameter Description		Range	Sensitivity	Final value
E , MPa	Young's modulus	10..100	E ($\uparrow\downarrow$): Packing compression ($\downarrow\uparrow$), pressure drop ($\downarrow\uparrow$), pressure fluctuations ($\uparrow\downarrow$)	30
ν , -	Poisson's ratio	0.1..0.5	ν ($\uparrow\downarrow$): no significant effects observed	0.2
μ_p , -	Particle-particle friction coefficient	0.0001..1	μ_p ($\uparrow\downarrow$): Packing compression ($\downarrow\uparrow$), pressure drop ($\downarrow\uparrow$)	0.1
μ_w , -	Particle-wall friction coefficient	0.1..0.5	μ_w ($\uparrow\downarrow$): Packing compression ($\downarrow\uparrow$), pressure drop ($\downarrow\uparrow$)	0.1
μ_R , -	Particle rolling friction coefficient	0.1..0.5	μ_R ($\uparrow\downarrow$): Packing compression ($\uparrow\downarrow$), pressure drop ($\uparrow\downarrow$)	0.35
e , -	Coefficient of restitution	0.001..0.5	e ($\uparrow\downarrow$): no significant effects observed	0.5
e_{max} , -	Maximum coefficient of restitution	0.1..0.9	e_{max} ($\uparrow\downarrow$): pressure fluctuations ($\downarrow\uparrow$)	0.9
V , m s ⁻¹	Characteristic impact velocity	0.0001..1	V ($\uparrow\downarrow$): Packing compression ($\downarrow\uparrow$), pressure drop ($\downarrow\uparrow$)	0.1
η_{DEM} , mPa·s	Characteristic fluid viscosity	0.1..1	η_{DEM} ($\uparrow\downarrow$): pressure fluctuations ($\uparrow\downarrow$)	1
St_{crit} , -	Critical Stokes number	0.1..0.9	St_{crit} ($\uparrow\downarrow$): pressure fluctuations ($\uparrow\downarrow$)	0.3
ρ_p , g cm ⁻³	Particle density	1.0..2.0	ρ_p ($\uparrow\downarrow$): Packing compression ($\downarrow\uparrow$)	1.15

values of these parameters were determined.

The simulated hydrodynamic as well as the mechanical packing behavior was compared to measurements using the laboratory micro chromatography column. Thus, hydrodynamic load simulations were evaluated by comparing the packing pressure drop Δp and the packing height h as functions of the superficial flow velocity u_0 and by the local packing compression λ as a function of the axial packing position z/h .

Table 8.4 gives an overview of the sensitivity of the DEM model parameters on the simulation results with respect to packing pressure drop and packing compression. The arrows indicate an increase (\uparrow) or decrease (\downarrow) of the parameters. Packing compression

was investigated in detail considering the overall packing height as well as the axial packing compression profile. Numerical stability of the simulation was studied by measuring the pressure fluctuations, that cannot be explained by physical means but were found to arise from the stiff coupling of the CFD and DEM packages. All parameters were varied within the range given in Table 8.4. The results are commented in the following:

- Increasing (decreasing) the particle Young's modulus E led to a stiffer (softer) packing. Thus, packing compression was lower (higher) during hydrodynamic load and consequently was the packing pressure drop. Pressure fluctuations increased (decreased) slightly.
- By varying the Poisson's ratio ν , no significant effects on the simulation results were observed.
- Variation of the particle-particle friction coefficient μ_p had a sensitivity on the simulation results which was comparable to the Young's modulus. Higher friction coefficients led to reduced particle rearrangement and to lower packing compression during hydrodynamic load. Consequently the packing pressure drop decreased. By decreasing the friction coefficient however, the particles were able to slide more easily against each other which resulted in an increased packing compression during hydrodynamic load. Furthermore, the porosity of the packing was reduced and the pressure drop increased.
- Effects of the variation of the particle-wall friction coefficient μ_w were comparable to those of varying μ_p , but of less significance on the simulation results.
- The particle rolling friction coefficient μ_R influenced the momentum transfer in the total packed bed due to particle rotation [Goniva et al. 2012]. Increase (decrease) of μ_R led to an increase (decrease) of axial force transmission within the packing which was observed by a higher (lower) packing compression during hydrodynamic load. Consequently the pressure drop was also higher (lower).
- By varying the coefficient of restitution e as well as the maximum coefficient of restitution e_{max} , no significant effects on the simulation results were observed. This might be due to the fact that the final value of the coefficient of restitution used by the model depends on the characteristic impact velocity V [Legendre et al. 2005].
- The characteristic impact velocity V , as already discussed earlier, had a significant influence on the simulation results, i.e. on the packing stiffness. Increasing

(decreasing) this parameter caused the packing to appear stiffer (softer) which lowered (increased) packing compression and pressure drop. However, decreasing this parameter led to an increase in numerical pressure fluctuations and to unphysical particle vibrations of a frequency proportional to the DEM calculation time step. Hence, this parameter was chosen as high as possible (i.e. $V = 0.1 \text{ m s}^{-1}$).

- The characteristic fluid viscosity η_{DEM} , the critical Stokes number St_{crit} and the particle density ρ_p had no significant influence on the simulation results within the range of values considered, but only minor effect on the numerical stability and pressure fluctuations.

The final values of the friction parameters μ_p , μ_w , μ_R , the characteristic impact velocity V and the critical Stokes number St_{crit} (Table 8.4) were obtained by stepwise variation of those parameter and by comparing the simulated packing pressure drop, bed subsidence and axial packing compression profiles with the experimental values. The parameters Young's modulus E , Poisson's ratio ν , maximum coefficient of restitution e_{max} , characteristic fluid viscosity η_{DEM} and the particle density ρ_p were obtained by experimental particle characterization (see Table 8.1).

8.3.2. Hydrodynamic Packing Compression

Figure 8.5 shows the normed packing pressure drop as a function of the superficial fluid flow velocity for both measured and simulated packing behavior.

Using the set of parameters given in Table 8.4, the measured pressure-flow dependency was reproduced with great accuracy by the simulation model.

Figure 8.6 compares the packing compression behavior of the laboratory columns with that of the simulated column. The simulated characteristic packed bed compression during hydrodynamic load matched the measured data sufficiently good. The packing height of the simulated column was slightly under-predicted by the model, however, the differences are acceptable (Figure 8.6 A). Good agreement was achieved concerning the axial packing compression profile (Figure 8.6 B). Here, the compression profile is exemplarily given at a superficial flow velocity of $u_0 = 2763 \text{ cm h}^{-1}$. The agreement of axial compression profiles at lower superficial flow velocities was similar.

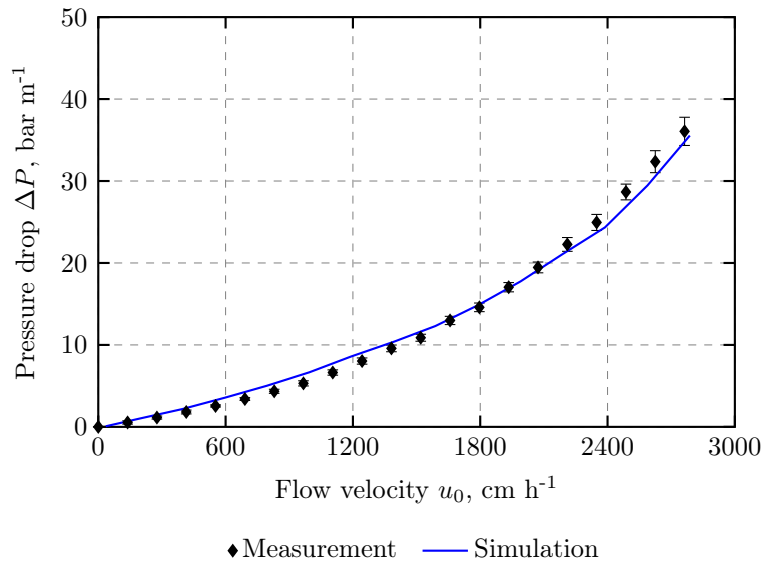


Figure 8.5.: Comparison of measured and simulated packing pressure-flow dependency. Simulations were carried out using the parameter set given in Table 8.4.

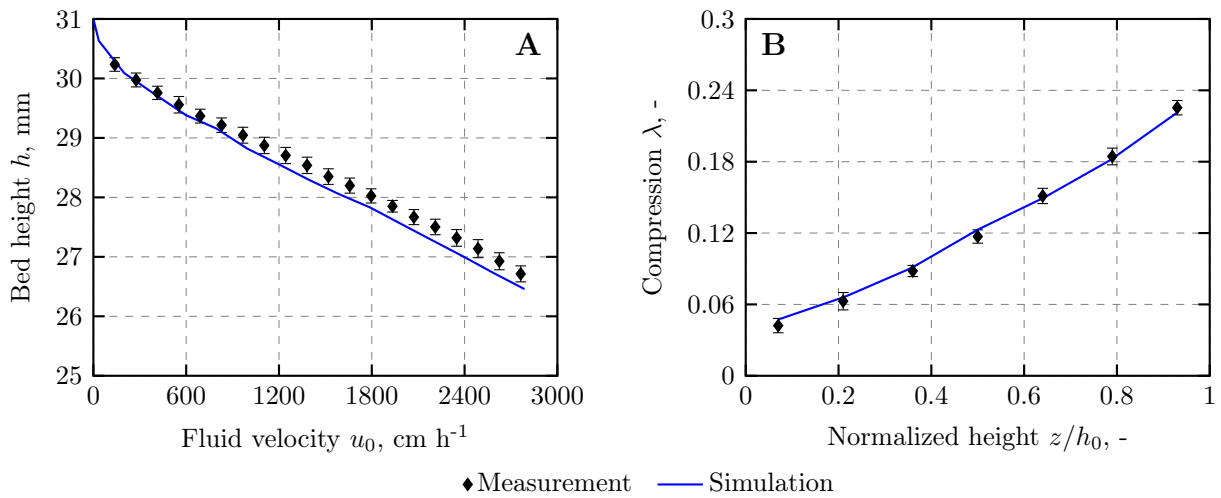


Figure 8.6.: Comparison of the measured and simulated packing compression behavior during hydrodynamic load. (A) Packing height as a function of the superficial flow velocity. (B) Axial packing compression profile at a superficial flow velocity of $u_0 = 2763 \text{ cm h}^{-1}$. Simulations were carried out using the parameter set given in Table 8.4.

8.3.3. Mechanical Packing Compression

In Figure 8.7 the measured and simulated axial packing compression profile during mechanical packing compression of 12.5% is compared. The plunger was lowered manually

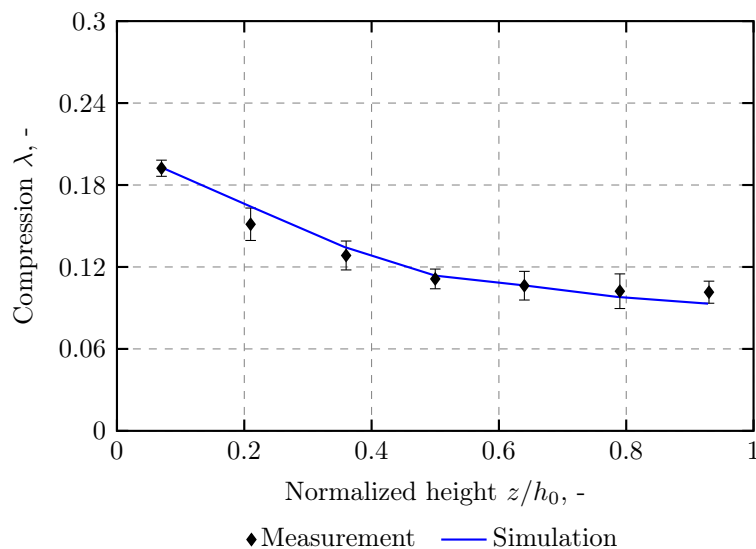


Figure 8.7.: Comparison of the measured and simulated packing compression behavior during mechanical load. The packing was compressed mechanically by 12.5% by lowering the plunger with a velocity of 20 mm min^{-1} .

with a velocity of approximately 20 mm min^{-1} . In the DEM simulation, the plunger was approximated by a moving solid boundary which was lowered by the same velocity as in the laboratory experiment.

The simulation matched the measured packing compression behavior with great accuracy. The packing compression exponentially decreased from the top of the packing to the column outlet.

8.4. Conclusion

The particle-based modeling of the hydrodynamic behavior of the micro chromatography column using the coupled Euler-Lagrange simulation approach was carried out successfully and for the first time. In comparison to earlier one- or two-dimensional continuum models reported in literature [e.g. Keener et al. 2004a,b; McCue et al. 2007; Tran et al. 2007; Hekmat et al. 2013] the simulation model developed in this work is based on the individual particle behavior and addresses the local interparticle micromechanics coupled to fluid mechanics correctly.

The column was approximated by a cylinder geometry using frictional walls. The filter frits of the micro column were considered as ideal flow distributors so that a con-

stant fluid flow velocity was assumed at the inlet of the column. The column packing was represented by discrete particles with the experimentally determined particle size distribution of resin SEP (see Figure 6.1). The dynamic behavior of the packing itself is governed by the individual particle interactions, which required the identification and definition of a proper particle contact model. Compression of single particles revealed a pronounced simultaneous force relaxation during compression which resulted in a rather linear than power-law force-displacement relation within a broad range of compression velocities and compression levels. This behavior was similar to a Hookean particle interaction behavior. Comparison of the normal force calculations using the linear Hooke and the nonlinear Hertz particle contact model with experimental data showed a better agreement for the Hooke model which then was used as the particle contact model.

However, only a few parameters required by the Hooke contact model could be determined experimentally (Young's modulus E , Poisson's ratio ν , coefficient of restitution e and particle density ρ). Others, such as the friction coefficients μ , were difficult to determine by experiments. The parameters characteristic impact velocity V and critical Stokes number St_{crit} result from the derivation of the Hooke model but physical meaningful values cannot be defined within an inhomogeneous dense particle packing. According to the derivation of the Hooke particle contact model, the characteristic impact velocity is defined as the initial relative velocity of two colliding spheres from which the maximum particle overlap can be calculated (see Section 3.1.1 for details, i.e. Equation (3.16)) assuming that further particle properties (mass, Young's modulus, and radius) are known.

The critical Stokes number is a model parameter that accounts for viscous effects of the surrounding fluid during impacting particles. This parameter was studied by freely moving and impacting bubbles [Legendre et al. 2005] and realistic values can only hardly be translated to dense particle systems in which particle movement and collision is influenced by rather the particle network than the fluid viscosity. However, appropriate values of these parameters were determined in detailed parameter sensitivity studies so that the simulation results matched the measured column behavior with sufficient accuracy.

During the sensitivity studies, a correlation of the particle Young's modulus with the characteristic impact velocity was identified, which had an influence on the packing stiffness. Fitting of the measured particle force-displacement data to the linear Hooke model resulted in a Young's modulus of 30 MPa (Figure 8.1) for the assumed maximum

limit of the characteristic impact velocity of 0.1 m s^{-1} . It needs to be said that the Hooke particle contact model is a vast simplification of the measured force displacement behavior of the chromatographic particles. A more detailed model which considers the force relaxation behavior of the particles due to poroelastic and viscoelastic mechanisms was not yet available within the DEM framework. As a consequence, the linear model required a value of the particle Young's modulus which is in between the limits of the instantaneous particle modulus (67 MPa) as an upper bond and the relaxed particle modulus (4 MPa) as a lower bond (see Table 6.6). Furthermore, the model would fail in calculating the correct force relaxation at different compression velocities, i.e. variation of the acceleration of fluid flow. However, as chromatographic columns are mostly operated at standard protocols, the temporal change of the fluid velocity, i.e. during start and shut-down of chromatographic operation, can be considered as constant ($du/dt = \text{const.}$). Future work should be dedicated to the implementation of more detailed particle interaction models such as the Standard Linear Solid or the Prony series model.

Besides the determination of the model parameter values, methods were identified which significantly reduce the computational effort without reducing accuracy. By using the *coarse-grain* approach the number of particles was reduced by a factor of 27 which led to a significant reduction of calculation time by a factor of 17 from $\text{CG} = 1$ to $\text{CG} = 3$. A further speed-up of simulation time was achieved by reducing the simulation domain from a three-dimensional cylindrical column to a pseudo two-dimensional domain representing a slice of the column with finite thickness. Herewith, the number of particles was reduced by a factor of 12.2 which resulted in a 6.5 fold decrease in calculation time using less than half of the number of CPU cores required for the 3D simulation case. Evaluation of these model simplifications revealed equal results and accuracy in terms of packing pressure drop and packing compression characteristics compared with the 3D simulation case without coarse graining.

The final simplified model was able to reproduce the measured hydrodynamic column packing behavior in terms of packing pressure drop and packing compression with great accuracy. As the modeled packed bed behavior results from the single particle mechanics, which were explicitly considered in this modeling approach, local packed bed properties such as the porosity distribution were described correctly. This is i.e. true during simulation of the dynamic packing behavior by either hydrodynamic or mechanical load which is a great advantage over previously reported continuum model approaches.

9. Analysis of Particle Migration During Column Operation

During cyclic application of packing compression and relaxation, e.g. due to high- and low-flow cycles, migration and rearrangement of particles was observed by microscopic imaging (see Figures 7.4 and 7.5). The migration of smaller particles through the void between larger particles may lead to internal erosion, pore clogging and to the formation of flow channels within the bulk of the medium. In this chapter, the results of a systematic particle migration study are discussed which give information about particle migration and rearrangement in chromatographic packings during cyclic operation.

9.1. Experimental Particle Migration Study

The influence of the column diameter as well as the influence of the particle size distribution on the migration of particles within a compressible chromatographic packing was investigated in different laboratory experiments. The experimental methods are described in detail in Section 5.4.4. The results shown here were obtained with TOY particles SP-650 and Butyl-650 of different particle sizes.

9.1.1. Influence of The Column Diameter

Figures 9.1 and 9.2 show the migration of colored SP-650M tracer particles in the 9.6 mm and 12.5 mm i.d columns during an operation of 450 high-flow/low-flow cycles at flow velocities of 1630 cm h^{-1} and 81.5 cm h^{-1} , respectively. Both, tracer particles and packing particles were SP-650M of the same size. The tracer particles were given on top of the sedimented packed bed of unlabeled particles.

As can be seen, a small portion of colored tracer particles migrated from the column top towards the bottom during the compression-relaxation cycles applied. Interestingly,

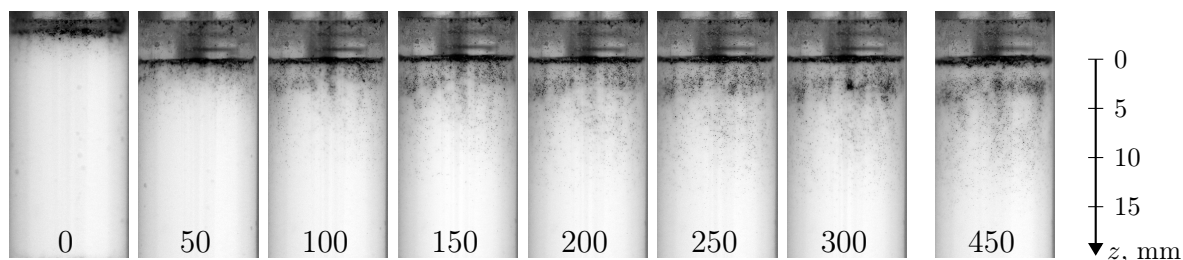


Figure 9.1.: Migration of Toyopearl SP-650M tracer particles in the 9.6 mm i.d. column during cyclic column operation. The bulk packing was built by sedimentation of SP-650M particles. Each photograph was taken after 50 compression-relaxation cycles as indicated by the numbers. The last photograph was taken after the 450th cycle. Labeled tracer particles which were given on the top of the packing migrated over a distance of 3-4 mm in the column wall region.

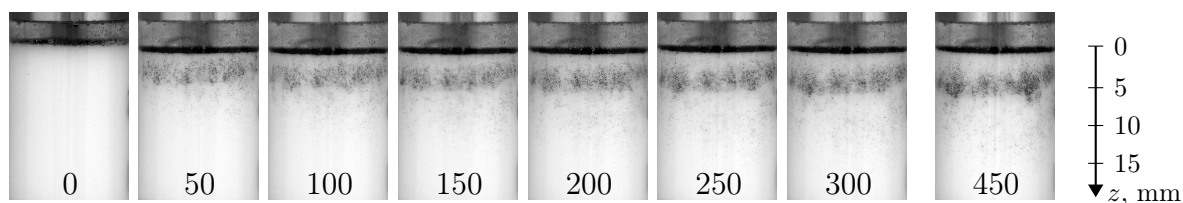


Figure 9.2.: Migration of Toyopearl SP-650M tracer particles in the 12.5 mm i.d. column during cyclic column operation. The bulk packing was built by sedimentation of SP-650M particles. Each photograph was taken after 50 compression-relaxation cycles as indicated by the numbers. The last photograph was taken after the 450th cycle. Labeled tracer particles which were given on the top of the packing migrated over a distance of 5-7 mm in the column wall region.

a small band of tracer particles was formed in the upper quarter of the packing after the 250th cycle. The tracer particles stopped migrating over a distance of 3-4 mm and accumulated at this position at the column margin. Only a few, presumably smaller, particles migrated over a larger distance than this characteristic distance.

A similar observation was made in the 12.5 mm i.d. column (see Figure 9.2). The tracer particles migrated noticeably over a distance of 5-7 mm in the column wall region and accumulated at this distance. Compared to the smaller column, the migration distance is a little larger in the 12.5 mm i.d. column.

Figure 9.3 shows a half-cut of the quick-frozen packing after the 450th cycle of both packings. Apparently, particle migration occurred only at the column wall region. The half-cut packing showed no noticeable migration of tracer particles in the inner packing regions.

Operating the columns of 9.6 mm, 12.5 mm, and 16.25 mm i.d. at a lower flow velocity

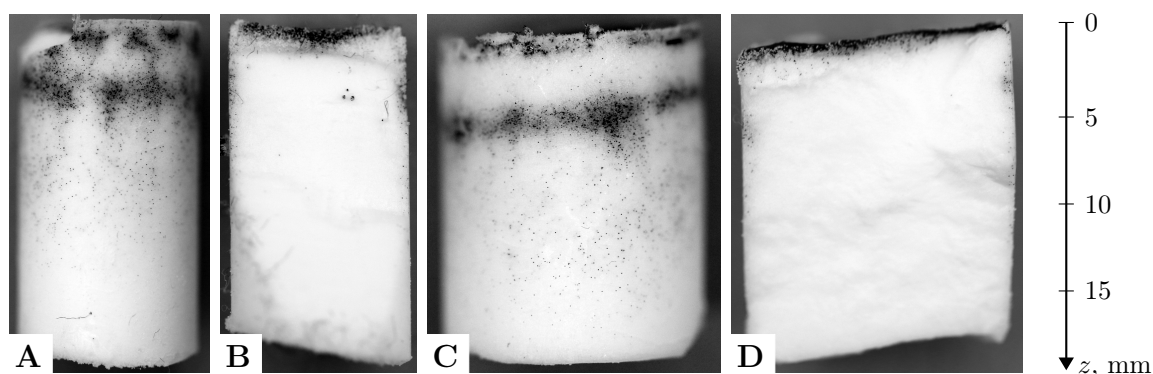


Figure 9.3.: Particle migration in the inner packing regions using Toyoparl SP 650M resin. The photographs show the frozen packing after the 450th operation cycle which was cut into halves. (A) Column wall region and (B) inner packing region of the 9.6 mm i.d. column. (C) Column wall region and (D) inner packing region of the 12.5 mm i.d. column.

of 964 cm h⁻¹ resulted in very little particle migration at the column wall region. In the inner packing region, also no particle migration was noticed (results not shown).

As a conclusion, a little increased particle migration was observed in the larger column. As all repeated experiments showed the same trend, it is assumed that this behavior is caused by the increased compression-relaxation dynamics of the larger column due to decreased influence of the wall effect.

9.1.2. Influence of The Particle Size

Packing of 100 μm Particles

Figure 9.4 shows the migration of the Butyl-650C tracer particles that were sedimented on top of the packed bed during 450 high-flow/low-flow cycles. Here, the tracer particles had the same size as the bulk packing particles, which was 100 μm . The 12.5 mm i.d. column was used. Similar to the smaller SP-650M particles, a band of tracer particles migrated noticeably in the column wall region toward the column outlet. Here again, the particles stopped migrating at a distance of about 5-7 mm from the packing top.

Compared to the SP-650M particle packing, the migration band was more pronounced and showed a waved shape. This might be due to the broader particle size distribution of the Butyl-650C particles, which allows smaller particles to migrate more easily and over a wider distance. Furthermore, the band of migrating particles was much denser than in Figure 9.2 which means that the number of migrating particles was higher. This

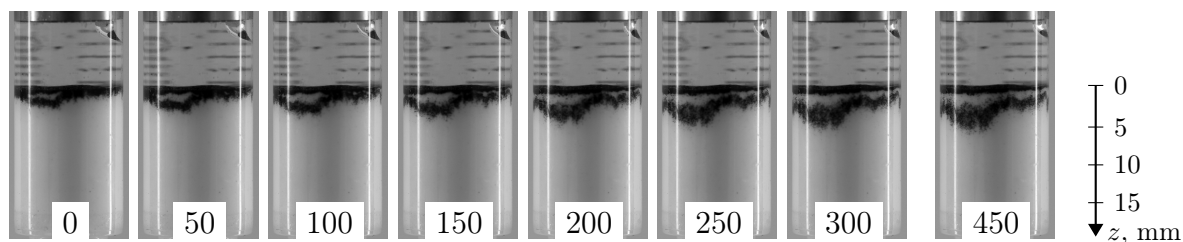


Figure 9.4.: Migration of Toyopearl Butyl-650C tracer particles in the 12.5 mm i.d. column during cyclic column operation. The bulk packing was built by sedimentation of Butyl-650C particles. Each photograph was taken after 50 compression-relaxation cycles as indicated by the numbers. The last photograph was taken after the 450th cycle.

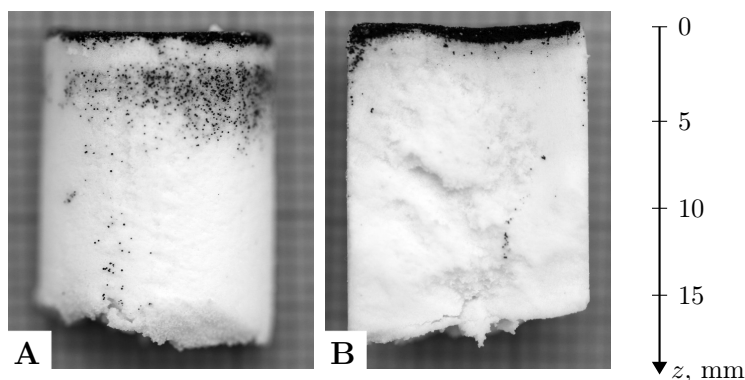


Figure 9.5.: Particle migration in the inner packing regions using Butyl-650C resin. The photographs show the frozen packing after the 450th operation cycle which was cut into halves. (A) view of the column wall region and (B) view of the inner packing region.

effect was observed at all repeated experiments. It is assumed that the hydrophobic surface of the particles has a significant impact on particle migration, i.e. at the column wall region. Hydrophobicity might promote the separation of the packing particles from the column wall during packing compression-relaxation, so that smaller particles were pushed by the flow into the resulting crack.

In contrast to the near-wall packing region, no particle migration was noticed in the inner packing regions, as shown in Figure 9.5. The few tracer particles that are visible in the cutting plane in Figure 9.5 B were brought there during the cutting action.

Packing of 100 μm Particles Mixed With 35 μm Tracer Particles

Figures 9.6 and 9.7 show the migration of smaller tracer particles in the 9.6 mm and 12.5 mm i.d. column. This measurements were carried out using 100 μm Butyl-650C

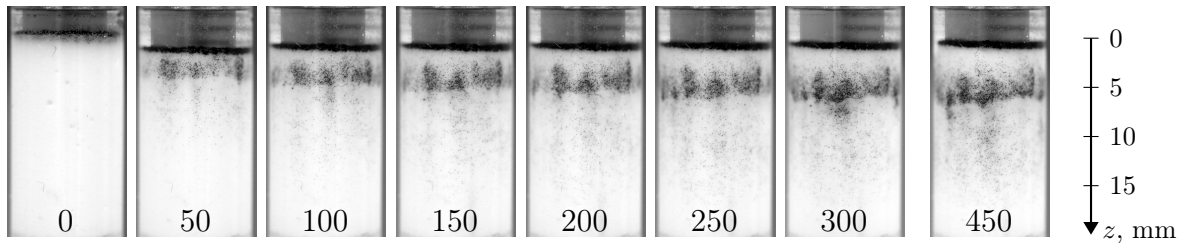


Figure 9.6.: Migration of Toyopearl Butyl-650S tracer particles in the 9.6 mm i.d. column during cyclic column operation. The bulk packing was build by sedimentation of Butyl-650C particles. Each photograph was taken after 50 compression-relaxation cycles as indicated by the numbers. The last photograph was taken after the 450th cycle.

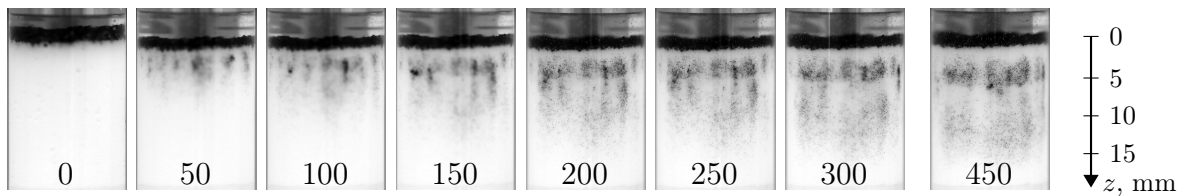


Figure 9.7.: Migration of Toyopearl Butyl-650S tracer particles in the 12.5 mm i.d. column during cyclic column operation. The bulk packing was build by sedimentation of Butyl-650C particles. Each photograph was taken after 50 compression-relaxation cycles as indicated by the numbers. The last photograph was taken after the 450th cycle.

particles for the bulk packing and 35 μm Butyl-650S particles as tracer particles.

Both packings of different diameter showed particles migrating over a distance of 4-6 mm from the packing top. Additionally, it was observed that some tracer particles migrated nearly from the packing top to the bottom. This is different to the behavior observed using a packing of nearly equal particle sizes (see Figures 9.1 and 9.4) and can be attributed to the smaller size of the tracer particles.

As a conclusion, it is assumed that the characteristic migration distance is correlated to the packing density and packing compression-relaxation dynamics, i.e. the movement and velocity of the particles, which is known as the *granular temperature* [e.g. Trujillo and Herrmann 2003; Biggs et al. 2008]. This means that presumably in a distance of 4-6 mm from the packing top the packing density is considerably higher than in regions above that distance. Furthermore, the rate of packing compression-relaxation gets slower with increasing distance from the packing top. This is due to the wall support which increases towards the column outlet and acts against the packing movement, as indicated by the hysteretic behavior of the different packing regions (see section 7.1 for detailed

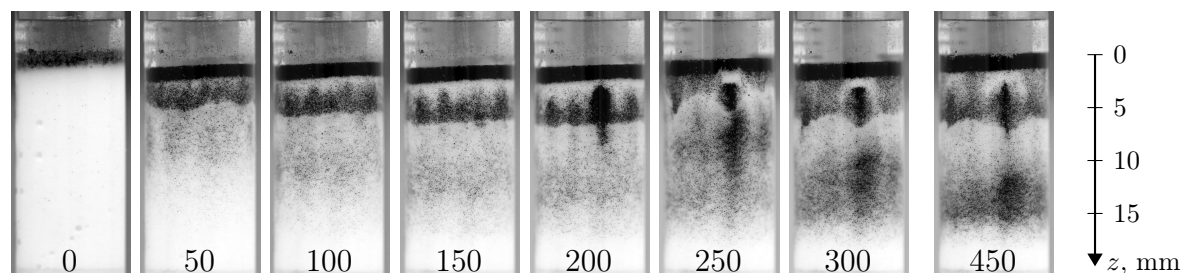


Figure 9.8.: Effect of the flow velocity on the migration of small Toyopearl Butyl-650S tracer particles in the 9.6 mm i.d. column. The flow velocity during the high flow cycle was set to 2763 cm h^{-1} . Each photograph was taken after 50 compression-relaxation cycles as indicated by the numbers. The last photograph was taken after the 450th cycle.

discussion). Consequently, the rate and magnitude of opening and closing interparticle voids which is directly related to the granular temperature, is retarded. Hence, only smaller particles were able to migrate over larger distances.

By increasing the flow velocity of the high-flow cycle but keeping the cycle times constant increases the dynamic compression-relaxation behavior of the packing. This results in a higher and faster packing compression and relaxation. Consequently, the rate and magnitude of opening and closing interparticle voids is affected. Figure 9.8 shows the 9.6 mm i.d. column being operated at high-flow cycles of 2763 cm h^{-1} .

As can be seen, considerably more tracer particles migrated at the column wall region towards the column outlet. Here again, a tracer band profile can be identified in the characteristic migration distance of 4-6 mm. However, a large part of the tracer particles passed this distance with increasing number of compression-relaxation cycles, but stopped by forming a second band profile at a migration distance of 14-16 mm. As a consequence of this experiment, it can be stated that the higher the packing oscillation during compression-relaxation the higher the degree of particle migration. Here again, no particle migration in the inner packing region was observed (results not shown). Particle migration occurred only in the packing wall region.

In another experiment the tracer was distributed homogeneously as shown in Figure 9.9 (A). The packing was compressed mechanically by 10% by lowering the plunger. The initial distribution of tracer particles within the packing was analyzed by quick-freezing the the packed column without any fluid flow application and cutting it into halves. The inner distribution of the tracer particles was similar to the visible outer distribution as shown in Figure 9.9 A. During operation by 450 high-flow/low-flow cycles no particle

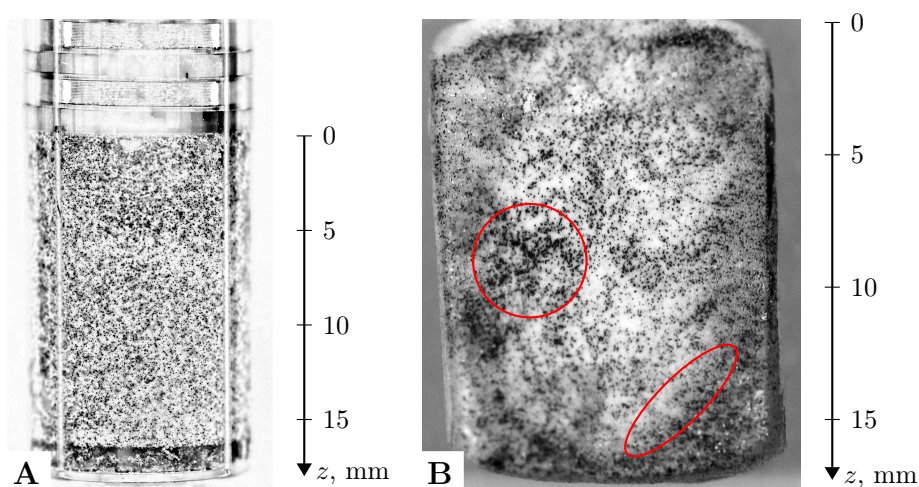


Figure 9.9.: Homogeneous distribution of Butyl-650S tracer particles in the Butyl-650C packing. Prior to operation the packing was compressed by 10% resulting in a packing height of 18 mm. (A) shows the side view of the column before column operation and (B) a cut of the frozen packing after 450 compression/relaxation cycles.

migration was noticed in the column wall region. However, in the inner packing region clustering of tracer particles was noticed as indicated in Figure 9.9 B. However, as the distribution of tracer particles of this particular packed bed cannot be measured by the quick-freezing method prior to column operation, it can only be assumed that the clustering of particles was the result of cyclic column operation.

9.2. Computational Particle Migration Study

The computational particle migration study was carried out in the pseudo two-dimensional simulation domain with the dimensions given in Table 5.2. The bed height was set to 30 mm and contained 5000 particles of bidisperse or polydisperse particle size distribution. The columns were operated by 30-150 simulated high-flow/low-flow cycles, each lasting 1.5 s. The fluid flow velocity of the high-flow cycle was set to 2763 cm h^{-1} and the low-flow cycles was operated at 81.5 cm h^{-1} .

9.2.1. Bidisperse Particle Size Distribution

Figure 9.10 shows the simulation of a bidisperse particle packing of small ($75 \mu\text{m}$) and large particles ($210 \mu\text{m}$) in a ratio of 3/2 (number/number). The smaller tracer particles

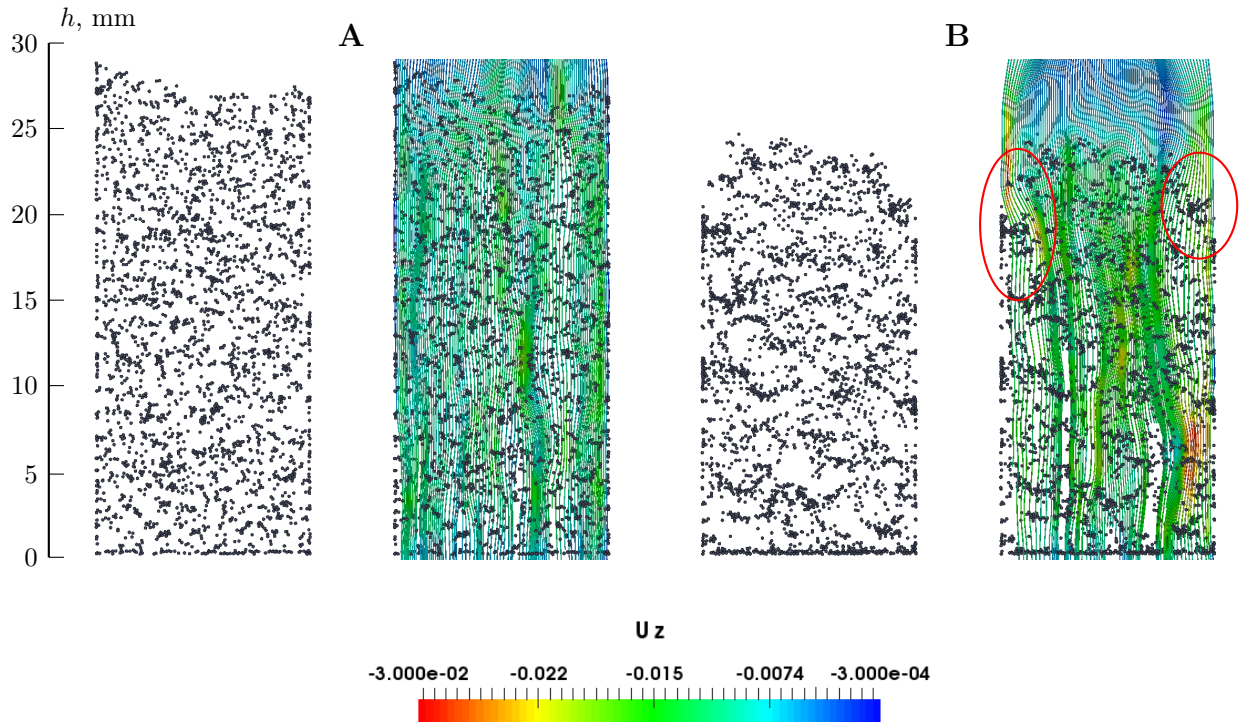


Figure 9.10.: Simulated particle rearrangement and migration in a packing with a bidisperse particle size distribution. Only the smaller particles are shown. (A) Packing structure and distribution of the smaller particles as well as the fluid flow distribution during the first high-flow cycle. (B) Packing structure and distribution of the smaller particles as well as the fluid flow distribution during the 30th high-flow cycle.

were homogeneously distributed within the packing prior to cyclic operation. During the 1st cycle (Figure 9.10 A) the small tracer particles were still homogeneously distributed which led to a homogeneous flow velocity distribution as it can be seen by the colored stream lines. After the 30th high-flow cycle (Figure 9.10 B), it was observed that the smaller particles migrated and formed particle clusters. These clusters did not migrate further through the packing but increased in size with ongoing column operation. It is assumed that the formation of clusters of smaller particles was initiated by local pore clogging, which then led to a steady accumulation of smaller particles at this position. Within these clusters, the packing porosity was noticeably lower than in locations of larger particles which led to a reduction of the local hydraulic conductivity and to the development of erosional channels. As can be seen, the formation of small particle clusters had a serious effect on the local flow velocity distribution. The stream lines indicated that the flow bypassed these high packing density regions forming flow channels.

9.2.2. Polydisperse Particle Size Distribution

In another simulation, a realistic particle size distribution (based on the Sepharose particle size distribution, see Figure 6.1) was considered. The particle migration was significantly lower so that the column was operated by 150 high-flow/low-flow cycles to measure a certain degree of particle migration.

Figure 9.11 shows the migration of the smallest particles from the 1st to the 150th operation cycle. The initially homogeneously distributed smaller particles (Figure 9.11 A) migrated along the pathways as shown in Figure 9.11 B during the 150 column operation cycles. As can be seen, particle migration was high in the column wall region. The tracked particles migrated towards the column outlet but also into the inner packing region. This indicates that the compression-relaxation dynamics of the packing and its

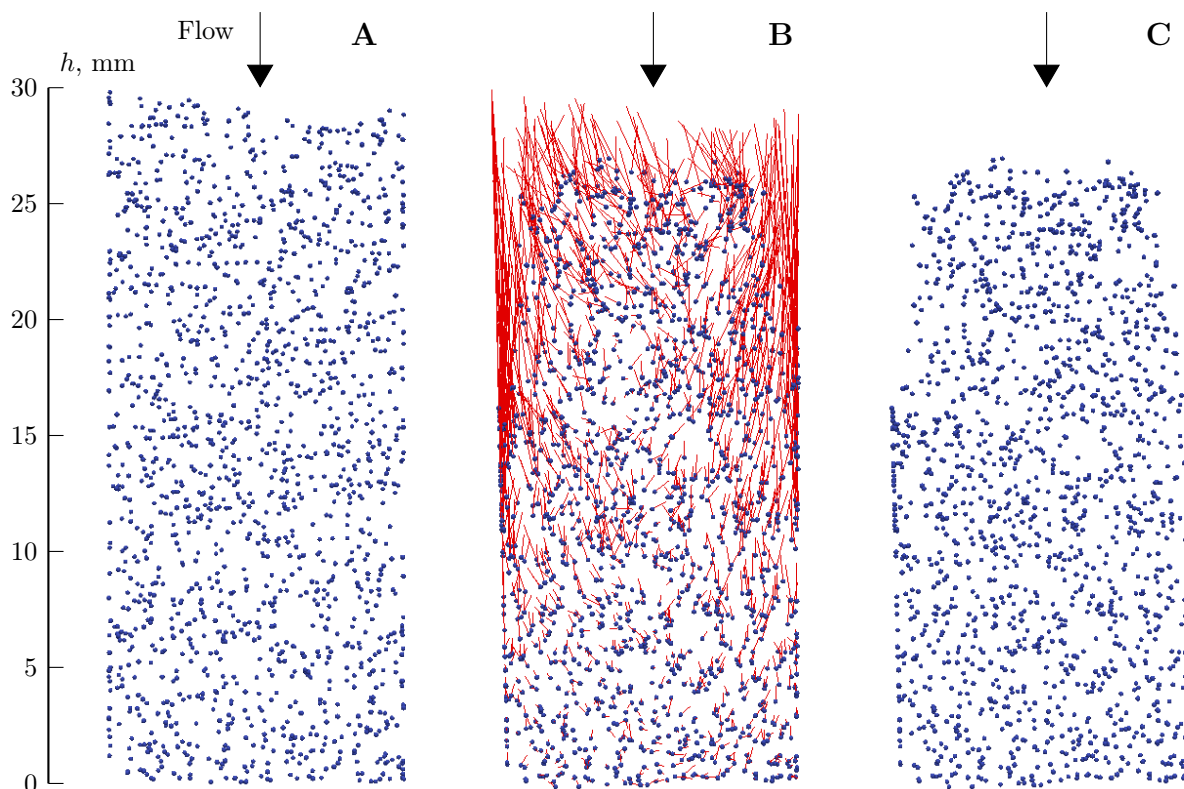


Figure 9.11.: Simulated particle migration in a packing of a polydisperse particle size distribution. Only the smallest particles are shown. (A) Packing structure and homogeneous distribution of the smallest particles during the first high-flow cycle. (B) Migration pathways of the smallest particles during 150 operation cycles. (C) Packing structure and distribution of the smallest particles during the 150th high-flow cycle.

granular temperature is more pronounced in the upper column wall region. This led to increased opening and closing of interparticle void space through which the particles can migrate. In contrast, the region near the column outlet showed less change in the packing structure. The tracked particles nearly kept its initial position or migrated only over a very small distance. The reduced granular temperature of the particles from the top to the bottom of the packing is correlated with a reduced column wall support. A stabilizing effect of the wall support, acting against the packing movement and particle rearrangement, can only be expected if a certain degree of axial packing compression is present (see Equation (3.75), in which the wall support term depends on the axial

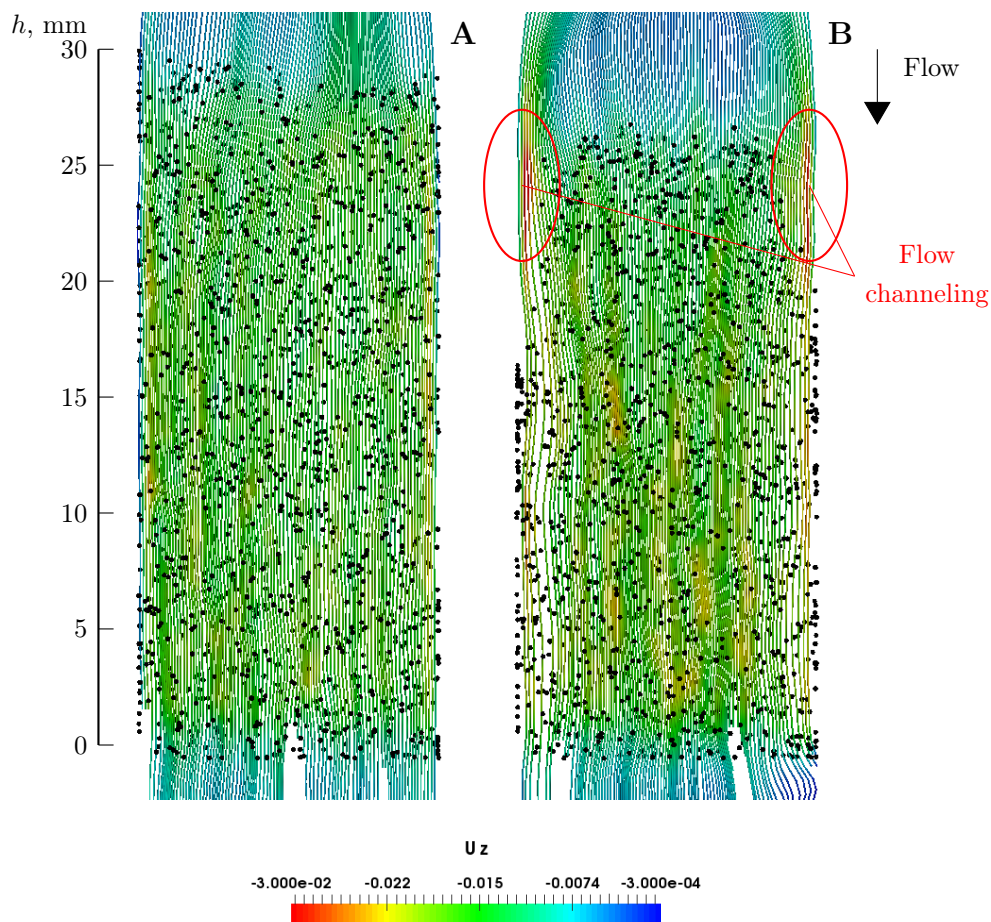


Figure 9.12.: Simulated influence of particle migration on the fluid flow distribution. Only the smallest particles are shown. (A) Homogeneous packing structure and fluid flow distribution during the first high-flow cycle. (B) Inhomogeneous packing structure leading to flow channeling during the 150th high-flow cycle.

packing stress σ).

In the upper packing region, the migration of smaller particles led to a radial particle size distribution profile, leading to an accumulation of larger particles in the column wall region. As a consequence, the interparticle porosity increased locally.

Figure 9.12 shows the effect of the changing particle size distribution profile on the fluid flow behavior. In Figure 9.12 A, a homogeneous flow velocity profile can be seen as a consequence of the initially homogeneous packing structure. The local increase in packing porosity in the column wall region led to higher flow velocities and a channeling of the stream lines in this region as indicated in Figure 9.12 B.

9.3. Conclusion

The migration and rearrangement of particles during column operation by high-flow/low-flow cycles was investigated in laboratory experiments and in-silico. The influence of the column wall support on particle migration was evaluated experimentally by varying the column diameter only and keeping the experimental conditions constant. The experimental results showed no noticeable particle migration at high-flow velocities below 1630 cm h^{-1} independent of the column diameter. At flow velocities of 1630 cm h^{-1} or higher, particle migration was observed in the two columns analyzed, which had a diameter of 9.6 mm and 12.5 mm. Additionally, the migration distance in the 12.5 mm column was a little larger. Two conclusions were drawn from these experiments: i) Particle migration requires cyclic application of a certain hydrodynamic load, i.e. certain magnitude of compression and relaxation of the packing. The higher the packing compression and subsequent relaxation, the higher the possibility of opening and closing of interparticle voids, through which smaller particles can migrate. ii) An increase of column diameter, i.e. the column aspect ratio, led to an increase of particle migration. With increasing column aspect ratio, the wall support decreases which also results in an enforced compression-relaxation behavior of the packing.

By varying the size of the tracer particles, the influence of the particle size distribution was evaluated. In the first experiment, tracer particles of the same size as the packed bed particles were used so that particle migration in a monodisperse - as best it can be - packing was analyzed. In a second experiment, the tracer particles were only of $1/3$ of the size of the packed bed particles. Hence, particle migration in a bidisperse -

as best it can be - packing was investigated. The results showed a significantly larger particle migration of the smaller tracer particles. Nevertheless, independent of size of the tracer particles, an accumulation or clustering of tracer particles at a distance of 4-7 mm from the packing top was observed in all experiments in the column wall region. The formation of clusters of particles of the same size is described as a typical effect of sedimentation in soft granular systems [Kohl and Schmiedeberg 2014].

Based on these findings it is suggested that the distance of particle migration is limited and depends on the size of the particles as well as on the local packing density. The packing density increases with increasing packing compression from the top to the bottom of the packing (see Figure 7.3) during hydrodynamic load. Consequently, at a certain height of the packing, the interparticle pores are smaller than the migrating particle which leads to a clogging of that pore. Other migrating particles then accumulate in this particular region. A similar observation of cluster formation was made by homogeneously distributing the smaller tracer particles within the packing (see Figure 9.9). However, none of the experiments carried out showed any particle migration from the packing top into the packing core region. Most of the particle migration was observed at the column wall region.

Computational simulation of an ideal bidisperse packing in which the tracer particles had 1/3 of the size of the packed bed particles showed the same behavior of clustering and tracer particle accumulation. As the packing density of those clusters was higher than in the bulk packing, the fluid flow bypassed these regions and flow channels were formed. The simulation of particle migration in a packed bed of polydisperse particle size distribution revealed that particles migrated from the column wall region towards the column outlet as well as into the packing core region leading to a pronounced radial particle size distribution profile in the upper packing region. The higher porosity at the wall region then led to an increase in fluid flow velocity and a formation of flow channels in that region. Based on this finding the formation of bypass flows observed in industrial application may be explained.

However, this behavior is different to the laboratory experiment of homogeneously distributed tracer particles within the packing. In laboratory the packing was compressed by 10% by lowering the plunger and no particle migration was observed at the column wall region. This can be explained by an increased wall support due to the applied compression of the packing, which reduced the dynamic opening and closing of interparticle voids. Furthermore, it is assumed that in the laboratory experiment the fluid flow

distribution at the column inlet is not as ideal as in the simulated column.

From the findings of the particle migration study carried out in laboratory as well as in-silico the following can be stated: The migration of particles in a saturated, granular, and porous medium may lead to internal erosional effects, changes of the local porosity of the packing and formation of flow channels within the packed bed. However, the migration of particles can only take place if the packed bed exhibits a pronounced dynamic compression-relaxation behavior, i.e. a high granular temperature [Trujillo and Herrmann 2003; Biggs et al. 2008], resulting in substantial particle movement. In order to prevent particle migration, the column needs to be packed resulting in a reduction of packing oscillation and consequently in a decrease of interparticle void space.

10. Analysis of Different Column Packing Strategies ³

It is well known that packing non-uniformity and inhomogeneity may cause peak asymmetry and limit the performance of packed-bed chromatographic columns. However, understanding of the reasons leading to packing non-uniformity is still limited. The following chapter is dedicated to the systematic analysis of common column packing methods of compressible resins with focus on the hydrodynamic packing heterogeneity, packing asymmetry and hydrodynamic packing long-term stability. The experimental methods, evaluation criteria, terms and definitions are described in Section 5.4.5.

10.1. Influence of Friction Forces on the Column Packing Process

The influence of particle friction on the packed bed compression behavior during the dynamic axial compression (DAC) packing method was already discussed in Section 7.2 using packings of wet and semi-dry Sepharose (SEP) particles. This influence was further analyzed regarding compression force transmission by performing a numerical study of packed bed compression. A pseudo two-dimensional packing of 2200 discrete particles with the experimentally acquired particle size distribution of SEP particles was compressed in-silico by nearly 20% by DAC (compression force $F_{mech} = 0.48$ N) as well as by flow packing with a high flow rate ($u_0 = 2763$ cm h⁻¹). The size of the simulation domain was 10 mm, 0.4 mm and 10 mm in x-, y- and z-direction limited by periodic boundaries in y-direction and frictional walls in x- and z-direction.

³Selected results presented in this chapter were published in: Dorn M, Eschbach F, Hekmat D, Weuster-Botz D (2017): Influence of different packing methods on the hydrodynamic stability of chromatography columns. *J Chromatogr A* **1516**: 89-101.

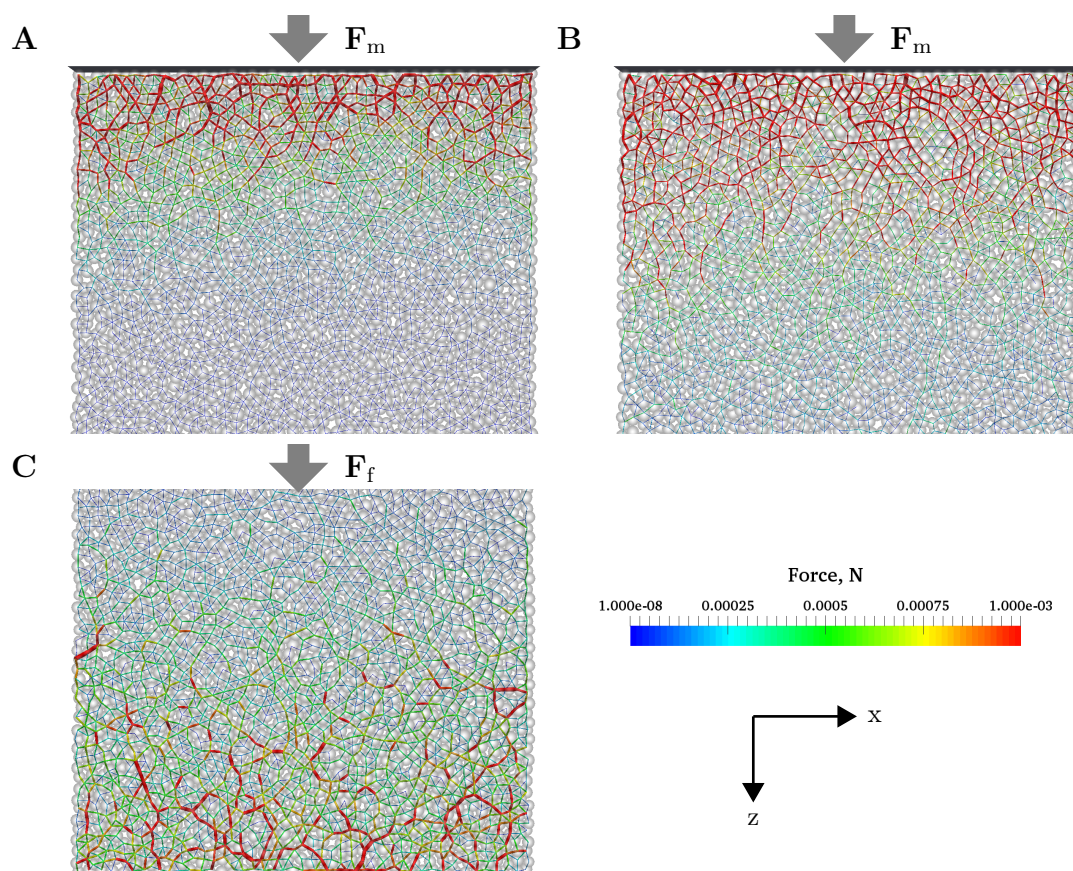


Figure 10.1.: Simulation of the force transmission in a frictional particle packed bed. The force chain network is colored and scaled according to the magnitude of compression force. Mechanical compression of (A) wet packing with low friction, $\mu = 0.1$, (B) semi-dry packing with increased friction, $\mu = 0.5$ and (C) flow compression of packing, $\mu = 0.1$. F_m and F_f indicate the mechanical compression force and fluid drag force.

Figure 10.1 shows the interparticle connection forces in a packing during DAC of (A) particles with a low friction coefficient of $\mu = 0.1$ (e.g. a wet packing), (B) particles with a high friction coefficient of $\mu = 0.5$ (e.g. a semi-dry packing) and (C) and during flow packing ($\mu = 0.1$). Particle-wall friction was set to 0.5 in all cases. Further particle properties were set to the values given in the methods section. The interparticle connection forces form a force chain network which is scaled and colored according to the magnitude of compression pressure of the individual particles. During the DAC method (Figure 10.1 A, B), high particle compression forces are located in the upper packing region close to the plunger which is represented by the plate in Figures 10.1 A and B. It can be noticed that the particle compression pressure decayed with increasing distance

from the plunger.

Moreover, it can be seen by comparing Figures 10.1 A and B that the axial force transmission is influenced by the friction between the particles as well as between the particles and the column wall. In the packing with lower friction (Figure 10.1 A), the compression force decayed over a shorter span of particles compared to the packing with higher friction (Figure 10.1 B) which is in agreement with the measured packing compression profiles of the wet and semi-dry packed columns shown in Figures 7.6 and 7.7. Furthermore, shorter and more horizontally oriented force chains can be identified in the system with lower friction. This observation indicates that the forces were transmitted increasingly in radial direction (along the x-direction). In contrast to this, longer force chains are visible in the system with higher friction due to stronger axial force transmission (along the z-direction).

On the basis of these findings, the difference in compression behavior of the wet material and the semi-dry material can be explained. During the packing compression of the wet DAC packing, the interparticle fluid may act as a lubricant decreasing friction. Hence, the particles can slide more easily against each other promoting particle rearrangement. As a consequence, the axial compression force is distributed more evenly in radial direction among the individual particles and finally dissipated to the column wall. The packing compression behavior of the semi-dry packing is governed by higher friction between the particles which prevented them from sliding against each other. This resulted in an increased force transmission in axial direction.

Flow packing, in contrast, led to packing compression behavior which differed noticeably from the mechanical packing compression method. High particle compression pressures are located in the lower packing sections close to the column outlet as it can be seen in Figure 10.1 C. Moreover, the force distribution is much more heterogeneous in axial as well as in radial direction. Fewer force chains transmitting high forces can be identified. Compared to the DAC packing method, wall support is clearly less present during flow compression. Here, the force chains did not show any significant contact to the column wall. During DAC, the force chains are noticeably connected to the outer particle layer closest to the column wall which indicates a strong influence of the wall effect. As pointed out by Shalliker et al. [2002], friction prevents the particles from being homogeneously packed but at the same time, friction is required to stabilize and keep the packed bed in place. As the packing compression behavior depends on the small-scale particle dynamics, the packed bed behavior can be influenced by the way the column is

packed. Particle sliding and rearrangement as well as the wall effect can be intensified or reduced by the application of different column packing strategies for the purpose of increased hydrodynamic packing stability.

10.1.1. Comparison of Different Column Packing Methods at Different Hydrodynamic Loads

Based on the findings of the analysis of packed bed properties during dynamic axial compression and flow compression, columns packed by different methods were operated at different hydrodynamic loads and analyzed experimentally regarding hydrodynamic packing stability and axial packing homogeneity. Therein, the relative hydrodynamic load of $RHL = 1$ is defined to be equal to the flow rate applied during the flow packing method in order to achieve the desired packing compression (1.6 L h^{-1}). Figure 10.2 shows the axial packing density profiles of the laboratory column packed according to five different packing strategies. On the upper left, a schematic drawing of the laboratory column is given which was divided into seven equally sized sections (see Figure 5.1). By measuring the individual height of each section during the column packing process, the packing density in each section was calculated according to Equation (3.74). The gravity settled packed bed porosity was not experimentally accessible. Therefore, a value of 0.38 was assumed according to literature data [e.g. Stanley et al. 1996; DePhillips and Lenhoff 2000; Cherrak et al. 2002; Bowes et al. 2009].

Table 10.1 shows the deviations S_{mean} and S_{init} (see Section 5.4.5 for details) as measures of the inhomogeneity of the axial packing density profile and of the variation of the packing density profile during the reference hydrodynamic load of $RHL = 0.75$, respectively.

The initial packing profiles given in Figure 10.2 refer to the axial packing density profiles right after the column packing procedure was completed. Figure 10.2 A shows the axial packing density profiles after DAC packing. After overnight storage, no remarkable change in the packing density profile was observed, only the uppermost section relaxed. However, the profile changed significantly during increasing hydrodynamic load. The packing density in section 1 was decreased and the lower packing sections were considerably compressed. As can be seen in Table 10.1, this resulted in the largest deviation from the initial profile of $S_{init} = 0.07$.

Figure 10.2 B shows the results of a column packed by flow packing. During the

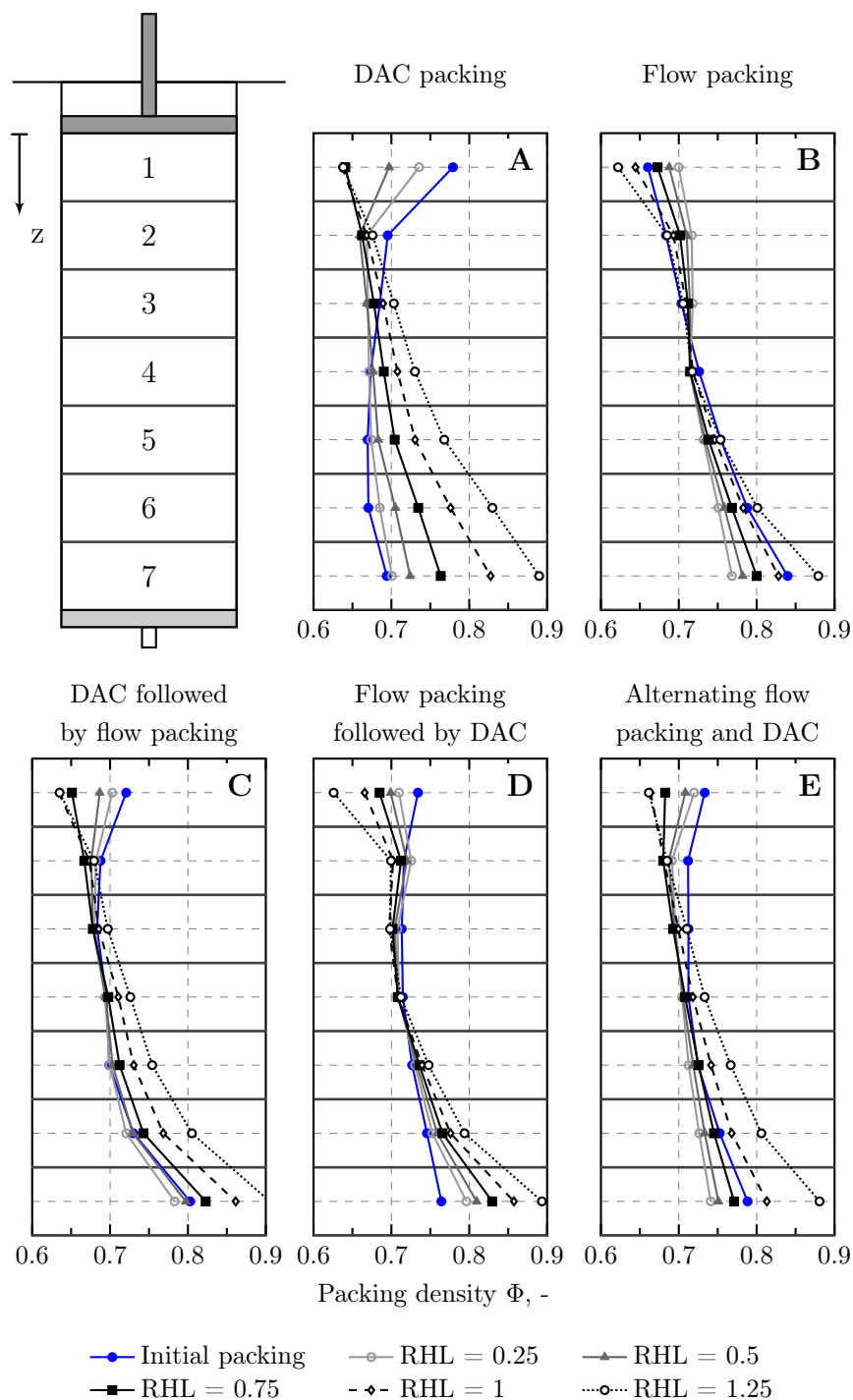


Figure 10.2.: Measured variations of the axial packing density profiles of the laboratory column during different hydrodynamic loads applied after packing. The column was packed according to five different column packing methods (A) DAC, (B) flow packing, (C) DAC (10% packing compression) followed by flow packing (10% packing compression), (D) flow packing (10% packing compression) followed by DAC (10% packing compression), (E) alternating 2.5% flow packing followed by 2.5% DAC performed 4 times. Packed columns were operated at different relative hydrodynamic loads (RHL).

Table 10.1.: Deviations S_{mean} and S_{init} of the different column packing methods during a relative hydrodynamic load of $RHL = 0.75$.

Deviation	S_{mean}	S_{init}
DAC	0.04	0.07
Flow packing	0.04	0.02
DAC and flow packing	0.06	0.03
Flow packing and DAC	0.05	0.03
Alternating flow packing and DAC	0.03	0.03

overnight storage, the packing density profile changed from the initial packing state (blue curve) to a force-equilibrated state where the packing density increased near the top of the column and decreased near the bottom of the column. It is assumed that the compression energy which was stored to a large extent in (visco)-elastic particle compression of the lower packing sections caused a compression of the upper packing sections during the overnight force equilibration time period. However, this equilibrated packing density profile changed with increasing hydrodynamic load. When the hydrodynamic load was increased, the packing density profiles reversed again leading to increased compression of the lower packing sections and to a relaxation of the upper packing section. Substantial changes in the packing density profile were observed when reaching the hydrodynamic load of the column packing procedure ($RHL = 1.0$) and even more when exceeding this load ($RHL = 1.25$).

The following packing strategies were combinations of the previously discussed flow packing and DAC. As a consequence, the hydrodynamic compression behavior of the columns packed by these methods is comparable to flow packed or DAC packed columns leading to a relaxation of the upper packing sections and to a compression of the lower packing sections. The column packed by DAC and subsequent flow compression (Figure 10.2 C) showed a minor deviation of the initial packing density profile up to hydrodynamic loads of $RHL = 0.75$ ($S_{init} = 0.03$). Hence, the hydrodynamic packing stability was increased by combining DAC and the flow packing method. When the applied hydrodynamic load was increased up to $RHL = 1.25$, a pronounced increase of packing density in the lowermost section was observed.

By switching the sequence of DAC and flow packing (Figure 10.2 D), a different hydrodynamic packing behavior was obtained. Compared to profiles shown in Figure

10.2 C, the packing was more homogeneous ($S_{mean} = 0.05$ instead of 0.06) whereas the average variation of the packing density profile during load was identical ($S_{init} = 0.03$).

The best hydrodynamic stability was achieved by an alternating repetition of flow packing and DAC as indicated in Figure 10.2 E. Up to relative hydrodynamic loads of $RHL = 0.75$, the packing showed a more homogeneous packing compression in axial direction ($S_{mean} = 0.03$) and the smallest variations in its axial packing density profile ($S_{init} = 0.02$) compared to the other packing strategies.

10.1.2. Measured Column Behavior During Long-Term Cyclic Operation

Three column packing methods, DAC, flow packing, and alternating flow packing and DAC were analyzed with regard to the long-term hydrodynamic stability of the packing. For this purpose, the packed columns were operated at 25 sequential simulated load/elution/equilibration cycles in which the packing was compressed and relaxed alternately. The axial packing density profiles were measured during each cycle (Figure 10.3). The variation of the packing density profile during operation is given in Figure 10.4 as the deviation from the initial packing density profile S_{init} .

Figure 10.3 A shows axial packing density profiles resulting from the DAC packing method which was packed with semi-dry particles. The initial packing profile was obtained by lowering the plunger with a rate of 30 mm min^{-1} leading to a packing compression of 20%. This caused an exponentially decreasing initial packing density profile from column top to bottom. During cyclic operation, the packing density decreased in the uppermost packing section and increased in the lower packing section right after the first cycle. No considerable variation of the axial packing density profiles was observed from the 15th cycle to the 25th cycle as depicted in Figure 10.4 by a nearly constant deviation from the initial packing density profile of $S_{init} \approx 0.043$. Hence, under the applied hydrodynamic load, the packing quickly reached a stable packing density profile during cyclic operation. Flow packing resulted in a pronounced initial axial packing density profile in which the lowermost section 7 was compressed as mentioned above. The packing top section was less compressed. During cyclic operation, the packing density profile varied noticeably as it can be seen from Figure 10.3 B and from Figure 10.4 by a steadily increasing deviation of the packing density profile from the initial packed state. The packing top section was compressed gradually and the packing bottom sec-

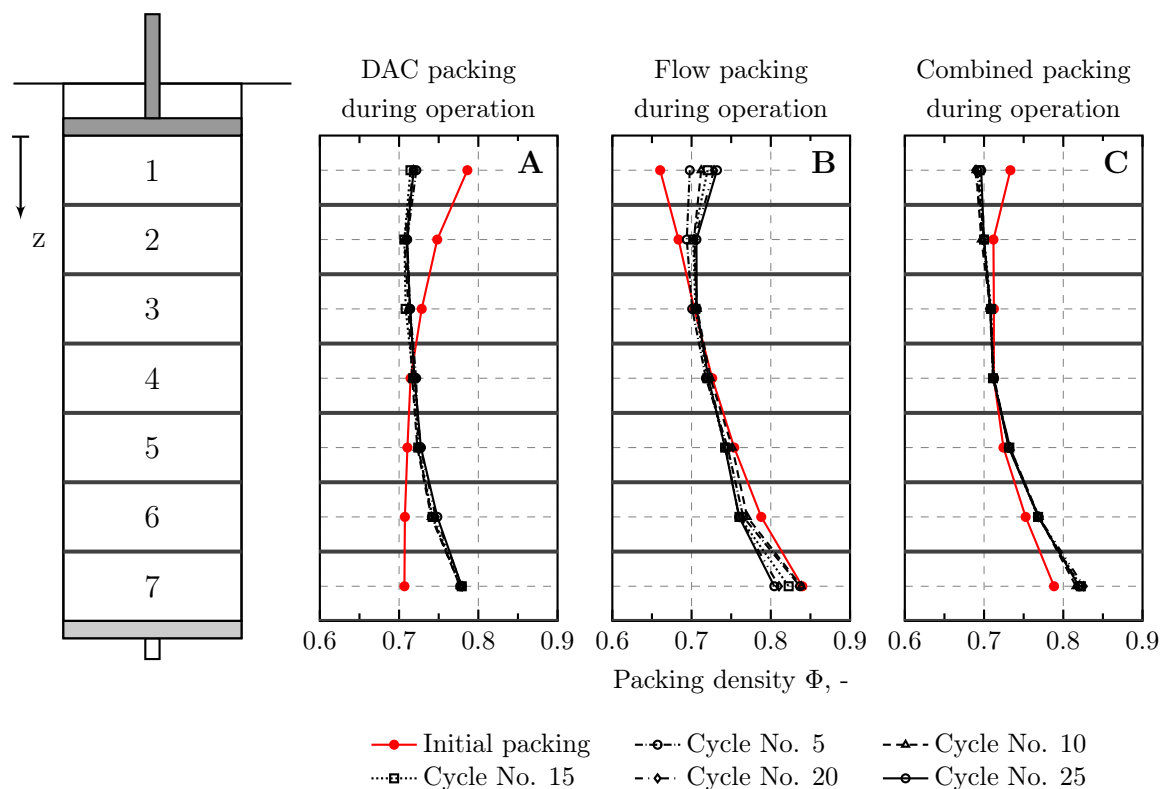


Figure 10.3.: Measured long-term axial packing density profiles of columns packed according to different methods. (A) DAC, (B) flow packing and (C) alternating flow packing and DAC. Standard deviations were less than 1 %

tion was relaxed gradually. It can be deduced that hydrodynamic stability was not achieved within the 25 operation cycles. This may be due to two reasons: i) flow packing led to a highly compressed packing bottom region, which, as a direct consequence of the interparticle as well as particle-wall friction effects, is difficult to relax; ii) the direction of fluid drag forces and packing relaxation was opposite. During flow packing, the major part of the compression energy was stored in the highly compressed lower packing sections. During cyclic operation, fluid drag pushed the particles downwards while the particles were pushed upwards during packing relaxation. This slowed the process of force equilibration of the column. In contrast to this, fluid drag forces and packing relaxation acted in the same direction during DAC packing leading to a faster force equilibration of the column. Alternating flow packing and DAC resulted in a similar hydrodynamic long-term stability as the straight DAC packing method as shown in Figure 10.3 C. Only very small changes of the packing density were measured in the

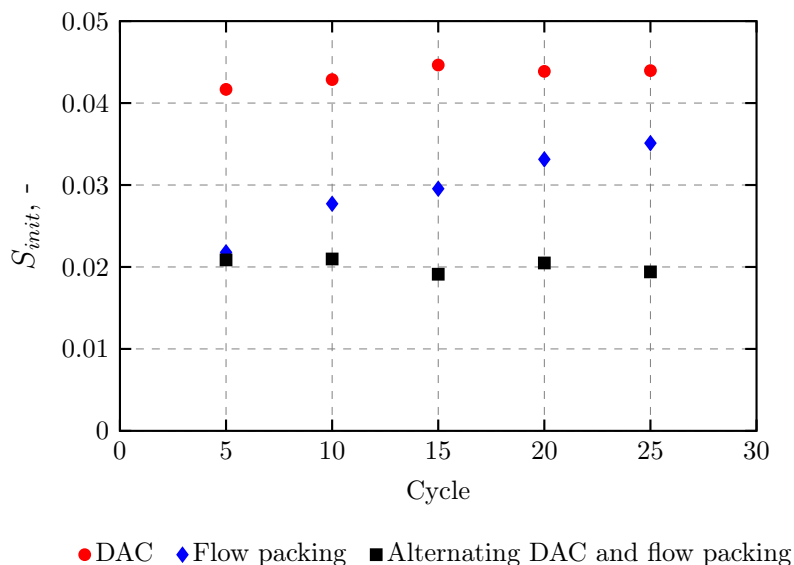


Figure 10.4.: Measured variation of the packing density profiles from the initial profile. The packing density variations are given via parameter S_{init} for the three packing methods during cyclic operation.

uppermost and lowermost packing section whereas in the middle sections, the packing density was unchanged. Compared to the DAC and flow packed column, this column showed the least differences between the initial and the long-term packing density profile ($S_{init} \approx 0.02$). As a consequence, it is deduced that alternating combination of flow packing and DAC is the most appropriate column packing method which distributes the compression forces more homogeneously among the particles and avoids regions of high particle compression stress as observed in DAC and flow packed columns.

It is difficult to correlate the changes of the axial packing density to column performance, i.e. flow distribution and packing asymmetry [Yuan et al. 1999; Williams et al. 2002; Teeters and Quiñones-García 2005]. Radial variations of the packing configuration and porosity distribution are known to have a serious effect on often observed packing and peak asymmetry [Yuan et al. 1999]. However, the results of this study showed that axial packing density variations become increasingly important when the packing exhibits a pronounced compression-relaxation behavior. In particular if the packing shows a wide particle size distribution, migration of smaller particles may be enforced with pronounced axial variations of the packing compression-relaxation behavior. Furthermore, differences between the wall friction and the interparticle friction may lead to differences

of the packing relaxation behavior of the near-wall packing region compared to the inner packing region. Either leads to radial variations of the packing properties and is highly influenced by the axial variations and packing compression-relaxation behavior.

10.2. Simulated Column Behavior During Long-Term Cyclic Operation

In order to analyze the impact of the axial packing compression-relaxation variations on the fluid flow distribution within the column, computer simulations of the packing behavior during hydrodynamic load were carried out. Therein, the and flow packing were compared to each other. For this purpose, the simulated column was packed according to the different column packing methods, DAC, flow packing and alternating DAC and flow packing and the hydrodynamic behavior of the columns were compared to each other. The packed column was then operated by 10 simulated high-flow/low-flow cycles using the same fluid velocity and packing height as in the experiments. The simulation set-up is given in Section 5.5.2. This amount of cycles was found to be sufficient as no further changes were obtained with ongoing simulated cyclic operation. The computational effort of the simulations for each cyclic column operation was about 10 h on a 16 core Intel Xeon E5 processor (2.3 GHz).

Figure 10.5 shows the simulated axial packing density profiles of columns packed by (A) DAC, (B) flow packing, and (C) alternating flow packing and DAC. The overall packing compression was 20 % as in the experiments.

DAC packing resulted in an exponentially decreasing initial packing density profile from column top to bottom. Already after the fourth simulated operational cycle, the packing density profiles showed no further variation leading to a constant deviation of $S_{init} \approx 0.05$.

The simulated flow packed column (Figure 10.5 B) in contrast showed minor changes in the axial packing density profile in nearly all operation cycles similar to the measurements. The lower packing sections relaxed and the upper packing sections were compressed as a result of force relaxation. This led to an increasing deviation of the packing density profile from the initial packed state from $S_{init} = 0.01$ to $S_{init} = 0.02$.

As in the experiments, the simulated behavior of the column packed by alternating flow packing and DAC exhibited the least axial deviation from the initial packing density

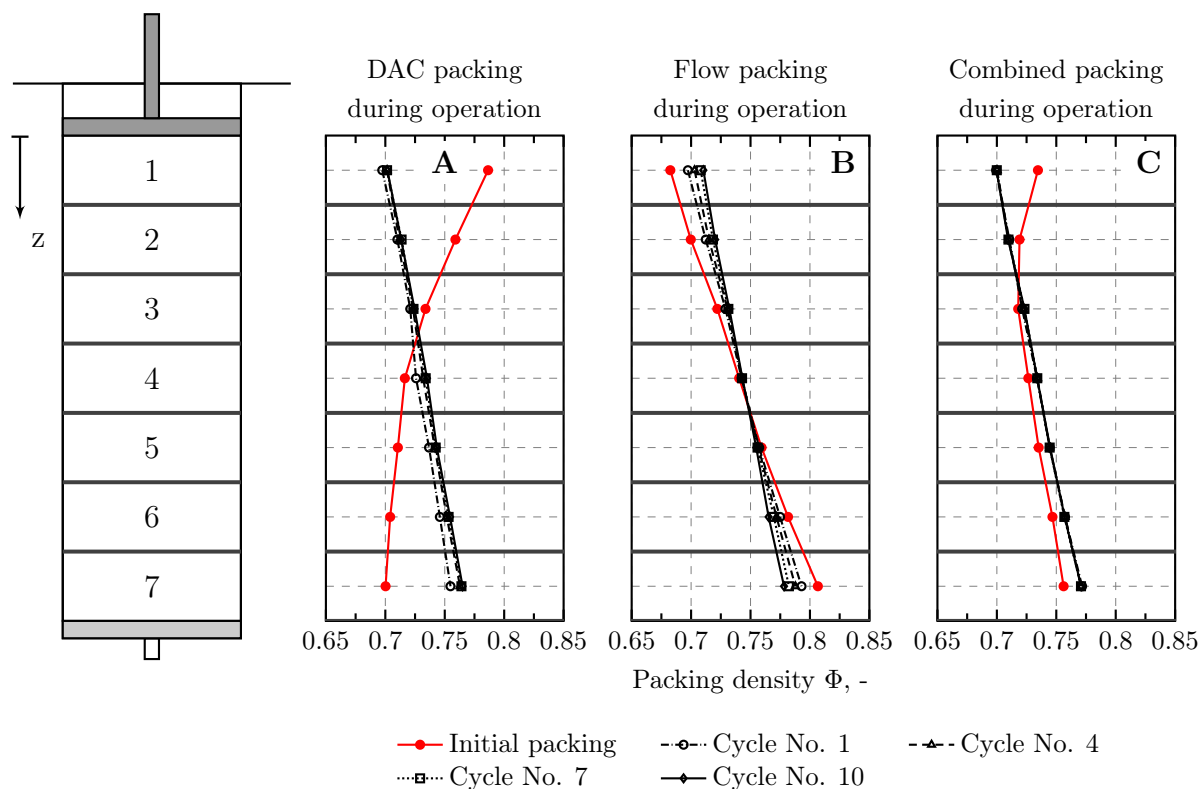


Figure 10.5.: Simulation of the axial packing density profiles during long-term operation of columns packed according to different methods. (A) DAC, (B) flow packing and (C) alternating flow packing and DAC.

profile ($S_{init} \approx 0.01$). The packing was force-equilibrated right after the first simulated cycle and kept being hydrodynamically stable during further simulation.

The simulated axial packing density profiles reproduced the measured packing behavior qualitatively although the model was not able to reflect the measured axial packing density gradients as pronounced (see Figure 10.6). The deviations of the simulated packing density profiles were lower than the deviations of the measured profiles as a consequence of the inability of the model to reproduce the pronounced packing density gradients. This is most probable due to the fact that in the DEM model, particle-particle interactions are described according to a simplified linear Hookean behavior which does not account for simultaneous force relaxation during constant load. Moreover, the packing density profiles obtained from laboratory measurements were calculated using Equation (3.74) and based on the assumption that the gravity settled packing porosity is $\epsilon_0 = 0.38$ [e.g. Stanley et al. 1996; DePhillips and Lenhoff 2000; Cherrak et al. 2002;

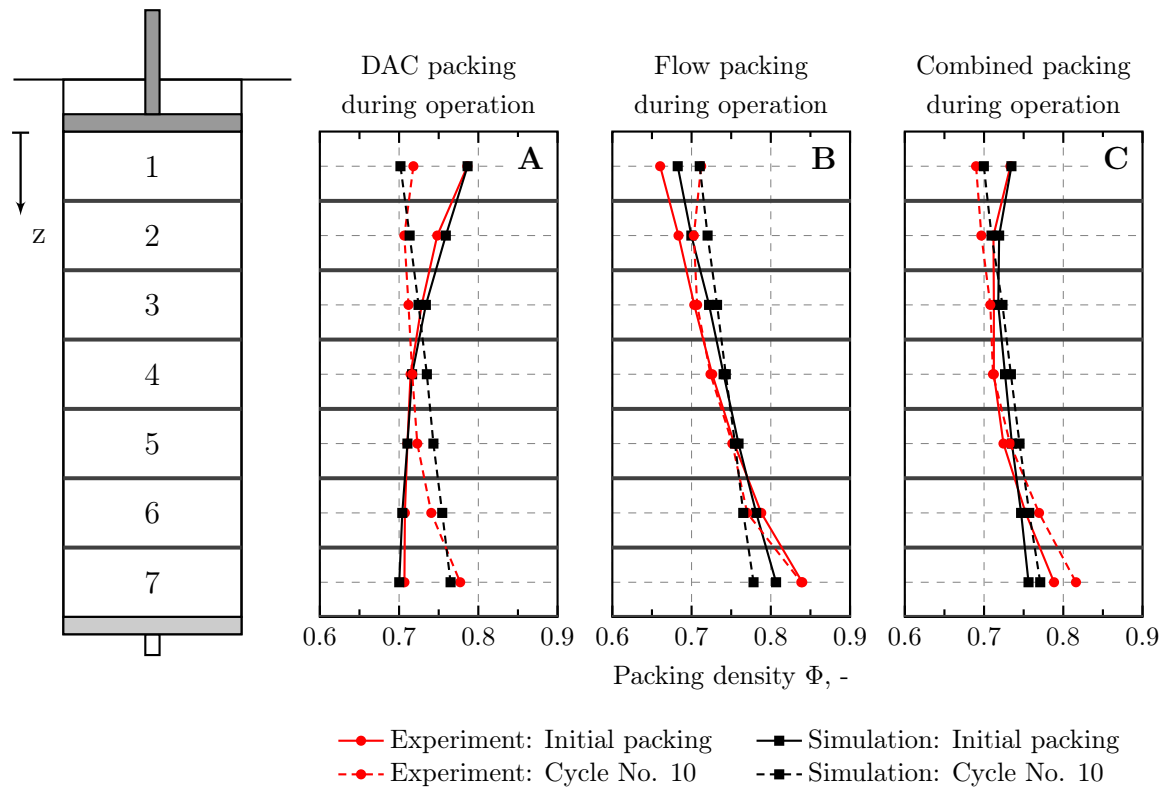


Figure 10.6.: Comparison of the simulated and measured axial packing density profiles of columns packed according to different methods. The initial packing density profile as well as the packing density profile after during the 10th cycle are given. (A) DAC, (B) flow packing and (C) alternating flow packing and DAC.

Bowes et al. 2009]. Though, this value depends on the fluid environment as well as on the column geometry and is, due to the high intraparticle porosity, difficult to measure. A different gravity settled packed bed porosity would than lead to different packing density gradients. In contrast to this, the packing density resulting from simulations was calculated directly by the model. However, the dynamic behavior of the packed beds as well as the relative changes of the packing density profiles were still reproduced by the model in a sufficient manner.

10.2.1. Analysis of Simulated Force Distribution

Figure 10.7 shows the force probability distribution of the interparticle contact forces, i.e. the probability $P(F)$ that the force is between F and $F + dF$, as a function of the dimensionless force $F/\langle F \rangle$. $\langle F \rangle$ is the average contact force of the particles.

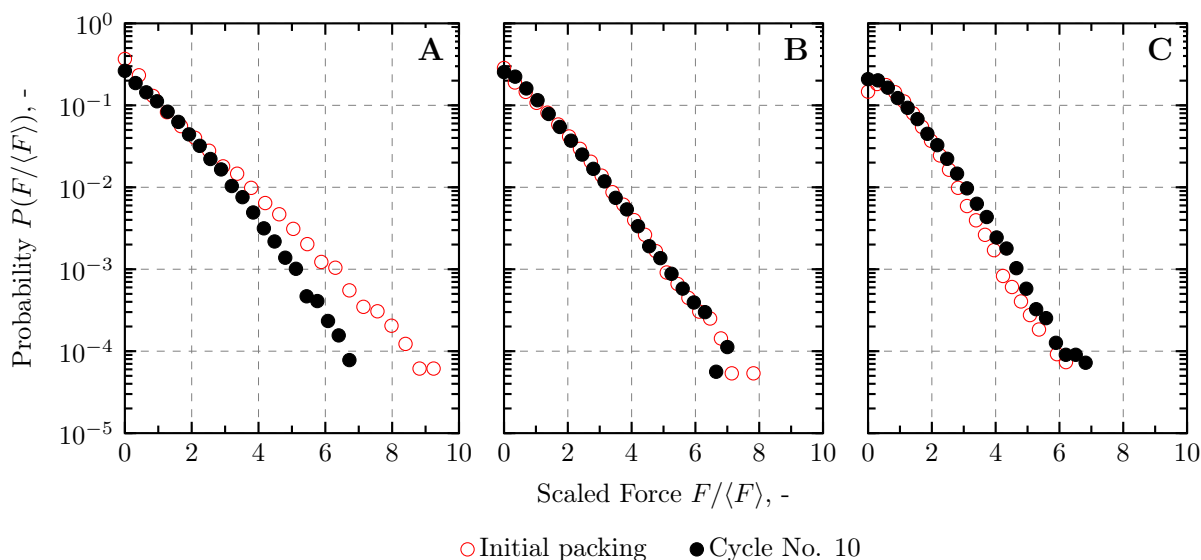


Figure 10.7.: Force probability distribution in the simulated columns packed according to different methods. (A) DAC, (B) flow packing and (C) alternating flow packing and DAC. The force probability distribution is a measure for the packing inhomogeneity in terms of the compression force distribution.

As can be seen, very large and very low particle contact forces coexist in the columns packed by the different methods. The DAC packing resulted in forces of up to nine times the average force (see Figure 10.7 A). During operation, the forces were equilibrated, but there is still a probability of 0.04% that particles are stressed with more than six times the average particle force. The probability to encounter such high forces during the flow packing method is considerably lower. However, the probability distribution kept nearly constant during cyclic column operation (see Figure 10.7 B). By alternating application of flow packing and DAC, the probability of high particle stresses was decreased further. Here, the probability to encounter forces reaching six times the average force was lower than 0.01%. Moreover, the probability to encounter forces lower or equal to the average force was increased, as can be seen by the rather flat distribution at $F/\langle F \rangle < 1$ (see Figure 10.7 C). This indicates that the packing was further stabilized by strengthening the presence of small lateral forces, i.e. the weak force chain network (see Figure 3.12).

Figure 10.8 shows the angular distribution of 99.5% of contact forces and demonstrates the coexistence of the strong and weak contact force network.

The angle of the contact forces is measured against the xy-plane of the simulated columns. Consequently, an angle of -90° is consistent with the direction of hydrody-

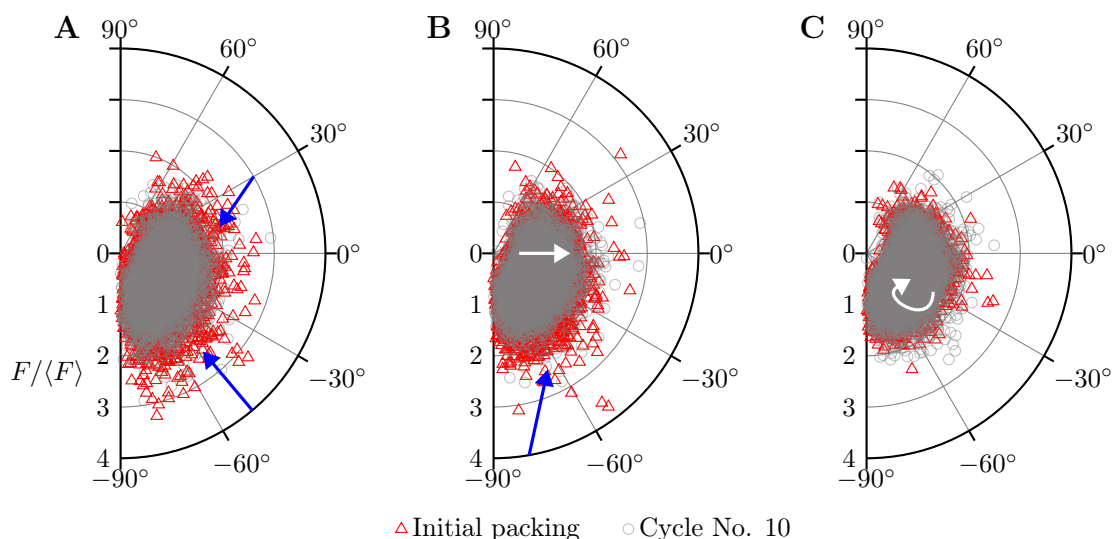


Figure 10.8.: Angular distribution of contact forces in packings packed by different methods. (A) DAC, (B) flow packing and (C) alternating application of flow packing and DAC. The angle is measured against the xy -plane of the column and indicates the direction of interparticle contact forces. The arrows indicate the change of the force chain network during cyclic column operation.

dynamic load, i.e. the fluid flow in axial direction, and indicates the direction of the strong force chain network. An angle of 0° is orthogonal to the direction of fluid flow and indicates the weak lateral oriented force chain network. The Figure shows that by applying the DAC packing method (A) high particle contact forces, i.e. over three times the average contact force, are present in lateral as well as in axial column direction as indicated by the red triangles. This is consistent with the pronounced force chain network displayed in Figure 10.1 A. During column operation, the large stresses were relaxed as indicated by the blue arrows. As expected, flow packing (B) led to a rather coarse force chain network (see Figure 10.1 C) exhibiting a few but high contact forces. As can be seen further, during column operation, the axially oriented contact forces were relaxed and the laterally oriented forces were strengthened. Alternating application of DAC and flow packing (C) already led to a nearly equal ratio of axially and laterally oriented contact forces resulting in a stable particle packing. As already shown before, the packing did not exhibit significant changes in its packing density and so the contact force chain network kept nearly constant.

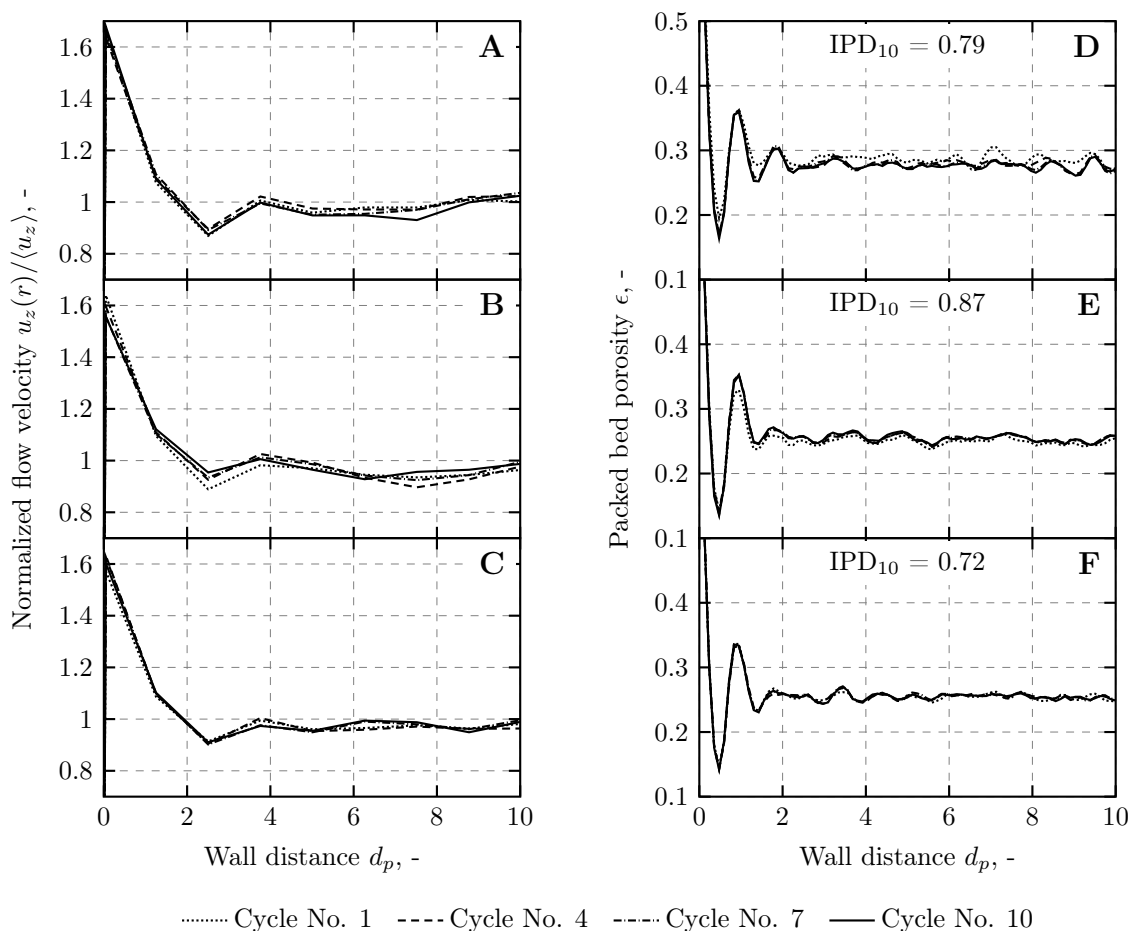


Figure 10.9.: Simulated radial fluctuations of the axial flow velocity and porosity distribution. (A, D) DAC, (B, E) flow packed column, and (C, F) column packed by alternating flow packing and DAC. The wall distance is given in mean particle diameters d_p . The local axial flow velocity $u_z(r)$ was normalized to the average inner packing axial flow velocity $\langle u_z \rangle$. The integral porosity deviation (IPD) is given exemplarily for the 10th simulated operation cycle.

10.2.2. Analysis of Simulated Radial Fluctuations of the Axial Flow Velocity

Based on the simulations, a detailed analysis of the packing heterogeneity in terms of packing asymmetry and fluid flow distribution was possible. Figure 10.9 shows the simulated radial fluctuations of the axial fluid flow velocity as well as the of the packed bed porosity obtained by the different column packing methods during cyclic operation. The local axial flow velocity $u_z(r)$ was normalized to the average axial flow velocity $\langle u_z \rangle$ (see Figure 10.9 A-C). According to the boundary conditions, the axial flow velocity

at the wall is zero. Close to the column wall, the simulation results showed an about 1.6-fold higher flow velocity than the average flow velocity. In the simulations, the wall effect was prominent up to a distance from the column wall of about four average particle diameters. The differences of the flow velocity distributions of the three different packings during simulated operation were small but visible. The DAC packed column showed the largest variations of axial flow velocity in radial directions with a 1.65-fold increased velocity in the vicinity of the column wall.

However, due to the coarse grain approach which was used in the simulation model, the CFD cell size was increased. This led to limited radial and axial resolution of the calculated flow velocity distribution as could be seen in Figure 10.9 A-C. Values between the flow velocities calculated by the model were interpolated linearly.

The effect of increased flow velocity in vicinity of the column wall was consistent with results of Knox and co-workers [Knox and Parcher 1969; Knox et al. 1976].

Due to the geometrical wall effect, the particles are unable to form a dense packing configuration against the rigid flat surface of the column wall. Hence, the first particle layer with contact to the column wall is highly ordered and differs from subsequent layers, because the interstitial void between the column wall and the first layer of particles cannot be partially occupied by other particles. This results in a higher packing porosity and packing permeability in the column wall region. The subsequent particle layers exhibit an increasing random packing configuration toward the packing bulk. Figures 10.9 D-F show the geometrical wall effect resulting in oscillating porosity profiles. The mean particle diameter of the particle size distribution was chosen as reference diameter. As can be seen, the porosity oscillations were reduced significantly after a distance of about two particle diameters to the column wall. Hence, based on radial profiles of the porosity and axial velocity, the region from a distance of four particle diameters towards the column center was defined to be the packing bulk region which can be characterized by the packing bulk porosity ϵ_{bulk} . To obtain a quantitative measure of the packing heterogeneity and contribution of the local packing porosity distribution to transcolum eddy dispersion, the integral porosity deviation (IPD) parameter was calculated according to Equation (3.64) [Bruns et al. 2012a]. This calculation was performed over the whole packing cross section (equivalent to $48 d_p$). Based on the radial porosity distribution given in Figures 10.9 D-F, the bulk porosity ϵ_{bulk} was calculated in a region ranging from $4 d_p$ from the column wall to the column axis. As illustrated in Figures 10.9 D-F,

DAC, flow packing and the combined packing method resulted in different local porosity distributions. The DAC packed column (Figure 10.9 D) exhibited two visible oscillations of the porosity profile over a distance of two particle diameters from the column wall, whereas only one oscillation was observed for the other two packings. This indicates a higher ordered packing structure in the column wall region for the DAC packed column. However the porosity profiles varied slightly during ongoing operation cycles for both DAC and flow packed columns (Figure 10.9 D, E). The alternating combination flow packing and DAC (Figure 10.9 F) resulted in the least variations of the packing porosity profile. This method also resulted in the lowest IPD of 0.72 after the 10th simulated cycle and therefore showed the least deviations of local porosity from the packing bulk porosity. In contrast, the IPD values were 0.79 for the DAC packed column and 0.87 for the flow packed column which indicated a lower packing homogeneity.

10.2.3. Evaluation of Axial Hydrodynamic Dispersion

The observed porosity oscillations as well as the deviations of the local porosity from the packing bulk porosity cause the radial variations of the axial fluid flow velocity as shown in Figure 10.9.

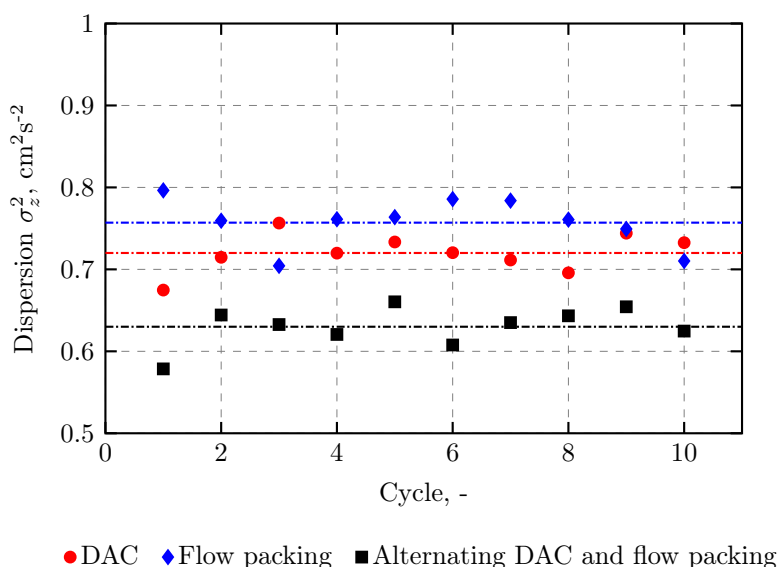


Figure 10.10.: Calculated axial hydrodynamic dispersion in columns packed by the three different packing methods during operation. 10 load/elution/equilibration cycles were simulated. Mean values are given by the dash-dotted lines.

To evaluate the variations of the axial fluid flow velocity, the overall packing induced axial fluid dispersion σ_z^2 was calculated as the second central statistical moment of the local fluid flow velocity according to Equation (3.65) for 10 simulated load/elution/equilibration cycles (Figure 10.10). σ_z^2 was calculated regardless of thermodynamic molecular diffusion effects. The average hydrodynamic dispersion values for DAC and flow packing were $0.72 \text{ cm}^2 \text{ s}^{-2}$ and $0.76 \text{ cm}^2 \text{ s}^{-2}$, respectively. The combined column packing method led to a higher degree of packing homogeneity as this packing showed the least axial hydrodynamic dispersion with an average value of $0.63 \text{ cm}^2 \text{ s}^{-2}$. Hence, the calculated packing induced dispersion confirmed what was expected on the basis of the calculated IPDs. Moreover, pronounced fluctuation of the packing dispersion during cyclic operation was observed for all three packings. These fluctuations were attributed to radial variations of the axial flow velocities (see Figure 10.9) which are caused by the variations of the axial packing density profiles (see Figure 10.5). The column packed by the flow packing method shows a steadily decreasing hydrodynamic dispersion from the 7th operation cycle on which indicates that the packing was still engaged in the force equilibration process. This observation was in accordance with above mentioned statement that the column had not reached a stable consolidated state during cyclic operation (see Figure 10.4).

10.3. Conclusion

A systematic modeling-based analysis of different column packing methods was carried out focusing on packing homogeneity and hydrodynamic long-term packing stability. Macroscopic measurements of the hydrodynamic packing behavior of the laboratory column revealed distinct differences in the local axial packing density during hydrodynamic load. The axial packing density gradient and consequently the hydrodynamic packing stability were found to vary considerably for different column packing strategies. Dynamic axial compression (DAC) led to a significant increase in packing density near the top of the column whereas flow packing resulted in increasing packing density towards the column outlet.

Using coupled CFD-DEM modeling, the measured packing behavior was reproduced qualitatively providing valuable information regarding the intrinsic packing properties that up to now have been inaccessible. Frictional effects between the particles as well as

between the particles and the column wall were found to influence the axial and radial compression force transmission within the packing during the column packing process. While friction played a minor role during flow packing at high flow rate, it became noticeable during DAC and affected the force transmission and axial packing density gradient. The simulations revealed that during DAC, particle rearrangement led to an increased wall support in the region adjacent to the plunger which acted against the packing compression. As a consequence, a dense force chain network was present in this region showing a strong contact to the column wall (see Figure 10.1 A, B).

It was found further that the axial compression force transmission is increased in packings with higher interparticle friction reducing the rearrangement of particles. During flow packing, a rather coarse force chain network was identified in the region near the column outlet and showed only minor contact to the column wall. Hence, the influence of the wall support was significantly lower than during DAC (see Figure 10.1 C).

As a consequence, straight application of flow packing and DAC methods led to larger deviations of local particle stress in axial direction which had a negative effect on the compression force equilibration of the packed bed and therefore on hydrodynamic packing and resin stability.

Combinations of both packing strategies were shown to reduce the high particle stress during the column packing process as well as the pronounced packing density gradients.

Experimental and in-silico analysis of a column packed by alternating application of flow packing and DAC gave the best results with respect to hydrodynamic long-term packing homogeneity and stability. The axial packing density gradient was less pronounced and stayed nearly constant during cyclic hydrodynamic load in comparison to the other packing methods investigated. The simulated results clearly showed that the alternating application of flow packing and DAC improved the axial compression force transmission leading to a more homogeneous packed bed. The probability to encounter large particle stresses (i.e. six times the average particle stress) was reduced by a factor of four compared to the DAC packing. Additionally, the orientation of the force chain network indicated a balanced distribution of axially and laterally oriented contact forces. This resulted in a hydrodynamically stable packing configuration in which the wall support was increased by the laterally oriented force chain network (see Figure 10.8 C). DAC and flow packed columns exhibited a rather axially oriented force chain network during cyclic column operation which then had a less stabilizing effect and resulted in an increased deviation of the axial packing density profiles (see Figures

10.4 and 10.8 A, B).

Based on the improved compression force transmission by alternating application of DAC and flow packing, the resulting packed bed exhibited the lowest integral porosity distribution (IPD) and hydrodynamic dispersion (σ_z^2). Analysis of the packed bed homogeneity in terms of radial flow and porosity distribution confirmed the measured results and demonstrated that the observed dynamics had a noticeable effect on column hydrodynamic stability.

11. Conclusions

The operation of chromatography columns at its hydrodynamic design limits may lead to a complex hysteretic, thus, history-dependent packed bed behavior or even integrity breaches [Larson et al. 2003; Hekmat et al. 2011]. Experimental analysis of the hydrodynamic conditions in a chromatography column by either optical or acoustic methods (e.g. Photoacoustic Tomography, PAT) is limited due to the opaque and highly porous microscopic particles. The theoretical investigations reported so far used one or two-dimensional mathematical models and did not provide information about the local fluid flow fields or packing stress states within the column. Furthermore, the individual particle behavior as well as the interparticle micromechanics coupled with the fluid flow is not considered within these modeling approaches. Hence, the detailed causes of the above mentioned packing behavior are still largely unknown [Hekmat et al. 2013].

To address these issues, computer simulations provide a valuable method to obtain detailed information about the packed bed behavior being influenced by the local liquid phase conditions as well as by the properties of individual particles. Furthermore, the impact of those parameters which are not experimentally accessible can be evaluated.

Therefore, the present thesis aimed at the development of a novel three-dimensional mechanistic model of a chromatography column in order to investigate the transient hydrodynamic packed bed behavior as a function of the single particle properties and the fluid flow at constant temperature. A three-dimensional deterministic column model was created by applying Computational Fluid Dynamics (CFD) coupled with the Discrete Element Method (DEM).

In contrast to existing modeling approaches, the new model developed in this work considered the packed bed as a composition of discrete particles of defined sizes, densities, and stiffnesses. Therein, the behavior of each single particle was described by force and momentum equations.

Modeling the packed bed using the DEM required the knowledge of the mechanical

properties of the chromatographic particles, i.e. mean diameter, particle size distribution, mean density, Young's modulus, Poisson's ratio, coefficient of restitution, and friction coefficients. Therefore, a detailed characterization of agarose-based particles (CM Sepharose 6FF[®], resin "SEP") and different methacrylic particles (Toyopearl[®], resin "TOY") was carried out. Both particles differ in their backbone material and intraparticle porosity ($\epsilon_{SEP} = 0.84$, $\epsilon_{TOY} = 0.63$ [e.g. DePhillips and Lenhoff 2000; Yao and Lenhoff 2006]) so that a different mechanical behavior was expected. By applying high-resolution micromanipulation, the compression-relaxation behavior of individual SEP and TOY particles was investigated.

The particles analyzed showed a pronounced particle size distribution (PSD) in which the SEP particles exhibited a wider PSD than the TOY particles. The mean particle diameter of the SEP and TOY particles was calculated to 86.9 μm and 65 μm which were similar to the values provided by the vendors (SEP: 90 μm and TOY: 65 μm). The measured particle densities in wet state were 1.14 g cm^{-3} (SEP) and 1.34 g cm^{-3} (TOY), which can be attributed to the high intraparticle porosities of the resins. The determined particle densities were comparable to literature data of similar resins.

The micromanipulation experiments revealed that both particles, SEP and TOY, exhibited pronounced force relaxation during compression. The obtained force-over-displacement functions (at a constant displacement rate) and the force-over-time functions (at a constant displacement) were adequately described by two different material models - the former by the *Standard Linear Solid (SLS)* model and the latter by a force relaxation model expressed by *Prony-series*.

It was found that the force-relaxation behavior could be described by two relaxation times from which it was concluded that two different relaxation mechanisms were involved. It is likely that the longer relaxation time τ_1 , which was ~ 15 s for the SEP particles and ~ 6 s for the TOY particles, characterized the viscoelastic force relaxation due to conformational changes of the polymer matrix. The shorter relaxation time τ_2 , which was ~ 0.5 s for both particles, was attributed to poroelastic relaxation due to water release of the swollen particle during compression. This time-dependent compression behavior typically could be described by an instantaneous and relaxed shear or Young's modulus, the first characterizing the particle stiffness on the short time range and the second on the long time range [Yan et al. 2009; Toohey et al. 2016]. It was further found, that the instantaneous modulus revealed a strong dependency on the compression velocity, which can be attributed to the poroelastic material behavior. The relaxed modulus,

in contrast, was nearly independent of the compression velocity. This parameter predominantly depended on the viscoelastic solid matrix behavior and characterized the particle stiffness after poroelastic effects had decayed. Within the range of compression velocities applied, the instantaneous and relaxed moduli of the SEP particle were in a range of 12-67 MPa and 4-5 MPa and for the TOY particle in a range of 10-51 MPa and 4-6 MPa, respectively.

The Poisson's ratio was determined to 0.2 by microscopic measurements for both particles which was in accordance with the value assumed by Yan et al. [2009] for agarose micro-particles.

The coefficient of restitution can be regarded as a measure of the viscoelastic energy dissipation during particle compression/relaxation. The determined values of 0.93 and 0.8 for the SEP and TOY particle indicated that a relatively small portion of 7-20% of the compression energy was converted into plastic material deformation. Hence, both particles were not able to recover completely to their initial spherical shape.

Based on this information, the DEM model of the packed bed was developed. The column was approximated by a rigid impenetrable cylinder with frictional walls. The experimentally acquired data of the SEP media, i.e. the PSD and particle density, were used to characterize the simulated particles. As the dynamic behavior of the packed bed is governed by the individual particle interactions, the identification and definition of a proper particle contact model was necessary. Experimental results revealed pronounced simultaneous force relaxation during particle compression which resulted in a rather linear force-displacement relationship (instead of a power law relationship) within a broad range of compression velocities and compression levels. This behavior was similar to a Hookean particle interaction behavior. On the basis of the particle characterization experiments, the linear Hooke model is a vast simplification of the measured time-dependent force displacement behavior of the chromatographic particles. However, a more detailed particle contact model which takes the poro-viscoelastic behavior of the particles into account was not available.

Due to the approximation according to a linear particle compression behavior, the value of the Young's modulus to be used within the Hooke model needed to be within the limits of the instantaneous particle modulus as an upper bound (66 MPa) and the relaxed particle modulus as a lower bound (4 MPa). A Young's modulus of 30 MPa resulted in a particle behavior which was in best accordance with the measured behavior.

Further model parameters (e.g. friction coefficients, characteristic impact velocity, critical Stokes number) were experimentally not accessible and needed to be obtained from parameter studies.

Within CFD, the fluid properties were set to those of water at 20 °C. The CFD-DEM column model was evaluated and improved continuously by comparing the simulated packing behavior with different laboratory measurements. The final model reproduced the measured column behavior with good accuracy in terms of packing pressure drop, packing compression as well as axial packing compression profiles. As a great advantage over common continuum models, the coupled CFD-DEM approach allowed for the consideration and detailed analysis of the above mentioned phenomena which occur locally and temporarily in the column [Larson et al. 2003; Hekmat et al. 2011].

For the laboratory investigations, micro chromatography columns of different diameters (9.6 mm, 12.5 mm, 16.25 mm and 20 mm) were designed and manufactured. These columns were equipped with a transparent column corpus enabling various optical measurements. The columns were packed with SEP particles and the macroscopic packing behavior during operation was measured by a high-resolution camera.

Experimental results demonstrated that both, hydrodynamic and mechanical load, led to inverse packing compression profiles. During hydrodynamic load, the packing showed a linear increase in packing compression from the top to the bottom of the packing. In contrast to this, mechanical compression from the top of the packing resulted in a high compression in the top region which then exponentially decreased towards lower packing regions.

Simulations of mechanical packing compression revealed that frictional forces determine how the compression force is transmitted through the packing. Thus, in packings with low particle friction, rearrangement of particles led to absorption of the compression energy in the uppermost packing section. In packings with increased particle friction, rearrangement of particles was less and the compression energy was transmitted over a larger distance to the lower packing sections. The same effects were observed in laboratory experiments during mechanical compression of a semi-dry packing (where the interparticle fluid was drained before the experiment) and a wet particle packing. The former resulted in an exponentially decreasing compression profile at which the section adjacent to the plunger experienced the highest compression and the section opposite to the plunger the lowest. In contrast to this, a nearly constant compression of the packing

sections in the middle of the column was observed in a wet packing, whereas the uppermost and lowermost packing sections showed a higher compression. Based on these findings, it was assumed that the interstitial fluid acts as a lubricant during packing compression, thus, enabling the particles to slide more easily against each other.

Besides particle friction, the packing compression behavior was also influenced by the so called 'wall effect'. Resulting from the friction between the particles and the column wall, the wall effect acts against the direction of packing movement and might have a stabilizing effect on the dynamic packing compression-relaxation behavior (this effect is also known as 'wall support') [Lan et al. 2012; Gerontas et al. 2015]. However, the wall effect is difficult to deal with numerically and various modeling approaches were reported addressing this issue [e.g. Keener et al. 2002; Tran et al. 2007]. Laboratory experiments of packing compression and relaxation using columns of different diameters from 9.6 mm to 50 mm revealed an approximately logarithmic dependency of the packing pressure drop and overall packing compression on the column diameter. However, a simple continuum model which was based on the balance of axial forces on an incremental slice of the packing showed that the dependency of the macroscopic packing parameters on the column diameter is much more complex. Nevertheless, the continuum model was able to reproduce the measured scale dependency of the packing pressure drop for SEP and TOY packings as well as the packing compression behavior for TOY packings.

The investigation of the dynamic packing behavior on the particle scale was carried out using fluorescence microscopy as well as micro computer tomography. Different techniques were developed to label SEP and TOY particles with a fluorescent dye. Fluorescent microscopy measurements revealed the existence of a pronounced force chain network, which was assumed to carry the major compression force through the column during flow or mechanical packed bed compression. Next to highly stressed particles aligned in a force chain, several less stressed particles as well as interparticle voids were detected [Dorn and Hekmat 2016]. Inhomogeneous force distribution and the existence of force chain networks are typical phenomena in frictional granular systems [e.g. Makse et al. 2000; van Hecke 2010]. However, these phenomena were not reported in the context of chromatographic packings so far. The force chain network was also apparent in the packing compression simulations which confirmed that high and low particle stresses coexist in these packings and that up to six times the average particle stress was carried by the force chains.

Micro computer tomography measurements of the packing at the particle scale turned

out to be challenging due to two reasons: First, the X-ray attenuation of the particles was very similar to the surrounding fluid, which might be due to the high porosity of the particles as well as, due to the comparable atomic masses of the particle material and the surrounding fluid (water). Second, analysis of the dynamic packing behavior during cyclic column operation was not possible due to the extremely long measurement times (> 15h) required to obtain an adequate resolution of the packing structure via micro computer tomography. A screening of various contrast enhancing agents only resulted in a marginally improved contrast.

During cyclic column operation at high and low flow velocities, particle rearrangement and migration of smaller particles was observed. These effects are known to contribute to a stepwise consolidation of the packing and to an increase in packing inhomogeneity [Di Giuseppe et al. 2010; Kong et al. 2010]. This phenomenon was investigated in more detail in laboratory experiments as well as in-silico by tracking tracer particles in different mono-, bi-, and polydisperse packings. Oxidized TOY particles used as tracer particles were placed on top of the packings or distributed homogeneously within the packing. During the measurements, particle migration was observed in the column wall region only. In the inner packing region, no particle migration was visible as it was found out by flash-freezing of the packing and cutting it into halves. A similar behavior was observed in the simulations and a pronounced particle size segregation over the column radius took place during cyclic operation. It was concluded that this effect may contribute to the formation of flow channels in the column wall region. Both, experiments and simulation showed an increase of particle migration in bidisperse packings.

The investigations carried out demonstrated the shortcomings of chromatography columns packed with compressible polymeric resins in terms of the hydrodynamic behavior. The consequences of these shortcomings were described (see Table 11.1). In order to mitigate these shortcomings and, hence, to maintain packing integrity over a larger number of operation cycles, chromatography columns usually are packed by either flow or mechanical packing compression. However, it was shown that both compression methods lead to a pronounced inhomogeneity of axial packing density distribution (Figure 11.1 A) and particle stress distribution (Figure 11.1 B). However, the combination of flow packing and mechanical compression (DAC) turned out to be a promising packing strategy. Several combinations of both compression methods were investigated in laboratory as well as in-silico. The different packing strategies were evaluated regarding

Table 11.1.: Hydrodynamic shortcomings of chromatography columns packed with compressible polymeric resins and possible consequences.

Shortcomings	Possible consequences
Inhomogeneous compression force transmission during column packing by flow or mechanical compression leading to inverse packing density gradients	<ul style="list-style-type: none"> • Oscillating behavior of high packing density regions between both ends of the column during cyclic column operation • Inhomogeneous particle stress distribution • Particle aging and erosion • Decreasing particle surface to volume ratios • Inhomogeneous flow distribution
Oscillating packing behavior and compression-relaxation hysteresis	<ul style="list-style-type: none"> • Increased particle migration • Formation of clusters of smaller particles • Medium wall separation • Formation of packing cracks and bypass flows
Geometrical wall effect	<ul style="list-style-type: none"> • Increased flow velocity in vicinity of the column wall • Increased migration of smaller particles • Formation of bypass flows
Wall support	<ul style="list-style-type: none"> • Increased packing and particle stress in larger columns • Inhomogeneous packing density and flow distribution • Packed bed collapse

hydrodynamic packing stability (i.e. oscillations of the packing density profile, expressed by the deviation from the initial packing density profile, S_{init}), packing porosity distribution (expressed as the integral porosity deviation, IPD), and fluid dispersion (σ_z^2) during long-term cyclic column operation. A stepwise alternating application of DAC and flow packing (termed as the 'hybrid' packing method) resulted in the most homogeneous packing density profile (Figure 11.1 A) and significantly reduced high particle stresses during the column packing process (Figure 11.1 B). Moreover, the hybrid packing method revealed the the best hydrodynamic packing stability over time, and the most homogeneous packing porosity and fluid flow distribution (Figure 11.1 C). The simulations were able to reflect the experimental trend in a qualitative manner.

In summary, the dynamic macroscopic packed bed behavior of chromatographic columns was investigated using a novel modeling approach by explicit consideration of the single particle properties as well as the coupling of the interparticle micromechanics with fluid flow.

For this purpose, single agarose-based and methacrylic-based chromatography particles were characterized mechanically for the first time. Both revealed a time-dependent

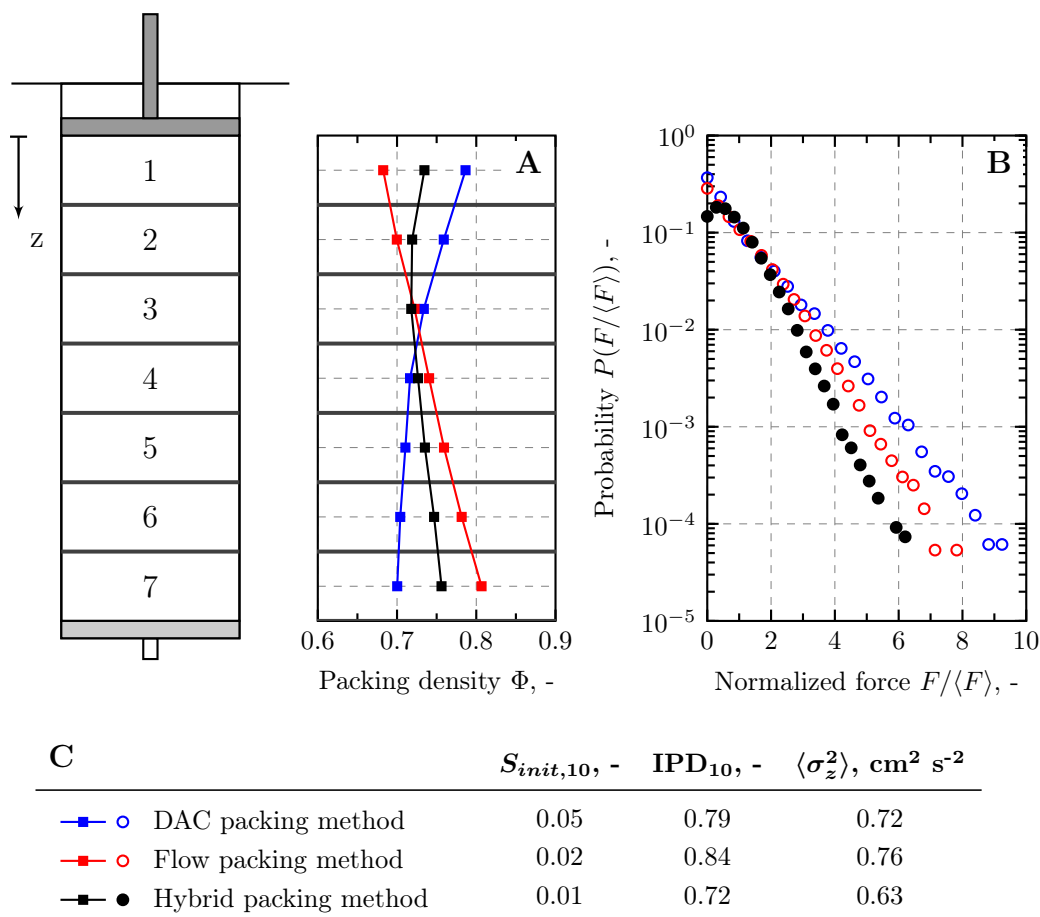


Figure 11.1.: Comparison of different simulated column packing methods. The hybrid packing method, as a combination of stepwise application of DAC and flow packing was compared to conventional DAC and flow packing in terms of (A) initial axial packing density profiles and (B) particle stress distribution. (C) Hydrodynamic packing stability during long-term column operation was evaluated by the deviation of the axial packing density profile from the initial axial packing density profile (S_{init}). The integral porosity deviation (IPD) is a measure of the packing porosity distribution. Both parameters are given after the 10th operating cycle. The homogeneity of the flow velocity distribution is given by the dispersion σ_z^2 averaged over the number of operating cycles. $IPD = 0$ and $\sigma_z^2 = 0 \text{ cm}^2 \text{ s}^{-2}$ would indicate an ideal homogeneous packing.

compression-relaxation behavior in which poroelastic and viscoelastic effects are dominant at different timescales. Generally, both particles exhibited a small abiding deformation after compression due to viscoelastic loss which was larger for the methacrylic particle.

The CFD-DEM chromatography column model, which was developed on the basis of the measured particle properties, reproduced the laboratory column packing behavior with great accuracy in terms of packing pressure drop, bed subsidence, and axial packing

compression profiles.

It was shown that hydrodynamic and mechanical packing compression led to inverse packing density profiles. The former resulted in a linearly increasing and the latter in an exponentially decreasing packing compression profile from packing top to bottom.

The model revealed hydrodynamically relevant packed bed parameters such as particle stress distributions that were experimentally inaccessible but cause pronounced packed bed inhomogeneities. In this context, a force chains network was identified which differed significantly in density and distribution depending on the column packing method. Particle migration was induced by the dynamic changes of the axial packing density profiles during column operation leading to erosional effects and flow channeling.

Finally, a simulation-based improvement of column packing methods by alternating application of flow and mechanical compression was achieved resulting in an enhanced hydrodynamic packing stability as well as in a more homogeneous distribution of particle stresses, packing density, and flow velocity.

12. Outlook

Due to the strong potential of the coupled CFD-DEM model, simulations of larger columns with increased number of particles as well as longer column operation cycles are of considerable interest. However, the computational effort scales with the amount of particles which leads to a significant increase of computing time. Therefore, future work should be dedicated to the development of further strategies to reduce the computational effort. Besides the two methods presented in this work – the implementation of a coarse grain approach as well as the simulation of a rotationally symmetric slice of the column instead of a cylinder – an increase of the DEM time-step might be a promising approach. As the current model requires small time-steps ($\sim 1e-6$ s) for numerical stability, temporal averaging of the particle motion will reduce the amount of particle calculations per time-step of the DEM model significantly. Herein, the equilibrium state of the particles in the packed bed (i.e. particle position and compression) will be extrapolated based on a known change of the flow field. As an example, during the start of a high-flow cycle the change of the fluid flow velocity within a given time is known a priori as well as the maximum flow velocity. Then, the equilibrium states of the particles at maximum flow velocity can be extrapolated and each particle can be relaxed to its equilibrium position within the given time range. The motion and compression of the particles will be described by a simple relaxation function. After the next coupling step with CFD, the equilibrium states of the particles will be updated. Using this approach, the DEM time-step can be increased by a factor of about 1000 to be in the range of the CFD time-step ($\sim 1e-3$ s).

Furthermore, evaluation of the column performance and flow field homogeneity by the HETP (Height Equivalent to Theoretical Plate) parameter should be carried out in laboratory experiments as well as by simulations. HETP values can be obtained by experimental investigation of column peak asymmetry by tracer dispersion measurements. This requires the implementation of a high-resolution tracer detection technique (e.g. by UV detection). The simulation model can be extended by consideration of a second

fluid phase which will enable the simulation of diffusion effects and hence the calculation of HETP values.

Experimental analysis of fluid flow through the packing by application of a Nuclear Magnetic Resonance (NMR)-based imaging method (Magnetic Resonance Imaging (MRI)) could help to evaluate the simulation model in terms of calculated axial as well as radial flow fields.

Bioseparation aspects, such as variable protein concentration, changes of the fluid viscosity, pH, or ionic strength are known to influence the hydrodynamic column behavior. Based on the mentioned methods for reduction of the computational effort, these bioseparation aspects might be taken under consideration in the future by developing an extended simulation model.

13. Glossary

13.1. List of Abbreviations

CFD	Computational fluid dynamics
CLSM	Confocal laser scanning microscopy
DAC	Dynamic Axial Compression
DEM	Discrete element method
DR	Density measurement unit
FRC	Flow controlling unit
HCP	Hexagonal Close Packing
HETP	Height Equivalent of Theoretical Plates
i.d.	in diameter
J	Jamming point
Micro CT	Micro computer tomography
MPI	Message passing interface
MRI	Magnetic Resonance Imaging
NMR	Nuclear Magnetic Resonance
PISO	Pressure implicit with splitting of operators
PMMA	Polymethyl methacrylate
PAT	Photoacoustic Tomography
PRC	Pressure regulating unit
PSD	Particle size distribution
RCP	Random close packing
RLP	Random loose packing
SEM	Scanning electron microscopy
SEP	CM Sepharose 6FF [®]
SLS	Standard linear solid
TOY	Toyopearl [®] SP-650 (different particle sizes)
TR	Temperature measurement unit
UVM	UV microscopy
VANS	Volume Averaged Navier-Stokes Equations

13.2. Latin Symbols

A	a	Particle contact radius	m
	A	Cross-sectional column area	m ²
	A_p	Particle surface area	m ²
	A_{ratio}	Aspect ratio	-
B	B	Packing bulk modulus, characterizes the stiffness of a particle packing during compression	Pa
	B_0 - B_i	Parameters of the Prony series model (Equation 3.28)	N
C	c	Characteristic speed of bulk elastic waves	m s ⁻¹
	c	Karman factor	-
	C	Concentration of the solvent in a swollen particle	mol m ⁻³
	CG	Coarse graining level, determines how many particle are treated as one coarse grain particle	-
D	C_0 - C_i	Parameters of the Prony series model (Equation 3.27)	Pa
	Co	Courand number	-
	D	Diffusion coefficient	m ² s ⁻¹
	D	Column diameter	m
	d	Dimension of space	-
	d	Distance of two particles	m
	d_{32}	Sauter mean particle diameter, defined as the diameter of a sphere that has the same volume/surface area as a particle of interest	m
	d_p	Particle diameter	m
	$d_{p,min}$	Minimum particle diameter	m
	$d_{p,max}$	Maximum particle diameter	m
E	E	Young's modulus, characterizes the stiffness of a particle	Pa
	E	Photon Energy	keV
	e	Coefficient of restitution, determines the ratio of elastic deformation energy to overall deformation energy	-
	e_{max}	Maximum coefficient of restitution	-
	$E(t = 0)$	Instantaneous Young's modulus, defines the stiffness of a viscoelastic particle prior to force relaxation	Pa
	$E(t \rightarrow \infty)$	Relaxed Young's modulus, defines the stiffness of a particle in relaxed state	Pa
	E^*	Plain strain Young's modulus, defines the average stiffness of two colliding particles of different stiffnesses	Pa
F	F	Force	N
	F_0	Instantaneous force	N

	F_0	Coefficient in the Koch-Hill drag force calculation (Equation (4.6))	-
	F_3	Coefficient in the Koch-Hill drag force calculation (Equation (4.6))	-
	F_b	Body force	N
	F_f	Fluid drag force	N
	F_g	Weight force	N
	F_∞	Relaxed force	N
	F_m	Mechanical compression force	N
	F_n	Normal force	N
	F_ν	Viscous force	N
	F_p	Pressure force	N
	F_t	Tangential force	N
	$F_{t,s}$	Static friction force	N
	F_w	Wall contact force	N
	F'	Repulsive force	N
G	G	Shear modulus, defines the shear stiffness of a particle under shear stress	Pa
	G^*	Plain strain shear modulus, defines the average shear stiffness of two colliding particles of different shear stiffnesses	Pa
	G_0	Shear modulus of the free spring in the SLS model	Pa
	G_1	Shear modulus of the spring in the Kelvin or Maxwell element	Pa
	G_{SLS}	Shear modulus of the SLS model	Pa
	$G(t = 0)$	Instantaneous shear modulus, defines the shear stiffness of a viscoelastic particle prior to force relaxation	Pa
	$G(t \rightarrow \infty)$	Relaxed shear modulus, defines the shear stiffness of a viscoelastic particle at relaxed state	Pa
	$g(\tau_p)$	Dimensionless poroelastic force function	-
	g	Gravitational acceleration	m s ⁻²
H	H	Packing height	m
	H_0	Initial packing height	m
	H_{ratio}	Packing height to particle diameter ratio	-
I	I_0	Incident photon intensity	W m ⁻²
	I_A	Absorbed photon intensity	W m ⁻²
	IPD	Integral porosity deviation, is the sum of local porosity deviations from the (constant) bulk packing porosity	-
K	K	Constant (used in Equation 3.12)	N m ^{-3/2}
	k	Intrinsic particle permeability	m ²

	k_n	Normal elastic constant	N m^{-1}
	K_{pf}	Momentum exchange coefficient	$\text{kg s}^{-1} \text{m}^{-2}$
	k_t	Tangential elastic constant	N m^{-1}
	K^*	Kozeny constant	-
L	l	Length	m
	L	Packing length	m
	L_0	Initial packing length	m
M	m	Mass	kg
	m^*	Characteristic mass of two colliding particles	kg
	$m_{p,dry}$	Dry particle mass	kg
	M^r	Rolling resistance torque	Nm
	M_d^r	Dynamic rolling resistance torque during particle rolling	Nm
	M_s^r	Static rolling resistance torque necessary to bring a particle into rolling motion	Nm
N	N	Counting variable	-
	N_c	Number of particle contacts	-
	N_{verlet}	Duration of a valid Verlet list	-
P	p	Pressure	Pa
	P	Normed pressure	Pa m^{-1}
	P	Probability	-
Q	Q	Volumetric flow rate	$\text{m}^3 \text{s}^{-1}$
	$Q(d)$	Cumulative particle size distribution	-
	$q(d)$	Particle size distribution density	m^{-1}
R	R	Particle radius	m
	R	Column radius	m
	r	Radial coordinate, distance	m
	R_d	Dynamic friction resistance	N
	r_h	Hydraulic pore radius of the particle	m
	R_h	Hydraulic pore radius of the packing	m
	R_n	Normal reaction force	N
	R_p	Particle friction resistance	N
	R_{pf}	Momentum exchange coefficient	N m^{-3}
	R_s	Static friction resistance	N
	R_w	Wall friction resistance	N
	R^*	Plain strain particle radius	m
	\vec{r}	Position vector of a particle	m
	RCF	Ramp correction factor, accounts for simultaneous force relaxation during ramp loading sequence of compression load relaxation experiments	-
	Re	Reynolds number	-
	Re_p	Particle Reynolds number	-

	Re_B, Re'_B	Bulk porous media Reynolds numbers	-
	RHL	Relative hydrodynamic load, is defined as the ratio of hydrodynamic load during column operation to hydrodynamic load during flow packing	-
S	s	Skin parameter, defines an additional cutoff distance used for the particle contact detection algorithm in the DEM code	m
	S_{init}	Average deviation of the actual packing density profile from the initial packing density profile	-
	S_{mean}	Average deviation of the actual packing density profile from the actual mean packing density	-
	S_n	Hertz constant for normal contact (Equation (4.19))	N m ⁻¹
	S_t	Hertz constant for tangential contact (Equation (4.19))	N m ⁻¹
	St_{crit}	Critical Stokes number	-
T	t	Time	s
	t_c	Particle collision or contact time	s
	t_{exp}	Experiment duration time	s
	T_r	Rolling friction torque	Nm
U	u	Fluid velocity	m s ⁻¹
	u_0	Superficial fluid velocity	m s ⁻¹
	u_f	Fluid velocity in CFD calculations	m s ⁻¹
	u_i	Interstitial fluid velocity	m s ⁻¹
	u_p	Particle velocity in CFD calculations	m s ⁻¹
	u_z	Fluid velocity in axial or z direction of the column	m s ⁻¹
V	V	Characteristic impact velocity, a DEM parameter that defines the initial relative velocity of two colliding particles	m s ⁻¹
	V	Relative velocity of two colliding particles	m s ⁻¹
	V_0	Initial relative velocity of two colliding particles	m s ⁻¹
	v	Particle velocity	m s ⁻¹
	v_{max}	Maximum particle velocity	m s ⁻¹
	v	Displacement velocity of the indenter (Equation 3.26)	m s ⁻¹
	V	Packing volume	m ³
	V_0	Initial packing volume	m ³
	V_{cell}	CFD cell volume	m ³
	V_f	Fluid volume	m ³
	V_p	Particle volume	m ³
	$V_{p,dry}$	Dry particle volume	m ³
	V_s	Solid volume	m ³
	V_v	Void volume	m ³
	v'	Particle velocity after collision	m s ⁻¹

W	W	Compression work	J
	W'	Expansion work	J
	ΔW	Plastic deformation work	J
X	x, y, z	Coordinates	-
	x	Mass thickness of a probe (Equation (5.2))	kg m ⁻²
Y	Y	Young's modulus, DEM notation, (see E)	Pa
	Y^*	Plain strain Young's modulus, DEM notation, (see E^*)	Pa
	y	Wall distance	m
Z	z	Coordination number, defines the number of particles having direct contact to a particle of interest	-
	Z	Atomic number	-
	z_0	Initial coordination number	-
	z_{crit}	Critical coordination number	-
	z_{iso}	Isostatic coordination number	-
	z_{iso}^μ	Isostatic coordination number in frictional packings	-

13.3. Greek Symbols

α	Coefficient of the Ergun equation (Equation (3.62))	Pa s m ⁻¹
α_f	Void fraction in particle packings	-
α_p	Particle fraction in particle packings	-
β	Coefficient of the Ergun equation (Equation (3.62))	Pa s ² m ⁻³
β	Coefficient in the Koch-Hill drag force calculation (Equation (4.6))	Pa s m ⁻¹
β	Coefficient in the Hertz contact model (Equation (4.20))	N m ⁻³
δ	Particle overlap	m
Δ	Particle displacement	m
Δ_{max}	Maximum particle displacement	m
δ^*	Maximum particle overlap during collision	m
δ_n	Normal particle overlap	m
δ_t	Tangential particle overlap	m
δ'	Particle overlap during rebound	m
ϵ	Porosity	-
ϵ_{bulk}	Bulk packing porosity	-
ϵ_i	Intraparticle porosity	-
ϵ	Strain	-
ϵ_0	Strain of the free spring in the SLS model	-
ϵ_1	Strain of the spring in the Kelvin or Maxwell element	-

$\dot{\epsilon}_2$	Strain rate of the dashpot in the Kelvin or Maxwell element	s^{-1}
η	Viscosity of the dashpot in the Kelvin or Maxwell element	Pa s
η_{DEM}	Fluid viscosity used in the DEM model	Pa s
η_f	Fluid viscosity	Pa s
γ_n	Normal damping constant	$N m^{-1} s^{-1}$
γ_t	Tangential damping constant	$N m^{-1} s^{-1}$
κ	Permeability of the particle packing	m^2
λ	Compression, defines the ratio of volume of a compressed body to its initial volume	-
λ	Characteristic wavelength of bulk elastic waves	m
λ	X-ray wavelength	m
λ_{bed}	Overall packed bed compression, defines the ratio of the compressed packing volume to the initial packing volume	-
λ^r	Characteristic distance used in the rolling friction model	m
μ	Friction coefficient	-
μ_d	Dynamic friction coefficient	-
μ_p	Interparticle friction coefficient	-
μ_d^r	Dynamic rolling friction coefficient	-
μ_s^r	Static rolling friction coefficient	-
μ_s	Static friction coefficient	-
μ_w	Wall friction coefficient	-
μ/ρ	X-ray mass attenuation coefficient	$m^2 kg^{-1}$
ν	Particle Poisson's ratio, defines the ratio of transverse strain to axial strain during uniaxial particle compression	-
ν	Packing Poisson's ratio, defines the ratio of transverse strain to axial strain during uniaxial packing compression	-
ν_f	Kinematic fluid viscosity	$m^2 s^{-1}$
ω	Particle angular frequency	s^{-1}
Φ	Packing density	-
Φ_{crit}	Critical packing density	-
ρ	Density	-
ρ_f	Fluid density	$kg m^{-3}$
ρ_p	Particle density	$kg m^{-3}$
$\rho_{p,dry}$	Dry particle density	$kg m^{-3}$
σ	Stress	Pa
σ_0	Stress of the free spring in the SLS model	Pa

σ_1	Stress of the spring in the Kelvin or Maxwell element	Pa
σ_2	Stress of the dashpot in the Kelvin or Maxwell element	Pa
σ_g	Gravitational stress	Pa
σ_r	Radial stress	Pa
σ_z^2	Hydrodynamic dispersion	$\text{m}^2 \text{s}^{-2}$
τ	Relaxation time	s
τ	Stress tensor (Equation (4.2))	$\text{m}^2 \text{s}^{-2}$
τ_p	Dimensionless poroelastic relaxation time	-
τ_R	Ramp loading period	s
τ_w	Wall stress	Pa

14. List of Figures

3.1	Elastic contact between two spheres.	8
3.2	Rolling friction of a sphere at the contact surface.	11
3.3	Viscoelastic material behavior in the relationship of stress and strain. . .	15
3.4	Schematic representation of the SLS model types.	16
3.5	Solvent migration in the particle induced by an external load.	20
3.6	Limiting conditions of viscoelastic and poroelastic relaxation.	21
3.7	Porosity near solid walls.	25
3.8	Correlation of the contact number and the packing density.	33
3.9	Bulk (B) and shear (G) modulus as a function of the excess packing density.	34
3.10	Visualization of force chains.	36
3.11	Probability distribution of contact forces in a jammed packing.	37
3.12	Angular distribution of contacts in a force chain network.	38
3.13	Modes of packing compaction.	39
3.14	Forces acting on an axial segment of the compressible packed bed.	40
4.1	Simple linear spring-dashpot model.	47
4.2	Normal force calculated by the Hertz and Hooke contact model.	49
4.3	Particle within the computational domain.	52
5.1	Process flow chart and micro chromatography column.	56
5.2	Column operating set-up.	57
5.3	Schematic representation of the micromanipulation method using a flat punch indenter tip.	60
5.4	UVM measurements of the packing behavior.	64
5.5	Modular structure of the simulation programs.	71
5.6	Exemplary CFD mesh geometry for three-dimensional simulation cases. .	72
5.7	Boundary properties of the simulation cases.	74
5.8	Schematic representation of the <i>coarse grain</i> method.	76

6.1	Particle size distribution of resins SEP and TOY.	78
6.2	Scanning Electron Microscopy (SEM) images of resins CER, SEP and TOY. 80	
6.3	SEM images of a broken Sepahrose and Toyopearl particle.	81
6.4	Measured force relaxation of Sepharose and Toyopearl particles at three compression depths.	82
6.5	Exemplary compression force relaxation data of a Sepharose and a Toy- opearl particle.	83
6.6	Quasi-static compression of chromatographic particles.	86
6.7	Exemplary quasi-static compression data of both chromatographic particles. 87	
6.8	Normalized force relaxation responses for Sepharose and Toyopearl particles. 88	
6.9	Micro Computer Tomography (Micro CT) images of a Sepharose particle during micro manipulation.	90
6.10	Measured hysteresis of Sepharose and Toyopearl particles during compres- sion load relaxation experiments.	92
7.1	Packing pressure drop and bed height as a function of the fluid velocity. .	96
7.2	Particle Reynolds number as a function of the fluid velocity.	97
7.3	Packing compression-relaxation behavior at different hydrodynamic loads. 98	
7.4	CLSM images of the packing structure under hydrodynamic load.	99
7.5	UV-fluorescence microscopy images of the packing structure under hydro- dynamic load.	100
7.6	Semi-dry packing compression-relaxation behavior at different mechanical loads.	102
7.7	Wet packing compression-relaxation behavior at different mechanical loads. 103	
7.8	UV-fluorescence microscopy of the packing structure during mechanical compression.	104
7.9	Micro CT image of a packing of CaCl ₂ coated TOY particles.	105
7.10	X-ray attenuation of different material packings as a function of the pho- ton energy.	106
7.11	Micro CT image of TOY particles submerged in a contrast enhancing agent solution.	107
7.12	Influence of the column diameter on the packed bed pressure drop.	108
7.13	Logarithmic dependency of the packing pressure drop on the column di- ameter.	109

7.14	Characteristic packing compression-relaxation hystereses at different column diameters.	110
7.15	Logarithmic dependency of the packing compression on the column diameter.	111
7.16	Simulated packing behavior as a function of the column diameter according to the wall support model.	113
8.1	Comparison of nonlinear Hertz and linear Hooke particle contact models.	118
8.2	Effect of the amount of coarse graining on hydrodynamic column performance.	123
8.3	Effect of the amount of coarse graining on mechanical packing compression behavior.	124
8.4	Variation of the particle-particle as well as the rolling friction coefficients.	126
8.5	Comparison of measured and simulated packing pressure-flow dependency.	130
8.6	Comparison of the measured and simulated packing compression behavior during hydrodynamic load.	130
8.7	Comparison of the measured and simulated packing compression behavior during mechanical load.	131
9.1	Migration of Toyopearl SP-650M tracer particles in the 9.6 mm i.d. column during cyclic column operation.	136
9.2	Migration of Toyopearl SP-650M tracer particles in the 12.5 mm i.d. column during cyclic column operation.	136
9.3	Particle migration in the inner packing regions.	137
9.4	Migration of Toyopearl Butyl-650C tracer particles in the 12.5 mm i.d. column during cyclic column operation.	138
9.5	Particle migration in the inner packing regions using the Butyl-650C resin.	138
9.6	Migration of Toyopearl Butyl-650S tracer particles in the 9.6 mm i.d. column during cyclic column operation.	139
9.7	Migration of Toyopearl Butyl-650S tracer particles in the 12.5 mm i.d. column during cyclic column operation.	139
9.8	Effect of high flow velocity on the migration of small Toyopearl Butyl-650S tracer particles in the 9.6 mm i.d. column.	140
9.9	Homogeneous distribution of Butyl-650S tracer particles in the packing. .	141

9.10	Simulated particle rearrangement and migration in a packing with a bidisperse particle size distribution.	142
9.11	Simulated particle migration in a packing of a polydisperse particle size distribution.	143
9.12	Simulated influence of particle migration on the fluid flow distribution.	144
10.1	Simulation of the force transmission in a frictional particle packed bed.	150
10.2	Measured variations of the axial packing density profiles of the laboratory column during different hydrodynamic loads applied after packing.	153
10.3	Measured long-term axial packing density profiles of columns packed according to different methods.	156
10.4	Measured variation of the packing density profiles from the initial profile.	157
10.5	Simulation of the axial packing density profiles during long-term operation of columns packed according to different methods.	159
10.6	Comparison of the simulated and measured axial packing density profiles of columns packed according to different methods.	160
10.7	Force probability distribution in the simulated columns packed according to different methods.	161
10.8	Angular distribution of contact forces in packings packed by different methods.	162
10.9	Simulated radial fluctuations of the axial flow velocity and porosity distribution.	163
10.10	Calculated axial hydrodynamic dispersion in columns packed by the three different packing methods during operation.	165
11.1	Comparison of different simulated column packing methods.	176
B.1	Portable process control set-up.	215
B.2	Microfluidic flow cell.	216
B.3	Sequence of a coupled CFD-DEM simulation.	218
C.1	5-Amino-2,4,6-triiodoisophthalic acid x-ray tomography contrast agent	228
C.2	SLS model	229

15. List of Tables

3.1	Characteristics of ordered packings of equal rigid spheres.	24
5.1	Prepared packings and columns to use for the particle migration study. . .	67
5.2	Geometric properties of the CFD mesh.	73
6.1	Particle size distribution of various chromatographic resins on methacrylic and agarose basis.	78
6.2	Measured particle density of resin SEP and TOY.	79
6.3	Coefficients of the compression load relaxation model using $N = 2$	84
6.4	Fitted and calculated parameters of the SLS model.	87
6.5	Instantaneous and relaxed shear and Young's moduli of Sepharose and Toyopearl particles obtained by compression load relaxation experiments.	90
6.6	Instantaneous and relaxed shear and Young's moduli of Sepharose and Toyopearl particles obtained by quasi-static compression experiments. . .	91
7.1	Fitted parameters according to the TOY and SEP packings used in the continuum wall support model	114
8.1	DEM model parameters required by the Hooke contact model.	119
8.2	Computational effort and performance of simulations using different coarse graining values.	122
8.3	Computational effort and performance of simulations using 3D and pseudo 2D models.	125
8.4	DEM model parameters required by the Hooke contact model.	127
10.1	Deviations S_{mean} and S_{init} of the different column packing methods during a relative hydrodynamic load of RHL = 0.75.	154

11.1 Hydrodynamic shortcomings of chromatography columns packed with compressible polymeric resins and possible consequences.	175
A.1 Chromatographic media.	211
A.2 Chemicals and contrast agents.	212
A.3 Fluorescent dyes.	212
A.4 Optical measuring equipment.	213
A.5 Further equipment.	213
A.6 Software and operating systems.	213
B.1 Further parameters of the DEM-model.	216
B.2 Column wall and particle parameters of the DEM-model.	217
B.3 Boundary and initial conditions of the CFD-model	217
B.4 CFD-DEM coupling settings and submodels used in the simulations.	219
B.5 Numerical schemes used in the simulations.	219
C.1 Standard Laplacian transformation correlations.	231

16. Bibliography

- Alexander, S. (1998). ‘Amorphous solids: their structure, lattice dynamics and elasticity’. In: *Phys. Rep.* 296.2-4 (1998), pp. 65–236.
- Andreotti, B., Forterre, Y., and Pouliquen, O. (2013). *Granular Media*. Cambridge: Cambridge University Press, 2013.
- Baker, M. J. (2011). ‘CFD simulation of flow through packed beds using the finite volume technique’. Doctoral thesis. University of Exeter, 2011.
- Baumberger, T. and Caroli, C. (2005). ‘Solid Friction from stick-slip to pinning and aging’. In: *Adv. Phys.* 55.3 (2005), pp. 279–348.
- Baumberger, T., Heslot, F., and Perrin, B. (1994). ‘Crossover from creep to inertial motion in friction dynamics’. In: *Nature* 367.6463 (1994), pp. 544–546.
- Bear, J. (1988). *Dynamics of Fluids in Porous Media*. New York: Dover, 1988.
- Bemberis, I., Noyes, A., and Natarajan, V. (2003). ‘Column packing for process-scale chromatography: guidelines for reproducibility’. In: *BioPharm Int* July (2003), pp. 23–30.
- Bey, O. and Eigenberger, G. (1997). ‘Fluid flow through catalyst filled tubes’. In: *Chem. Eng. Sci.* 52.8 (1997), pp. 1365–1376.
- Biggs, M. J., Glass, D., Xie, L., Zivkovic, V., Buts, A., and Curt Kounders, M. A. (2008). ‘Granular temperature in a gas fluidized bed’. In: *Granul. Matter* 10.2 (2008), pp. 63–73.
- Biot, M. A. (1941). ‘General theory of three-dimensional consolidation’. In: *J. Appl. Phys.* 12.1925 (1941), pp. 110–113.
- Biot, M. A. (1956). ‘Theory of deformation of a porous viscoelastic anisotropic solid’. In: *J. Appl. Phys.* 27.5 (1956), pp. 459–467.
- Biot, M. A. (1962). ‘Mechanics of deformation and acoustic propagation in porous media’. In: *J. Appl. Phys.* 33.4 (1962), pp. 1482–1498.
- Biot, M. A. (1963). ‘Theory of Stability and Consolidation of a Porous Medium Under Initial Stress’. In: *J. Math. Mech.* 12.4 (1963), pp. 521–542.

- Boschetti, E. (1994). ‘Advanced sorbents for preparative protein separation purposes’. In: *J. Chromatogr. A* 658.2 (1994), pp. 207–236.
- Bowes, B. D., Koku, H., Czymmek, K. J., and Lenhoff, A. M. (2009). ‘Protein adsorption and transport in dextran-modified ion-exchange media I. Adsorption’. In: *J. Chromatogr. A* 1216.45 (2009), pp. 7774–7784.
- Bruns, S., Grinias, J. P., Blue, L. E., Jorgenson, J. W., and Tallarek, U. (2012a). ‘Morphology and separation efficiency of low-aspect-ratio capillary ultrahigh pressure liquid chromatography columns’. In: *Anal. Chem.* 84.10 (May 2012), pp. 4496–4503.
- Bruns, S., Stoeckel, D., Smarsly, B. M., and Tallarek, U. (2012b). ‘Influence of particle properties on the wall region in packed capillaries’. In: *J. Chromatogr. A* 1268 (2012), pp. 53–63.
- Bulmer, M. G. (1979). *Principles of Statistics*. New York: Dover, 1979.
- Carta, G. and Jungbauer, A. (2010). *Protein Chromatography*. WILEY-VCH Verlag, 2010.
- Chang, Y. K. and Chase, H. A. (1994). ‘Direct extraction of proteins using STREAMLINE ion exchangers in expanded beds’. In: *ICHEME - Adv. Biochem. Eng.* 118. Warwickshire: Institution of Chemical Engineers, 1994.
- Chantler, C. T., Olsen, K., Dragoset, R. A., Chang, J., Kishore, A. R., Kotochigova, S. A., and Zucker, D. S. (2005). *X-ray Form Factor, Attenuation, and Scattering Tables*. 2005. URL: <http://physics.nist.gov/PhysRefData/FFast/html/form.html> (visited on 03/06/2017).
- Cheng, L., Xia, X., Scriven, L. E., and Gerberich, W. W. (2005). ‘Spherical-tip indentation of viscoelastic material’. In: *Mech. Mater.* 37.1 (2005), pp. 213–226.
- Cherrak, D. E., Al-Bokari, M., Drumm, E. C., and Guiochon, G. A. (2002). ‘Behavior of packing materials in axially compressed chromatographic columns’. In: *J. Chromatogr. A* 943.1 (2002), pp. 15–31.
- Coulomb, C. A. (1785). ‘Premier-[troisième] mémoire sur l’électricité et le magnétisme’. In: *Académie R. des Sci.* (1785).
- Cundall, P. A. and Strack, O. D. L. (1979). ‘A discrete numerical model for granular assemblies’. In: *Géotechnique* 29.1 (1979), pp. 47–65.
- Daneyko, A., Hlushkou, D., Khirevich, S., and Tallarek, U. (2012). ‘From random sphere packings to regular pillar arrays: Analysis of transverse dispersion’. In: *J. Chromatogr. A* 1257 (2012), pp. 98–115.
- de Gennes, P. (1999). ‘Granular matter: a tentative view’. In: *Rev. Mod. Phys.* 71.2 (1999), S374–S382.

- DePhillips, P. and Lenhoff, A. M. (2000). ‘Pore size distributions of cation-exchange adsorbents determined by inverse size-exclusion chromatography’. In: *J. Chromatogr. A* 883.1-2 (2000), pp. 39–54.
- Di Giuseppe, E., Moroni, M., and Caputo, M. (2010). ‘Flux in porous media with memory: Models and experiments’. In: *Transp. Porous Media* 83.3 (Aug. 2010), pp. 479–500.
- Di Renzo, A. and Di Maio, F. P. (2004). ‘Comparison of contact-force models for the simulation of collisions in DEM-based granular flow codes’. In: *Chem. Eng. Sci.* 59.3 (2004), pp. 525–541.
- Dorn, M. and Hekmat, D. (2016). ‘Simulation of the dynamic packing behavior of preparative chromatography columns via discrete particle modeling’. In: *Biotechnol. Prog.* 32.2 (2016), pp. 363–371.
- Drescher, A. and de Josselin de Jong, G. (1972). ‘Photoelastic verification of a mechanical model for the flow of a granular material’. In: *J. Mech. Phys. Solids* 20.5 (1972), pp. 337–340.
- Dullen, F. A. L. (1992). *Porous Media - Fluid Transport and Pore Structure*. 2nd. New York: Academic Press, 1992.
- Dwivedi, P. N and Upadhyay, S. N. (1977). ‘Particle-fluid mass transfer in fixed and fluidized beds’. In: *Ind. Eng. Chem.* 16.2 (1977), pp. 157–165.
- Ellenbroek, W. G., Somfai, E., van Hecke, M., and Van Saarloos, W. (2006). ‘Critical scaling in linear response of frictionless granular packings near jamming’. In: *Phys. Rev. Lett.* 97.25 (2006), pp. 1–4.
- Ellenbroek, W. G., Zeravcic, Z., Van Saarloos, W., and van Hecke, M. (2009). ‘Non-affine response: Jammed packings vs. spring networks’. In: *EPL* 87.3 (2009), p. 34004.
- Ergun, S. (1952). ‘Fluid flow through packed columns’. In: *Chem. Eng. Prog.* (1952).
- Ettre, L. S. and Sakodyskii, K. I. (1993). ‘M.S. Tswett and the discovery of chromatography. I: Early work (1899-1903)’. In: *Chromatographia* 35.3-4 (1993), pp. 223–231.
- Felinger, A. and Guiochon, G. A. (1993). ‘Comparison of maximum production rates and optimum operating/design parameters in overloaded elution and displacement chromatography.’ In: *Biotechnol. Bioeng.* 41.1 (Jan. 1993), pp. 134–47.
- Gavara, Poondi, Bibi, Noor, Sanchez, Mirna, Grasselli, Mariano, and Fernandez-Lahore, Marcelo (2015). ‘Chromatographic Characterization and Process Performance of Column-Packed Anion Exchange Fibrous Adsorbents for High Throughput and High Capacity Bioseparations’. In: *Processes* 3.1 (2015), pp. 204–221.

- GE Healthcare (2014). *Sepharose™ Fast Flow ion exchange media and prepacked column formats*. 2014. URL: https://www.gelifesciences.com/gehcls%7B%5C_%7Dimages/GELS/Related%20Content/Files/1314742967685/litdoc18117722%7B%5C_%7D20130730230933.pdf.
- Geng, J., Reydellet, G., Clément, E., and Behringer, R. P. (2003). ‘Green’s function measurements of force transmission in 2D granular materials’. In: *Phys. D Nonlinear Phenom.* 182.3-4 (2003), pp. 274–303.
- Gerontas, S., Lan, T., Micheletti, M., and Titchener-Hooker, N. J. (2015). ‘Evaluation of a structural mechanics model to predict the effect of inserts in the bed support of chromatographic columns’. In: *Chem. Eng. Sci.* 129 (2015), pp. 25–33.
- Gilmour, T. H. J. (2009). ‘Notes on Technic. A method of staining Sephadex particles for the study of filter feeding systems in animals’. In: *Stain Technol.* 54.5 (2009), pp. 281–295.
- Golshan-Shirazi, S. and Guiochon, G. A. (1989). ‘Theory of Optimization of the Experimental Conditions of Preparative Elution Chromatography: Optimization of the Column Efficiency’. In: *Anal. Chem.* 61.2 (1989), pp. 1368–1382.
- Golshan-Shirazi, S. and Guiochon, G. A. (1990). ‘Optimization of the experimental conditions in preparative liquid chromatography with touching bands’. In: *J. Chromatogr.* 517 (1990), pp. 229–256.
- Goniva, C., Kloss, C., Deen, N. G., Kuipers, J. a. M., and Pirker, S. (2012). ‘Influence of rolling friction on single spout fluidized bed simulation’. In: *Particuology* 10.5 (2012), pp. 582–591.
- Govedarica, B., Ilić, I., Šibanc, R., Dreu, R., and Srčić, S. (2012). ‘The use of single particle mechanical properties for predicting the compressibility of pharmaceutical materials’. In: *Powder Technol.* 225 (2012), pp. 43–51.
- Guiochon, G. A. (2006). ‘The limits of the separation power of unidimensional column liquid chromatography’. In: *J. Chromatogr. A* 1126 (2006), pp. 6–49.
- Guiochon, G. A. and Lin, B. (2003). *Modeling for Preparative Chromatography*. New York: Elsevier Science, 2003.
- Hager, A., Kloss, C., Pirker, S., and Goniva, C. (2012). ‘Parallel Open Source CFD-DEM for Resolved Particle-Fluid Interaction’. In: *Proc. 9th Int. Conf. Comput. Fluid Dyn. Miner. Process Ind.* December (2012), pp. 1–6.

- Hassan, S., Titchener-Hooker, N. J., and Willoughby, N. (2005). ‘Determining particle density distribution of expanded bed adsorbents’. In: *Biotechnol. Bioeng.* 92.5 (2005), pp. 659–663.
- Heikens, D., Sjoerdsma, S. D., and Coumans, W. J. (1981). ‘A mathematical relation between volume strain, elongational strain and stress in homogeneous deformation’. In: *J. Mater. Sci.* 16.2 (1981), pp. 429–432.
- Hekmat, D., Kuhn, M., Meinhardt, V., and Weuster-Botz, D. (2013). ‘Modeling of transient flow through a viscoelastic preparative chromatography packing’. In: *Biotechnol. Prog.* 29.4 (2013), pp. 958–967.
- Hekmat, D., Mornhinweg, R., Bloch, G., Sun, Y., Jeanty, P., Neubert, M., and Weuster-Botz, D. (2011). ‘Macroscopic investigation of the transient hydrodynamic memory behavior of preparative packed chromatography beds’. In: *J. Chromatogr. A* 1218.7 (Mar. 2011), pp. 944–950.
- Hendrickson, B. and Devine, K. (2000). ‘Dynamic load balancing in computational mechanics’. In: *Comput. Methods Appl. Mech. Eng.* 184.2-4 (2000), pp. 485–500.
- Hertz, H. (1881). ‘Über die Berührung fester elastischer Körper’. In: *J. für die reine und Angew. Math.* 171 (1881), pp. 156–171.
- Hinrichsen, H. and Wolf, D. E., eds. (2004). *The Physics of Granular Media*. Weinheim: WILEY-VCH Verlag, 2004.
- Holdich, R. G. (2002). *Fundamentals of Particle Technology*. Shephed: Midland Information Technology and Publishing, 2002.
- Howell, D. W., Behringer, R. P., and Veje, C. T. (1999). ‘Fluctuations in granular media.’ In: *Chaos* 9.3 (1999), pp. 559–572.
- Hu, Y., Chen, X., Whitesides, G. M., Vlassak, J. J., and Suo, Z. (2011). ‘Indentation of polydimethylsiloxane submerged in organic solvents’. In: *J. Mater. Res.* 26.06 (2011), pp. 785–795.
- Hu, Y. and Suo, Z. (2012). ‘Viscoelasticity and poroelasticity in elastomeric gels’. In: *Acta Mech. Solida Sin.* 25.5 (2012), pp. 441–458.
- Hu, Y., You, J.-O., Auguste, D. T., Suo, Z., and Vlassak, J. J. (2012). ‘Indentation: A simple, nondestructive method for characterizing the mechanical and transport properties of pH-sensitive hydrogels’. In: *J. Mater. Res.* 27.01 (2012), pp. 152–160.
- Hu, Y., Zhao, X.-H., Vlassak, J. J., and Suo, Z. (2010). ‘Using indentation to characterize the poroelasticity of gels’. In: *Appl. Phys. Lett.* 96.12 (2010), pp. 11–14.

- Hubbell, J. H. and Kula, M. R. (2008). ‘Confocal laser scanning microscopy as an analytical tool in chromatographic research.’ In: *Bioprocess Biosyst. Eng.* 31.3 (Apr. 2008), pp. 241–259.
- Ioannidis, N., Bowen, J., Pacek, A., and Zhang, Z. (2012). ‘Manufacturing of agarose-based chromatographic adsorbents - Effect of ionic strength and cooling conditions on particle structure and mechanical strength’. In: *J. Colloid Interface Sci.* 367.1 (Mar. 2012), pp. 153–160.
- Issa, R. I. (1986). ‘Solution of the implicitly discretised fluid flow equations by operator-splitting’. In: *J. Comput. Phys.* 62.1 (1986), pp. 40–65.
- Jaeger, H. M., Nagel, S. R., and Behringer, R. P. (1996). ‘Granular solids, liquids, and gases’. In: *Rev. Mod. Phys.* 68.4 (1996), pp. 1259–1273.
- Jin, Y. and Makse, H. A. (2010). ‘A first-order phase transition defines the random close packing of hard spheres’. In: *Phys. A Stat. Mech. its Appl.* 389.23 (2010), pp. 5362–5379.
- Johnson, I. and Spence, M. T. Z., eds. (2010). *Molecular Probes Handbook, A Guide to Fluorescent Probes and Labeling Technologies, 11th Edition*. Life Technologies Corporation, 2010.
- Johnson, K. L. (1985). *Contact Mechanics*. Cambridge: Cambridge University Press, 1985.
- Jönsson, K. and Jönsson, B. T. L. (1992a). ‘Fluid flow in compressible porous media: I: Steady-state conditions’. In: *AIChE J.* 38.9 (1992).
- Jönsson, K. and Jönsson, B. T. L. (1992b). ‘Fluid flow in compressible porous media: II: Dynamic behavior’. In: *AIChE J.* 38.9 (1992), pp. 1349–1356.
- Jungbauer, A. (2005). ‘Chromatographic media for bioseparation’. In: *J. Chromatogr. A* 1065.1 (2005), pp. 3–12.
- Kafui, K. D., Thornton, C., and Adams, M. J. (2002). ‘Discrete particle-continuum fluid modelling of gas-solid fluidised beds’. In: *Chem. Eng. Sci.* 57.13 (2002), pp. 2395–2410.
- Kalcioglu, Z. I., Mahmoodian, R., Hu, Y., Suo, Z., and Van Vliet, K. J. (2012). ‘From macro- to microscale poroelastic characterization of polymeric hydrogels via indentation’. In: *Soft Matter* 8.12 (2012), pp. 3393–3398.
- Kapur, V., Charkoudian, J. C., Kessler, S. B., and Anderson, J. L. (1996). ‘Hydrodynamic Permeability of Hydrogels Stabilized within Porous Membranes’. In: *Ind. Eng. Chem. Res.* 5885.96 (1996), pp. 3179–3185.

- Kaufman, J. D., Miller, G. J., Morgan, E. F., and Klapperich, C. M. (2008). ‘Time-dependent mechanical characterization of poly(2-hydroxyethyl methacrylate) hydrogels using nanoindentation and unconfined compression’. In: (2008).
- Keener, R. N., Maneval, J. E., and Fernandez, E. J. (2004a). ‘Toward a robust model of packing and scale-up for chromatographic beds. 1. Mechanical compression’. In: *Biotechnol. Prog.* 20.4 (2004), pp. 1146–1158.
- Keener, R. N., Maneval, J. E., and Fernandez, E. J. (2004b). ‘Toward a Robust Model of Packing and Scale-Up for Chromatographic Beds. 2. Flow Packing’. In: *Biotechnol. Prog.* 20.4 (2004), pp. 1159–1168.
- Keener, R. N., Maneval, J. E., Östergren, K. C. E., and Fernandez, E. J. (2002). ‘Mechanical deformation of compressible chromatographic columns’. In: *Biotechnol. Prog.* 18.3 (2002), pp. 587–596.
- Khirevich, S., Daneyko, A., Hölzel, A., Seidel-Morgenstern, A., and Tallarek, U. (2010). ‘Statistical analysis of packed beds, the origin of short-range disorder, and its impact on eddy dispersion’. In: *J. Chromatogr. A* 1217.28 (2010), pp. 4713–4722.
- Kloss, C., Goniva, C., Hager, A., Amberger, S., and Pirker, S. (2012). ‘Models, algorithms and validation for opensource DEM and CFD-DEM’. In: *Prog. Comput. Fluid Dyn.* 12 (2012), pp. 140–152.
- Knox, J. H., Laird, G. R., and Raven, P. A. (1976). ‘Interaction of radial and axial dispersion in liquid chromatography in relation to the “infinite diameter effect”’. In: *J. Chromatogr. A* 122 (1976), pp. 129–145.
- Knox, J. H. and Parcher, J. F. (1969). ‘Effect of the column to particle diameter ratio on the dispersion of unadsorbed solutes in chromatography’. In: *Anal. Chem.* 41.12 (Oct. 1969), pp. 1599–1606.
- Knox, J. H. and Pyper, H. M. (1986). ‘Framework for maximizing throughput in preparative liquid chromatography’. In: *J. Chromatogr. A* 363.1 (1986).
- Koch, D. L. and Hill, R. J. (2001). ‘Inertial effects in suspension and porous-media flows’. In: *Annu. Rev. Fluid Mech.* 33 (2001), pp. 619–647.
- Koh, J.-H. and Guiochon, G. A. (1998). ‘Effect of the column length on the characteristics of the packed bed and the column efficiency in a dynamic axial compression column’. In: *J. Chromatogr. A* 796.1 (1998), pp. 41–57.
- Kohl, M. and Schmiedeberg, M. (2014). ‘Particle segregation in a sedimenting bidisperse soft sphere system’. In: *Soft Matter* 10.24 (2014), p. 4340.

- Kong, X. Z., Kinzelbach, W., and Stauffer, F. (2010). ‘Compaction and size segregation in a liquid-saturated grain packing due to pulsation effect during air injection’. In: *Chem. Eng. Sci.* 65.9 (2010), pp. 2680–2688.
- Kraul & Wilkening u. Stelling GmbH (2017). *Ethanol-Wasser-Gemische*. 2017. URL: http://www.kwst.com/fileadmin/media/PDF/Dichte%7B%5C_%7DEthanol%7B%5C_%7DWasser%7B%5C_%7DGemische%7B%5C_%7D0513.pdf (visited on 01/10/2017).
- Ladisch, M. R. (2001). *Bioseparations Engineering: Principles, Practice, and Economics*. Wiley-Interscience, 2001.
- Ladisch, M. R. and Tsao, G. T. (1978). ‘Theory and practice of rapid liquid chromatography at moderate pressures using water as eluent’. In: *J. Chromatogr.* 166 (1978), pp. 85–100.
- Lan, T., Gerontas, S., Smith, G. R., Langdon, J., Ward, J. M., and Titchener-Hooker, N. J. (2012). ‘Investigating the use of column inserts to achieve better chromatographic bed support’. In: *Biotechnol. Prog.* 28.5 (2012), pp. 1285–1291.
- Larson, T. M., Davis, J., Lam, H., and Cacia, J. (2003). ‘Use of process data to assess chromatographic performance in production-scale protein purification columns’. In: *Biotechnol. Prog.* 19.2 (2003), pp. 485–492.
- Lecheler, S. (2009). *Numerische Strömungsberechnung*. Wiesbaden: Vieweg+Teubner GWV Fachverlage GmbH, 2009.
- Lee, E. H. and Radok, J. R. M. (1960). ‘The Contact Problem for Viscoelastic Bodies’. In: *J. Appl. Mech.* 27.3 (1960), pp. 438–444.
- Legendre, D., Daniel, C., and Guiraud, P. (2005). ‘Experimental study of a drop bouncing on a wall in a liquid’. In: *Phys. Fluids* 17.9 (2005), pp. 1–13.
- Levison, P. R. and Mumford, C. (1997). ‘Performance comparison of low-pressure ion-exchange chromatography media for protein separation’. In: *J. Chromatogr. A* 760.1 (1997), pp. 151–158.
- LIGGGHTS (2016). *LAMMPS improved for general granular and general heat transfer simulations*. 2016. URL: <http://www.cfdem.com>.
- Lin, D. C., Dimitriadis, E. K., and Horkay, F. (2007). ‘Elasticity of rubber-like materials measured by AFM nanoindentation’. In: *Express Polym. Lett.* 1.9 (2007), pp. 576–584.
- Lin, D. C., Shreiber, D. I., Dimitriadis, E. K., and Horkay, F. (2009). ‘Spherical indentation of soft matter beyond the Hertzian regime: Numerical and experimental validation of hyperelastic models’. In: *Biomech. Model. Mechanobiol.* 8.5 (2009), pp. 345–358.

- Lottes, F., Arlt, W., Minceva, M., and Stenby, E. H. (2009). ‘Hydrodynamic impact of particle shape in slurry packed liquid chromatography columns’. In: *J. Chromatogr. A* 1216.30 (July 2009), pp. 5687–5695.
- Lovoll, G., Maloy, K. J., and Flekkoy, E. G. (1999). ‘Force measurements on static granular materials’. In: *Phys. Rev. E* 60.5 (1999), p. 7.
- Magnanimo, V., La Ragione, L., Jenkins, J., Wang, P., and Makse, H. A. (2008). ‘Characterizing The Shear And Bulk Moduli Of An Idealized Granular Material’. In: *Europhys. Lett.* 81.3 (2008), p. 34006.
- Mahadevan, A. and Orpe, A. V. (2012). ‘Flow-induced channelization in a porous medium’. In: *EPL* 98.5 (June 2012), p. 58003.
- Majmudar, T. S. and Behringer, R. P. (2005). ‘Contact force measurements and stress-induced anisotropy in granular materials.’ In: *Nature* 435.7045 (2005), pp. 1079–1082.
- Makse, H. A., Gland, N., Johnson, D. L., and Schwartz, L. M. (1999). ‘Why Effective Medium Theory Fails in Granular Materials’. In: *Phys. Rev. Lett.* 83.24 (1999), pp. 5070–5073.
- Makse, H. A., Johnson, D. L., and Schwartz, L. M. (2000). ‘Packing of Compressible Granular Materials’. In: *Phys. Rev. Lett.* (2000), p. 4.
- Mattei, G., Gruca, G., Rijnveld, N., and Ahluwalia, A. (2015). ‘The nano-epsilon dot method for strain rate viscoelastic characterisation of soft biomaterials by spherical nano-indentation’. In: *J. Mech. Behav. Biomed. Mater.* 50 (2015), pp. 150–159.
- Mattice, J., Lau, A., Oyen, M. L., and Went, R. (2006). ‘Spherical indentation load-relaxation of soft biological tissues’. In: *J. Mater. Res.* 21 (2006), pp. 2003–2010.
- McCue, J. T., Cecchini, D., Chu, C., Liu, W. H., and Spann, A. (2007). ‘Application of a two-dimensional model for predicting the pressure-flow and compression properties during column packing scale-up’. In: *J. Chromatogr. A* 1145.1-2 (Mar. 2007), pp. 89–101.
- Mukhopadhyay, S. and Peixinho, J. (2011). ‘Packings of deformable spheres’. In: *Phys. Rev. E - Stat. Nonlinear, Soft Matter Phys.* 84.1 (2011), pp. 2–6.
- Müller, E. (2005). ‘Properties and Characterization of High Capacity Resins for Biochromatography’. In: *Chem. Eng. Technol.* 28.11 (2005), pp. 1295–1305.
- Müller, E., Chung, J.-T., Zhang, Z., and Sprauer, A. (2005). ‘Characterization of the mechanical properties of polymeric chromatographic particles by micromanipulation.’ In: *J. Chromatogr. A* 1097.1-2 (Dec. 2005), pp. 116–23.

- Nguyen, V. B., Wang, C. X., Thomas, C. R., and Zhang, Z. (2009). ‘Mechanical properties of single alginate microspheres determined by microcompression and finite element modelling’. In: *Chem. Eng. Sci.* 64.5 (2009), pp. 821–829.
- Norouzi, H. R., Zarghami, R., Sotuddeh-Gharebagh, R., and Mostoufi, N. (2016). *Coupled CFD-DEM Modeling: Formulation, Implementation and Application to Multiphase Flows*. 1st ed. Chichester: John Wiley & Sons, Ltd, 2016.
- O’Hern, C., Silbert, L. E., and Nagel, S. R. (2003). ‘Jamming at zero temperature and zero applied stress: The epitome of disorder’. In: *Phys. Rev. E* 68.1 (2003), p. 11306.
- OpenFOAM Foundation (2016). *OpenFOAM User Guide*. 2016. URL: <https://cfd.direct/openfoam/user-guide/> (visited on 04/20/2017).
- Östergren, K. C. E. and Trägårdh, A. C. (1997). ‘Numerical Study of Two-Dimensional Compaction, Flow, and Dispersion in a Chromatographic Column’. In: *Numer. Heat Transf. Part A Appl.* 32.3 (1997), pp. 247–265.
- Östergren, K. C. E. and Trägårdh, A. C. (1998). ‘Deformation of a chromatographic bed during steady-state liquid flow’. In: *AIChE J.* 4.1 (1998).
- Östergren, K. C. E. and Trägårdh, A. C. (1999). ‘Modelling and analysis of axial flow through and compression of a non-rigid chromatographic bed’. In: *Chem. Eng. J.* 72.2 (1999), pp. 153–161.
- Oyen, M. L. (2014). ‘Mechanical characterisation of hydrogel materials’. In: *Int. Mater. Rev.* 59.1 (2014), pp. 44–59.
- Patankar, N. A., Singh, P., Joseph, D. D., Glowinski, R., and Pan, T. W. (2000). ‘A new formulation of the distributed Lagrange multiplier/fictitious domain method for particulate flows’. In: *Int. J. Multiph. Flow* 26.9 (2000), pp. 1509–1524.
- Patankar, S. V. and Spalding, D. B. (1980). *Numerical heat transfer and fluid flow*. New York: McGraw-Hill Book Company, 1980.
- Plimpton, S. J. (1995). ‘Fast parallel algorithms for short-range molecular dynamics’. In: *J. Comput. Phys.* 117 (1995), pp. 1–19.
- Pöschel, T. and Schwager, T. (2005). *Computational Granular Dynamics*. Berlin - Heidelberg: Springer-Verlag, 2005.
- Rad, M. N. S., Khalafi-Nezhad, A., Asrari, Z., Behrouz, S., Amini, Z., and Behrouz, M. (2009). ‘One-Pot Synthesis of Sulfonamides from Primary and Secondary Amine Derived Sulfonate Salts Using Cyanuric Chloride’. eng. In: *Synthesis (Stuttg.)* 23 (2009), pp. 3983–3988.

- Radjai, F., Roux, S., and Moreau, J. J. (1999). ‘Contact forces in a granular packing.’ In: *Chaos* 9.3 (1999), pp. 544–550.
- Rathore, A. S. and Velayudhan, A. (2003). *Scale-Up and Optimization in Preparative Chromatography*. New York - Basel: Marcel Dekker, 2003.
- Reid, F. J. L. and Smith, L. A. (2005). *Performance and Profiling of the LAMMPS Code on HPCx*. Tech. rep. HPCx UoE Ltd., 2005.
- Sabine, P. and Plumptre, C. (1985). *Statistics*. London: Palgrave Mcmillan UK, 1985.
- Sakai, M., Abe, M., Shigeto, Y., Mizutani, S., Takahashi, H., Viré, A., Percival, J. R., Xiang, J., and Pain, C. C. (2014). ‘Verification and validation of a coarse grain model of the DEM in a bubbling fluidized bed’. In: *Chem. Eng. J.* 244 (2014), pp. 33–43.
- Schilde, C., Burmeister, C. F., and Kwade, A. (2014). ‘Measurement and simulation of micromechanical properties of nanostructured aggregates via nanoindentation and DEM-simulation’. In: *Powder Technol.* 259 (2014), pp. 1–13.
- Schmidt, I., Lottes, F., Minceva, M., Arlt, W., and Stenby, E. H. (2011). ‘Estimation of chromatographic columns performances using computer tomography and CFD simulations’. In: *Chemie-Ingenieur-Technik* 83.1-2 (2011), pp. 130–142.
- Schmidt, I., Minceva, M., and Arlt, W. (2012). ‘Selection of stationary phase particle geometry using X-ray computed tomography and computational fluid dynamics simulations’. In: *J. Chromatogr. A* (2012).
- Schmidt-Traub, H., ed. (2005). *Preparative Chromatography of Fine Chemicals and Pharmaceutical Agents*. 1st ed. Weinheim: WILEY-VCH Verlag, 2005.
- Schwager, T. and Pöschel, T. (2007). ‘Coefficient of restitution and linear-dashpot model revisited’. In: *Granul. Matter* 9.6 (2007), pp. 465–469.
- Schwarze, R. (2013). *CFD-Modellierung: Grundlagen und Anwendungen bei Strömungsprozessen*. Berlin: Springer Vieweg, 2013.
- Scott, G. D. (1960). ‘Packing of spheres’. In: *Nature* 188 (1960), pp. 908–909.
- Scott, G. D. and Kilgour, D. M. (1969). ‘The density of random close packing of spheres’. In: *J. Phys. D. Appl. Phys.* 2.6 (1969), pp. 863–866.
- Shadday, M. A. (2006). ‘A one-dimensional transient model of down-flow through a swelling packed porous bed’. In: *Chem. Eng. Sci.* 61.8 (2006), pp. 2688–2700.
- Shalliker, R. A., Wong, V., Broyles, B. S., and Guiochon, G. A. (2002). ‘Visualization of bed compression in an axial compression liquid chromatography column’. In: *J. Chromatogr. A* 977.2 (2002), pp. 213–223.

- Snyder, L. R., Dolan, J. W., and Cox, G. B. (1989). ‘Preparative high-performance liquid chromatography under gradient conditions : III. Craig simulations for heavily overloaded separations’. In: *J. Chromatogr. A* 484 (1989), pp. 437–450.
- Somfai, E., van Hecke, M., Ellenbroek, W. G., Shundyak, K., and Van Saarloos, W. (2007). ‘Critical and noncritical jamming of frictional grains’. In: *Phys. Rev. E - Stat. Nonlinear, Soft Matter Phys.* 75.2 (2007), pp. 1–4.
- Song, C., Wang, P., and Makse, H. A. (2010). ‘Theory of random packings’. In: *AIP Conf. Proc.* 1227.2 (2010), pp. 271–279.
- Soriano, R., Bautista, L. F., Escobedo, J. F., Martínez, M., and Aracil, J. (2000). ‘Use of Anion Exchangers for the Separation of Two Isoenzymes of Glucoanalyse from *Aspergillus niger*’. In: *Proc. IEX 2000*. Ed. by J.A. Greig. London: Imperial College Press, 2000.
- Stanley, Brett J., Sarker, M., and Guiochon, G. A. (1996). ‘Consolidation of the packing material in chromatographic columns under dynamic axial compression. IV. Mechanical properties of some packing materials’. In: *J. Chromatogr. A* 741.2 (1996), pp. 175–184.
- Stickel, J. J. and Fotopoulos, A. (2001). ‘Pressure-Flow Relationships for Packed Beds of Compressible Chromatography Media at Laboratory and Production Scale’. In: *Biotechnol. Prog.* 17.4 (2001), pp. 744–751.
- Stieß, M. (2009). *Mechanische Verfahrenstechnik – Partikeltechnologie 1*. Berlin - Heidelberg: Springer-Verlag, 2009.
- Stock, S. R. (2009). *Micro computed tomography: Methodology and Applications*. Boca Raton, FL: CRC Press, 2009.
- Susanto, A. and Herrmann, T. (2007). ‘Investigation of pore diffusion hindrance of monoclonal antibody in hydrophobic interaction chromatography using confocal laser scanning microscopy’. In: *J. Chromatogr. A* 1149.2 (May 2007), pp. 178–188.
- Teeters, M. A. and Quiñones-García, I. (2005). ‘Evaluating and monitoring the packing behavior of process-scale chromatography columns’. In: *J. Chromatogr. A* 1069.1 (2005), pp. 53–64.
- Teske, C. A., Schroeder, M., and Simon, R. (2005). ‘Protein-Labeling Effects in Confocal Laser Scanning Microscopy’. In: *J. Phys. Chem. B* (2005), pp. 13811–13817.
- Teske, C. A. and von Lieres, E. (2006). ‘Competitive adsorption of labeled and native protein in confocal laser scanning microscopy’. In: *Biotechnol. Bioeng.* 2005 (2006).

- Thömmes, J. (1999). ‘Matrices for Fluidized Bed Adsorption’. In: *New Enzym. Org. Synth.* Ed. by T. Scheper. Heidelberg: Springer-Verlag, 1999. Chap. 2.3.
- Tiller, Frank M. and Lu, W.-M. (1972). ‘The Role of Porosity in Filtration VIII: Cake Nonuniformity in Compression-Permeability Cells’. In: *AIChE J.* 18.3 (1972), pp. 569–572.
- Tirella, A., Mattei, G., and Ahluwalia, A. (2014). ‘Strain rate viscoelastic analysis of soft and highly hydrated biomaterials’. In: *J. Biomed. Mater. Res. - Part A* 102.10 (2014), pp. 3352–3360.
- Tkachenko, A. V and Witten, T. A. (1999). ‘Stress propagation through frictionless granular material’. In: *Phys. Rev. E* 60.1 (1999), pp. 687–696.
- Toohey, K. S., Kalyanam, S., Palaniappan, J., and Insana, M. F. (2016). ‘Indentation analysis of biphasic viscoelastic hydrogels’. In: *Mech. Mater.* 92 (2016), pp. 175–184.
- Tran, R., Joseph, J. R., and Sinclair, A. (2007). ‘A Framework for the Prediction of Scale-Up When Using Compressible Chromatographic Packings’. In: *Biotechnol. Prog.* 23.2 (2007), pp. 413–422.
- Trujillo, L. and Herrmann, H. J. (2003). ‘Hydrodynamic model for particle size segregation in granular media’. In: *Phys. A Stat. Mech. its Appl.* 330.3-4 (2003), pp. 519–542.
- Tsuji, Takuya, Yabumoto, Keizo, and Tanaka, Toshitsugu (2008). ‘Spontaneous structures in three-dimensional bubbling gas-fluidized bed by parallel DEM-CFD coupling simulation’. In: *Powder Technol.* 184.2 (2008), pp. 132–140.
- van Buijtenen, M. S., van Dijk, W.-J., Deen, N. G., Kuipers, J. A. M., Leadbeater, T., and Parker, D. J. (2011). ‘Numerical and experimental study on multiple-spout fluidized beds’. In: *Chem. Eng. Sci.* 66.11 (2011), pp. 2368–2376.
- van Hecke, M. (2010). ‘Jamming of soft particles: geometry, mechanics, scaling and isotaticity’. In: *J. Phys. Condens. Matter* 22.3 (2010), p. 033101.
- Verhoff, F. H. and Furjanic Jr., J. J. (1983). ‘Compressible packed bed fluid dynamics with application to a glucose isomerase reactor’. In: *Ind. Eng. Chem. Process Des. Dev.* (1983), pp. 192–198.
- Verlet, L. (1967). ‘Computer "Experiments" on Classical Fluids. I. Thermodynamical Properties of Lennard-Jones Molecules’. In: *Phys. Rev.* 159.1 (1967), pp. 98–103.
- Versteeg, H. K. and Malalasekera, W. (2007). *An introduction to computational fluid dynamics: The finite volume method*. 2nd. Harlow, England and New York: Pearson Education Ltd., 2007.

- Wang, Q.-M., Mohan, A. C., Oyen, M. L., and Zhao, X.-H. (2014). ‘Separating viscoelasticity and poroelasticity of gels with different length and time scales’. In: *Acta Mech. Sin.* 30.1 (2014), pp. 20–27.
- Whitaker, S. (1986). ‘Flow in porous media I: A theoretical derivation of Darcy’s law’. In: *Transp. Porous Media* 1.1 (1986), pp. 3–25.
- Wickramasinghe, S., Carlson, J., Teske, C. A., Hubbell, J. H., and Ulbricht, M. (2006). ‘Characterizing solute binding to macroporous ion exchange membrane adsorbers using confocal laser scanning microscopy’. In: *J. Memb. Sci.* 281.1-2 (Sept. 2006), pp. 609–618.
- Williams, A., Taylor, K., Dambuleff, K., Persson, O., and Kennedy, R. M. (2002). ‘Maintenance of column performance at scale’. In: *J. Chromatogr. A* 944.1-2 (2002), pp. 69–75.
- Yan, Y., Zhang, Z., Stokes, J. R., Zhou, Q. Z., Ma, G. H., and Adams, M. J. (2009). ‘Mechanical characterization of agarose micro-particles with a narrow size distribution’. In: *Powder Technol.* 192.1 (May 2009), pp. 122–130.
- Yang, W.-C. (2003). *Handbook of Fluidization and Fluid-Particle Systems*. New York - Basel: Marcel Dekker, 2003.
- Yao, Y. and Lenhoff, A. M. (2006). ‘Pore size distributions of ion exchangers and relation to protein binding capacity’. In: *J. Chromatogr. A* 1126.1-2 (2006), pp. 107–119.
- Yuan, Q. S., Rosenfeld, A., Root, T. W., Klingenberg, D. J., and Lightfoot, E. N. (1999). ‘Flow distribution in chromatographic columns’. In: *J. Chromatogr. A* 831.2 (1999), pp. 149–165.
- Zener, C. M. (1948). *Elasticity and anelasticity of metals*. Chicago, Illinois: University of Chicago Press, 1948.
- Zhao, L. and Zhang, Z. (2004). ‘Mechanical characterization of biocompatible microspheres and microcapsules by direct compression.’ In: *Artif. Cells. Blood Substit. Immobil. Biotechnol.* 32.1 (2004), pp. 25–40.
- Zhou, Z. Y., Kuang, S. B., Chu, K. W., and Yu, a. B. (2010). ‘Discrete particle simulation of particle–fluid flow: model formulations and their applicability’. In: *J. Fluid Mech.* 661 (2010), pp. 482–510.
- Zhu, H. P., Zhou, Z. Y., Yang, R. Y., and Yu, a. B. (2007). ‘Discrete particle simulation of particulate systems: Theoretical developments’. In: *Chem. Eng. Sci.* 62.13 (2007), pp. 3378–3396.

- Zhu, H. P., Zhou, Z. Y., Yang, R. Y., and Yu, a. B. (2008). 'Discrete particle simulation of particulate systems: A review of major applications and findings'. In: *Chem. Eng. Sci.* 63.23 (2008), pp. 5728–5770.
- Ziółkowski, D. (1988). 'Fluid Flow inside Packed Beds'. In: *Chem. Eng. Process* 23 (1988), pp. 137–164.

A. Materials and Equipment

Table A.1.: Chromatographic media.

Product name	Material	d_p , μm	Manufacturer
Affi Gel 102	Agarose	100	Bio-Rad Laboratories GmbH, München, Germany
Blue Sepharose 6FF [®]	Agarose	90	GE Healthcare Europe, Munich, Germany
Sepharose 6FF [®]	Agarose	90	GE Healthcare Europe, Munich, Germany
TOYOPEARL AF-Amino-650M	Hydroxylated methacrylate	65	Tosoh Bioscience, Stuttgart, Germany
TOYOPEARL Butyl-650S	Hydroxylated methacrylate	35	Tosoh Bioscience, Stuttgart, Germany
TOYOPEARL Butyl-650M	Hydroxylated methacrylate	65	Tosoh Bioscience, Stuttgart, Germany
TOYOPEARL Butyl-650C	Hydroxylated methacrylate	100	Tosoh Bioscience, Stuttgart, Germany
TOYOPEARL SP-650M	Hydroxylated methacrylate	65	Tosoh Bioscience, Stuttgart, Germany
TOYOPEARL SP-650C	Hydroxylated methacrylate	100	Tosoh Bioscience, Stuttgart, Germany
TOYOPEARL SuperQ-650C	Hydroxylated methacrylate	100	Tosoh Bioscience, Stuttgart, Germany
TOYOPEARL MegaCap II SP-550EC	Hydroxylated methacrylate	200	Tosoh Bioscience, Stuttgart, Germany

Table A.2.: Chemicals and contrast agents.

Product name	Manufacturer	Article Number
Acetonitrile, $\geq 99.5\%$ purity	Sigma Aldrich	L110001
Bromothymol blue	Merck	103026
Calcium chloride	Sigma Aldrich	449709-10G
Dimethyl sulfoxide, $\geq 99.7\%$ purity	Sigma Aldrich	D2650-5X10ML
Ethanol, $\geq 99.5\%$ purity	Merck	100986
Imeron 400 MCT	Bracco Imaging Deutschland GmbH	701061
Iodine, $\geq 99.9\%$ purity	Sigma Aldrich	326143-10G
Phenolphthalein	Sigma Aldrich	105945-100G
Phosphotungstic acid solution, 10 % (w/v)	Sigma Aldrich	HT152-250ML
Potassium permanganate	Merck	105080
Silver nitrate, $\geq 99.9\%$ purity	Sigma Aldrich	204390-10G
Sodium hydroxide	Roth	9356
Sodium bicarbonate	Sigma Aldrich	S5761-500G
Triethylamine, $\geq 99\%$ purity	Sigma Aldrich	T0886-100ML

Table A.3.: Fluorescent dyes. All purchased from ThermoFisher Scientific (life technologiesTM), Darmstadt, Germany.

Dye	O-10465	O-6185	F-2181	A-30052
Name	Oregon Green [®] 488 Cadaverine	Oregon Green [®] 488-X, Succinimidyl ester	5(6)-SFX (Fluorescein-5-(and-6)-Carboxamido) Hexanoic Acid, Succinimidyl ester)	(6-Alexa Fluor [®] 488 Sulfodichlorophenol (SDP) ester
Reactive group	Amine	Succinimidyl ester	Succinimidyl ester	SDP ester
Molecular weight	496.4	622.5	586.5	884.91
Excitation, nm	494	494	494	495
Emission, nm	521	521	522	519
Reacting particle	Toyopearl SP-650	Toyopearl Amino-650	AF Toyopearl Amino-650	AF Toyopearl Amino-650

Table A.4.: Optical measuring equipment.

Equipment	Manufacturer
Optical microscope type Axioplan	Carl Zeiss, Göttingen, Germany
LSM510 META confocal laser scanning microscope	Carl Zeiss, MicroImaging GmbH, Jena, Germany
Micro Computer Tomograph type Xradia Versa XRM-500	Carl Zeiss, Oberkochen, Germany
Micro Computer Tomograph type XradiaXCT-400	Carl Zeiss, Oberkochen, Germany

Table A.5.: Further equipment.

Equipment	Manufacturer
Centrifuge 5415 R	Eppendorf, Hamburg, Germany
Vortex Genie 2	Scientific Industries, New York, USA
Rotary Shaker RM-2M	NeoLab, Heidelberg, Germany
Drying oven E28	Bindner, Tuttlingen, Germany
Micropipette 20 μ L, 200 μ L, 1000 μ L	Brand, Wertheim, Germany
pH electrode BlueLine 24 pH	Schott, Mainz, Germany
pH-meter CG 843	Schott, Mainz, Germany
Water bath	Thermo Haake, Karlsruhe, Germany

Table A.6.: Software and operating systems.

Software	Version	Manufacturer
Experimental data processing software		
Windows	7, SP2	Microsoft Corporation
AxioVision	4.7.2	Carl Zeiss, Göttingen, Germany
ImageJ	1.49s	National Institutes of Health, USA, (https://imagej.nih.gov/ij)
FlowDDE,	3.43	Bronkhorst High-Tech, Germany, (http://www.bronkhorst.com/en/products/accessories_and_software/bronkhorst_flowware/)
FlowPlot,		
FlowView		
Canon EOS Utility	2.14.20a	Canon U.S.A., Inc., Melville, NY, USA (https://www.usa.canon.com/internet/portal/us/home/support/details/cameras/dslr/eos-70d?tab=Drivers&Downloads)
Simulation and data processing software		
Linux Mint	17.3	Clement Lefebvre and community (www.linuxmint.com)
Liggghts [®]	3.3.1	DCS Computing GmbH, Linz, Austria (https://www.cfdem.com)
OpenFOAM	3.0.x	OpenCFD Ltd., Bracknell, UK (https://openfoam.org/)
CFDEM coupling [®]	3.3.0	DCS Computing GmbH, Linz, Austria (https://www.cfdem.com)
ParaView	5.0.0	Sandia National Laboratory, Kitware Inc, Los Alamos National Laboratory, USA (www.paraview.org)
MATLAB	2014b	The MathWorks, Natick, Massachusetts, USA

B. Supplementary Information

B.1. Laboratory Equipment

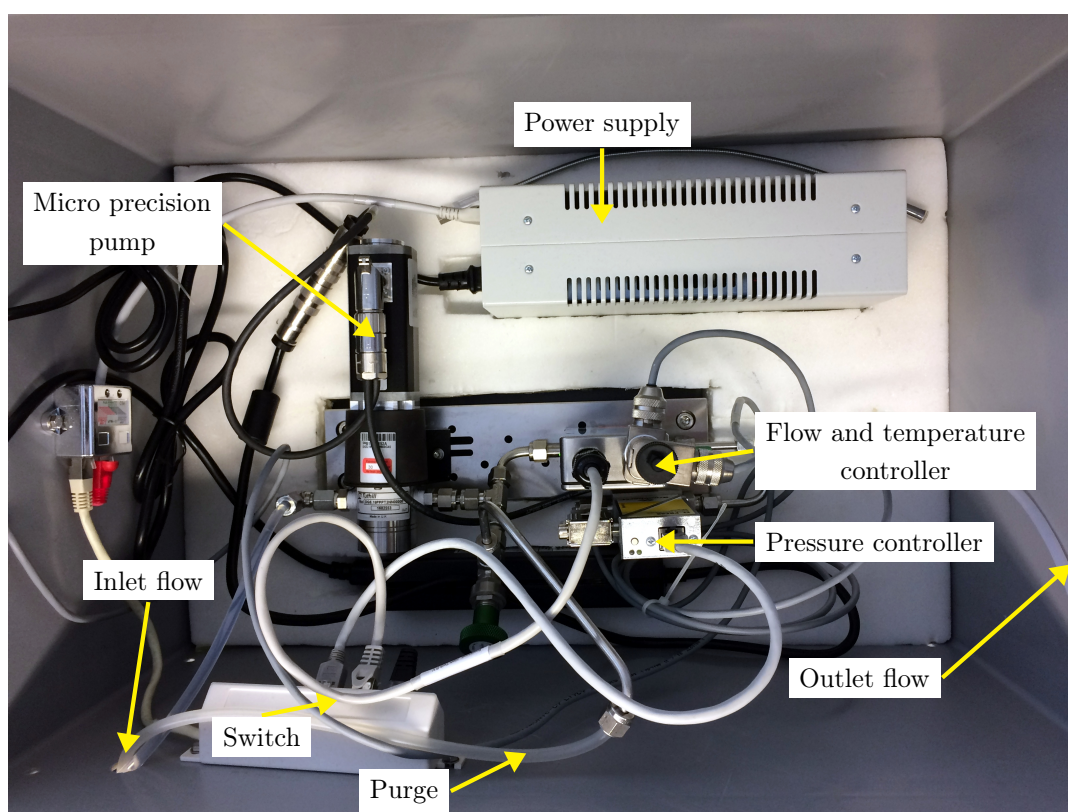


Figure B.1.: Portable process control set-up. The process control set-up consisting of the micro precision pump, the controller units for flow, temperature and pressure, and the power supply was built in a portable transport box, so that the column operation experiments could be carried out at different institutes in which the different microscopes and computer tomographs were located. The computer with the process control software was connected to the switch. The purge tube was necessary to remove air that accumulated within the tubing.

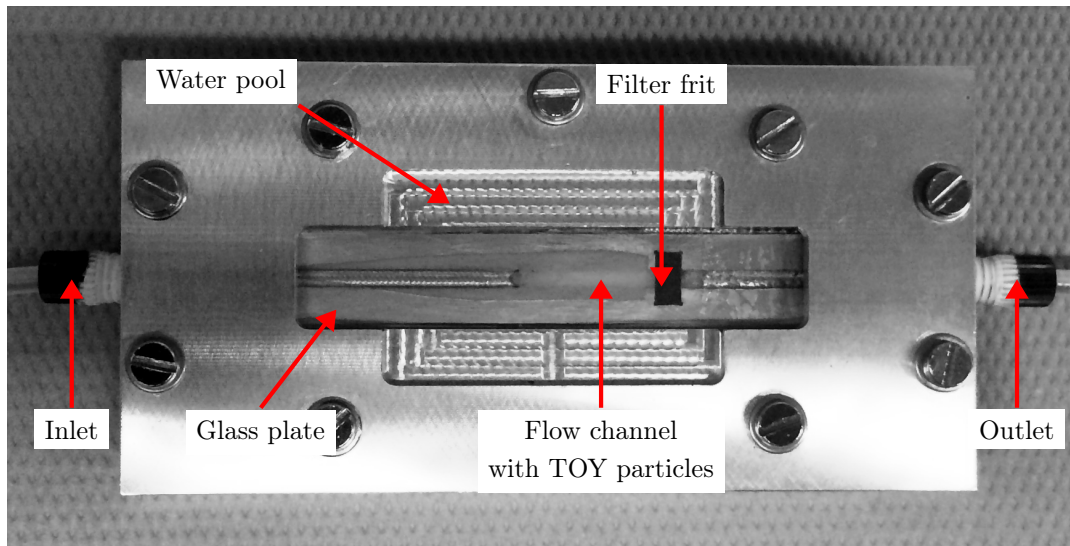


Figure B.2.: Microfluidic device for Confocal Laser Scanning Microscopy (CLSM) measurements. The device contained a water pool, so that the optical lenses of the CLSM could be submerged in water or oil in order to reduce optical refraction of laser beam.

B.2. CFD-DEM Simulations

Table B.1.: Further parameters of the DEM-model.

DEM parameter	Value
characteristicVelocity, m s ⁻¹	0.1
particle density, kg m ³	1140
gravity, m s ⁻²	9.81
timestep, s	2e-6
neighbor	0.00002 bin

Table B.2.: Column wall and particle parameters of the DEM-model. Parameters are given in DEM notation for the column wall (w), for the particles (p) as well as for the interaction of particles with the column wall (w-p, p-w).

DEM parameter	Value		Contact specific values			
	w	p	w-w	w-p	p-w	p-p
youngsModulus, Pa	1e10	3e7				
poissonsRatio, -	0.5	0.2				
coefficientRestitution, -			0.5	0.5	0.5	0.5
MaximumRestitution, -			0.9	0.9	0.9	0.9
coefficientFriction, -			0.0	0.1-0.5	0.1-0.5	0.1
coefficientRollingFriction, -			0.35	0.35	0.35	0.35
FluidViscosity, Pa s			1e-3	1e-3	1e-3	1e-3
CriticalStokes			0.3	0.3	0.3	0.3

Table B.3.: Boundary and initial conditions of the CFD-model. Fluid flow velocities were stepwise increased as in the laboratory experiments.

Parameter	Initial condition		Boundary conditions	
	<i>internalField</i>	<i>inlet</i>	<i>outlet</i>	<i>wall</i>
Ksl	uniform 0	zeroGradient	zeroGradient	zeroGradient
p, $\text{m}^2 \text{s}^{-2}$	uniform 100	zeroGradient	fixedValue value uniform 100	zeroGradient
rho, kg m^{-3}	uniform 1000	zeroGradient	zeroGradient	zeroGradient
U, m s^{-1}	uniform (0 0 $-U_z$)	fixedValue value uniform (0 0 $-U_z$)	zeroGradient	fixedValue value uniform (0 0 0)
Us, m s^{-1}	uniform (0 0 $-U_z$)	zeroGradient	zeroGradient	zeroGradient
voidfraction	uniform 1	zeroGradient	zeroGradient	fixedValue value uniform 1
dSmoothing, m	uniform 0	zeroGradient	zeroGradient	zeroGradient
sSmoothField	uniform 0	zeroGradient	zeroGradient	zeroGradient
vSmoothField	uniform 0	zeroGradient	zeroGradient	zeroGradient

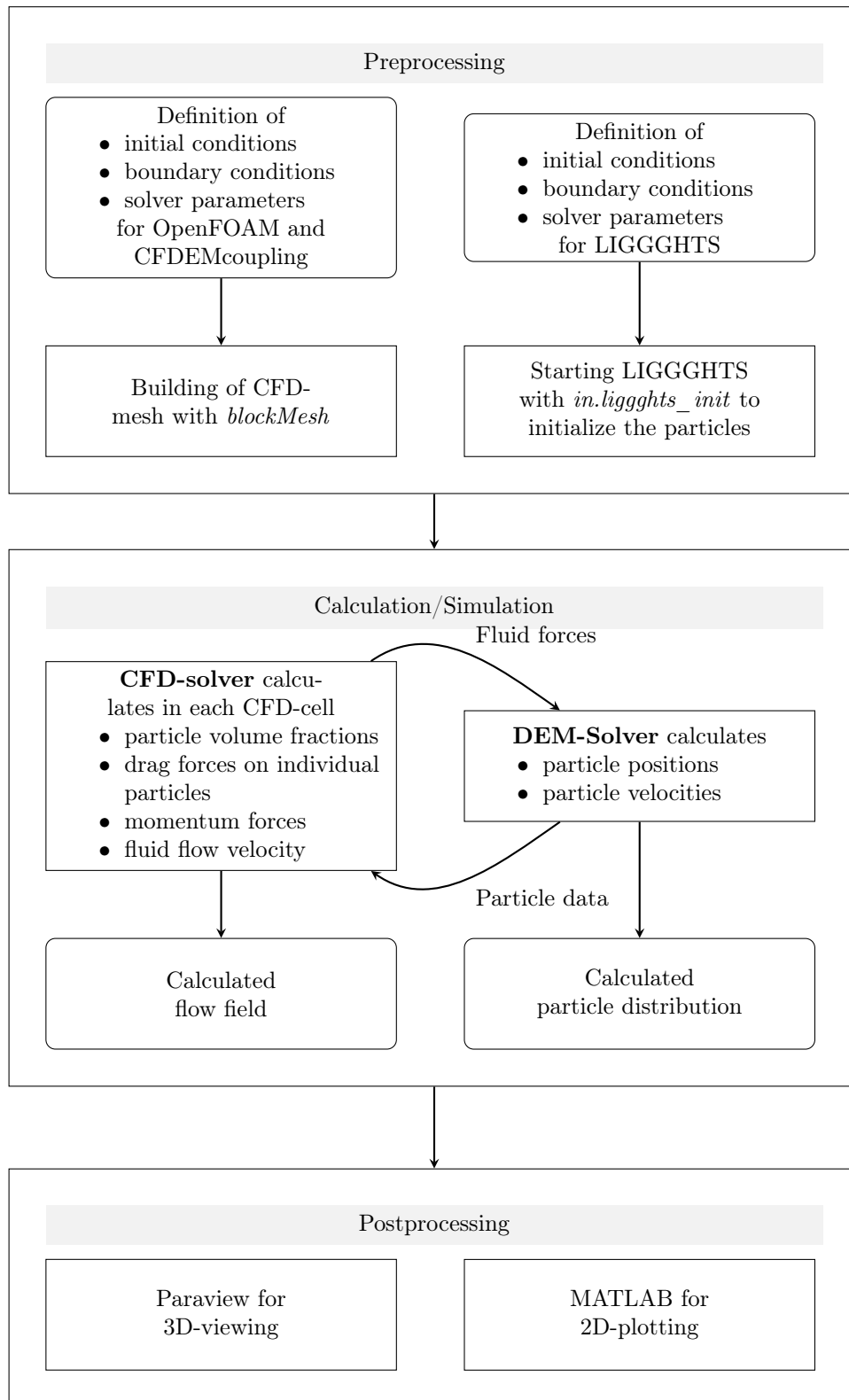


Figure B.3.: Sequence of a coupled CFD-DEM simulation.

Table B.4.: CFD-DEM coupling settings and submodels used in the simulations.

Modell	Type	Properties	Value
modelType	A		
couplingInterval		1000	
voidFractionModel	divided	alphaMin	0.01
		scaleUpVol	1.0
locateModel	engine	treeSearch	true
meshMotionModel	noMeshMotion		
regionModel	allRegion		
IOModel	trackIO		
probeModel	off		
dataExchangeModel	twoWayMPI	liggghtsPath	../DEM/in.liggghts_run
averagingModel	dense		
clockModel	standardClock		
smoothingModel	constDiffSmoothing	lowerLimit	0.1
		upperLimit	10000
		smoothingLength	50e-5
forceModels	KochHillDrag	velFieldName	U
		densityFieldName	rho
		voidfractionFieldName	voidfraction
		interpolation	true
		implForceDEM	true
		scale (Coarse Grain)	3.0
	gradPForce	pFieldName	p
		voidfractionFieldName	voidfraction
		velocityFieldName	U
		interpolation	true
	viscForce	velocityFieldName	U
		interpolation	true
momCoupleModel	implicitCouple	velFieldName	U
		granVelFieldName	Us
		voidfractionFieldName	voidfraction
turbulenceModelType	RASProperties		

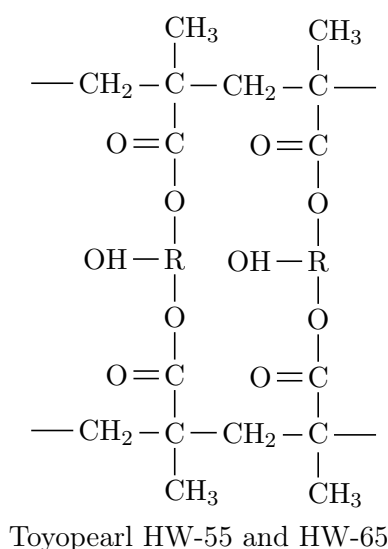
Table B.5.: Numerical schemes used in the simulations.

Discretization	Scheme	Characteristic
Time $\partial/\partial t$	CrankNicolson 0.3	bonded, implicit
Gradient terms ∇U	Gauss linear	second order accurate, robust
Convective terms $\nabla \cdot (\rho UU)$	Gauss MUSCL phi	second order accurate, robust
Diffusion terms $\nabla \cdot (D\nabla U)$	Gauss linear orthogonal	second order accurate, robust
Interpolation	linear	

C. Supplementary Methods

C.1. Fluorescent Labeling of Chromatographic Particles

The Toyopearl[®] particles used in this work are based on the *HW-65* and *HW-55* methacrylate-matrix, whose chemical structure can be seen in Scheme 1.



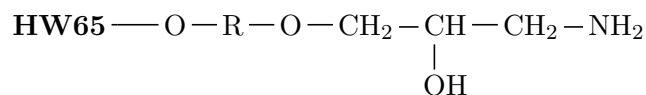
Scheme 1: Chemical structure of Toyopearl HW-65 and HW-55 base matrix. R = Hydroxylated Aliphatic Group. (Source: <http://www.separations.us.tosohbioscience.com/Products/ProcessMedia/ByMode/SEC/ToyopearlHW65.htm>)

C.1.1. Relevant Particle Properties

Chromatography Based on a Methacrylic Matrix

Toyopearl[®] AF-Amino-650M. The AF-Amino-650M is a reactive Toyopearl affinity resin designed for coupling proteins and low molecular weight ligands. Basically it is the

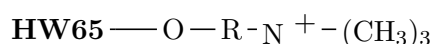
HW-65 base matrix coupled with an amine group (NH₂) ligand. A schematic view of this coupling is given in Scheme 2. The ligand density is declared to be 100 μmol/mL.



Scheme 2: Chemical ligand structure of reactive Toyopearl AF-Amino-650M resin.

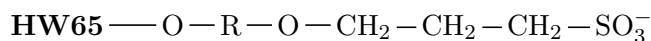
AF-Amino-650M resins are able to bond carboxyl groups (peptide bond formation) or aldehyde groups (reductive amination). The mean particle diameter is 65 μm.

Toyopearl[®] SuperQ-650. The SuperQ-650 are strong anion exchange resins designed for coupling therapeutic proteins. A positively charged nitrogen ligand is connected to the HW-65 base polymer as shown in Scheme 3. The SuperQ-650 resins are available in three different particle sizes, S, M and C.



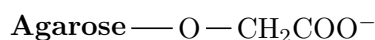
Scheme 3: Chemical ligand structure of Toyopearl SuperQ-650 resin.

Toyopearl[®] MegaCap II SP-550EC and SP-650. MegaCap II SP-550EC and SP-650 are strong and weak cation exchange resins designed for purification of molecules from small peptides such as insulin up to 100 kDa. A negatively charged sulphonate ligand is connected to the HW-65 base polymer as shown in Scheme 4. The SP-650



Scheme 4: Chemical ligand structure of Toyopearl SP-650 resin.

resins are available in three different particle sizes, S, M and C. MegaCap II SP-550EC resins are based on the HW-55 matrix that has a mean pore size of 50 nm and a mean particle diameter of 200 μm.



Scheme 5: Chemical ligand structure of CM Sepharose Fast Flow and Affi-Gel 102 resin.

Chromatography Media Based on an Agarose Matrix

Sepharose 6 Fast Flow[®] belongs to the ion exchange chromatography media and consists of 6 % highly cross-linked agarose. Agarose is a biopolymer built of D-galactose and 3,6-anhydro-L-galactose monomers (repeating unit: C₁₂H₁₈O₉).

As there are several ion exchange resins, for strong and weak anion or cation exchange, the focus is on the weak cation exchange CM Sepharose 6FF[®]. The average particle size of the CM Sepharose Fast Flow is given by 90 μm by the manufacturer. For operating conditions the optimal fluid flow velocity is in a range of 300-600 cm h⁻¹ for CM Sepharose 6 FF[®]. As the same for the Toyopearl resins, the Sepharose particles need to be stored in a 20 % ethanol buffer.

C.1.2. Contrast Agents for Microscopic Particle Analysis

As the porous polymer particles are nearly transparent for light and X-rays the use of certain contrast agents is essential to obtain evaluable images. However, it resulted as challenging to bond appropriate contrast agents to the host polymer particles in a strong or covalent manner. As the column is in operation during packing analysis it needs to be assured that the contrast agents will not be resolved in the mobile phase or washed out. In the following, different contrast agents are presented, that can be used as contrast enhancing agents during application of Confocal Laser Scanning Microscopy (CLSM) as well as for Micro Computer Tomography (Micro-CT).

Covalent Bonding Between Polymer and the Fluorescent Contrast Agent

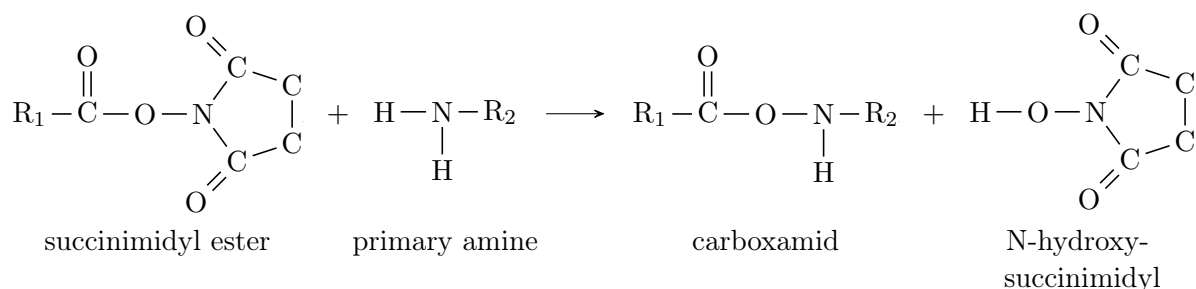
The use of CSLM in chromatography resin analysis is increasing in recent years. Information about its application for research on pore diffusion issues, adsorption kinetics or resin behavior can be found elsewhere [Teske et al. 2005; Teske and von Lieres 2006; Wickramasinghe et al. 2006; Susanto and Herrmann 2007; Hubbell and Kula 2008].

The existence of special ligands added to the resins base matrix allows to covalently bond selected fluorescent molecules and therefore to study the single beads using the

CLSM technique. This is especially the case for affinity chromatography resins as there are functional amine or carboxyl groups present.

Coupling to Aminated Resins. Most affinity chromatography resins contain functional primary amines ($R-NH_2$) as ligands so that peptide or amid bond formation is possible.

For CLSM analysis fluorescent molecules are needed to label each chromatography bead. Therefore amine-reactive fluorophores can be used that are mostly acylating reagents that form carboxamides, sulfonamides or thioureas upon reaction with amines [Johnson and Spence 2010]. Acylation is the chemical process of adding a acyl group ($R-CO-$) to a compound, in that case to the primary amine, where one hydrogen atom gets replaced. Hence fluorescent molecules such as succinimidyl esters are reliable reagents for amine modification as they form amide bonds that are as stable as peptide bonds. In the case of fluorophores containing esters the amid bond is formed by separating the ester from the acyl group and couple that group to the primary amine as shown in Scheme 6.



Scheme 6: Reaction of a primary amine with succinimidyl ester.

Excellent results were obtained by the use of sulfodichlorophenol (SDP) esters as fluorophores. Currently they are reported as the most hydrolytically stable stable amine-reactive dye, as they form the same strong amide bond as succinimidyl esters [Johnson and Spence 2010]. The used *Alexa Fluor[®] 488 5-SDP Ester* is sold by *life technologiesTM* (Life Technologies GmbH, Darmstadt, Germany) as an bright and highly photostable conjugate with good water solubility and pH insensitivity. Using an argon-ion laser this conjugate has a maximum adsorption wavelength of 488 nm and a maximum emission wavelength of 519 nm [Johnson and Spence 2010].

In comparison with succinimidyl based fluorescent dyes available on the market the *Alexa Fluor*[®] 488 5-SDP Ester (*life technologies*TM) is the most expensive one so that the succinimidyl esters *Oregon Green*[®] 488-X Succinimidyl Ester (O6185) and 5(6)-SFX (6-(Fluorescein-5-(and-6)-Carboxamido) Hexanoic Acid, Succinimidyl Ester) (F2181, *life technologies*TM) were selected as suitable enough for CLSM analysis.

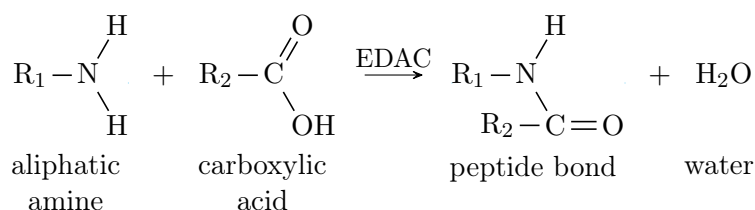
The particle dying is carried out as follows:

1. 150 μ L of particles in suspension were centrifuged at 800 rpm (centrifuge type: 5415 R, supplier: Eppendorf AG, Hamburg, Germany) and the supernatant removed with a pipette.
2. 1 mL of a sodium bicarbonate solution (0.1 M) was added, mixed with the beads, centrifuged at 800 rpm, and the supernatant was removed with a pipette. This washing step was repeated three times.
3. Afterwards the medium was suspended in 400 μ L sodium bicarbonate.
4. 1 mg dye in powder form was dissolved in 100 μ L DMSO (dimethyl sulfoxide).
5. This dissolved dye was added to the beads in 400 μ L sodium bicarbonate.
6. The particle suspension was mixed overnight using a rotary shaker (type: RM-2M, supplier: neoLab Migge, Heidelberg, Germany).
7. The suspension was centrifuged at 800 rpm and the supernatant removed with a pipette. The resulting beads were of bright orange color, the supernatant neon yellow.
8. 1 mL of purified water was added, mixed, centrifuged at 800 rpm, and the supernatant removed with a pipette. This washing step was repeated three times. The supernatant was clear after the second repetition.
9. Finally, 200 μ L purified water were added and the solution was stored at 4 °C.

Coupling to Carboxylated Resins. As carboxylic acids can be converted into esters, amides, acyl hydrazides or hydroxamic acids, the above listed carboxyl group containing weak affinity and ion-exchange chromatography media can also be labeled with fluorescent dyes.

The carboxylic acids can be coupled to hydrazines, hydroxylamines and amines in aqueous solution using water-soluble carbodiimides such as 1-ethyl-3-(3-dimethylaminopropyl

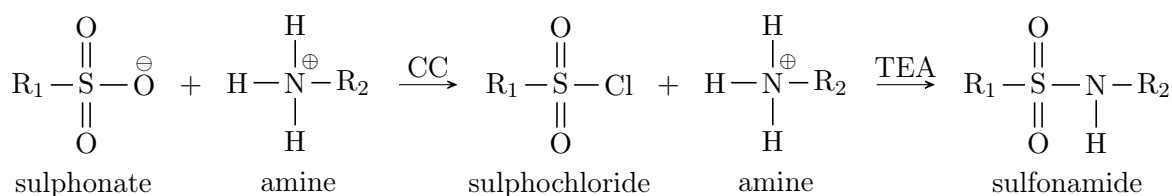
carbodiimide (EDAC, E2247). With amine group containing fluorophores nearly the same amid or peptide bond is possible. The carbodiimides are necessary because of its functionality as dehydration agents to activate carboxylic acids towards amide formation. This and further coupling techniques such as enzyme catalyzed transamidation are described elsewhere. [Johnson and Spence 2010] The dying process of carboxylated



Scheme 7: Reaction of a aliphatic amine with carboxylic acid.

resins is analogue to the aminated resins.

Coupling to Sulphonated Resins. ion-exchange chromatography resins that contain ligands with sulphonate groups can be made accessible for fluorophore labeling via a synthesis approach. Sulphonates are able to react with amides to sulphonamides with very low yield. Therefore the use of synthesis agents such as cyanurchlorid as described by Rad et al. [2009] can increase the yield. The basic reaction scheme is shown in Scheme 8.



Scheme 8: Reaction of a primary amine and a sulfonate group.

Here cyanurchlorid (CC) is necessary for the intermediate reaction to sulphochloride. Triethylamine (TEA) serves as base to neutralize the formed hydrochloric acid in sulphonamide formation. As amide containing fluorescent dyes for example *Oregon Green[®] 488 Cadaverine* (O10465, *life technologiesTM*) can be used as it already was tested successfully.

The particle dying is carried out as follows:

1. 150 μL of TOY particles in suspension were centrifuged at 800 rpm and the supernatant removed with a pipette.
2. 1 mL of a Acetonitrile was added, mixed with the beads, centrifuged at 800 rpm, and the supernatant was removed with a pipette. This washing step was repeated three times.
3. Afterwards the medium was suspended in 400 μL Acetonitrile.
4. 1 mg O10465 dye in powder form was dissolved in 400 μL DMSO (dimethyl sulfoxide).
5. This dissolved dye was added to the beads in 400 μL sodium bicarbonate.
6. The particle suspension was mixed for 5 h using a rotary shaker.
7. Adding 50 μL Triethylamine (TEA) and further mixing for 3 h using a rotary shaker.
8. The suspension was centrifuged at 800 rpm and the supernatant removed with a pipette.
9. 1 mL of purified water was added, mixed, centrifuged at 800 rpm, and the supernatant removed with a pipette. This washing step was repeated three times. The supernatant was clear after the second repetition.
10. Finally, 200 μL purified water were added and the solution was stored at 4 $^{\circ}\text{C}$.

Covalent bonding between polymer and iodine containing contrast agent

Few reports of computer tomographic application in chromatography resin analysis can be found in literature [Lottes et al. 2009]. This method is reported as useful for flow and hydrodynamics analysis in the inside of a packed chromatography bed [Schmidt et al. 2011, 2012]. For detailed analysis the resolution of the up to now used computer tomography is too low as each single bead needs to be evaluated. Therefore micro computer tomographic microscopy is a promising technique that meets the requirements for analysis of column hydrodynamics in laboratory scale.

Similar to the fluorescent dyes the X-ray contrast agents also need be covalently bonded to the polymer matrix. 5-Amino-2,4,6-triiodoisophthalic acid (Sigma-Aldrich, Taufkirchen, Germany) is a contrast agent used for X-ray tomography that contains a carboxyl as well as an amine group as coupling positions.

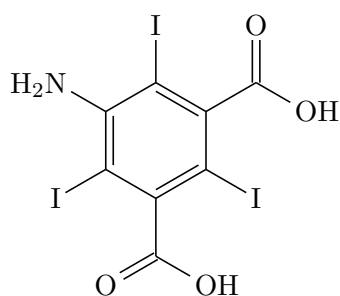


Figure C.1.: 5-Amino-2,4,6-triiodoisophthalic acid x-ray tomography contrast agent

However, it turned out, that this contrast agent did not bond successfully to the polymeric particle matrix, which is likely due to steric hindrance of the molecules at the particle surface. A molecule similar to 5-Amino-2,4,6-triiodoisophthalic acid containing a longer linker arm might be promising.

C.2. Derivation of the SLS model

The well-known *Standard Linear Solid* (SLS) model, also known as the Zener-k-model or Zener-m-model according to Zener [1948] is composed of a Kelvin-Voigt (spring and dashpot in parallel) or Maxwell element (spring and dashpot in series) in combination with a Hookean spring. The “k” and “m” stand for the Kelvin-Voigt and Maxwell type of the SLS model.

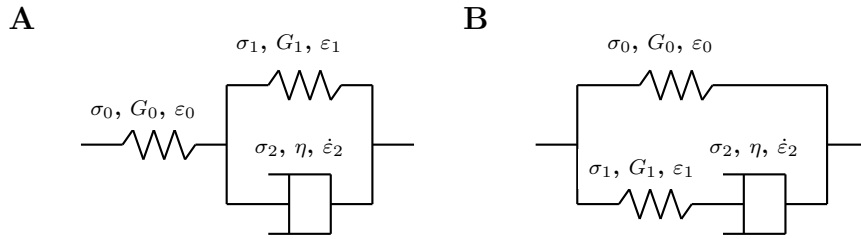


Figure C.2.: Schematic representation of the SLS model types. (A) shows the Kelvin type of the SLS model as a Voigt-element (spring and dashpot in parallel) in series with a free spring and (B) shows the Maxwell type of the SLS model as a Maxwell-element (spring and dashpot in series) in parallel with an equilibrium spring. G_0 is the shear modulus of the free spring and G_1 and η are the shear modulus and shear viscosity of the spring and dashpot of the Voigt or Maxwell element, respectively.

The overall stress-strain relation of the SLS model is derived as follows: In general, the following physical relations are given:

Parallel components:

$$\sigma_{tot} = \sigma_1 + \sigma_2 \quad (\text{C.1})$$

$$\varepsilon_{tot} = \varepsilon_1 = \varepsilon_2 = \varepsilon \quad (\text{C.2})$$

Series components:

$$\sigma_{tot} = \sigma_1 = \sigma_2 = \sigma \quad (\text{C.3})$$

$$\varepsilon_{tot} = \varepsilon_1 + \varepsilon_2 \quad (\text{C.4})$$

C.2.1. Kelvin type of the SLS model

Stress-strain relation of the Kelvin-Voigt element

For the parallel connection of a Hookean spring with a Newtonian dashpot, the stress, σ_{Kelvin} , is given by ($\varepsilon_1 = \varepsilon_2 = \varepsilon_K$):

$$\sigma_{Kelvin} = G_1 \varepsilon_K + \eta \dot{\varepsilon}_K \quad (C.5)$$

Stress-strain relation of the Kelvin-Voigt element in series with a free spring

As the strain the Hookean spring is $\varepsilon_0 = \sigma_0/G_0$, the strain of the Kelvin-Voigt element is

$$\varepsilon_K = \varepsilon_{tot} - \varepsilon_0. \quad (C.6)$$

Substitution of Equation (C.6) in Equation (C.5) and noting $\varepsilon_{tot} = \varepsilon$ gives

$$\sigma = G_1 \left(\varepsilon - \frac{\sigma_0}{G_0} \right) + \eta \left(\dot{\varepsilon} - \frac{\dot{\sigma}_0}{G_0} \right) \quad (C.7)$$

Rearrangement and $\sigma_0 = \sigma$ leads to a conventional differential equation with two independent variables

$$\sigma \left(1 + \frac{G_1}{G_0} \right) + \frac{\eta}{G_0} \dot{\sigma} = G_1 \varepsilon + \eta \dot{\varepsilon} \quad (C.8)$$

$$\sigma + \frac{\eta}{G_0 + G_1} \dot{\sigma} = \frac{G_0 G_1}{G_0 + G_1} \varepsilon + \frac{G_0 \eta}{G_0 + G_1} \dot{\varepsilon}. \quad (C.9)$$

Equation (C.9) can be simplified using Laplace transformation with $\sigma = \bar{\sigma}$, $\dot{\sigma} = s\bar{\sigma}$ and $\varepsilon = \bar{\varepsilon}$, $\dot{\varepsilon} = s\bar{\varepsilon}$

$$(G_0 + G_1)\bar{\sigma} + \eta s\bar{\sigma} = G_0 G_1 \bar{\varepsilon} + G_0 s\bar{\varepsilon}. \quad (C.10)$$

The response to a strain $\varepsilon(t) = \varepsilon_0 H(t) = \varepsilon_0/s$ (Heaviside function) is

$$\left(\frac{G_0 + G_1}{\eta} + s \right) \eta \bar{\sigma} = G_0 G_1 \frac{\varepsilon_0}{s} + G_0 \eta \varepsilon_0 \quad (C.11)$$

$$\bar{\sigma} = \left(\frac{G_0 G_1}{\eta} \frac{1}{s \left(\frac{G_0 + G_1}{\eta} + s \right)} + \frac{G_0}{\left(\frac{G_0 + G_1}{\eta} + s \right)} \right) \varepsilon_0 \quad (\text{C.12})$$

$$\bar{\sigma} = G^{SLS}(s) \varepsilon_0. \quad (\text{C.13})$$

Using the Laplacian transformation correlations given in Table C.1 Equation (C.13)

Table C.1.: Standard Laplacian transformation correlations.

Time domain $f(t) = \mathcal{L}^{-1}F(s)$	Laplace s-domain $F(s) = \mathcal{L}f(t)$
$u(t)$	$\frac{1}{s}$
$e^{-\alpha t} \cdot u(t)$	$\frac{1}{s+\alpha}$
$(1 - e^{-\alpha t}) \cdot u(t)$	$\frac{\alpha}{s(s+\alpha)}$

can be transformed back into

$$G^{SLS}(t) = \frac{G_0 G_1}{G_0 + G_1} \left(1 - e^{-\frac{G_0 + G_1}{\eta} t} \right) + G_0 e^{-\frac{G_0 + G_1}{\eta} t} \quad (\text{C.14})$$

$$= \frac{G_0}{G_0 + G_1} \left[G_0 e^{-\frac{G_0 + G_1}{\eta} t} + G_1 \right]. \quad (\text{C.15})$$

C.2.2. Maxwell type of the SLS model

Stress-strain relation of the Maxwell element

Following the rules given with Equation (A.1-A.4) the governing equation for the Maxwell element is

$$\dot{\varepsilon} = \dot{\varepsilon}_1 + \dot{\varepsilon}_2 = \frac{\dot{\sigma}_M}{G_1} + \frac{\sigma_M}{\eta}. \quad (\text{C.16})$$

Laplace transformation leads to

$$\bar{\sigma}_M = \frac{G_1 s}{s + 1/\tau} \bar{\varepsilon} \quad (\text{C.17})$$

where $\tau = \eta/G_1$.

Derivation of the SLS model

Adding the Hookean stress $\bar{\sigma}_0 = G_0 \bar{\varepsilon}_0$ of the equilibrium spring, the total stress is

$$\bar{\sigma} = G_0\bar{\varepsilon}_0 + \frac{G_1s}{s + 1/\tau}\bar{\varepsilon} = \left[G_0 + \frac{G_1s}{s + 1/\tau} \right] \quad (\text{C.18})$$

Since $\mathcal{L}^{-1}(1/(s + a)) = e^{-at}$, this can be inverted to

$$G^{SLS}(t) = G_0 + G_1e^{-t/\tau}. \quad (\text{C.19})$$

C.3. Integration of the SLS model

The integration of Equation (C.20) is carried out the following way.

$$F(t) = \frac{\sqrt{2R}}{3(1-\nu)} \int_0^t 2G(t-t^*) \frac{\partial}{\partial t^*} (\Delta^{3/2}(t^*)) dt^* \quad (\text{C.20})$$

The differential $\frac{\partial}{\partial t^*} (\Delta^{3/2}(t^*)) dt^*$, where $\Delta = vt$ and v being the displacement velocity, is substituted by dt^* according to

$$\frac{\partial \Delta^{3/2}(t^*)}{\partial t^*} dt^* = \frac{3}{2} v^{3/2} t^{*1/2} dt^*. \quad (\text{C.21})$$

Replacing $G(t)$ by Equation (C.15) leads to

$$F(t) = \frac{G_0\sqrt{2R}v^3}{(1-\nu)(G_0 + G_1)} \int_0^t \underbrace{(G_0 t^{*1/2} e^{-(t-t^*)/\tau})}_{g(t^*)} + \underbrace{G_1 t^{*1/2}}_{h(t^*)} dt^*. \quad (\text{C.22})$$

Integration of $g(t^*)$:

$$G(t) = \int_0^t g(t^*) dt^* = G_0 \int_0^t t^{*1/2} e^{-(t-t^*)/\tau} dt^* = G_0 e^{-t/\tau} \int_0^t t^{*1/2} e^{t^*/\tau} dt^* \quad (\text{C.23})$$

Substitution $u = t^*/\tau$ leads to $du/dt^* = 1/\tau$ and

$$G(t) = G_0 \tau^{3/2} e^{-t/\tau} \int \sqrt{u} e^u du \quad (\text{C.24})$$

evaluation of the integral using partial integration according to $f' = e^u$ and $g = \sqrt{u}$ leads to

$$\int \sqrt{u} e^u du = \sqrt{u} e^u - \int \frac{e^u}{2\sqrt{u}} du \quad (\text{C.25})$$

again with a substitution $v = \sqrt{u}$ and $dv/du = 1/(2\sqrt{u})$ follows for the second integral

$$\int \frac{e^u}{2\sqrt{u}} du = \frac{\sqrt{\pi}}{2} \cdot \frac{2}{\sqrt{\pi}} \int e^{v^2} dv = \frac{\sqrt{\pi}}{2} \operatorname{erfi}(v) \quad (\text{C.26})$$

where $\operatorname{erfi}(v)$ is the imaginary error function. Backsubstitution and taking Equation (C.25) leads to

$$\int \sqrt{u} e^u du = \sqrt{u} e^u - \frac{\sqrt{\pi}}{2} \operatorname{erfi}(\sqrt{u}) \quad (\text{C.27})$$

Backsubstitution of u in Equation (C.24) results in

$$G(t) = G_0 \tau^{3/2} e^{-t/\tau} \left(\sqrt{u} e^u - \frac{\sqrt{\pi}}{2} \operatorname{erfi}(\sqrt{u}) \right) \quad (\text{C.28})$$

$$= \left[G_0 \tau^{3/2} e^{-t/\tau} \left(\sqrt{\frac{t^*}{\tau}} e^{t^*/\tau} - \frac{\sqrt{\pi}}{2} \operatorname{erfi} \left(\sqrt{\frac{t^*}{\tau}} \right) \right) \right]_0^t \quad (\text{C.29})$$

$$= \left[G_0 \tau t^{*1/2} e^{(t^*-t)/\tau} - G_0 \tau^{3/2} e^{(t^*)/\tau} \frac{\sqrt{\pi}}{2} \operatorname{erfi} \left(\sqrt{\frac{t^*}{\tau}} \right) \right]_0^t \quad (\text{C.30})$$

$$= G_0 \tau t^{1/2} - G_0 \tau^{3/2} e^{-t/\tau} \frac{\sqrt{\pi}}{2} \operatorname{erfi} \left(\sqrt{\frac{t}{\tau}} \right) \quad (\text{C.31})$$

Integration of $h(t)$ leads to

$$H(t) = \int_0^t h(t) d\tau = G_1 \int_0^t \sqrt{t} d\tau = \frac{2}{3} G_1 t^{3/2}. \quad (\text{C.32})$$

Taking all together results in the force-time relation for viscoelastic material on the basis of the SLS model.

$$F(t) = \frac{G_0 \sqrt{2Rv^3}}{(1-\nu)(G_0 + G_1)} \left[\frac{2}{3} G_1 t^{3/2} + G_0 \tau t^{1/2} - G_0 \tau^{3/2} e^{-t/\tau} \frac{\sqrt{\pi}}{2} \operatorname{erfi} \left(\sqrt{\frac{t}{\tau}} \right) \right] \quad (\text{C.33})$$

The Maxwell type of the force-time correlation can be obtained by the same way.

$$F_M(t) = \frac{\sqrt{2Rv^3}}{(1-\nu)} \left[\frac{2}{3} G_0 t^{3/2} + G_1 \tau t^{1/2} - G_1 \tau^{3/2} \frac{\sqrt{\pi}}{2} e^{-t/\tau} \operatorname{erfi} \left(\sqrt{\frac{t}{\tau}} \right) \right] \quad (\text{C.34})$$